THE UNIVERSITY *of* EDINBURGH

Prodrugs Activated by Implantable Microsystems

Daniel J. Norman

THE UNIVERSITY
of EDINBURGH

Doctorate of Philosophy

The University of Edinburgh

2019

Lay Summary

Cancer can manifest in many forms and can vary greatly from patient-to-patient. It is often treated by giving a cancer patient a drug which will attack the cancer cells to prevent them from growing and spreading throughout the body. However, these drugs will also attack healthy cells, which gives rise to a long list of side-effects of cancer chemotherapies.

Increasing the selectivity of the drugs, i.e. to promote attack of the cancer cells over the healthy cells, allows the patient to receive higher and more effective doses while minimising the infliction of harsh side-effects. This can be done through the design of prodrugs: drugs that are inactive until they reach the desired site of action, whereupon they are activated by a biological process, e.g. enzymes, to the active drug. While this can be an effective strategy, the biological processes of cancers are very similar to healthy tissues and so there may be some prodrug that is activated in healthy tissues that will result in side-effects.

To overcome these issues, herein is described alternative strategies for prodrug activation using electrical and light signals. This allows a prodrug to be given and the activation to the active drug to be controlled externally. Therefore, the location and timing of the prodrug activation can be selected to maximise the therapeutic effect.

Abstract

The need to improve selectivity in cancer therapies has driven much research into the design and methods of activation of prodrugs. These are primarily reliant on biological processes that are present ubiquitously in tissues (healthy and cancerous) but with elevated levels in and around cancers. As such many therapies still suffer from dose-limiting toxicities from off-target effects.

Herein are described novel methods of prodrug activation that are reliant on physical stimuli — namely electrical and photochemical triggers — to generate the active drug species. These methods allow exogenous control over where, when and how much prodrug is converted facilitating minimisation of off-target effects by increasing the selectivity of the therapy. In conjunction with the Implantable Microsystems for Personalised Anti-Cancer Therapies project, it is envisioned that these activation systems will be translatable into a device implantable and activatable within a tumour.

In my thesis, prodrug activation systems were developed for Pt(IV) prodrugs that use either electrochemical or photochemical approaches to convert bio-inert prodrugs into the cytotoxic Pt(II) counterparts. This was accomplished utilising a redox mediator or photocatalyst to limit biological interferences and improve selectivity towards the Pt species.

In summary, these prodrug activation systems were brought from the stage of discovery to biological evaluation and validation, with significant optimisation of

their activation capabilities. The application of these novel prodrug activation strategies forms the basis for future research in to the improvement of cancer therapies for the benefit of the patient and demonstrates for the first time cancer prodrug activation using an electrochemical approach.

Declaration of Authorship

The research detailed within this thesis has been accumulated by the author in the duration of his PhD studentship between the dates of September 2015 and January 2019 under the supervision of Professor Mark Bradley, School of Chemistry, University of Edinburgh.

The work, data, and interpretation presented here are those of the author unless there was significant collaborative contribution made, in which case it has been clearly recognised. Where published work has been consulted or quotations made, the source has been clearly cited. This work has not been submitted for any other degrees or professional qualifications. Part of the work presented herein has been published as:

Norman, D., González-Fernández, E., Clavadetscher, J., Tucker, L., Staderini, M., Mount, A.R., Murray, A. F. and Bradley, M., *Chemical Communications*, **2018**, 54, 9242-9245.

Acknowledgments

First and foremost, I would like to thank Professor Mark Bradley for giving me the opportunity to carry out my doctoral studies within his group on such an exciting project. The enduring support and guidance I have received from Mark throughout the past four years has been a huge proponent in the completion of this work.

I would also like to express my gratitude to those who have offered training and support for the use of their equipment: Dr. Lorna Eades (ICP-MS), Dr. Lorna Murray and Juraj Bella (NMR), Prof. Andy Mount (electrochemistry), Drs Logan McKay and Faye Cruickshank (MS) and Dr. Dave Kelly (microscopy).

I am also very grateful to the training and support received from Dr. Eva González-Fernández in electrochemistry and Dr. Jessica Clavadetscher in cell culture. Thanks are also due to the whole IMPACT team for helpful discussions; in particular, Dr. Matteo Staderini. Your support and friendship is highly appreciated. I am also grateful to Dr. Annamaria Lilienkampf for her support.

Life in the lab would not nearly be as enjoyable without all of my fellow (past and present) group members, particularly Alessia, Vikki, Gavin, Paul, Antonio and Kevin. I am always very grateful for the countless discussion of ideas, reaction mechanisms and crosswords.

On the personal side, I would like to thank my family and in particular my mother, Sandra, my sister, Sarah and my three nieces (Sophie, Emily and Katie) for their

endless support throughout my studies and career. Thanks are also due to my friends outside of work, especially Fraser, Lucy and Tooler.

Finally, I would like to thank my partner, Cliohna, for her endless patience and support, and for making the most challenging years of my career, the most enjoyable years of my life.

Abbreviations

COX	Cyclooxygenase
CT	Computerised tomography
CV	Cyclic voltammetry
DIPEA	*N,N*-diisopropylethylamine
DPV	Differential pulse voltammetry
FBS	Foetal bovine serum
FDA	US Food and Drug Administration
FITC	Fluorescein isothiocyanate
FRET	Förster resonance energy transfer
HBTU	Hexafluorophosphate benzotriazole tetramethyl uranium
HDAC	Histone deacetylase
HIF-1α	Hypoxia-inducible factor 1-alpha
HPLC	High-performance liquid chromatography
ICP-OES	Inductively-coupled plasma optical emission spectroscopy
ICP-MS	Inductively-coupled plasma mass spectrometry
LED	Light-emitting diode
MB	Methylene blue
MMP	Matrix metalloproteinase
MRI	Magnetic resonance imaging

MTT	3-(4,5-Dimethylthiazol-2-yl)-2,5-diphenyltetrazolium bromide
OxPt	Oxaliplatin
PBS	Phosphate buffered saline
PDK	Pyruvate dehydrogenase kinase
PEG	Polyethylene glycol

Table of Contents

LAY SUMMARY I

ABSTRACT II

DECLARATION OF AUTHORSHIP IV

ACKNOWLEDGMENTS V

ABBREVIATIONS VII

CHAPTER 1 1

INTRODUCTION 1

1. Overview of Cancer Pathophysiology *1*

1.1 Surgery *5*

1.2 Radiotherapy *9*

1.3 Chemotherapy *15*

1.4 Prodrugs *34*

CHAPTER 2 49

AIMS AND OBJECTIVES 49

CHAPTER 3 50

ELECTROCHEMICAL ACTIVATION OF PT(IV) PRODRUGS 50

3.1 Introduction *50*

3.2 Aims of Chapter 3 *54*

3.3 Background *54*

3.4 Discovery and design of Pt(IV) electro-activation system *58*

3.5 Identification of a suitable redox mediator *67*

3.6 Fabrication of discrete redox mediator modified electrodes *75*

3.7 Characterisation of Pt(IV) reduction by the modified electrodes *85*

3.8 In vitro validation of the Pt(IV) prodrug activation systems *100*

Conclusions and Outlook *112*

CHAPTER 4 115

PHOTO-ACTIVATION OF PT(IV) PRODRUGS WITH SIMULTANEOUS GENERATION OF SINGLET OXYGEN 115

4.1 Introduction *115*

4.2 Aims of Chapter 4 *123*

4.3 Background *124*

4.4 Discovery and design of a photocatalysed Pt(IV) prodrug activation system *128*

4.5 Identification of "bio-inert" Pt(IV) prodrugs *129*

4.6 Design, synthesis and optimisation of photosensitisers *135*

4.7 Characterisation of photosensitiser 16 *140*

4.8 Fabrication of custom light sources *144*

4.9 Characterisation of photocatalytic Pt(IV) prodrug activation *148*

4.10 Validation of photocatalysed Pt(IV) prodrug activation in cellulo *153*

4.11 Extension of application of photocatalytic Pt(IV) prodrug activation *157*
4.12 Elucidation of the mechanism of photocatalytic Pt(IV) prodrug activation *161*
Conclusions and Outlook *167*

CHAPTER 5 **172**

EXPERIMENTAL 172
5.1 General *172*
5.2 Electrochemical measurements *173*
5.3 Small molecule synthesis *173*
5.4 Electrode cleaning and modification *199*
5.5 Fabrication of light sources *201*
5.6 In vitro assays *202*
5.7 Cell culture assays *207*

REFERENCES **214**

Chapter 1

Introduction

1. Overview of Cancer Pathophysiology

Cancer is a complex collection of diseases caused by genomic mutations that result in aberrant cell behaviour. Gain-of-function mutations that occur in oncogenes and loss-of-function mutations that occur in tumour suppressor genes have the potential to cause acquired characteristics of cancer cells, which have been codified by the 'hallmarks' of cancer (Figure 1.1)[1].

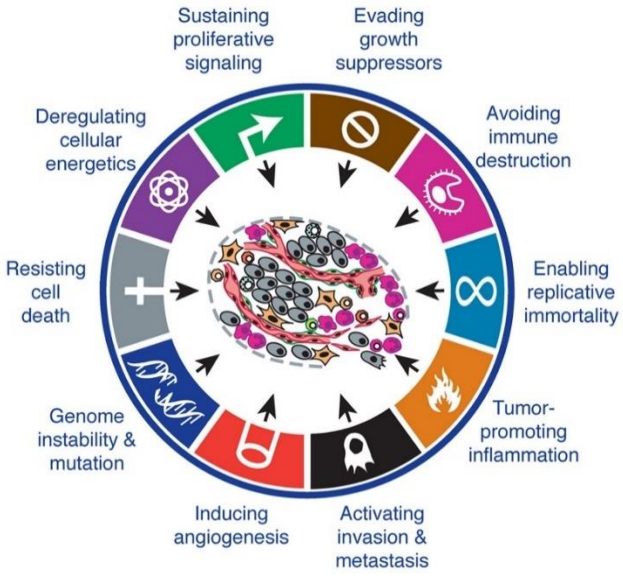

Figure 1.1. The hallmarks of cancer: the defining characteristics of which cancers will acquire to sustain tumour growth and progression. Image reproduced from reference [1] with permissions granted by Elsevier Publishing.

Cancerous cells often exhibit unchecked cell growth, division and replicative potential. As a result, a neoplasm (or tumour) may form as a mass of uncoordinated growth of cancer cells. The tumour microenvironment becomes hypoxic and acidic due to the rapidly increasing tumour mass, correlated with increasing oxygen consumption and carbon dioxide generation, which may be accompanied by a metabolic switch (termed the Warburg effect) from the regular oxidative phosphorylation pathways to glycolytic metabolism that produces lactate as a by-product[2].

Two of the most commonly mutated genes found in cancers are the p53 tumour suppressor gene and the Ras oncogene[3-5]. Both have myriad functions in the regulation of cellular signalling pathways. The p53 gene products are mainly responsible for conserving the integrity of the cell cycle. Over half of all human cancers display inactivated forms of p53 by missense mutations, typically in the DNA-binding domain. The inactivation of p53 allows cancers cells to bypass cell cycle checkpoints as well as to resist growth arrest and apoptotic signals. Certain mutations of p53 may not just prevent its regular function but also provide mutant isoforms of p53 with oncogenic capabilities[3]. The Ras superfamily of proteins have many functions within cellular signalling pathways but like p53 are implicated in cell cycle progression, as well as cell proliferation. As they are a critical component of a large number of signalling pathways, disruption of regular Ras function can have many consequences. The on/off conformations of Ras proteins are controlled by guanosine phosphates[5]. When complexed with guanosine triphosphate, Ras proteins are considered to be in an ‘on’ state

whereas those complexed with GDP are in an 'off' state. The structural conformation of Ras proteins is dramatically define by which guanosine phosphate is bound. Switching between the on and off states is controlled by the hydrolysis of GTP bound to the Ras protein to GDP by GTPase activating proteins. Oncogenic mutations of Ras occur at key amino acid residues that prevent the hydrolysis of GTP, thus disallowing the turning off of the Ras proteins. This drives the continual transmission of cell signalling pathways and spurs malignant cell growth and proliferation. The symptomatic tumour promoting outcomes of this is challenging to treat by chemical means. Blocking Ras-effector interactions requires an inhibitor to overcome the abundance of GTP and its high affinity for the GTP-binding pocket of Ras proteins[6].

In adults, angiogenesis – the formation of new vasculature – is a tightly regulated and transient process. A number of growth factors are involved in stimulating angiogenesis. However, in cancers, there is often 'always on' angiogenesis signals produced[7]. This is driven by the continuous growth of the tumour and thus, its accrescent requirement for nutrients. The vascular endothelial growth factor A (VEGF-A) is commonly over-expressed in cancers and has been found to be related to oncogene signalling[8] (e.g. hypoxia-inducible factor-1α[9] and transforming growth factor-β [10, 11]).

The ultimate cause of cancer-related death is generally not caused by the primary tumour but by secondary tumours caused by metastasis. Metastasis is a process in which tumour cells undergo morphological and biochemical changes before migration through vasculature or lymphatic systems from the primary source to

other organs where they can begin colonisation[12]. This generally proceeds *via* an epithelial-mesenchymal transition (EMT) [13]. Epithelial cells, that are typically adherent to basement membranes, become more suited to migration and invasion by becoming mesenchyme, with changes in their cell morphology, proteome and adherence facilitating their travel through the extra-cellular matrix. A key difference that is exhibited by cells undergoing EMT is reduced expression of E-cadherin and increased expression of N-cadherin[14]. E-cadherin has functions in cell-cell adhesion and reduced levels is correlated to an instability in adherens junctions[15]. N-cadherin, a mesenchymal-associated marker, promotes interactions with stromal and endothelial cells, which has been proposed to enable entry into the vasculature. It is also a trigger for continuous activation of the MAPK/ERK signalling pathway, which induces tumour cell proliferation and expression of other EMT-related transcription factors[16].

The complexity of cancer development, progression and resistance presents many difficulties and challenges in the treatment of such diseases.

Advances in Cancer Therapies

Over the past 40 years, despite an increasing incidence of cancers, 10-year survival rates have doubled: 50% of people diagnosed with cancer will now live for 10 years or more[17]. More robust diagnoses at earlier stages and advances in therapies provide better treatment outcomes. Treatment for cancer generally involves surgery, radiotherapy or chemotherapy; either alone or in combinations.

1.1 Surgery

Cancer surgery is most effective when there are clear boundaries between healthy and cancerous tissues, with the intertwining nature of some tumours pervading healthy tissues complicating surgeries. Generally, the tumour and the surrounding healthy tissue is removed with clear margins to ensure cancerous tissue is completely removed. The nearest lymph nodes would also be removed in case they contain cancerous cells. Cancers that have undergone metastasis (where the primary tumour spreads to secondary sites) typically cannot be treated *via* surgery alone, due to the scope and locations of the secondary tumour(s). Chemotherapy or radiotherapy may be used as a neo-adjuvant therapy to minimise the size and pervasion of the tumour before surgery, while surgery is also limited by the challenges in differentiating cancerous tissue from healthy tissue.

Fluorescence-guided surgery is an emerging technique whereby a fluorescent probe that specifically targets cancerous tissue is administered, allowing the margins of the tumours to be seen upon illumination with a specific wavelength of light[18]. Indocyanine green has seen broad use as a probe for fluorescence-guided surgery for a range of cancers but while providing sufficient contrasting for surgery, ICG is far from ideal[19, 20]. This approved fluorescent probe for guided surgery is a "blood pool agent"; meaning that it is slowly excreted allowing delayed imaging of the vasculature. This can be used to identify tumours of certain types but it does not have any specific targeting towards cancers. Optimally, a fluorescent probe would be specifically targeted to cancer and

undergo fluorescence turn-on inside the cancer extra-cellular matrix or cells and ideally would be quenched until activation to provide maximal contrast. LUM015 is a probe undergoing clinical testing that is a FRET-based cathepsin protease substrate peptide[21]. Upon cleavage by the enzyme cathepsin, which is over-expressed by tumour cells, and there is a "turn-on" in fluorescence as the fluorophore is liberated from the quencher thus allowing visualisation of tumour margins (Figure 1.2). LUM015 has shown to be well tolerated by human patients and is currently in clinical trials for further evaluation[22-24].

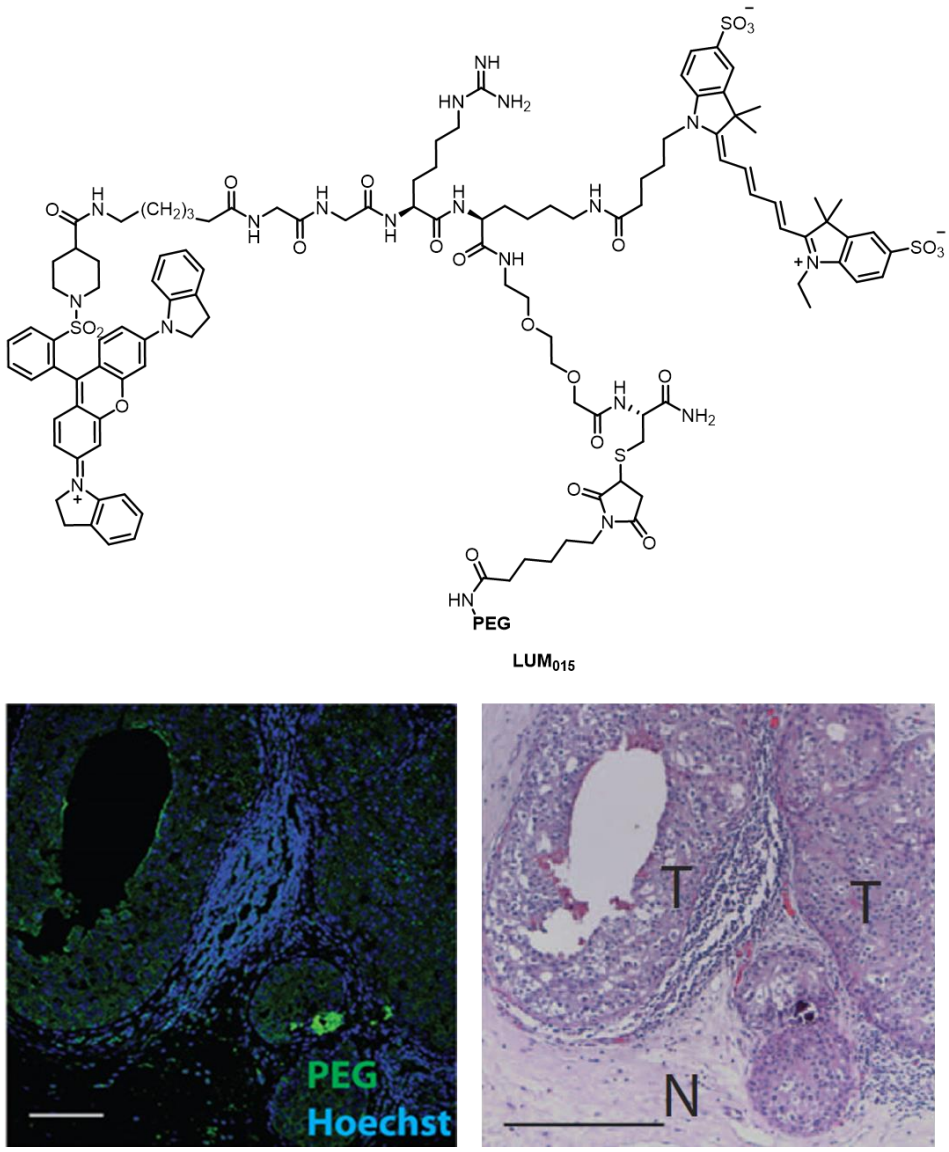

Figure 1.2. The structure of LUM015 (top), a fluorescent probe used for visualising the margins of tumours to enable surgical resection. It is composed of a quencher (QSY21) conjugated to a Cy5 fluorophore through a GGRK peptide, with a 20 kD polyethylene glycol chain attached *via* the C-terminus. Activated LUM015 is seen here with green fluorescence generated in a breast cancer tumour sample extracted from a LUM015-injected patient (bottom, left). The corresponding histology analysis (bottom, right) of the same sample to show that the probe has good correlation with the tumour tissue (labelled "T") and the healthy breast tissue (labelled "N"). Images reproduced from

reference [21] with permissions granted by The American Association for the Advancement of Science.

Cell-penetrating peptides can also be used for fluorescence-guided surgery, as demonstrated by the work of Tsein[25]. Cell-penetrating peptides are typically composed primarily of positively charged residues that can be laden (either covalently or non-covalently) with a cargo to facilitate the increased uptake of the cargo[26, 27]. The mechanisms for how cell-penetrating peptides do this varies case-by-case but can occur *via* endocytosis, passive diffusion or transient pore formation[28, 29]. In the latter case, the positively-charged residues form strong interactions with the phosphate groups of the phospholipids in the cell membrane, distorting its structure and ultimately forming a cylindrical tertiary structure through the membrane to form a pore[28].

Tsein has exploited these features of cell-penetrating peptides to enable their use in fluorescence-guided surgery. To afford cancer cell selectivity, the cellular association of the cell-penetrating peptide is blocked by the conjugation of a negatively charged sequence with an enzyme-cleavable linker[30]. Enzymes that are over-expressed by cancer cells, in this case MMP-2 and MMP-9, cleave the linker between the cell-penetrating peptide and the inhibitory domain (see Figure 1.3). The cell-penetrating peptide, with a fluorescent label, can then penetrate into the cancer cells to provide visual guidance of tumour margins. This strategy has shown promise in murine xenograft models and benefited surgery with a higher survival rate by lowering the post-operative residual tumour volume[31].

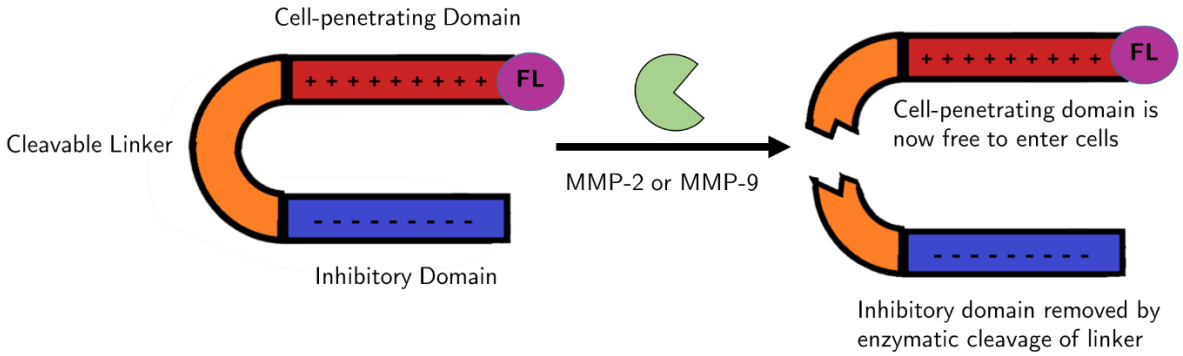

Figure 1.3. Activatable cell-penetrating peptides, composed of a polycationic domain and an inhibitory polyanionic domain with an enzyme-cleavable linker, allow "turn-on" in the vicinity of the tumour. The linker is a substrate for MMP-2 and MMP-9; enzymes that are over-expressed in many cancers. Upon cleavage of the linker, the cell-penetrating domain is then able to enter cells and the fluorescent label (FL) enables fluorescence-guided surgery.

Other recent improvements in surgical treatment of cancer include intraoperative imaging with CT and MRI. This has led to vast improvements particularly for the treatment of neurological tumours, such as glioblastoma[32].

1.2 Radiotherapy

Radiotherapy has evolved considerably since the discovery of its therapeutic application in the early 1900's. Pivotal research by Curie and Becquerel in the 1920's in to radioactivity improved understanding and accessibility of radioactive materials and shortly after, the application of radioactivity to clinical radiotherapy for diagnosis and treatment was initiated[33-35]. Since then, radiotherapy has become an established and highly effective route for the

treatment of cancer and has undergone significant transformations in tandem with technological advances. Today, radiotherapy for cancer is typically given *via* an external beam of high-energy X-rays (rather than using radioactive materials)[36, 37]. An X-ray is a type of ionising radiation produced by the acceleration of electrons to produce photons with wavelengths around 1 nm. These high-energy photons can penetrate deeply into tissues and can induce damage to DNA either by directly producing double- and single-strand breaks in DNA or indirectly, producing secondary electrons that produce free radicals in cells that react with biomolecules. The discovery that the efficacy of radiotherapy is directly correlated to the oxygen concentration present in the sample by Gray in 1953, provided further insight into the molecular mechanisms of radiotherapy[38]. Oxygen is required for the "fixation" of DNA damage i.e. the damage is made permanent and irreparable[39]. Therefore, oxygen depletion and highly reductive environments in tumours reduces the efficacy of radiotherapy by modulating factors required for the fixation of DNA damage: i) preventing the formation of reactive oxygen species and ii) preventing the cytotoxicity of reactive oxygen species through chemical restitution i.e. reductive repair of DNA damage (see Figure 1.4).

Figure 1.4. The DNA damage caused by ionised radiation therapy in normoxic conditions is more effective due to oxygen-fixation (top). In hypoxic and highly reductive environments, commonly present in tumours, the effect of ionising radiation can be overcome by reductive or hypoxic environments, preventing the fixation of DNA damage (bottom).

In conjunction with instrumentation, radiotherapy can be given in a highly controlled manner. The CyberKnife® technology utilises a robotic arm and a three-dimensional rotatable platform to deliver radiotherapy with sub-millimetre precision (Figure 1.5), monitoring patient breathing rhythms to limit the damage done to healthy tissue[40].

Figure 1.5. The components of CyberKnife radiotherapy. The robotic arm allows three-dimensional movement around the patient on the treatment couch which can also move. The "synchrony camera" monitors breathing motions.

Radiation therapy can also be given via brachytherapy where discrete radiation emitters are placed in and around the tumour margins[41]. Typically, a radioisotope contained in a capsule (called a "seed") is inserted with the use of imaging-guided applicators. This affords a very accurate placement of the capsules and has proven effective particularly for prostate cancer. The low dose and range of the emitted radiation limits side effects is an advantage of brachytherapy as it causes little damage to surrounding tissue compared to external beam radiotherapy.

Despite the significant achievements in its development, radiotherapy is still hindered by the physiological factors behind many tumours. Monitoring of the tumour oxygen levels *in situ* would enable external beam radiotherapy to be more directed and applied to areas more likely to be resistant to therapy. The Implantable Microsystems for Personalised Anti-Cancer Therapy (IMPACT) project had the aim of delivering a microsystem packaged with sensors that would be implanted into a tumour to measure, in real-time, oxygen, pH and cell death throughout the course of the therapy e.g. to assess if cell death or apoptosis was occurring.

To do this, known sensing modalities for pH and oxygen were optimised towards their miniaturisation and robustness towards biological environments (see Figure 1.6). For oxygen sensing, a Clark electrode was used that utilises the electrochemical reduction of oxygen on a platinum electrode. The electrodes were micro-fabricated with a Nafion membrane as a solid electrolyte which also prevented biomolecule interference[42]. Two strategies were employed for pH sensing: an ion-sensitive field-effect transistor (ISFET) and a methylene blue-based sensor. ISFETs detect changes in pH by the relative level of protonation/deprotonation of the Si-OH groups of an SiO_2 layer by H^+ ions. The output current is ultimately related to the pH through this mechanism. The methylene blue-based sensor exploits the pH-sensitive redox waves of methylene blue. As protons are involved in the electrochemical reduction of methylene blue, the reduction potential will change proportionally to the concentration of H^+ ions

in solution, which can be extrapolated from square wave voltammograms and thus can measure pH in a robust and rapid manner.

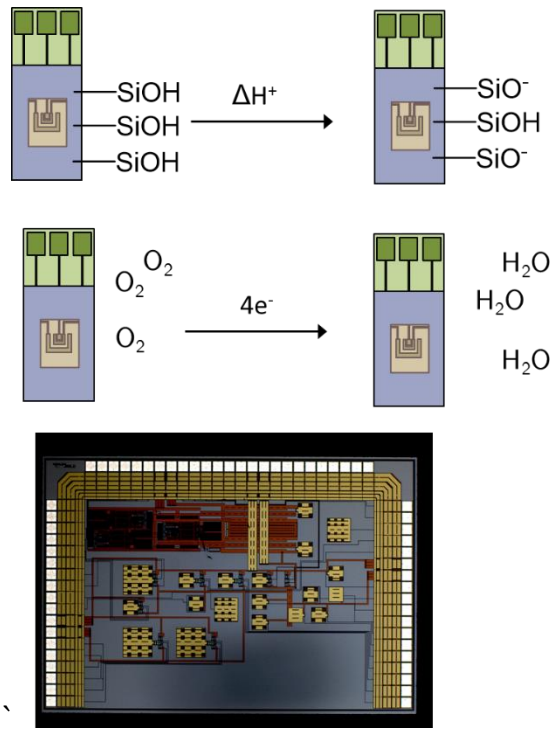

Figure 1.6. Representation of the sensing mechanisms of ISFETs (top) and Clark electrodes (middle) and a picture of a micro-fabricated electrode (bottom).

In order for the microsystem to detect the occurrence of cell death, biosensors were developed using a peptide substrate adhered to an electrode surface with a covalently-attached methylene blue as a redox probe[43, 44]. The peptide sequence was selected using known cleavage sites for the enzyme of interest. The probe was capable of approaching the electrode surface and undergoing electrochemical redox reactions which gives characteristic reduction and oxidation waves. Upon cleavage of the peptide by a protease, the redox reporter

is lost and a reduction in the amplitude of these waves is observed which can then be used to measure relative levels of the protease (Figure 1.7).

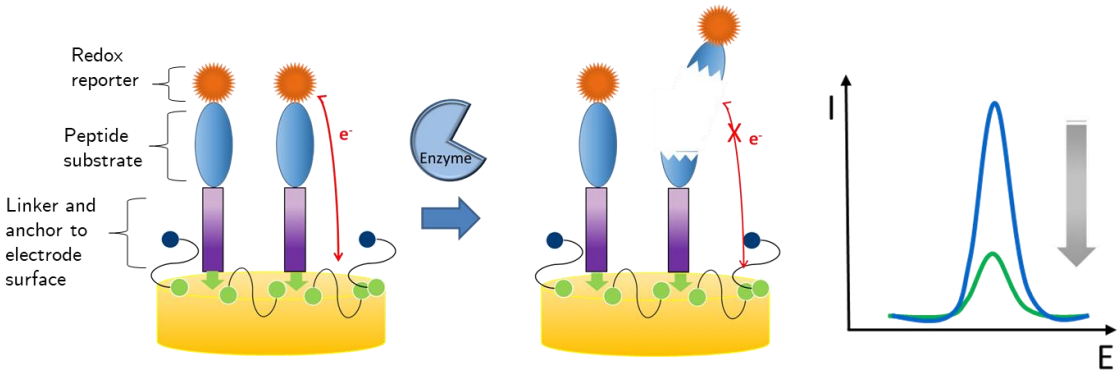

Figure 1.7. Representation of the sensing mechanism of the protease biosensor. Before cleavage of the peptide substrate, the redox reporter is capable of producing a current output by participating in redox reactions at the electrode surface (blue line). Following peptide cleavage, the signal decrease (green line) is correlated to the levels of protease.

The research in this thesis details approaches to exploit the implanted microchip and its placement within the tumour to allow it to act as a chemotherapeutic activator: switching bio-inert prodrugs into active drugs *via* an externally-controlled electrical or photochemical signal.

1.3 Chemotherapy

Cancer chemotherapy has advanced across multiple wide areas of remit. Along with the discovery and design of novel small molecule drugs, there has been a whole host of innovations with the discovery of new drug targets, new ways to hit these targets and new ways to deliver drugs to their targets. Paul Ehrlich

coined the term “chemotherapy” in the early 1900’s, during his search for a cure by chemical means for syphilis[45]. Ehrlich and Hata discovered, through the first iterative drug screening programme, Arsphenamine, an organoarsenic compound that possessed anti-microbial properties effective in treating syphilis-infected patients without killing the patients themselves! This was the first “magic bullet” therapy; that a drug could be given that targeted a disease-causing area of the body while remaining benignant to healthy areas. However, Ehrlich did not believe a “magic bullet” therapy for cancer could be realised, since treatment of cancer – composed of cells broadly similar to healthy tissue – is vastly different from treating an infection with divergent biology. However, significant progress has been made since these beliefs.

Early chemotherapy exploited key differences between cancerous and healthy tissues: namely the increased rate of cell division. Cancer cells are self-sufficient in growth signals and have limitless replicative capability allowing unchecked growth and division[46]. Chemotherapeutic agents derived from chemical warfare agents, such as nitrogen mustards, were thus found to have good cytotoxic activity against cancer cells over healthy cells due to their increased rates of cell division[47, 48]. Nitrogen mustards are non-specific DNA alkylators; forming an aziridinium ion by intramolecular S_N2 displacement of the alkyl halide by the amine; that is then attacked by the nucleophilic N7 positions of guanine residues in DNA (Figure 1.8).

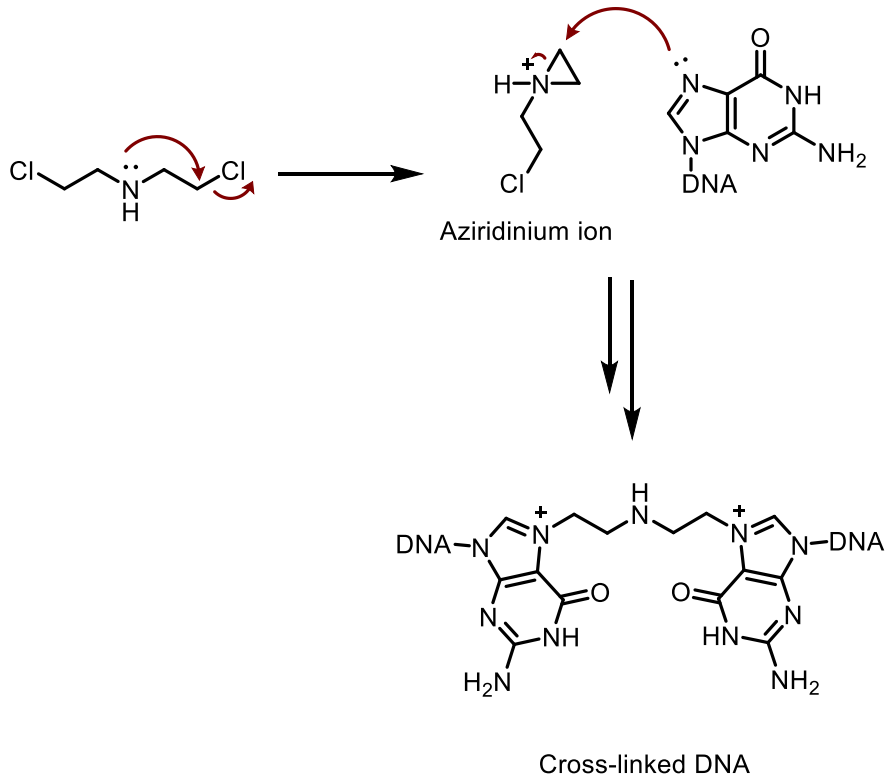

Figure 1.8. Mechanism of action of nitrogen mustards: formation of reactive aziridinium cycle followed by nucleophilic attack by guanine residues to form cross-linked DNA which results in cell death.

DNA lesions formed by nitrogen mustards (and other DNA alkylators) are typically detected by p53, a tumour suppressor protein that induces apoptosis[49]. However, over half of human cancers have a loss-of-function mutation in p53 expression thereby limiting the cytotoxic effect of nitrogen mustards and other DNA alkylators[4, 50].

1.3.1 Platinum Anti-cancer Therapies

Rosenberg is credited with the discovery of cisplatin, another DNA-chelator. Rosenberg was studying the effects of an electric field on the growth and division of *E. coli*[51]. There was an observed inhibitory effect on the division of bacteria which was postulated to be caused by the electric field generated with platinum electrodes; due to the assumed inertness and biocompatibility of platinum. In fact, there were degradation reactions occurring at the platinum surface which were producing platinate salts. The agents responsible were isolated and among them a highly potent anti-cancer agent was found and branded as cisplatin due to the arrangement of its ligands: *cis*-[$Pt(NH_3)_2Cl_2$] (Figure 1.9). In 1978, cisplatin attained FDA approval for the treatment of advanced testicular cancer which changed the outlook completely for those with this type of cancer. Prior to the clinical testing of cisplatin, 5-fluorouracil was the first-line treatment with a success rate of <10%[52]. Treatment with cisplatin saw cure rates rise beyond 90% for advanced testicular cancer. Later the same year, it was approved for advanced bladder and ovarian cancers. Currently, it is approved for 8 distinct cancer types and is used in around 40% of all chemotherapy regimens, either as a single agent or in combination with other drugs[53, 54].

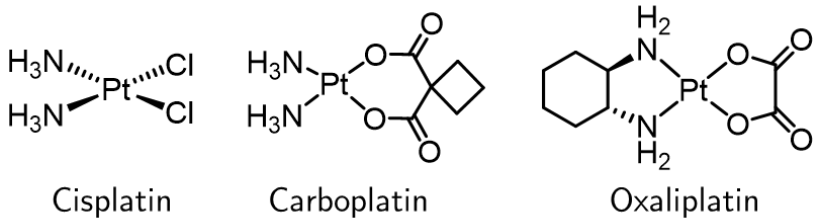

Figure 1.9. Structures of three FDA-approved platinum anti-cancer therapies: cisplatin, oxaliplatin and carboplatin.

The first in its class, cisplatin spurred a new frontier in the research of inorganic cancer therapies. Despite its extraordinary efficacy in treating cancers, cisplatin regimens inflict a harsh side effect profile on patients. The main dose-limiting toxicities of cisplatin are nephro-, oto- and gastrointestinal toxicity, among others and thus, the therapeutic window of cisplatin can be very narrow[55]. There are clinical procedures that aim to alleviate some of the dose-limiting toxicities of cisplatin, for example, hyper-hydration before and after cisplatin infusions limits nephrotoxicity. There are ongoing clinical trials for adjuvant otoprotective drugs but so far these have failed to provide much benefit in preventing hearing damage[56]. Anti-oxidant and deactivators of cisplatin applied locally or systemically have been examined, such as sodium thiosulfate, *N*-acetylcysteine and aspirin (Figure 1.10). These have not been successful in the clinic and currently there is no FDA-approved otoprotective therapy for use with cisplatin. Research on gastroprotective agents is in a similar state; with no FDA-approved agents [57].

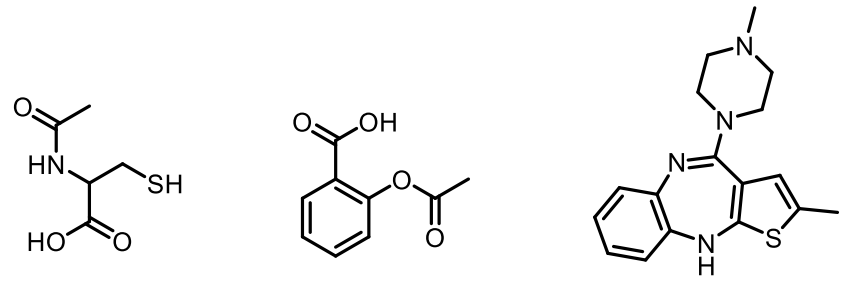

***N*-acetylcysteine** **Aspirin** **Olanzapine**

Figure 1.10. Structures of drugs in testing in combination with cisplatin to alleviate oto- or gastro-toxicities.

Elevated 5-hydroxytyptamine (serotonin) is implicated in the gastrotoxic effects of cisplatin[55]. As such, there is potential overlap for use of anti-psychotics which block serotonin receptors. Olanzapine is a serotonin antagonist/inverse agonist that lessened the severity and frequency of emesis in cisplatin-treated patients and is undergoing further clinical testing[58].

Improvements on cisplatin have been sought. Structure-activity relationships of cisplatin derivatives, modifying the two key sections of the pharmacophore: the am(m)ine non-leaving ligands and the anionic leaving ligands. These handles have allowed tuning of the properties of cisplatin derivatives to afford two 2nd generation platinum anti-cancer therapies: oxaliplatin and carboplatin. The 1,2-diaminocyclohexane ligand of oxaliplatin reduced nephrotoxicity and myelosuppression and provided routes of treatment for cancers where resistance was emergent or cisplatin was not effective, such as colorectal cancer[59, 60]. Due to its high risk of nephrotoxicity, cisplatin dosing must be preceded and followed by hyper-hydration to minimise kidney damage, whereas oxaliplatin does not require this procedure. Before the discovery of oxaliplatin, the front-line treatment for advanced colorectal cancer was 5-fluorouracil with a success rate of around 10-15%[61]. A combination therapy including 5-fluorouracil and oxaliplatin (FOLFOX) was found to have synergistic interactions and greatly improved the benefit of each therapeutic agent alone with a success rate of 50-78%. [62, 63]. The pharmacokinetics of the synergism of oxaliplatin and 5-fluorouracil is thought to occur through more than one mechanism. One of these is the possibility that oxaliplatin inhibits or induces the down-regulation of

dihydropyrimidine dehydrogenase, an enzyme involved in the metabolic inactivation of 5-fluorouracil[64]. Another is the fact that oxaliplatin can inhibit thymidylate synthase, which is a target of 5-fluorouracil, however it is unclear whether or how this causes the synergistic effect between the two drugs[65]. Likewise, 5-fluorouracil induces the up-regulation of the ABCC family of genes which can, through up-regulation of efflux transporters, reduce the glutathione cellular concentration (a species implicated in the detoxification of Pt therapies) thus decreasing oxaliplatin degradative metabolism[66].

Classically, Pt anti-cancer agents undergo aquation of the leaving ligands, to afford a potent electrophile, which can then react with DNA nucleobases; principally the nucleophilic N7 position of guanine residues (Figure 1.11)[67]. The aquation of the two chloride leaving ligands of cisplatin occurs due to the change in chloride concentration which in the blood is around 100 mM compared to the intracellular cytoplasm of 3-5 mM. Increased intracellular chloride concentrations have even been implicated as a mechanism of resistance to cisplatin, as it can prevent the active aquated species from being formed. The type of DNA lesions that can occur by binding of cisplatin are primarily intrastrand 1,2 guanine-guanine crosslinks with lower levels of intrastrand 1,2 adenine-guanine crosslinks and interstrand crosslinking also occurring[53, 68].

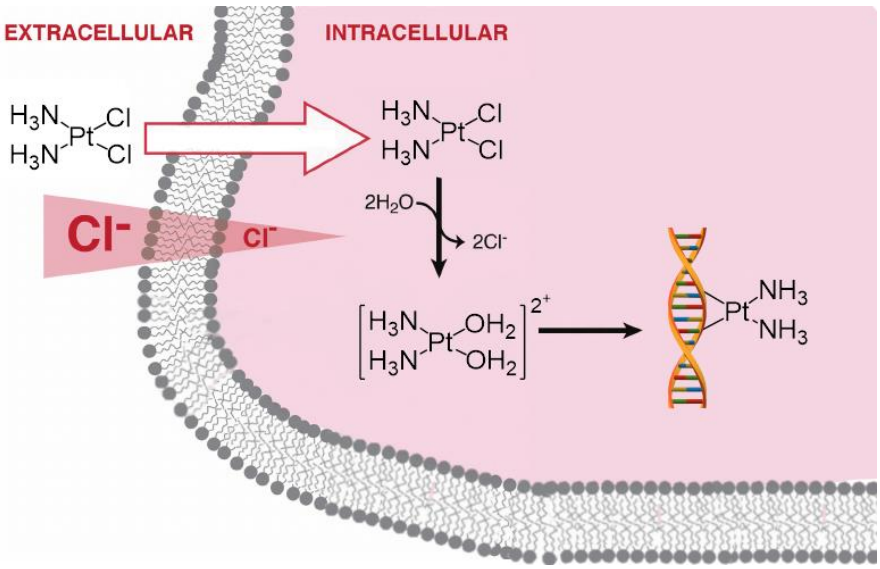

Figure 1.11. The main cellular mechanism of cisplatin: upon entry to the cell, cisplatin undergoes aquation, due to the lower chloride concentration inside cells, to form a highly reactive species that binds to DNA.

Although it is the major contributing factor to cell death, DNA chelation is not the only mechanism through which cisplatin damages cells. The highly reactive aquated electrophilic platinum complex is also reactive towards thiols and other naturally occurring nucleophiles found in biological systems. Oxidative stress caused by damage elicited by cisplatin on mitochondria can also be responsible for the onset of apoptosis[69]. The membrane potential in mitochondria decreases upon treatment with cisplatin which results in inhibited glycolysis pathways which prevents ATP generation and accumulation of glucose in cells[70, 71]. This effect was likely to be caused by the formation of reactive oxygen species in mitochondria, leading to down-regulation of glycolysis-regulated genes such as HIF1α. Gene regulation through microRNA (miRNA) modulation by cisplatin has also been identified as another mechanism of action.

One function of miRNAs is post-transcriptional gene regulation at the RNA level. After a gene is transcribed, a messenger RNA (mRNA) relays the signal for translation by ribosomes in the cytoplasm. miRNA can bind and inhibit mRNA from reaching the ribosome or induce degradation of the mRNA, thus altering ultimate protein expression. Cisplatin has been shown to interact with key miRNAs that can regulate apoptosis pathways such as BCL2 and the E2F family of genes[72, 73].

The ability of oxaliplatin to be used for cancers which have developed resistance to cisplatin or where cisplatin is not effective outright suggests divergent mechanisms of action are responsible. The dicarboxylate leaving ligands of oxaliplatin are thought to undergo a similar method of activation to the chloro leaving ligands of cisplatin. The dicarboxylate ligands are labile towards aquation and substitution with chloride. As a result of this, oxaliplatin IV infusions must be formulated differently than cisplatin[74]. Cisplatin is formulated in sodium chloride (typically 0.9%) solution whereas oxaliplatin must be formulated in a 5% dextrose carrier to prevent premature ligand substitution and complex degradation. Oxaliplatin, upon administration into a patient, can therefore undergo several possible ligand substitution pathways with intermediates of varying reactivity[75]. After oxaliplatin infusion in human patients, the dichloro and the monochloro-monoaqua complex can be identified in the plasma ultrafiltrate, suggesting the process of activation of oxaliplatin *in vivo* follows the pathway of i) chloride substitution of one or both of the carboxylate ligands then ii) aquation of the chloro ligand (Figure 1.12). Ultimately the mono- and di-aqua

complexes are still implicated as the damage-dealing species owing to their high reactivity.

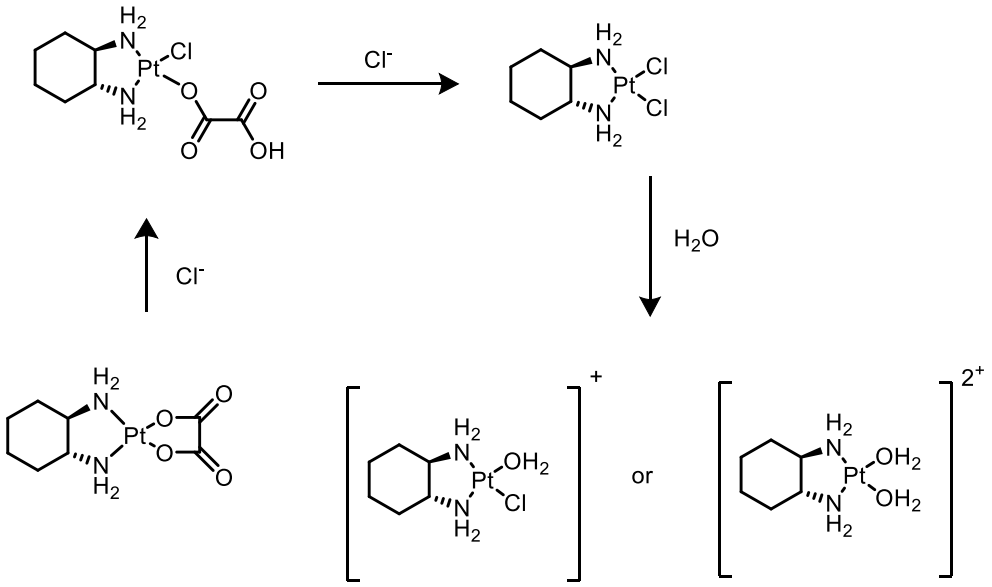

Figure 1.12. Proposed ligand substitution reactions occurring in the formation of the reactive species (hydrated forms) of oxaliplatin.

The di-hydrated complex shows increased cytotoxicity if dosed directly *in vitro* as the pre-formed complex, compared to oxaliplatin[76]. Like cisplatin, oxaliplatin causes crosslinking of genomic DNA with most occurring at the N7 position of guanine residues with intra-strand crosslinking as the dominant conjugate formed with a small amount of inter-strand crosslinks also being formed[77]. Divergent mechanisms of cytotoxicity of oxaliplatin from cisplatin may include, as mentioned above, thymidylate synthase inhibition, an enzyme responsible for the incorporation of thymidine during DNA synthesis. However, this has not been identified as a major contributing factor to oxaliplatin's potent effects.

There is evidence suggesting that oxaliplatin can engage with the immune system to elicit immunogenic effects[78]. Oxaliplatin can prompt the translocation and presentation of calreticulin on the cell membrane surface which is a promoter of macrophage recruitment[79]. Cisplatin does not affect calreticulin presentation and therefore does not stimulate an immunogenic response (or at least, not in this manner). It was also shown that pre-treatment of colorectal cancer cells with oxaliplatin could induce an anti-cancer immunogenic response when injected into a murine model, whereas pre-treated cells with cisplatin did not[79, 80].

Yet another difference identified between the mechanisms of oxaliplatin and cisplatin concerns ribosomal biogenesis stress. In 2017, seminal work by Lippard and Hemann *et al* claimed that oxaliplatin does not kill cells through the DNA-damage response but rather through a ribosomal biogenesis stress pathway[81]. By comparing the RNA interference profiles of cell-death signalling pathways to a reference set of drugs with established discrete mechanisms of action, the pathway of cell-death brought on by each investigated drug afforded insight into the mechanism of action. Upon treatment of cells with either cisplatin, carboplatin or oxaliplatin, it was found that oxaliplatin's signature differed from that of cisplatin and carboplatin and more closely resembled that of a transcription-translation inhibitor. The tumour suppressor protein, p53, was found to be upregulated by cisplatin through a Chk2-dependent manner. Chk2 is activated in response to double strand breaks, which can occur during the attempted repair of cisplatin-DNA adducts[82]. Oxaliplatin also upregulated p53 but did so in a Chk2-independent manner. From an analysis of the ribosomal RNA

synthesis, it was seen that oxaliplatin shared similar phenotypes with Actinomycin D, a drug known to induce ribosomal biogenesis stress[83]. Drug-induced cell death via ribosomal debilitation proceeds *via* RPL11-dependent inhibition of MDM2, the negative regulator of p53. Oxaliplatin was found to greatly increase RPL11 levels whereas cisplatin effected no change. To explain the high efficacy of oxaliplatin relative to cisplatin for the treatment of colorectal cancer, gene expression was examined and ribosome-associated pathways were found to be highly enriched in colorectal cancers where a so-called 'translation addiction' existed as a factor of tumourigenesis. Other cancers that have 'translation addiction' may also be prime yet undiscovered targets for treatment by oxaliplatin.

1.3.2 Emergence of Resistance to Platinum Therapies

A major shortcoming of platinum-based anti-cancer therapies is the intrinsic or acquired resistance of tumours. The low level of cross-resistance between cisplatin and oxaliplatin enables circumvention of cisplatin-resistant cancers to be treated with oxaliplatin, where applicable. However, oxaliplatin is not suited to the treatment of all cisplatin-resistant cancers. Therefore, there has been a large body of research into the mechanisms of resistance of Pt drugs. Generally, resistance can be accrued by mechanisms preventing the Pt drug from reaching its intended targets or by mechanisms that overcome the cytotoxic effects caused by Pt drugs after they have bound to their targets.

In the former case, changes in the levels of cellular transmembrane transporters can prevent the uptake of Pt species. Cisplatin is thought to enter cells *via* a mixture of passive diffusion and active transport[84, 85]. Several active transporters have been implicated in the transport of cisplatin into cells. Of these, the family of copper uptake transporters have been identified as playing a major role in cellular accumulation of cisplatin and acquired resistance[86]. A study identified a copper influx transporter CTR1 as a mediator of cisplatin uptake and demonstrated that pre-administration of copper chelators could enhance cisplatin uptake in a murine model[87]. In another study, CTR1 was also shown to affect accumulation of carboplatin and oxaliplatin[88]. Knock-out of the CTR1 protein in mice, increased resistance to cisplatin and carboplatin treatment but affected cytotoxicity of oxaliplatin treatment to a lesser degree, suggesting there are again different mechanisms that apply to oxaliplatin but not cisplatin or carboplatin. The relative expression of CTR1 has been validated as a prognostic marker for efficacy of cisplatin and carboplatin treatment in humans[89]. Conversely, increased efflux of Pt species can also prevent their cytotoxicity and this is largely caused by over-expression of the copper efflux transporters[90, 91].

Glutathione, an endogenous reductant, acts as a detoxifier in the cytoplasm and can deactivate Pt drugs and flag them for efflux and metabolism (Figure 1.13)[92]. Enzymes associated with glutathione biosynthesis and the conjugation of the reductant to the Pt species have been shown to be up-regulated in cells with acquired resistance to cisplatin[93, 94]. However, there are to date no

clinical studies verifying this effect *in vivo*. Regardless, prodrugs of Pt species comprising inhibitors of glutathione have shown potentiating cytotoxic effects (*vide infra* Section 1.4.1).

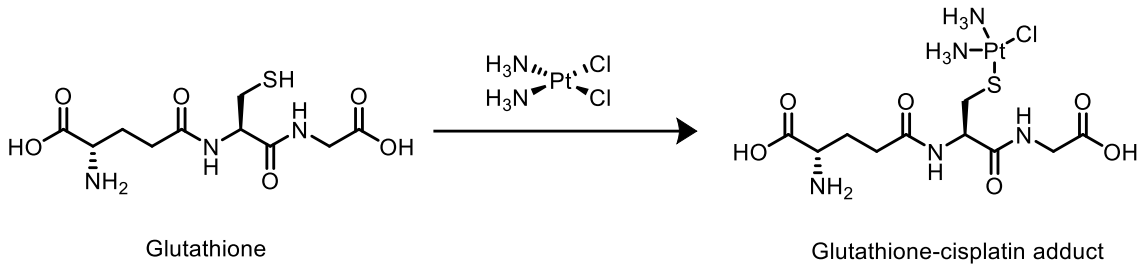

Figure 1.13. Structure of glutathione and its adduct with cisplatin, marking it for metabolism and efflux from the cell.

DNA damage-mediated cell death is a critical pathway for cisplatin toxicity. DNA repair mechanisms, such as nucleotide excision repair and mismatch repair, can be modulated to effect resistance in cancer. Nucleotide excision repair involves the identification of damaged bases in DNA, followed by incision at either end of the lesion, removal of the oligomer containing the damaged base and re-synthesis of the strand. The exact biomolecules responsible for the excision are known to be the heterodimer, ERCC1/XPF. The under- or over-expression of this dimer corresponds to heightened sensitivity or resistance, respectively, of cells towards cisplatin[95, 96]. Resistance to oxaliplatin has also been demonstrated to follow some of the mechanisms employed to resist cisplatin, such as increased expression of ERCC1/XPF and efflux transporters[97, 98]. However, in light of the dissimilarity that oxaliplatin elicits its cytotoxic effects relative to cisplatin it will

be of interest if ribosomal-associated pathways are modulated to effect resistance.

1.3.3 Targeting and selectivity strategies

Despite its less severe side effect profile than cisplatin, oxaliplatin is not a targeted therapy and does have off-target toxicities caused by eliciting effects in non-cancerous tissues. There have been a number strategies employed in attempts to target Pt therapies to cancers.

Glucose Transport Targeting

Cancers generally have greatly enhanced glucose uptake relative to normal cells[99]. A metabolic switch can occur in some cancers, the Warburg effect, where glycolysis is favoured over oxidative phosphorylation[46]. This may be a circumvention for the hypoxic conditions in which tumours often inhabit, as unchecked cell division outgrows blood (and thus, oxygen) supply, as glycolysis can occur in anaerobia. It may also be a result of down-regulation of mitochondrial signalling messengers as an anti-apoptotic measure[100]. The Warburg effect has been exploited for improving drug selectivity.

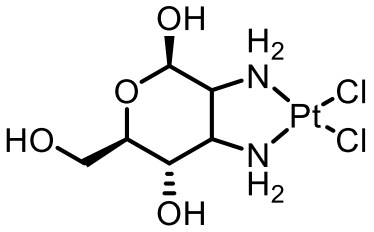

Figure 1.14. Structure of glucose transporter-targeted Pt(II) complex.

Over-expression of glucose transporters on cancer cells can allow preferential uptake of glucose-conjugated drugs[101]. Many Pt(II) complexes with incorporated sugar-containing ligands have been synthesised and characterised for their cancer-killing capabilities, with the sugar moiety comprising the non-leaving ligands or as part of the leaving ligand[102-104]. Replacement of the ammine ligands of cisplatin with 2,3-diamino-2,3-dideoxy-D-glucose afforded a Pt(II) complex which was less potent a chemotherapeutic agent than cisplatin but allowed higher doses to be given (Figure 1.14) [105]. This complex was demonstrated to increase the survival time of tumour-bearing mice 3-fold compared to the untreated control. Extension of the leaving ligand of oxaliplatin with a linker terminated with a glucose unit was shown to greatly enhance water solubility and uptake via active transport by the GLUT1 glucose transporter[106]. There was a dramatic increase in the IC_{50} of these complexes where a GLUT1 inhibitor was co-incubated *in vitro*. In addition, the maximum tolerated dose was around triple that of oxaliplatin in nude mice providing a higher therapeutic index.

Nanoparticle and Polymeric Delivery Systems

The discrepancies of Pt-based cancer therapy in bioavailability and targeting have spurned development of drug delivery systems. “Re-packaging” of known drugs to overcome their limitations (insolubility, non-specific targeting, low bioavailability, etc.) can provide a more affordable and efficient means of

increasing the utility of these drugs relative to the financial expenditure and time required for the discovery of new drug entities. There have been huge developments made in the field of drug delivery with a broad scope of innovations providing solutions to the range of issues drugs can have[107-109].

There have been a number of liposomal formulation drugs that have been FDA-approved in the past two decades[110]. Liposomes are spherical vesicles with an aqueous solution core encapsulated with a hydrophobic membrane. The biphasic nature of liposomes allows both hydrophilic and hydrophobic molecules to be encapsulated effectively. They may also be coated to effect changes in their uptake and pharmacokinetics. PEGylation can reduce clearance and increase half-life, while also preventing phagocytic engulfment[111]. It is a contested issue whether PEGylation enables greater tumour accumulation[112, 113]. The so-called "enhanced permeation and retention effect", caused by the "leaky" vasculature, created in a rapid manner to facilitate a tumour's rapid growth, may facilitate increased tumour accumulation of liposomes[114, 115]. However, the enhanced permeation and retention effect has been shown to be an unreliable factor in humans[116, 117]. This strategy has been applied to doxorubicin, an anthracycline anti-cancer drug, which suffers from a dose-limiting cardiotoxicity. Liposomal formulation of doxorubicin limits entry into cells with tight junctions, such as cardiac cells, due to the larger size of the particles compared to the molecule itself[118]. PEGylation of liposomal doxorubicin also affords longer circulation time and increases the maximum tolerated dose[119, 120].

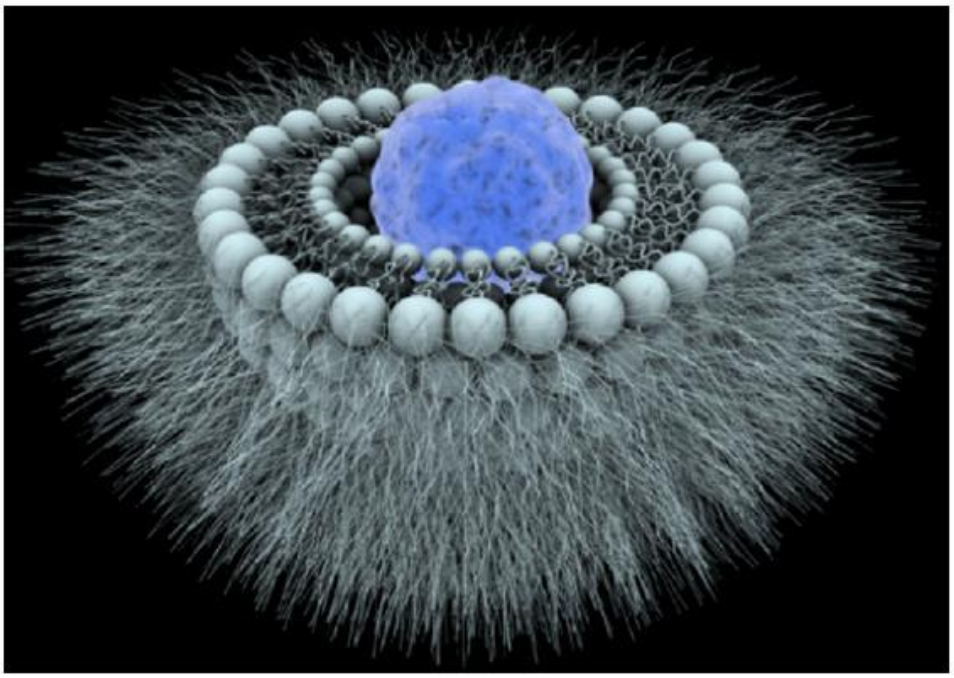

Figure 1.15. Depiction of Lipoplatin: the blue sphere is the cisplatin-containing core in Tris-HCl buffer (0.1 M, pH 7.5) which is encased by a lipid bilayer with the PEGylated lipid strands protruding outwards.

Cisplatin in a liposomal formulation can overcome issues with its low bioavailability and cell uptake[121]. The protective layer of lipids prevents premature reaction of cisplatin with biomolecules and may also be able to overcome resistance by bypassing the down-regulated transporters of cisplatin and directly fusing with the cell membrane to release its cytotoxic cargo[122]. One formulation, Lipoplatin, has been under extensive study for a range of cancers (Figure 1.15). Lipoplatin is a PEGylated liposomal formulation with an average particle size of 110 nm. Currently, Lipoplatin has been tested clinically for treatment of pancreatic, metastatic breast, advanced gastric and inoperable

non-small cell lung cancer, as well as head and neck cancer and mesothelioma[123-127]. Throughout all of these studies, the therapy was well-tolerated and did not exhibit such severe nephrotoxicity as cisplatin alone. Results have been promising, particularly in pancreatic and non-small cell lung cancers. Despite nearly equal response and overall survival compared to cisplatin, the much more tolerable toxicity profile of Lipoplatin successfully saw it through a non-inferiority Phase III trial for the treatment of non-small cell lung cancer[128]. Lipoplatin is also being assessed for orphan drug status for pancreatic cancer and is in "registrational" Phase II/III trials currently.

Micellar formulations of cisplatin also are in clinical testing. Micelles are comprised of a hydrophobic core surrounded by a hydrophilic layer. NC-6004, a micellar nanoparticle with cisplatin derivative conjugated to poly-glutamate in its hydrophobic core with a PEG outer shell, is in Phase III clinical trials for pancreatic cancer in a combination therapy with gemcitabine[129]. As with Lipoplatin, nephrotoxicity was reduced with the micellar formulation.

No other nanoparticle delivery systems are in clinical trials however more exotic and ambitious nanoparticle drug delivery systems for cisplatin have been developed and are in pre-clinical testing stages, including magnetic nanoparticles[130], metal-organic frameworks[131] and silica mesoporous nanoparticles with a photosensitiser for combined chemotherapy and photodynamic therapy[132].

1.4 Prodrugs

A prodrug is an inactive or protected form of a drug that is activated into the parent active drug after administration. It has long been used as a strategy to modify the physicochemical properties of drugs that may contribute to undesirable pharmacokinetic effects, such as poor absorption or stability in the harsh conditions of the stomach and GI tract[133]. Ionisable species, such as free amines and carboxylic acids that result in charged molecules at physiological pH can hinder absorption of orally administered drugs. Additionally, masking of charges increases lipophilicity and improves cell membrane permeability. The most common pro-moiety, i.e. masking group, is an ester masking a carboxylic acid; accounting for just under half of all marketed prodrugs[134]. Intracellular esterases can then hydrolyse the prodrug into its active carboxylic acid form. The inverse can also be applied for the delivery of drugs containing a hydroxyl group with an ester as a pro-moiety. For example, the prodrug abiraterone acetate, a treatment for prostate cancers, utilises a simple acetic acid ester to increase oral bioavailability and delay first-pass deactivating metabolism over the parent drug with a free hydroxyl (Figure 1.16) [135, 136]. Similarly, the boronic acid-containing drug, ixazomib, is administered orally as a citric acid boronic ester that serves to increase the stability of the oxidation-sensitive site[137].

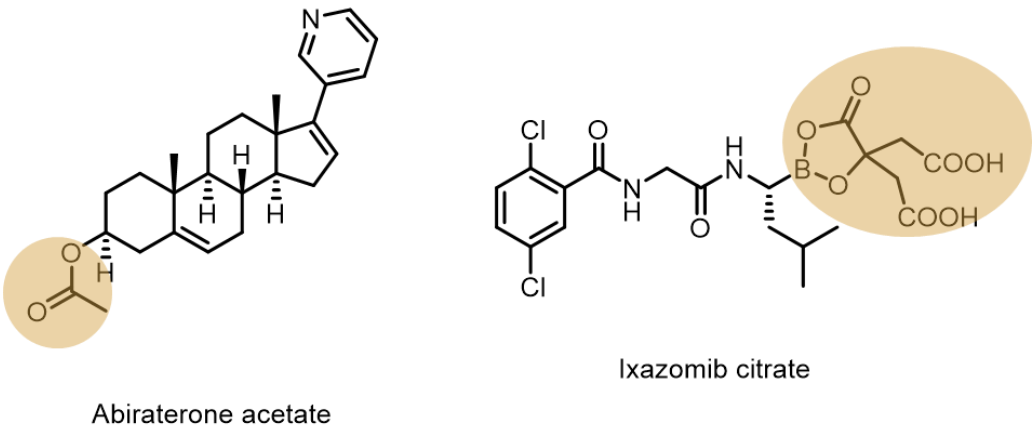

Figure 1.16. Structures of the cancer prodrugs abiraterone acetate and ixazomib citrate. Pro-moieties are highlighted in orange.

Prodrugs can also be used to increase the selectivity of therapies, by design of a pro-moiety that facilitates either uptake or activation at the desired site. For instance, enzymes that are upregulated in cancers but not in healthy tissues can be used to prevent off-target effects and focus therapy at the site of the cancer[138].

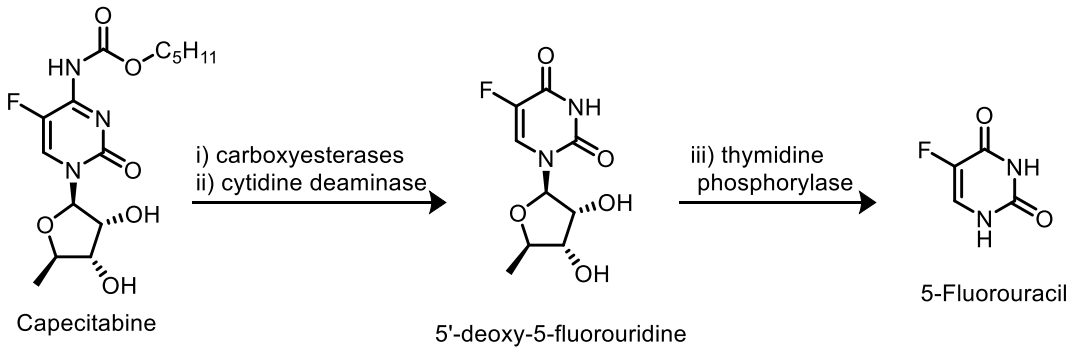

Figure 1.17. Structures of 5-Fluorouracil, 5'-deoxy-5-fluororidine and Capecitabine.

With adept rational prodrug design, a change in administration route may become possible. This is desirable as it benefits the patient's quality of life, as well as lessens the burden on healthcare providers as hospital stay times are reduced. A prime example of the utility prodrugs can offer is capecitabine, a prodrug of 5-fluorouracil (Figure 1.17). 5-Fluorouracil has been a mainstay of chemotherapy for a wide remit of cancers since its discovery in the 1950's. However, it suffers from a poor pharmacokinetic and metabolic profile, with low oral bioavailability, that requires it to be delivered in a continuous intravenous infusion[139]. The developmental process of capecitabine began with the discovery of another 5-fluorouracil prodrug: 5'-deoxy-5-fluorouridine. This prodrug was found to be suitable for oral administration but its severe dose-limiting intestinal-related toxicities prevented its successful utilisation[140, 141]. The installation of a carbamate with a lipophilic tail on 5'-deoxy-5-fluorocytidine increased oral absorption and alleviated the dose-limiting toxicities by preventing 5-fluorouracil from being prematurely formed during the absorption process[142]. Capecitabine is a prodrug that requires three stages of activation: i) removal of the carbamate by carboxylesterases (located primarily in the liver) ii) conversion of the cytidine to uridine by cytidine deaminase (located primarily in the liver and some cancer cells) followed by iii) removal of the ribose by thymidine phosphorylase to generate the active drug, 5-fluorouracil. Capecitabine is now a front-line therapy for a range of cancers.

1.4.1 Pt(IV) Prodrugs

All of the Pt(II) therapies discussed above are administered intravenously. Oral administration is not possible because of the highly reactive nature of these species. Pt(II) species are square planar low-spin d^8 coordination complexes and are prone to substitution reactions[143]. This prevents oral administration as the complex will undergo reactions before systemic absorption. To circumvent this, a prodrug strategy utilising the Pt(IV) oxidation state can be employed. In oxidation state IV, the complex takes an octahedral geometry with a low-spin d^6 configuration that is more substitution-inert. In addition, the Pt(IV) complexes are six-coordinate and so have two additional handles for functionalisation. The Pt(IV) species are considered prodrugs as they require reduction to the corresponding Pt(II) complex before they can elicit their cytotoxic effects[144, 145]. This has led to myriad applications in targeted and multi-functional therapies. Pt(IV) prodrugs have been widely investigated as an alternative therapy to overcome the extensive side-effects of Pt(II) drugs and to enhance cancer cell selectivity, outcomes for treatment and to facilitate the design and development of novel delivery systems.

A prime example of this is the Pt(IV) prodrug "Asplatin" or "Platin-A"[146, 147], which consists of cisplatin oxidised to the Pt(IV) oxidation state with one axial ligand containing a molecule of aspirin (see Figure 1.18). The design of this prodrug allows, upon reduction of the Pt(IV) centre, release of both active cisplatin and aspirin to elicit DNA-binding and COX-2 inhibition, respectively [147]. COX-2 inhibition by aspirin reduces tumour-associated inflammation, one of the "hallmarks" of cancer progression[1, 148, 149]. This prodrug was shown to

be an effective agent on prostate cancer cells *in vitro*. Recently, it has also been shown to reduce some of the most severe side-effects of cisplatin treatment, namely oto- and neuro-toxicity primarily by reducing inflammation, in a guinea pig model[150].

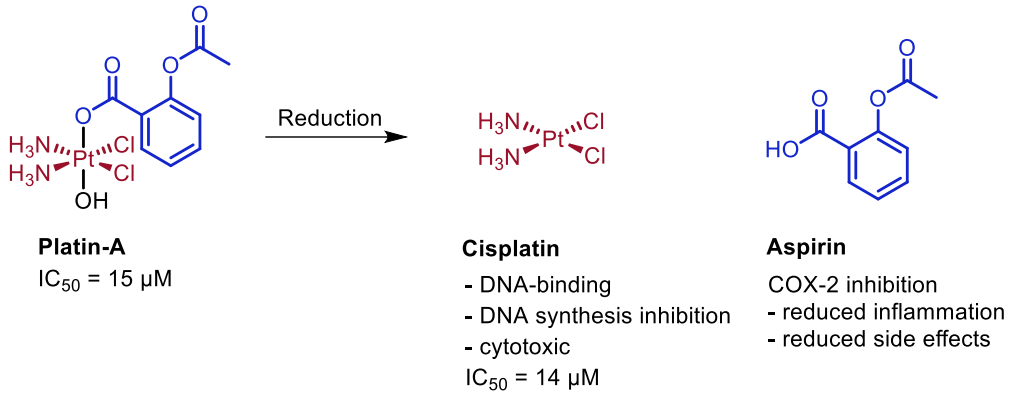

Figure 1.18. Dual-action Pt(IV) prodrug Platin-A releases a molecule of aspirin along with cisplatin upon reduction/activation. IC_{50} values are for a human prostate cancer cell line, PC3, with an incubation time of 72 h.

The additional axial ligands incorporated following the oxidation of Pt(II) to Pt(IV) have also been utilised to potentiate the antineoplastic effects following drug activation by the addition of adjuvant therapies as ligands. There are myriad examples of this, one such being the addition of a nucleotide excision repair (NER) inhibitor as a ligand (Figure 1.19)[151]. Nucleotide excision repair can mediate cisplatin cytotoxicity by repair of the DNA lesions caused by DNA-binding of cisplatin[152, 153]. The inhibitor was capable of binding and blocking the XPF-binding site of the ERCC1/XPF dimer with the hypothesis that cisplatin damage would not be recognised and repaired thus sensitising cells to cisplatin.

The prodrug exhibited high potency and overcame cisplatin resistance in both ovarian and lung cancer cell lines.

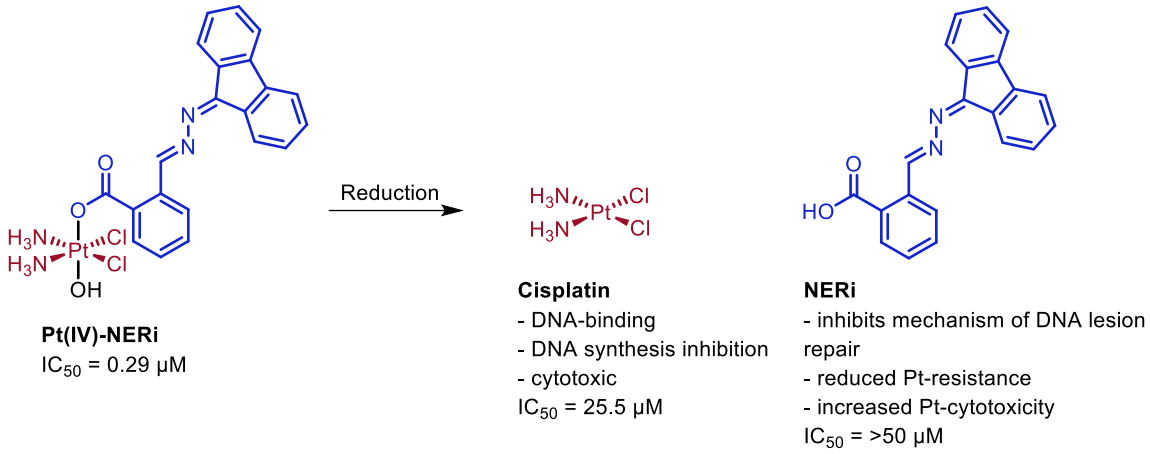

Figure 1.19. Dual-action Pt(IV) prodrug which releases a nucleotide excision repair inhibitor upon reduction/activation, leading to enhanced cytotoxic effects and helps to overcome resistance mechanisms. IC_{50} values are for A549CisR, a cisplatin-resistant lung carcinoma cell line, after 72 h incubation.

Another example is ethacraplatin, a Pt(IV) prodrug with a glutathione-*S*-transferase inhibitor[154]. As mentioned above, glutathione is implicated in the detoxification of cisplatin, and glutathione-*S*-transferase (GST) is an enzyme that catalyses the conjugation of the reactive thiol of glutathione to electrophilic centres. Ethacrynic acid is a known inhibitor of glutathione-*S*-transferase and was readily incorporated into a Pt(IV) prodrug via the free carboxylate (see Figure 1.20). The resultant prodrug not only increased the cytotoxicity compared to cisplatin alone, but also potentiated the inhibition of glutathione-*S*-transferase relative to ethacrynic acid alone. The way in which ethacrynic acid binds to the enzyme is known to be with the carboxylate directed towards the solvent region

and as such it was anticipated that the Pt(IV) prodrug would bind in a similar mode, devoid of any Pt-enzyme interactions[155]. X-ray crystallographic studies were used to probe the binding and elucidated that the Pt(IV) prodrug was docking at a different site than ethacrynic acid alone[156]. Ethacraplatin was observed to bind to the dimer interface of glutathione-*S*-transferase, where it was reduced to the Pt(II) complex with release of the two axial ligands, ethacrynic acid. The resultant Pt moiety remains bound in the dimer interface.

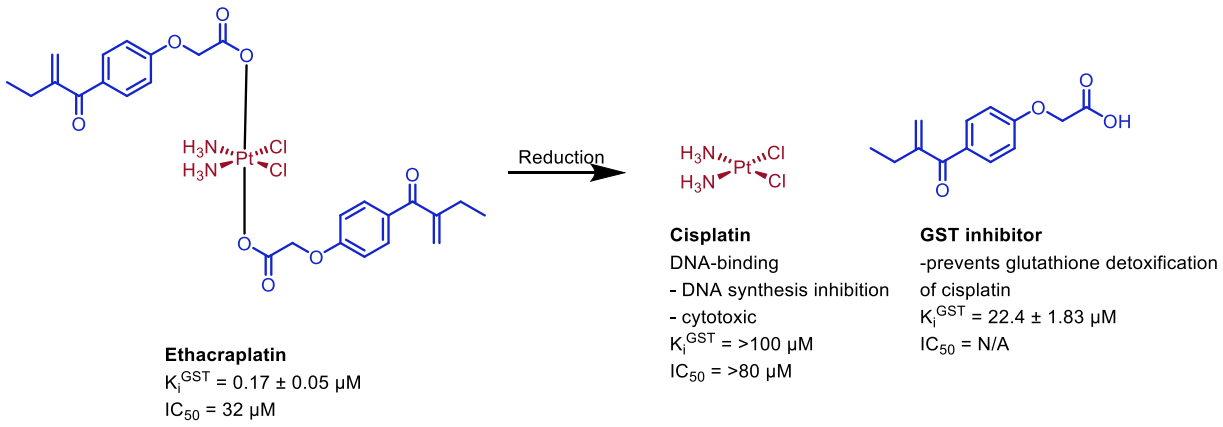

Figure 1.20. Dual-action Pt(IV) prodrug, ethacraplatin, which releases a glutathione-*S*-transferase inhibitor upon reduction to overcome glutathione-mediated resistance to cisplatin. IC_{50} values are for a human breast carcinoma MCF-7 cell line after 24 h incubation.

Taking this "multiple-action" concept further, is an example of two different Pt(IV) prodrugs linked to each other by a di-carboxylate ligand with the other axial ligand of each Pt centre comprised of a carboxylate anti-cancer drug (one an HDAC inhibitor, the other a PDK inhibitor) to give a "quadruple-action" prodrug (Figure 1.21)[157].

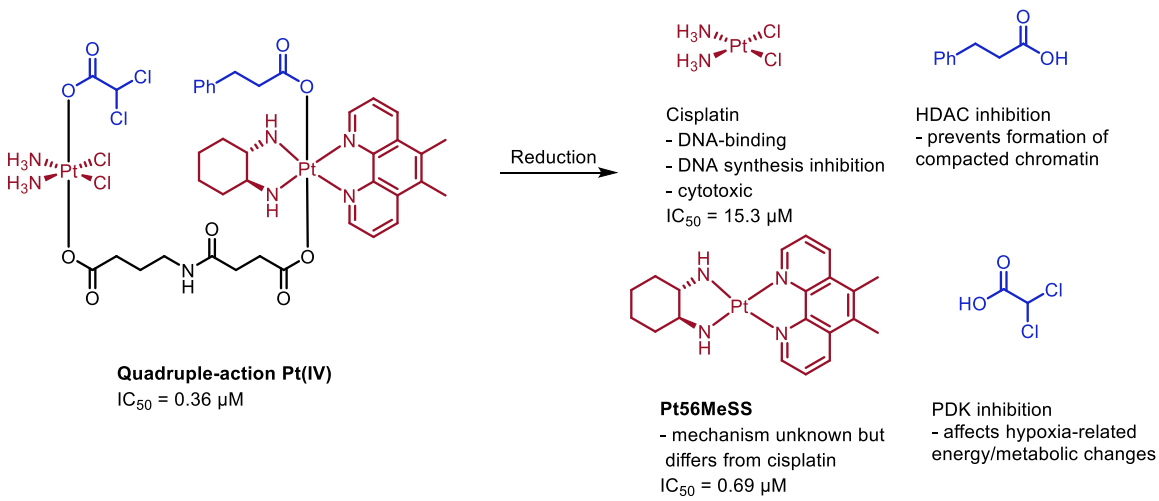

Figure 1.21. Quadruple-action dinuclear Pt(IV) complex. Reduction/activation releases two Pt(II) anti-cancer agents with discrete mechanisms of cytotoxicity, an HDAC inhibitor and a PDK inhibitor. IC_{50} values are for human colorectal carcinoma HCT-15 cell line after 72 h incubation.

The reduction of the two Pt(IV) centres releases two cytotoxic Pt(II) species with disparate mechanisms of action: cisplatin, that binds to DNA to form cytotoxic lesions and Pt56MeSS which is unable to complex DNA as a result of its bidentate nitrogen-donor ligand and has been postulated to induce cell cycle arrest through actions in the mitochondria[158]. Phenyl butyrate is a known HDAC inhibitor, presumed to de-condense chromatin to expose DNA to cisplatin and potentiate its cytotoxicity. Dichloroacetic acid has been used in a prior Pt(IV) prodrug, Mitaplatin, and may be capable of inducing a switching back of cancer cell metabolism to oxidative phosphorylation (see section 1) which hinders the tumour capabilities of tolerating oxygen-deficient environments[159].

Of prominence in the Pt(IV) prodrug field is satraplatin which is currently in clinical testing for a range of cancers[160]. The cyclohexamine equatorial ligand

and the two acetate axial ligands increase the lipophilicity and, in combination with the stability of Pt(IV) complexes, allowed satraplatin to become the first orally administered platinum anti-cancer agent. Once activated (via reduction to the Pt(II) complex and loss of the acetate axial ligands) the mechanism of action is similar to that of cisplatin[161]. In 2009, the results of a large-scale phase III clinical trial were published reporting that satraplatin was well-tolerated but did not benefit overall survival (relative to cisplatin) in hormone-refractory prostate cancer despite delaying pain and disease progression[162]. These results have shown that satraplatin may find use in scenarios where use of cisplatin is precluded such as renal dysfunction or in the elderly.

Using the two additional handles for functionalisation of Pt(IV) complexes has garnered a lot of interest in the design of multi-functional complexes[163, 164]. This is an attractive strategy to overcome issues with Pt therapy, such as side effects and resistance, as it prevents the active agents from being administered individually which can be complicated by variance in pharmacokinetic and distribution factors or each agent. For instance, they can be comprised of inhibitors associated with platinum therapy resistance.

As mentioned previously, modulation of glutathione-associated pathways has been linked to cisplatin resistance. Platin-B, is a Pt(IV) cisplatin analog designed to allow cisplatin to escape sequestration by glutathione[165]. The axial ligands, 6-bromohexanoic acid, can bind to the reactive cysteines of glutathione, preventing the detoxification of the cisplatin (Figure 1.22). The result was a

highly potent Pt(IV) agent that was active in a cisplatin-resistant ovarian cancer cell line, with an IC_{50} of 0.75 μM (almost 20-fold more potent than cisplatin).

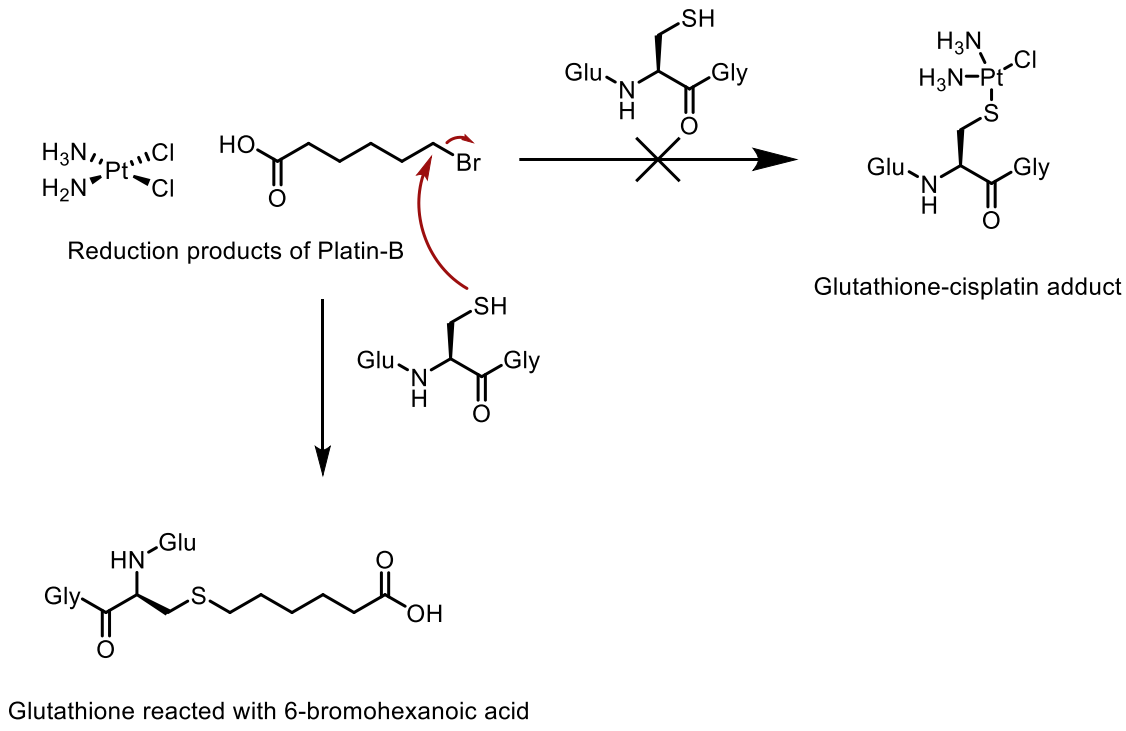

Figure 1.22. The reduction of Platin-B yields cisplatin and a glutathione inhibitor, preventing the sequestration of cisplatin by glutathione.

There are a huge number of Pt(IV) prodrugs developed that contain a secondary drug that activates upon intracellular reduction of the prodrug, thus anti-inflammatory drugs have been used to reduce inflammation-associated pro-tumour effects, such as aspirin[147, 166] and ibuprofen[167]; other cancer therapies, for instance, DNA alkylators to potentiate cytotoxic effects, such as chlorambucil[168] or HDAC inhibitors such as valproic acid[169, 170]; cell organelle-specific targeting motifs for the mitochondrion[171, 172] or for cell markers such as integrins[173, 174]. However, to date, no other Pt(IV) prodrugs

have been taken through to clinical testing stages and new therapies to replace the current Pt drugs remain a challenge at the forefront of cancer research.

1.4.2 Bio-orthogonal Prodrug Activation

The work discussed herein investigates methods for prodrug activation that do not rely on biological triggers but use physical actuators to generate 'on-demand' drug release. Related prodrug activation strategies that utilise bio-orthogonal chemistry to activate prodrugs, that are independent of metabolic pathways, have seen success in improving temporal and spatial selectivity. Bio-orthogonality, as first defined by Bertozzi, is the capability of chemical reactions to occur in biological milieu without interference or interaction with the biological system[175]. The participating moieties of the bio-orthogonal reaction must be inert and unreactive towards the biological environment. Examples of bio-orthogonal reactions include the Staudinger ligation, strain-promoted azide-alkyne click reactions, and tetrazine-dienophile inverse electron demand Diels-Alder reactions. The Staudinger reaction has been used previously as a de-caging reaction for doxorubicin that was protected with a 4-azidobebenzyloxy group (ACBZ-Dox)[176]. Reduction of the azido group by a phosphine, with release of dinitrogen, triggers a self-immolative 1,6-elimination to release the active doxorubicin (Figure 1.23). The disadvantages of the Staudinger reaction as a bio-orthogonal means of prodrug activation lie primarily in the phosphine. Its limited stability towards oxidation in air and the resultant phosphine oxide by-product of the reaction hinder the Staudinger reaction for use in bio-orthogonal chemistry *in vivo*.

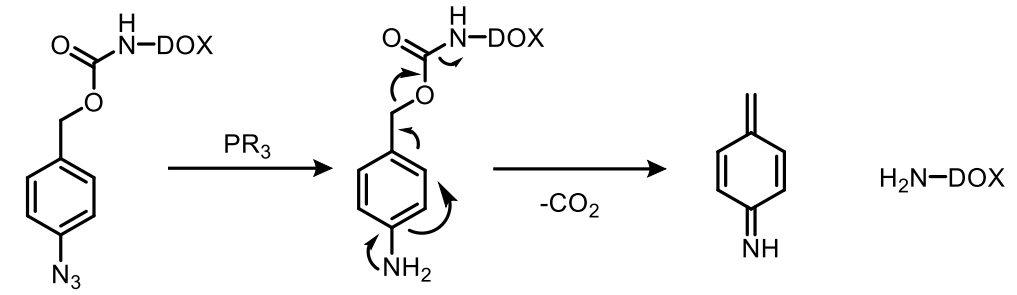

ACBZ-Dox

Figure 1.23. The Staudinger reaction is used to reduce the azide of the 4-azidobenzyloxycarbonyl (ACBZ) group to the amine which triggers an electronic cascade, resulting in the release of free doxorubicin (DOX), with carbon dioxide and azaquinone methide as by-products.

The inverse electron Diels-Alder reaction is well-suited for click-to-release applications due to its high reaction kinetics that are easily tuneable. Vinyl ethers can be used as pro-moieties for hydroxyl groups, such as for the protection of duocarmycin derivative, **Ve-Dcm** [177]. De-caging of phenol triggers a cyclisation to form a cytotoxic cyclopropanyl derivative (**Cyp-Dcm**) that acts as a DNA-alkylator. It was demonstrated that by incubation of a tetrazine coupling partner, the prodrug could be activated for a turn-on cytotoxic effect in A549 human lung cancer cells (Scheme 1.1).

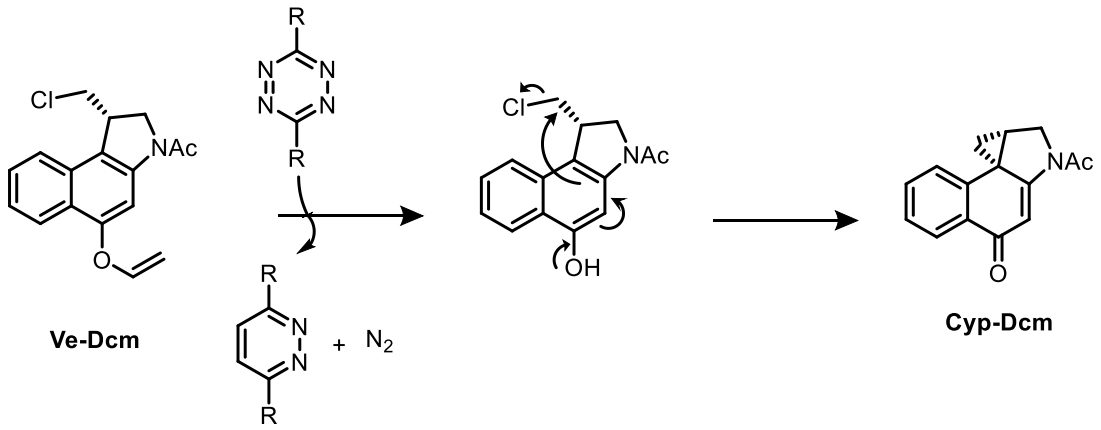

Scheme 1.1. Vinyl ether-protected duocarmycin derivative is decaged by inverse electron demand Diels-Alder reaction, following by a cyclisation reaction to form the active cyclopropanyl-containing compound.

The disadvantages of this system are the difficulty in the synthesis of tetrazines, limiting their optimisation, the lack of solubility and instability towards hydrolysis that they exhibit in aqueous conditions and the resultant pyridazine by-product debarring these reactions from being 'traceless'. In another embodiment, the pyridazine by-product was utilised for a dual-prodrug activation strategy. With the identification of a biologically-active pyridazine that inhibits the function of oncogenic microRNA-21, in combination with a vinyl ether-protected camptothecin (a potent topisomerase I inhibitor) prodrug was devised a tetrazine inverse electron demand Diels-Alder reaction that resulted in the simultaneous activation of two prodrugs: with the tetrazine as a pro-moiety for the pyridazine and the vinyl ether being decaged to generate free camptothecin[178] (Scheme 1.2).

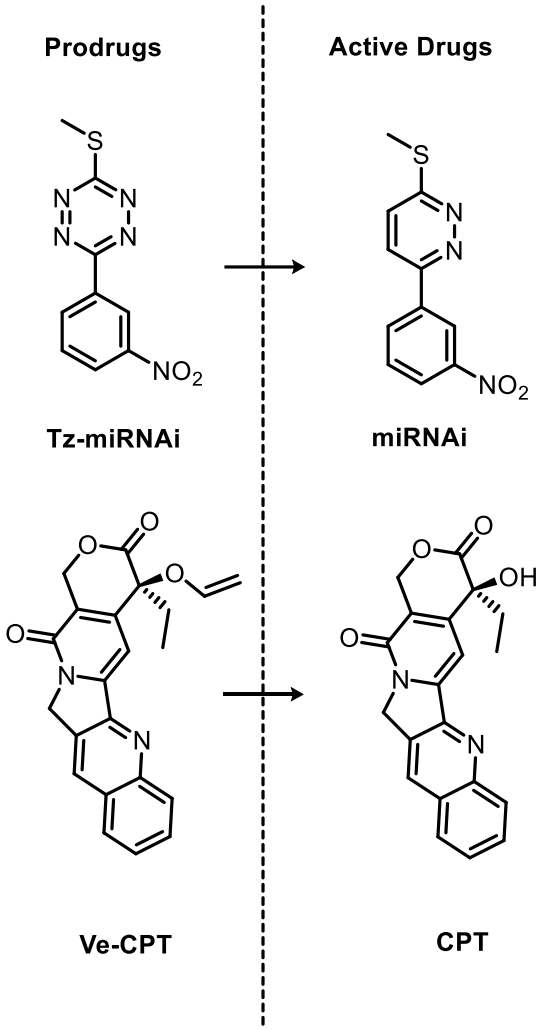

Scheme 1.2. Dual prodrug-prodrug activation through the use of a bio-active pyridazine, masked as a tetrazine and a camptothecin prodrug with a vinyl ether pro-moiety. Reaction of the tetrazine with the vinyl ether results in two active drugs being formed simultaneously.

Another method of bio-orthogonal prodrug activation is the use of a biocompatible organometallic catalyst to perform the de-caging reaction. This moves away from the conventional two-component-ligation methods described above and allows the conversion of multiple prodrug molecules to active drug by the bio-orthogonal catalyst. Typical heavy metal catalysts (such as Pd and Cu

species) are associated with toxicity and instability to air and aqueous conditions. However, strategies have evolved to overcome these issues by the identification of non-toxic and stable catalysts, as well as formulations that prevent leaching and exposure of the free metal such as nanoparticles or resins (see reviews [179-181]). For example, Pd^0 particles can be made by the incorporation of $Pd(OAc)_2$ into swollen resins which can then be cross-linked to prevent any leaching of Pd while retaining its catalytic activity[182].

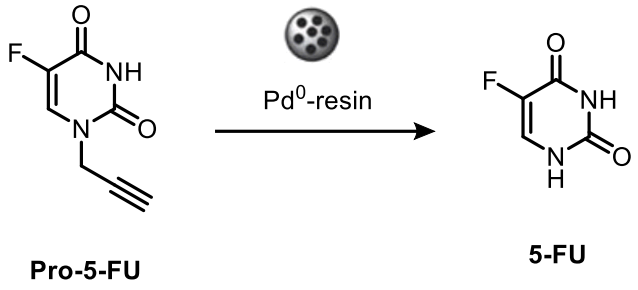

Pro-5-FU **5-FU**

Scheme 1.3. Catalytic de-caging of a proparygyl-protecting 5-fluorouracil prodrug (**Pro-5-FU**) to active drug **5-FU** by incubation with Pd^0-incorporated resin.

These Pd particles were shown to exhibit minimal toxicity in human colon and pancreatic cancer cells at an effective Pd concentration of ~288 μM and were effective at de-caging a prodrug of 5-fluorouracil (**Pro-5-FU**) for turn-on cytotoxicity (Scheme 1.3). Further, these particles were shown to be capable of functioning *in vivo* using a zebrafish embryo model and demonstrated by the turn-on of a caged and quenched fluorophore[183].

Chapter 2

Aims and Objectives

Platinum-based anti-cancer therapies are a mainstay of cancer treatment and Pt(IV) prodrugs have shown promise towards the improvement of the toxicities of these therapies. The research described herein investigates alternative methods of activating Pt(IV) prodrugs, with the ultimate aim of providing spatiotemporal control over the "turn-on" of a variety of cancer therapies.

The work described firstly explores the use of an electrochemical redox-mediated approach to prodrug activation by fabricating discrete devices that are capable of reducing and activating Pt(IV) prodrugs upon the application of an electrical signal. The second approach involved the development of a photocatalytic Pt(IV) reduction system using a photosensitiser which, upon illumination, generated both cytotoxic Pt(II) species and singlet oxygen simultaneously. These platforms were optimised and characterised *in vitro* for their reduction capabilities, and validated in a biological setting.

Chapter 3

Electrochemical Activation of Pt(IV) Prodrugs

Parts of this chapter are published in:

Norman, D., González-Fernández, E., Clavadetscher, J., Tucker, L., Staderini, M., Mount, A.R., Murray, A. F. and Bradley, M., *Chemical Communications*, **2018**, 54, 9242-9245.

† Indicates experiments carried out by J. Clavadetscher

3.1 Introduction

The discovery of platinum-based anticancer therapies represents a landmark in cancer research therapy and was based on the serendipitous observation by Rosenberg that Pt species generated during electrolysis with platinum electrodes inhibited division of bacteria[184]. Upon further investigation, $Pt(NH_3)_2Cl_2$ was identified as the agent responsible and spurred the FDA approval of the first Pt-based anticancer agent in 1978 under the name of cisplatin. Pt(II) anticancer chemotherapies such as cisplatin and the more recent, oxaliplatin and carboplatin are now commonplace and considered as work-horses of cancer therapy, with 10-20% of all cancer patients being prescribed a Pt-based therapy at some stage in their treatment regimen[53]. However, despite the clear benefits and efficacy of Pt-based therapies, they are hindered by severe side-effect and off-

target toxicity profiles. This is largely due to the high reactivity and lack of specificity of Pt(II) species. In addition, Pt(II) therapies are required to be administered intravenously due to the lack of, or the unpredictability of, bioavailability with oral administration.

In attempts to overcome these issues, the oxidised and more substitution-inert Pt(IV) derivatives have been explored as potential next-generation therapies[185, 186]. The change from a low-spin d^8 configuration to a low-spin d^6 configuration, with associated change from square planar to octahedral geometry, results in a lowered lability of ligands thus increasing stability towards biological nucleophiles. The kinetic inertness reduces the amount of Pt that is sequestered or detoxified on its approach to the tumour. This has provided experimental therapies with reduced toxicities and enabled a switch of the route of administration from intravenous to oral (see Chapter 1).

The difference in bioactivity between the Pt(IV) and Pt(II) oxidation states present an opportunity for selective drug activation.

Previous work has utilised biologically-endogenous reductants (such as ascorbic acid and glutathione) to reduce Pt(IV) prodrugs to their active counterparts (see Chapter 1). The use of mediators (that are not endogenous) to carry out the reduction-activation has not been well-explored, despite its potential to allow further control of site-selective and temporal control over prodrug activation. Sessler *et al* reported a macrocyclic metallotexaphyrin that was capable of reducing Pt(IV) species and explored its use for this purpose. Texaphyrins are

expanded porphyrins with the specific one used here named motexafin which was complexed with gadolinium. Motexafin gadolinium (MGd) had previously been shown to have a slight preferential accumulation in spontaneous mammary tumours in mice and functioned as a radiosensitiser[187]. MGd was explored for its use as a "redox catalyst" that could mediate the Pt(IV)-Pt(II) conversion and enable site-selectivity through the cancer-targeting motexafin (Scheme 3.1). This would thus remove dependence on endogenous reductants, which are ubiquitous and are found in healthy and cancerous tissues.

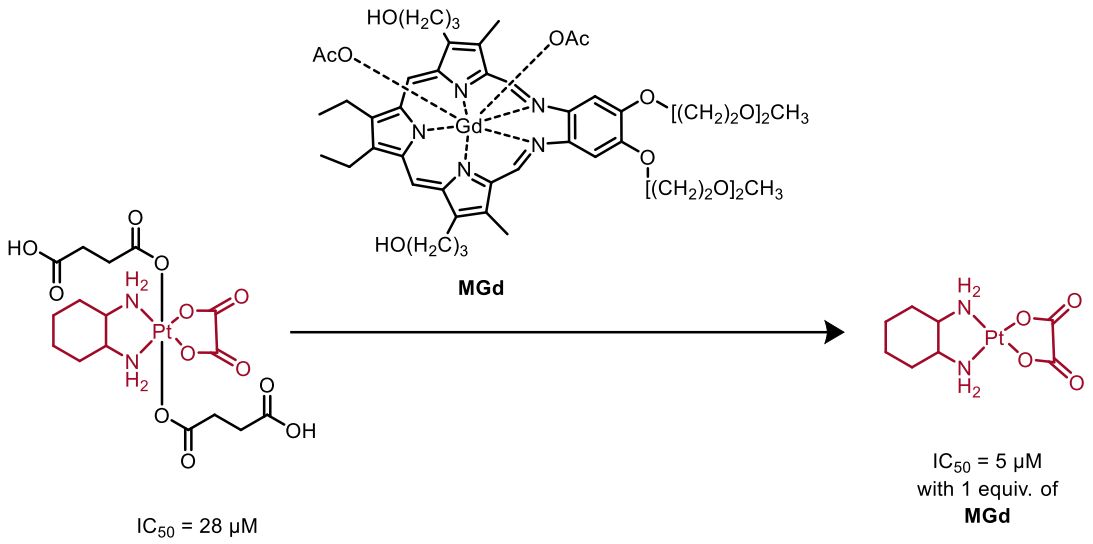

Scheme 3.1. Mediated reduction-activation of a Pt(IV) prodrug by motexafin gadolinium (MGd). IC_{50} values are for a human ovarian carcinoma cell line, A2780 with an incubation time of 5 days.

This work demonstrated the feasibility of a non-endogenous redox mediator as the actuator for Pt(IV) prodrug activation. However, the system required a high concentration of **MGd** (1 equivalent relative to Pt(IV) concentration) and a long incubation time for the turn-on of cytotoxicity. The catalyst also required reduction back

to its active oxidation state, proposed to be *via* ascorbic acid, therefore is not completely non-reliant on biological reductants. This study represents the closest related work to the investigations detailed in this chapter. To the best of our knowledge, there is only one published report of a prodrug activation system that uses electrochemical signals as an actuator[188]. It does so for cyclophosphamide (a nitrogen mustard used in the treatment of cancers) and uses an external three-electrode electrochemical cell with the effluent pumped to wells containing cells of the murine mammary carcinoma cell line EMT6 (Scheme 3.2).

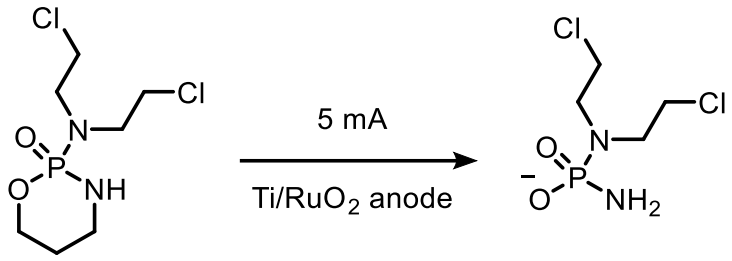

Scheme 3.2. Electrochemical oxidative activation of cyclophosphamide.

The oxidative activation of cyclophosphamide (a process conventionally carried out by liver enzymes) could be observed by the increase in cytotoxicity after 15 min of electrolysis, however required the use of an initial solution at 5 mM concentration. In addition, due to the high current density required the electrochemical source was required to be kept isolated from the cell media thus preventing translation to *in vivo* applications.

Therefore, the use of electrical signals for prodrug activation is a space that requires further exploration.

3.2 Aims of Chapter 3

Pt(IV) prodrugs have shown great promise for the delivery of cytotoxic Pt(II) anti-cancer agents overcoming issues with administration, solubility, reactivity and off-target toxicities. However, the method of activation for these prodrugs are biological and selectivity remains of great concern. The research presented in this chapter explores the use of a physical stimulus, namely electron delivery, to activate and turn-on Pt(IV) prodrugs. The application of a potential can be easily controlled and conceptually could be used from outside of the body enabling both spatial and temporal control over activation.

This was accomplished through the discovery of a redox mediator, capable of shuttling electrons from an electrode surface to a Pt(IV) species; reducing it to the active Pt(II) species. Immobilisation of the redox mediator on to a miniaturised electrodes afforded discrete devices which could be applied in a biological setting. The capability of this system to kill cancer cells by mediated electrochemical activation was validated on both 2D and 3D cell cultures.

3.3 Background

In conjunction with the Implantable Microsystems for Personalised Anti-Cancer Therapy project, where a device containing miniaturised electrodes for sensing local pH and oxygen levels is implanted into a tumour, a drug delivery system was envisaged that could use electrons to activate and “turn-on” therapies directly at the site where therapy is required. This differs from conventional prodrug

applications, where systemic biological stimuli are responsible for activation of the prodrug. As cancers are innately endogenous and share many similarities to healthy tissue, prodrugs reliant on biological stimuli suffer from selectivity issues. Over-expressed enzymatic processes are often exploited to increase the selectivity of prodrugs and conventional drugs. However, these enzymes are also found in healthy tissues, albeit at lower levels. For example, capecitabine is a prodrug of 5-fluorouracil whose primary target is the enzyme, thymidylate synthase, that is essential for DNA replication. The relative expression of thymidylate synthase has been shown to be 1.47-fold higher in human cancerous colorectal tissue samples compared to healthy colorectal tissue[189]. Thymidine phosphorylase, the enzyme that catalyses the conversion of an inactive intermediate of capecitabine to the active drug 5-fluorouracil, was found to be 5-fold higher in colorectal cancer tissues than in healthy tissues. This is of benefit to the efficacy and tolerability of capecitabine over 5-fluorouracil but regardless of the enhanced expression of both these enzymes in cancerous tissues, there will inevitably be activation of capecitabine and inhibition of thymidylate synthase occurring in healthy cells, albeit at lower levels than in cancerous cells.

An electrochemical-based approach to prodrug activation offers an alternative to overcome this hurdle. A prodrug may be administered, which is bio-inert, i.e. it is non-toxic in its caged state and cannot be activated biologically, but can be activated via electron delivery, that could be controlled externally by a healthcare professional. This could afford unprecedented control of where, when and how much prodrug is converted to active therapy.

Pt(IV) species are very much suited for this application, being redox-active with the reduction waves for Pt(IV)-Pt(II) occurring at relatively low potentials (less than -1 V for the dicarboxylate Pt(IV) species)[190, 191]. The general trend of the effect of the axial ligands on the reduction potential (E_P) of Pt(IV) complexes is seen in Figure 3.1. The addition of two ligands during the oxidation of Pt(II) to Pt(IV) also affords a handle for further functionalisation through which the biological effect could be modulated.

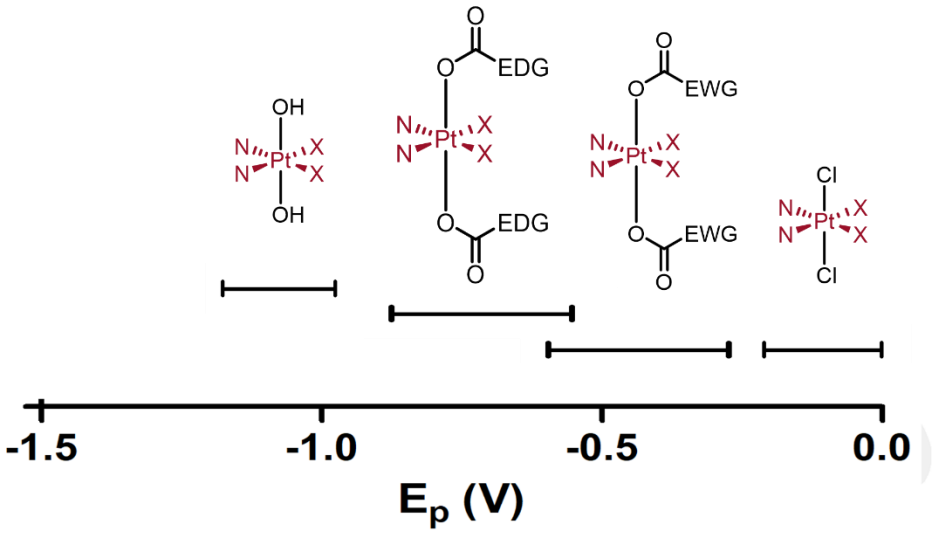

Figure 3.1. General trend of reduction potentials for Pt(IV) species with am(m)ine carrier ligands (N) and either halide or carboxylate leaving ligands (X). EDG = electron-donating group, EWG = electron-withdrawing group. The range of reduction potentials shown for each is based dependent on the type of equatorial ligands.

Therefore, a system was envisaged by which a potential could be applied *in vivo* to reduce (and thus activate) the Pt(IV) species. A redox mediator, which acts as a shuttle between the electrode surface and the prodrug would afford even

greater selectivity, through allowing a lower potential to be applied and thus reduce the biological interference from other redox-active species (see Figure 3.2)[192].

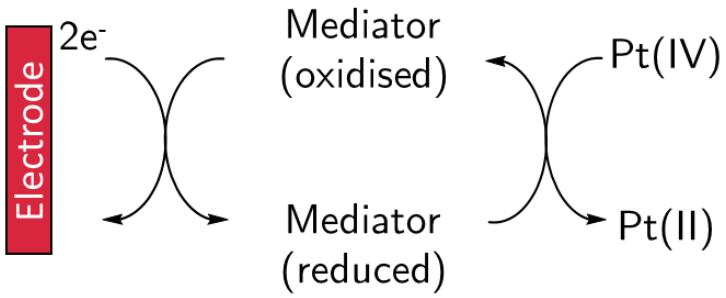

Figure 3.2. Representation of the mechanism of electro-catalytic conversion of Pt(IV) to Pt(II). A redox mediator, in the reduced form, can shuttle electrons from the electrode surface to the Pt(IV) species, becoming oxidised in the process. The reduced form of the redox mediator is then re-generated at the electrode surface.

Suitable redox mediators for the Pt(IV) reduction were explored. Previous work based on the electrochemical sensing of satraplatin (a Pt(IV) species) in complex biological media that utilised methylene blue as a redox mediator was used as a basis for this study[193]. This overcomes the issue of speciation that arises from ICP-MS quantitation where only total Pt content is measured[194]. Chronoamperometry is used to sense and measure the satraplatin concentration of samples, with higher current output being seen for higher concentrations of satraplatin after 20 seconds of applying the potential. The sensor is composed of a self-assembled monolayer (SAM) on a gold disk electrode with methylene blue

adhered to the electrode surface through a thiol-gold bond and back-filled with mercaptohexanol. Leucomethylene blue (LMB, the reduced form of methylene blue) is generated by applying a reductive potential (-0.3 V), which in turn can reduce satraplatin to its Pt(II) analogue. The current output is thus correlated to the levels of oxidised methylene blue formed, from which the satraplatin concentration can be calculated.

As the sensing mechanism utilised the Pt(IV) reduction through a redox cycle with methylene blue, I explored the use of this redox mediator as a prodrug activator as described below.

3.4 Discovery and design of Pt(IV) electro-activation system

A small library of cisplatin Pt(IV) analogues were synthesised to examine their suitability for reduction with the methylene blue-based redox mediator (Figure 3.3). Complexes **1-5** exhibited varying reduction potentials, allowing the effect between reduction potential of the Pt(IV) substrate and the redox mediator to be explored. Oxaliplatin Pt(IV) derivative, **6**, was also included in the assessment of suitable Pt(IV) prodrugs.

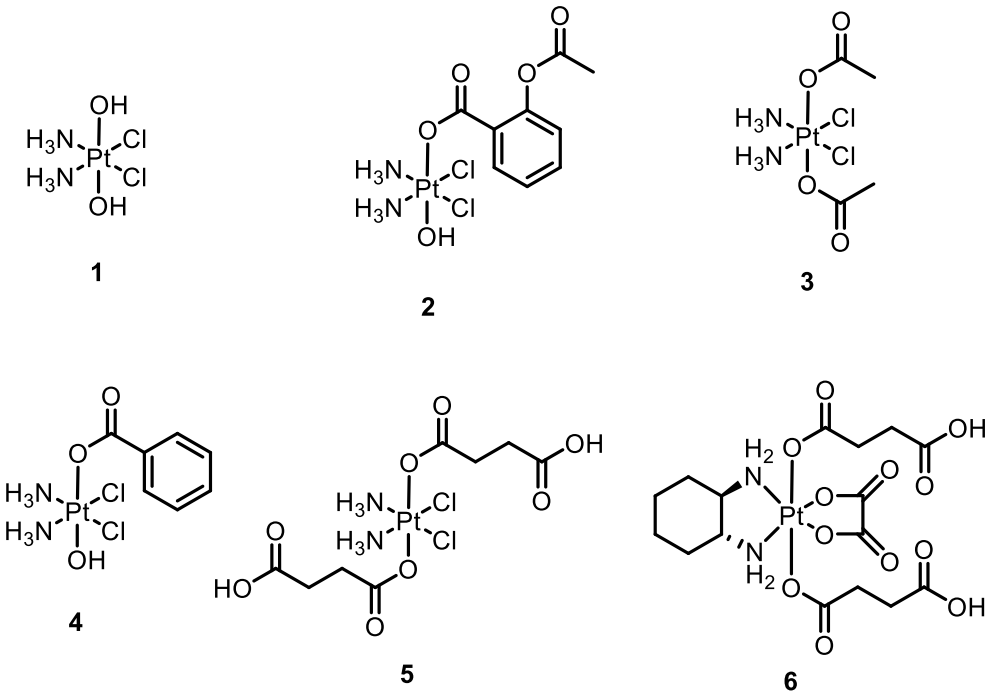

Figure 3.3. Structures of the small library of Pt(IV) complexes initially synthesised for analysis/characterisation with respect to the reduction potential and suitability towards electro-activation.

The purity and absence of undesired species (i.e. undesired mono-substituted complexes for compounds **3**-**6** or the undesired di-substituted for compound **2**) was verified by HPLC (Figure 3.4). The cisplatin derivatives, due to their polar character, elute much earlier than the oxaliplatin derivative **6**, hindering their usefulness as test compounds. With pure compounds in hand, the compounds were further confirmed by mass spectrometry and NMR.

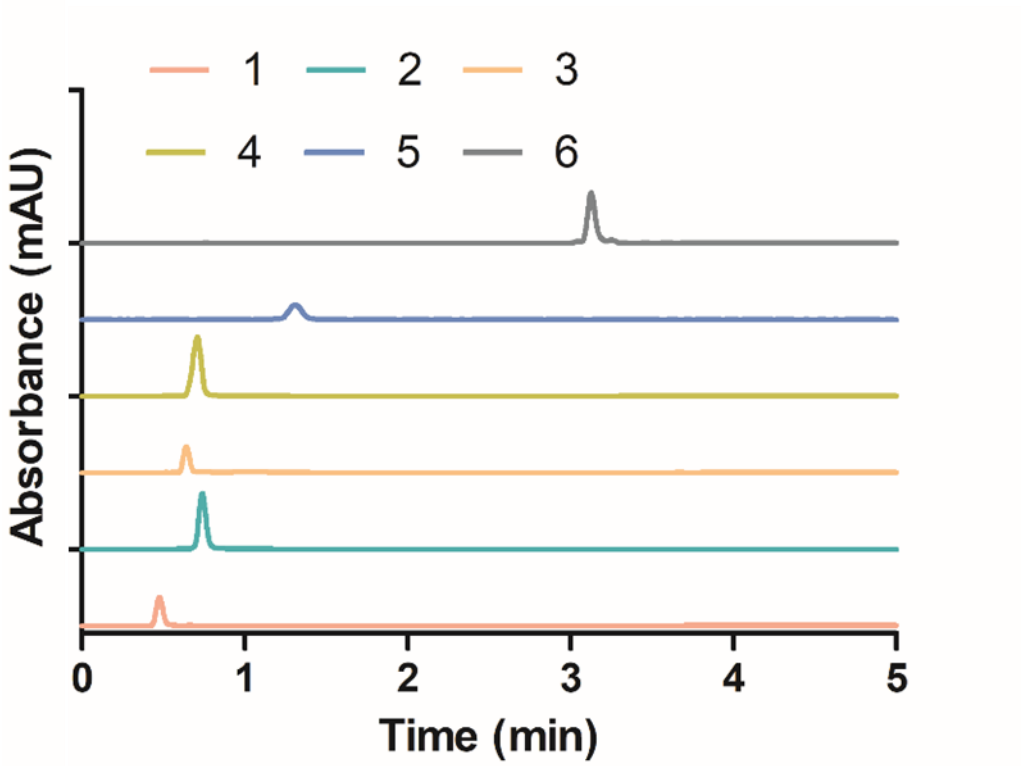

Figure 3.4. HPLC analyses of Pt(IV) prodrugs **1**-**6** with absorbance measured at 254 nm. Compounds were analysed with the same method, eluting H_2O/MeCN each containing 0.1% formic acid at a gradient of 95% H_2O to 5% H_2O over 10 minutes (for full spectra, see Chapter 5).

The redox processes of complexes **1**, **2**, **3**, **5** and **6** were measured by cyclic voltammetry at 1 mM in PBS (Figure 3.5), with compound **4** discounted due to its poor water solubility. The difference in peak reduction potentials (E_{red}) demonstrated the effect the axial ligands can have. The compounds showed the general relationship known for the reduction of Pt(IV) compounds; with compound **1** requiring a more reducing potential than the carboxylate platinum complexes.

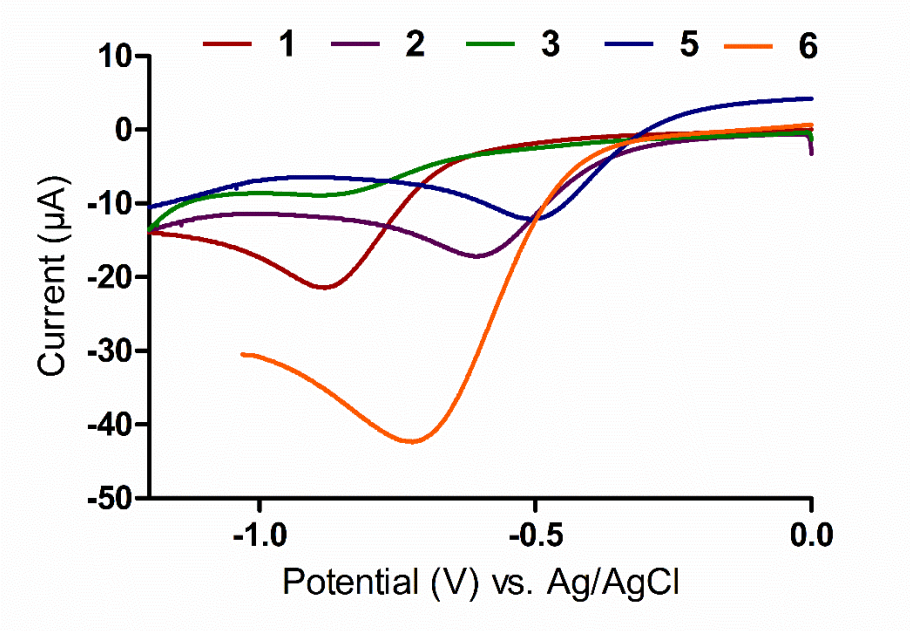

Figure 3.5. Cyclic voltammograms demonstrating the effect of the axial ligands on the reduction potential of the Pt(IV) complexes **1** (green line), **2** (purple line), **3** (blue line), **5** (red line) and **6** (orange line). Complexes were analysed at a concentration of 1 mM in PBS with a glassy carbon working electrode and a platinum mesh counter electrode and a Ag/AgCl reference electrode with potential swept from 0 to -1.2 V, except for **6** which was at 2 mM and potential swept from 0 to -1.05 V. Reverse scan has been omitted for clarity. Complex **4** was not soluble in aqueous media.

It can be seen that the diacetato complex (**3**) had a less negative reduction potential than the mono-succinato complex (**5**). This is likely to be a result of the two acetato ligands having a greater effect on the destabilisation of the Pt(IV) complex than a single succinato ligand. **1** required the most negative reduction potential, i.e. it is the most difficult to reduce, as its ligand is less bulky and has

less electron-withdrawing effects than the others. It has been shown previously that steric hindrance of axial and equatorial ligands can destabilise the complex and lead to less negative reduction potentials[195]. All values obtained for peak reduction potentials were corroborated by values found in literature[191]. The reduction processes for each compound were a single two-electron wave, with the reduction process and release of the axial ligands irreversible in all of the compounds analysed. The absence of a corresponding anodic oxidation peak in the cyclic voltammograms showing that the reduction process was irreversible.

A suitable constant reduction potential was selected from the previous CV experiments and applied, and the reaction monitored over time by NMR and LC-MS. LC-MS analyses showed the disappearance of **3** upon application of a fixed potential of −0.65 V (vs. Ag/AgCl) for 30 min, however cisplatin was not identifiable by LC-MS. Measurement of the consumption of **3** by electrochemical methods was also attempted. Cyclic voltammetry lacked the sensitivity to detect changes in low concentrations of **3** but it was found that differential pulse voltammetry (DPV) was sensitive enough to detect down to at least 100 μM.

Differential pulse voltammetry is a technique where the potential is sharply applied, held for a set interval time before sharply decreasing back down to the step potential. The current is sampled just before the pulse in potential and again just before the drop back down to the step potential. The twice-sampling operation of DPV lends it increased sensitivity through correction of the non-Faradaic background current.

DPV was employed to analyse the progress of Pt(IV)-Pt(II) conversion at sub-millimolar concentrations and a standard curve was generated using known concentrations of **3** (see Figure 3.6). The increased sensitivity of DPV compared to CV is demonstrated in Figure 3.7 where with CV the current begins to plateau around 300 μM. The peak reduction currents are correlated to the concentration through the relationship:

$$i_p = \frac{nFAD^{1/2}C}{\sqrt{\pi\tau_m}}\left(\frac{1-\sigma}{1+\sigma}\right)$$

where i_p is the current of the reduction peak, n is number of electrons transferred, F is the Faraday constant, A is the area of the electrode, D is the diffusion coefficient, C is analyte concentration, τ_m is transition time. The quotient $\left(\frac{1-\sigma}{1+\sigma}\right)$ is defined by:

$$\sigma = exp\left[\left(\frac{nF}{RT}\right)\left(\frac{\Delta E}{2}\right)\right]$$

where R is the gas constant, T is temperature and ΔE is the pulse amplitude.[196]

This facilitated the *in situ* monitoring of the conversion of **3** to cisplatin electrochemically.

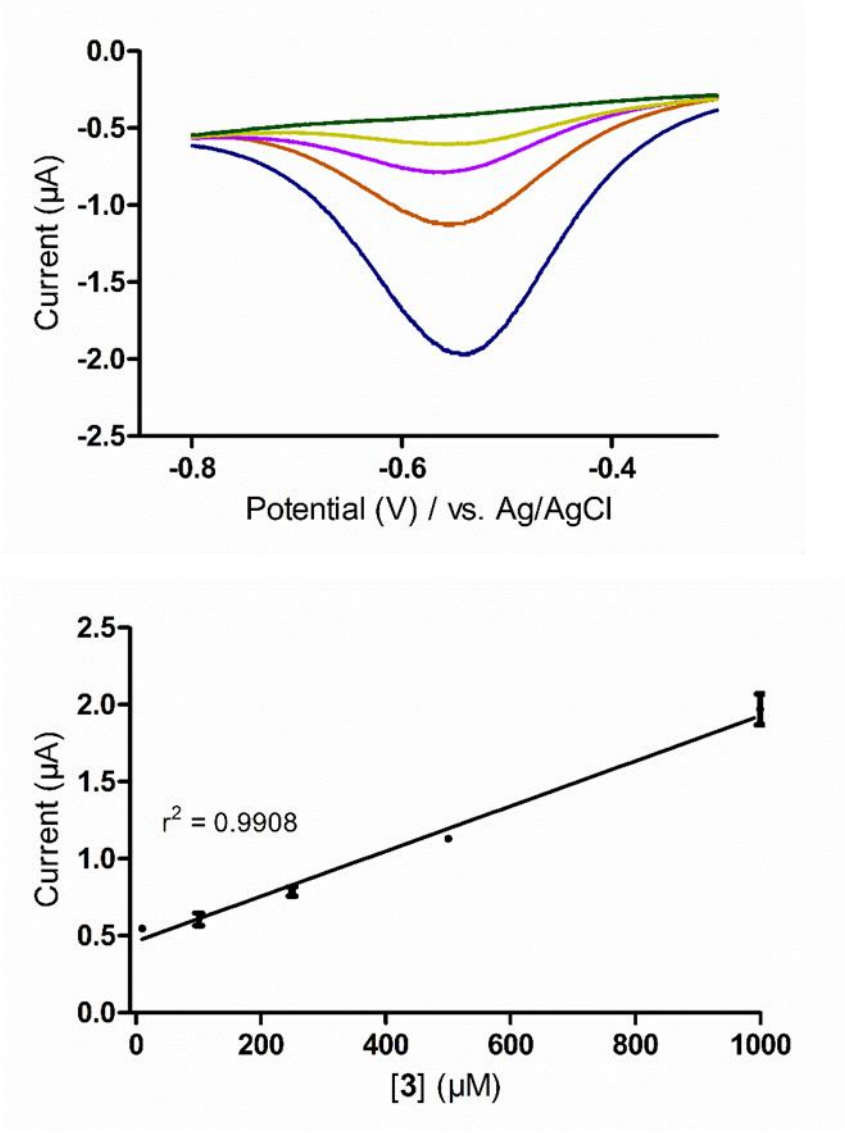

Figure 3.6. Differential pulse voltammograms for concentrations of **3** at 1000 μM (blue line), 500 μM (orange line), 250 μM (purple line), 100 μM (yellow line) and 10 μM (green line) in PBS with a glassy carbon macroelectrode (top) and the standard curve for differential pulse voltammetry analysis of **3** (bottom). Solid line is the fit with linear regression (n = 3). Potentials are referenced against Ag/AgCl reference electrode.

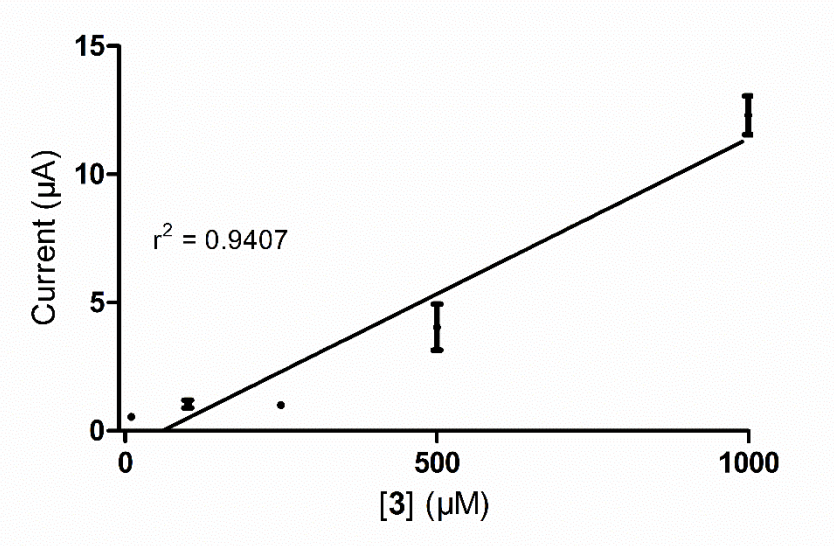

Figure 3.7. Standard curve of varying concentrations of **3** as measured by cyclic voltammetry. Potential was sweeped from 0 to -1 V with a glassy carbon macroelectrode in solutions of **3** and the peak reduction potential was taken for each concentration. Potentials are referenced against Ag/AgCl reference electrode.

However, the reduction potential of **3** was found to overlap with the reduction potential of the phosphate species in PBS. Therefore, DPV could not be effectively employed for the quantification of Pt(IV) species in PBS. Focus was turned to developing NMR as an analytical technique for the rapid and quantitative determination of Pt(IV) species in aqueous solutions. ^{195}Pt NMR affords sharp peaks over a large chemical shift range (-7000 to 1000 ppm) and as such, very small changes in structure can be seen with high resolution. In addition, there are clear differences in the range of chemical shift between the IV and II oxidation states: roughly 0 to 7500 ppm for Pt(IV) species and -6000 to -1000 ppm for Pt(II) species[197]. This method of analysis thus would afford a highly resolved, quantitative speciation. However, despite the relatively high natural abundance

of ^{195}Pt (33.8%), the minimum concentration for discernible peaks with good signal-to-noise ratio was found to be ~8 mM of Pt complex **3** which was deemed unsuitable (Figure 3.8).

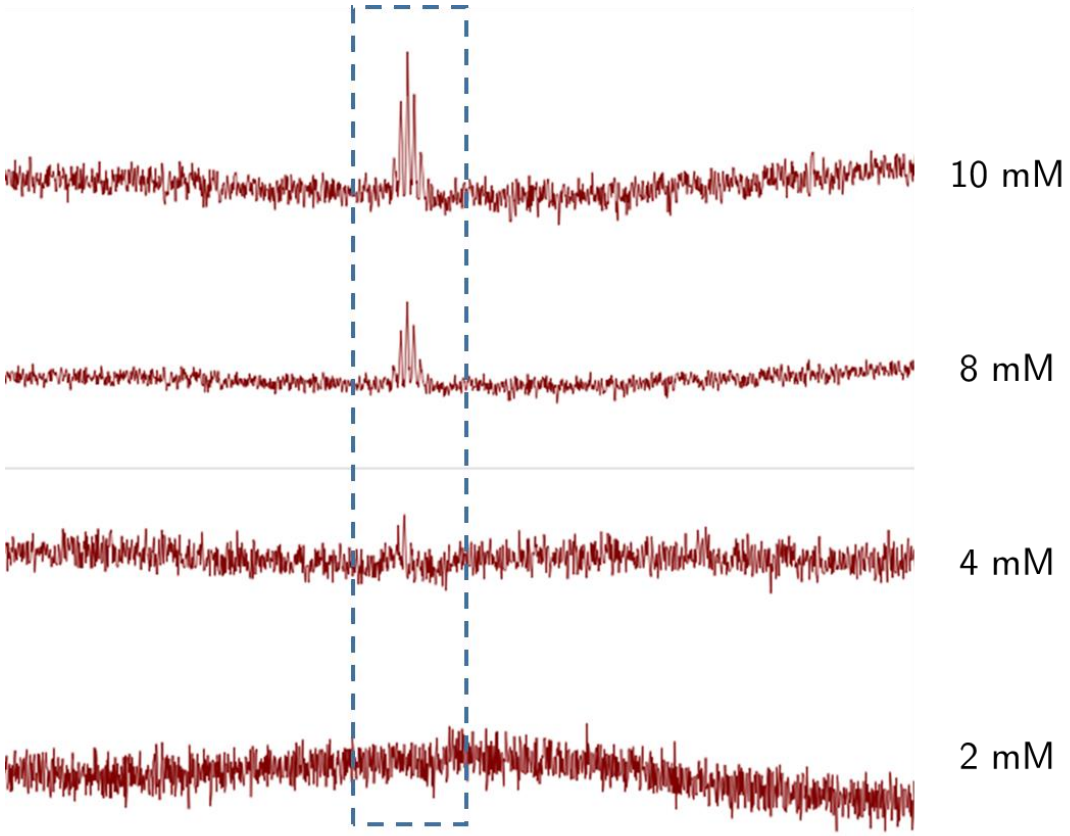

Figure 3.8. ^{195}Pt NMR spectra of **3**, demonstrating the ease of analysis and speciation but with limitations in concentrations required for suitable noise/signal ratios. Spectra were acquired with 1024 scans in D_2O and were post-processed with Whitaker Smoother.

^{1}H NMR was instead used, due to its high sensitivity allowing low concentrations to be analysed. Due to the strong residual H_2O solvent signal, presaturation acquisition methods were explored to suppress the solvent signal allowing lower

limits of detection for the Pt(IV)-Pt(II) conversion. PBS solutions were diluted 2-fold with D_2O to allow solvent-locking and 3-trimethylsilylpropane sulfonic acid sodium salt was used as internal standard, due to its good aqueous solubility and characteristic trimethylsilyl singlet at ~0 ppm. From Figure 3.9, it can be seen that concentrations down to 10 μM of **3** could be clearly measured.

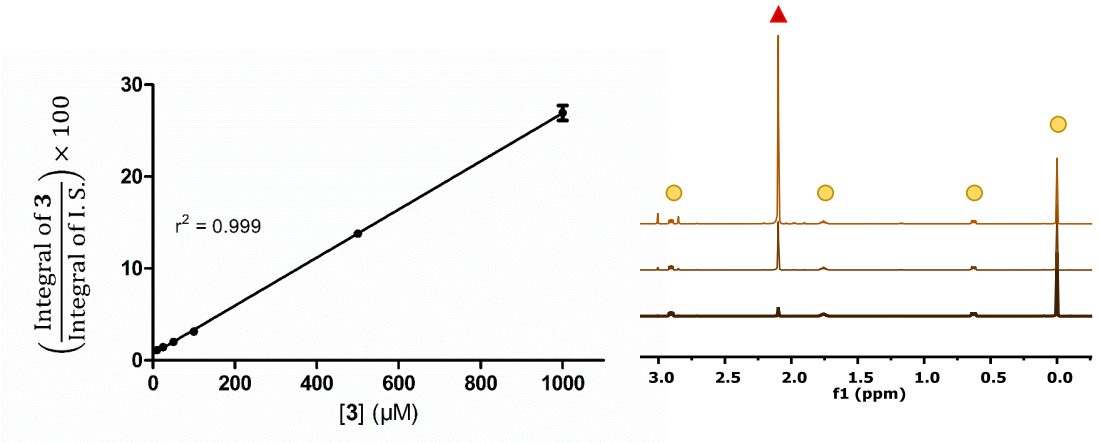

Figure 3.9. Standard curve of varying concentrations of **3** in PBS/D_2O with a constant internal standard (trimethylsilylpropylsulfonic acid) concentration of 100 μM, as analysed by ^1H NMR with water suppression. The signal corresponding the protons of the axial ligands of **3** (▲) at each concentration were calculated as a percentage of the signal of the trimethylsilyl moiety of the internal standard (●).

3.5 Identification of a suitable redox mediator

Macroelectrodes with a gold working electrode surface were modified by creating a ternary self-assembled monolayer (tSAM) with the methylene blue derivative (MB-PEG-SH) and backfilled with thiohexanol (Figure 3.10). The methylene blue derivative was synthesised by employing solid-phase synthesis

techniques (Scheme 3.3). Previous work has shown that backfilling facilitates travel of the immobilised redox mediator to the electrode surface, presumably by preventing stacking and aggregation of the methylene blue aromatic moieties[43].

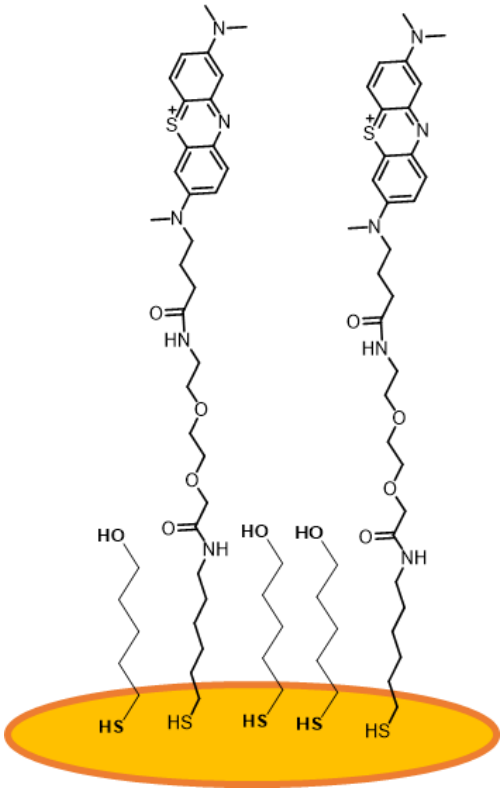

Figure 3.10. The ternary self-assembled monolayer composed of methylene blue units bound to the gold electrode surface, back-filled with thiohexanol.

This method allowed for efficient fabrication of a methylene blue-modified electrode (MB-tSAM) with immobilisation of the redox mediator to the electrode surface confirmed by CV. The characteristic reversible redox waves were observed, confirming the presence and the functionality of the methylene blue.

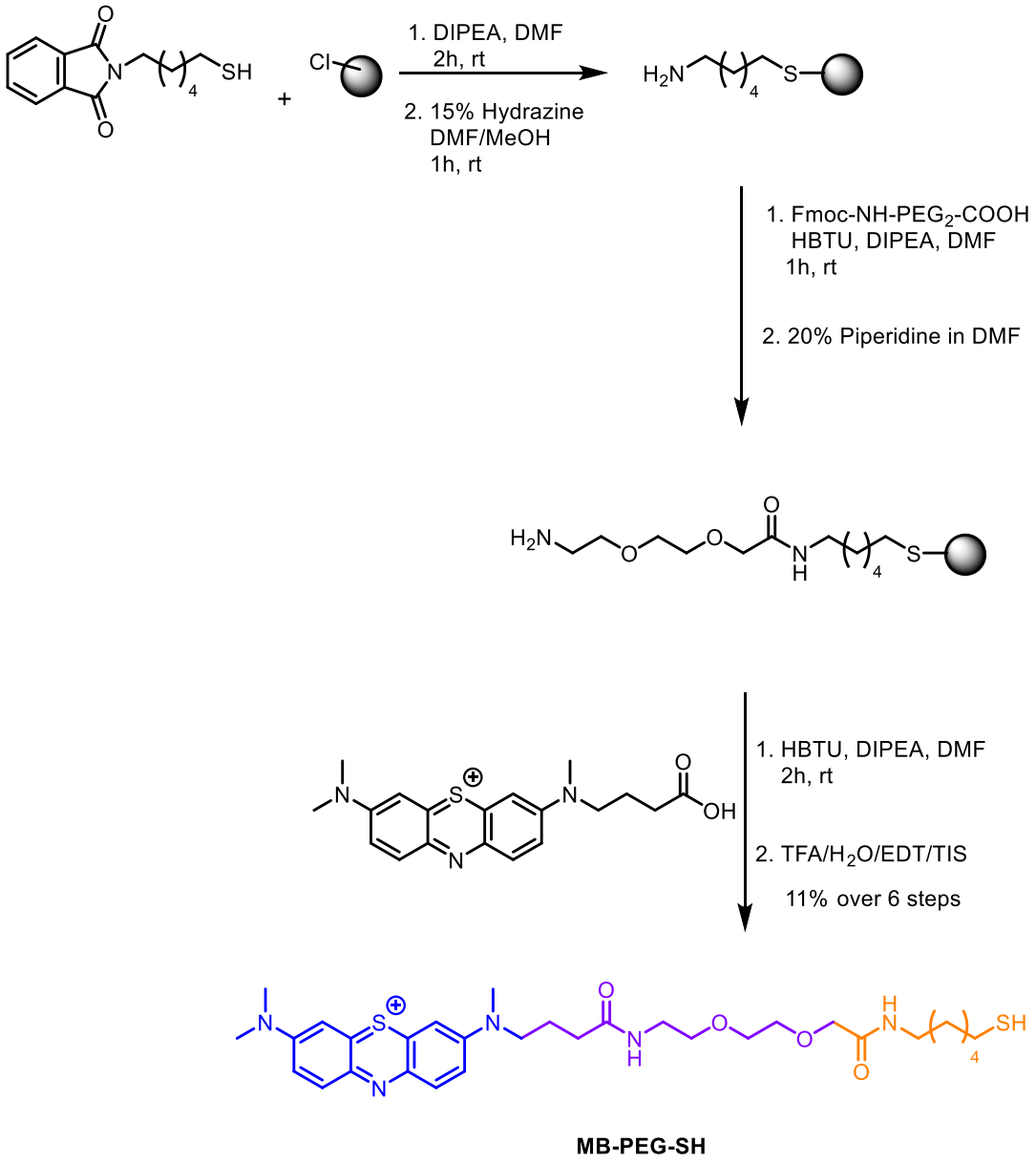

Scheme 3.3. Synthesis of methylene blue derivative used for the formation of the MB-tSAM. The grey bead represents the 2-chlorotrityl chloride linker on a polystyrene resin for solid-phase synthesis. The final product was composed of a methylene blue unit (blue), an ethylene glycol-based spacer (purple) and a mercaptohexamine moiety as an anchor (orange) to allow attachment.

With modified electrodes in hand, the capability of the MB-tSAM to reduce Pt(IV) species was interrogated. A potential of -0.3 V was applied to the MB-tSAM in a solution of Pt complex **3** (200 μM) in PBS and the reaction monitored by ^{1}H NMR and LC-ICP-MS. No detectable or significant reduction in the Pt(IV) species was observed via NMR analysis. However, LC-ICP-MS showed a slight decrease in the levels of Pt(IV) and slight increase in Pt(II) species. It was postulated that although the methylene blue was capable of reducing the Pt(IV), this occurred too inefficiently to be useful, with the small number of methylene blue molecules immobilised on the electrode surface deemed to be a major factor. Thus, further methods of methylene blue immobilisation were explored where the methylene blue concentration could be increased. Previous studies have shown that methylene blue can be electro-polymerised onto an electrode surface and using the work of Brett as a basis, electro-polymerisation on the glassy carbon electrodes was developed and optimised[198, 199]. The specific mechanism of electro-polymerisation of MB remains elusive and may be an outcome of multiple different cross-linking varieties (due to sweeping between highly oxidative and reductive potentials)[198]. Scheme 3.4 shows two possible methods of cross-linking: oxidative C-C bond formation or C-N bond formation, *via N*-demethylation.

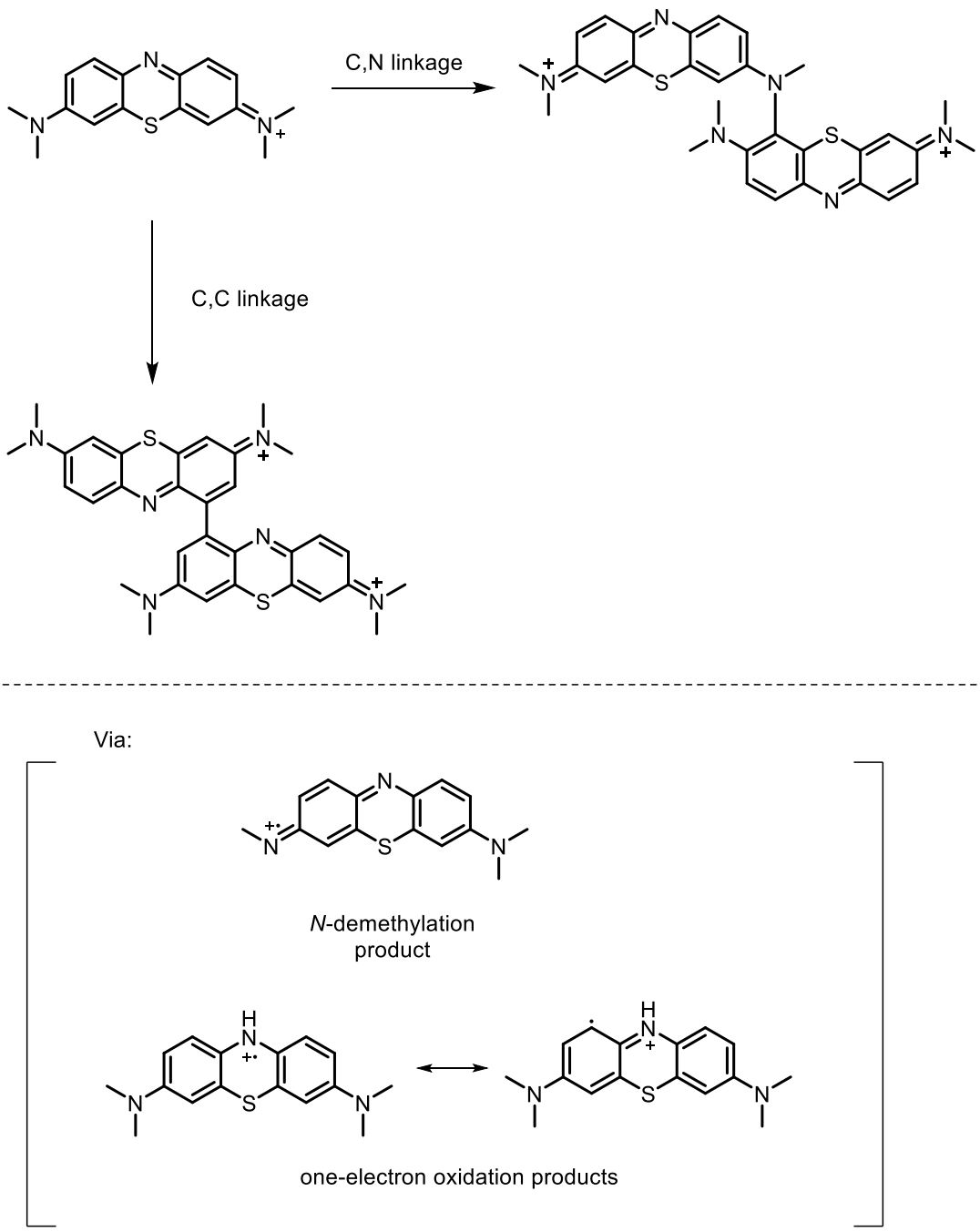

Scheme 3.4. Postulated cross-linking pathways for the electro-polymerisation of methylene blue monomers and the possible implicated one-electron oxidation species.

Regardless, this method of immobilisation afforded an efficient and reproducible route to polymethylene blue-modified electrodes (PMB) with tuneable control over the quantity of MB immobilised controlled by the application time and concentration of monomer solution. It was found that fifteen CV scans between - 0.6 V and +1.2 V at 50 mV.s^{-1} afforded robust devices, while increasing the number of deposition scans or lowering the scan rate yielded devices which showed reduced amplitude of methylene blue redox waves, suggesting that the approach of the redox mediator to the electrode surface was impeded by over-polymerisation (Figure 3.11).

The Pt(IV) reduction capabilities of the PMB electrodes were measured and analysed *via* NMR and LC-ICP-MS. As with the MB-tSAM modified electrodes, little conversion was observed. It was postulated that methylene blue was not a suitable redox mediator for the Pt(IV) reduction and so a screen of mediators in solution (with a 1:2 molar ratio of redox mediator:Pt(IV)) with a potential applied at the reduction potential for each respective mediator, and analysed by ^{1}H NMR.

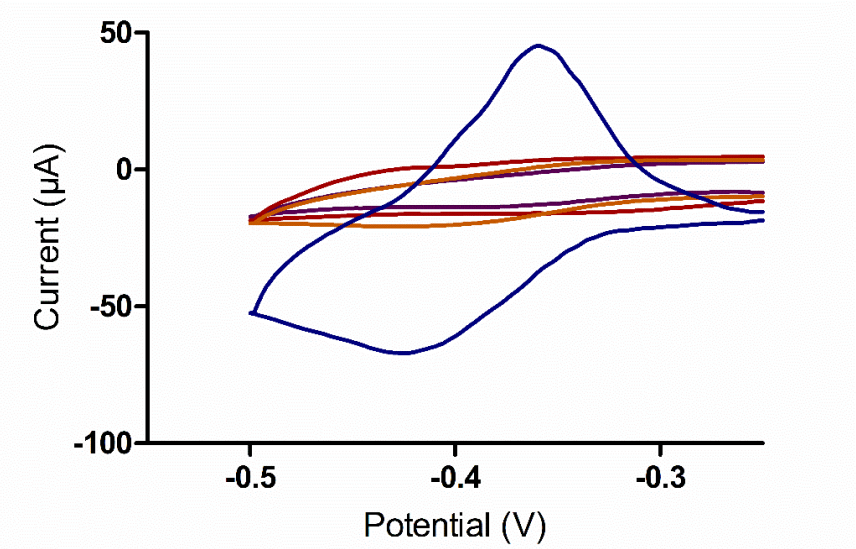

Figure 3.11. Cyclic voltammograms confirming the presence of polymerised methylene blue on screen-printed carbon ink electrodes. The optimal conditions were methylene blue (1 mM) in aqueous $(NH_4)_2SO_4$ (0.1 M) with the potential swept from -0.6 V to +1.2 V at 50 $mV.s^{-1}$ for fifteen scans (blue line). Increasing the scan rate to 200 $mV.s^{-1}$ (purple line) or 100 $mV.s^{-1}$ (red line) or increasing the number of scans to thirty yielded devices with much lower amplitude of the redox peaks of methylene blue. Potentials are referenced against a Ag pseudo-reference electrode.

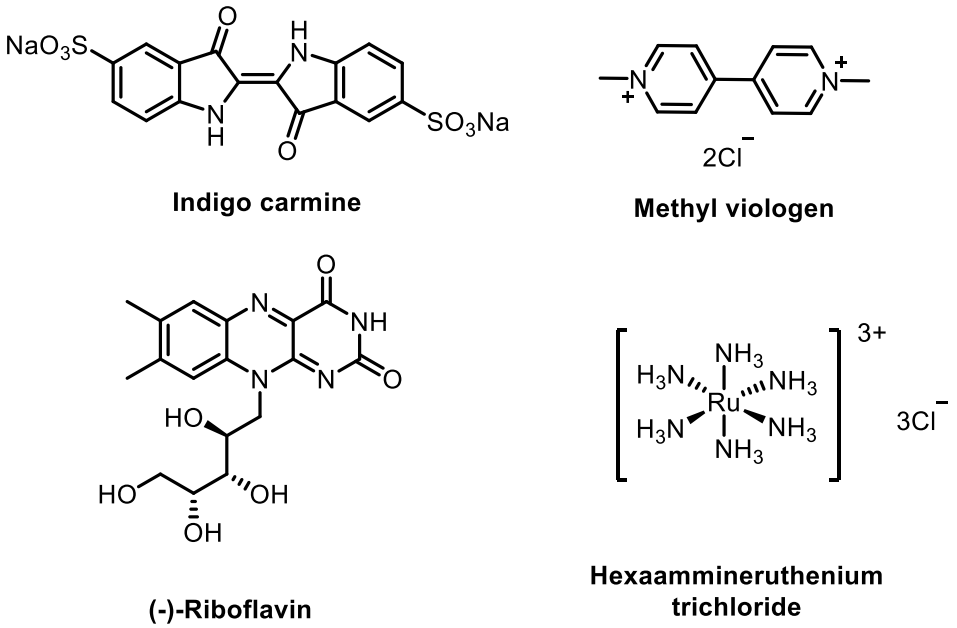

Scheme 3.5. Structures of the tested redox mediators

Redox mediators screened included indigo carmine, methyl viologen, (-)-riboflavin and hexammineruthenium chloride ($[Ru(NH_3)_6]Cl_3$) (Scheme 3.5). These redox mediators were selected due to their reduction potential occurring at a lower potential than that of the Pt(IV) complexes synthesised.

Of these, it was found that $[Ru(NH_3)_6Cl_3]$ offered the best performance in reducing the Pt(IV) species whereas indigo carmine and methyl viologen gave no conversion. Riboflavin gave modest conversion however was discounted due to its relatively high reduction potential. A bulk electrolysis experiment consisting of **6** (100 μM) and $[Ru(NH_3)_6]Cl_3$ (50 μM) was subjected to a constant potential of -0.4 V and was analysed by HPLC and showed good conversion of **6** to the active drug **OxPt** while in PBS (Figure 3.12).

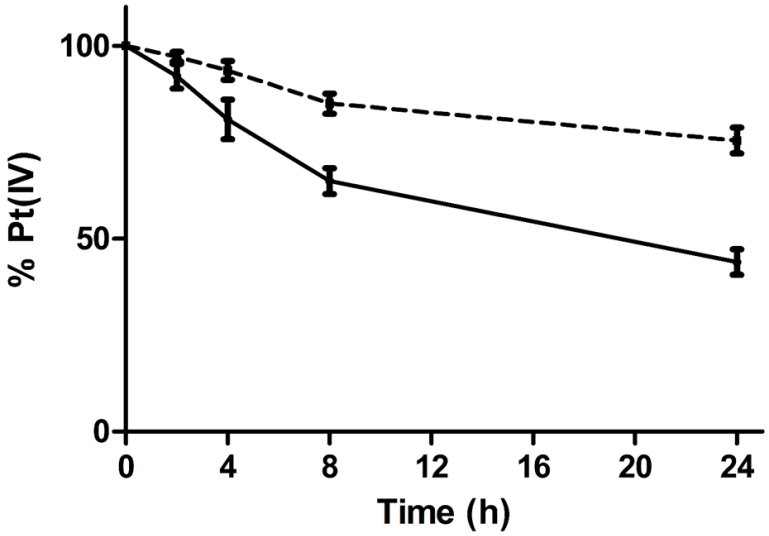

Figure 3.12. The conversion of **6** (100 μM) over time following the application of -0.4 V with and without $[Ru(NH_3)_6]Cl_3$ (50 μM) in PBS as measured by HPLC at 254 nm: solid line and dashed line, respectively.

3.6 Fabrication of discrete redox mediator modified electrodes

Immobilisation of $[Ru(NH_3)_6)Cl_2]$ onto an electrode surface presented a challenge due to the lack of handle for electropolymerisation. Therefore, a novel redox mediator, pentaammine(vinylpyridine)ruthenium chloride (**Vp-Ru**) based on $[Ru(NH_3)_6)Cl_2]$ was designed and synthesised with replacement of one ammine ligand with a vinylpyridine (Scheme 3.6). The installation of a vinyl moiety would theoretically afford the handle required for electropolymerisation. The substitution of the chloro ligand for the vinylpyridine was successful (as confirmed by LC-MS), however the product could not be isolated due to its instability.

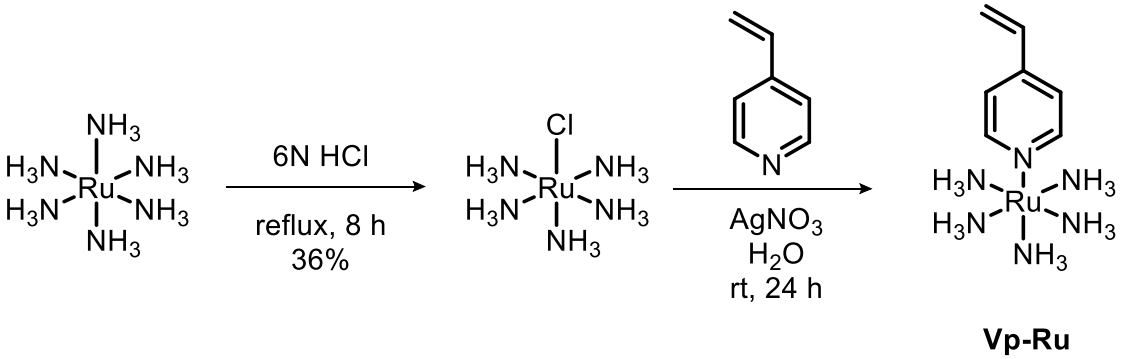

Scheme 3.6. Synthesis of monodentate vinylpyridine pentammine ruthenium complex.

Instead, direct adsorption of the redox mediator to the electrode surface, utilising a polymer support for the redox mediator was explored. Previous work by Unwin has shown that Nafion was an effective polymeric support for related redox mediators, including $Ru(bpy)_3Cl_2$[200]. Nafion is a polymer with a tetrafluoroethylene backbone with pendant sulfonates and is used as a proton conductor, in fuel cells, as the network of sulfonates allows a proton to be shuttled through the polymer[201]. Deposition of Nafion affords a porous structure that facilitates the transport of cations but excludes anions and electrons. This characteristic was exploited for the immobilisation $[Ru(NH_3)_6)Cl_2]$ to encase the redox mediator through electrostatic interactions between the positively charged redox mediator and the negatively charged Nafion polymer layer. As the Nafion layer excludes anions, it may also benefit the application of devices in biological complex systems by providing a blocking effect between potential interferents and the redox mediator and electrode surface. The redox mediator was found to act as a conduit of electrons from the electrode surface and the Pt(IV) species, with the mechanism hypothesised to be a chain of redox mediators shuttling

electrons to and from each other forming an electrocatalytic network throughout the Nafion volume.

The method of functionalising Nafion-bound $[Ru(NH_3)_6]Cl_3$ onto the glassy carbon disposable screen-printed electrodes was optimised to afford functional modified electrode devices (MED). Thin layer Nafion-coated electrodes were made by drop-coating the Nafion solution (5% w/v in water and lower aliphatic alcohols) directly onto the working electrode surface and allowing the solvent to air-dry. The dried Nafion-coated electrode was then soaked into an aqueous solution of the redox mediator (in the oxidised form), rinsed with water to remove any non-adherent redox mediator and stored wet (Figure 3.13). The modified electrodes were unable to be dried and re-wetted without loss of the redox mediator signals. This may be due to changes in the morphology of Nafion upon hydration-dehydration cycles preventing the redox mediator from being retained its adherence, as has been observed in other studies[202]. During fabrication of the electrodes, the oxidised form of the redox mediator, $[Ru(NH_3)_6]^{3+}$, was used. The reasons for this were two-fold: the increased positive charge will facilitate binding and integration of redox mediator into the Nafion layer and the oxidised form will need to be reduced electrochemically before it can reduce Pt(IV) species, thereby preventing any latent Pt(IV) reduction by only incubation of the modified electrode in a solution of **6** (without an applied potential).

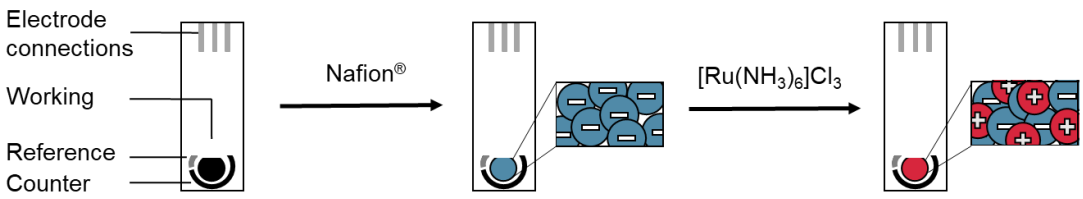

Figure 3.13. Fabrication of the modified screen-printed carbon electrodes. Hexaammineruthenium (the redox mediator) is encapsulated, exploiting its positive charge, into the negatively charged Nafion polymer layer.

Successful entrapment of the redox mediator was confirmed by CV analysis in PBS with the immobilised $[Ru(NH_3)_6]^{3+}$ showing the expected reversible redox behaviour. In comparison, the redox mediator in solution, i.e. non-adhered to electrode surface, the redox waves were shifted slightly more negatively when it was incorporated in Nafion (see Figure 3.14).

In addition, the redox mediator's interactions with the electrode surface was shown to be diffusion-limited by investigating the changes in peak current in response to changing the scan rate of the cyclic voltammetry. There was a linear proportional response in peak current (A) to the square root of the scan rate ($mV.s^{-1}$) demonstrating that the current associated with the redox mediator's processes were dependent upon the rate at which the mediator could diffuse to and from the electrode surface ("diffusion-limited"), as defined by the Cottrell equation:

$$I = \frac{nFAc_j^0\sqrt{D_j}}{\sqrt{\pi t}}$$

where I = peak current (A), n = number of electrons implicit, F = Faraday constant, A = area of electrode (cm^2), c_j^0 = initial concentration of mediator ($mol.cm^{-3}$), D = diffusion coefficient and t = time (s). Where redox processes fit linearly to the plot of I vs $t^{-1/2}$, there is a diffusion-limited process occurring whereas deviations from this suggest other possibilities. Therefore, it can be seen that the Nafion entrapment of the redox mediator does not hold the redox mediator tightly to the electrode surface, otherwise a "surface-controlled" processes would be observed where the peak current would be directly proportional to the scan rate. This is further evidence that an electron-shuttle network has been formed throughout the Nafion layer, where the redox mediator can move freely and transfer electrons from molecule to molecule.

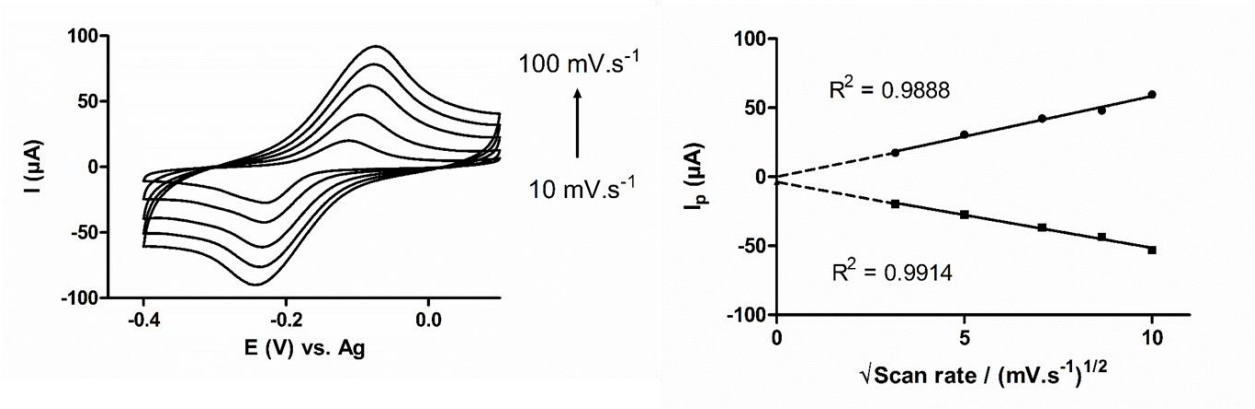

Figure 3.14. Cyclic voltammetry of the modified electrodes showed a dependence of peak current on scan rate (left) and plot of √Scan rate against peak current demonstrating the diffusion-limited process of the redox mediator's approach to electrode in the Nafion layer (right).

The modified electrodes were further characterised in terms of stability and leaching. CV analyses were taken at 0 and after 24 h in different biological media to assess the capability of the polymeric encapsulation of redox mediator to withstand interference from components of complex media. It can be seen from Figure 3.15 that the modified electrode was robust towards interference from biomolecules. There was a slight deviation from the expected redox behaviour in 10% FBS solution, which may be attributed to protein binding on the Nafion/electrode surface. Despite this, the characteristic redox waves can still clearly be observed.

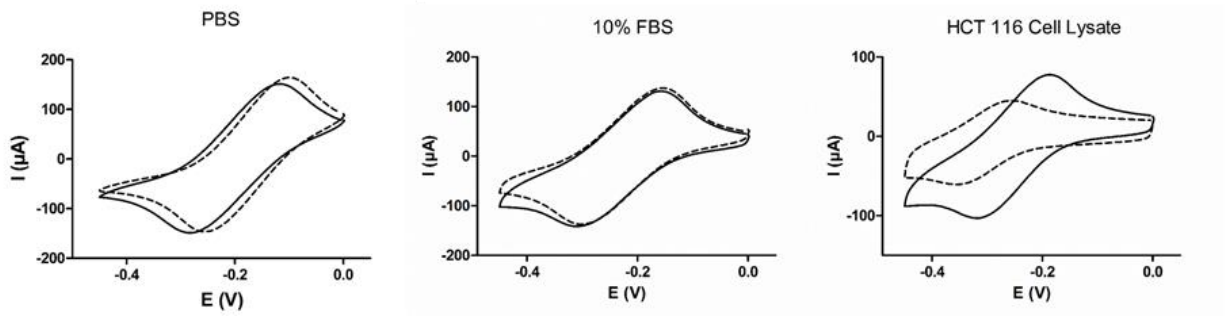

Figure 3.15. Cyclic voltammograms recorded for modified electrodes in phosphate buffered saline, foetal bovine serum, HCT 116 cell lysate before (dashed line) and after 24 h (solid line) incubation. Potentials are relative to the Ag pseudo-reference.

It is imperative for biological applications, particularly future *in vivo* experiments that the redox mediator does not leech out of the Nafion membrane. Leeching of the redox mediator would disable the Pt(IV) reduction/activation capabilities of the modified electrodes and would also lead to safety concerns. Therefore, the total quantity of redox mediator entrapped in the Nafion layer was quantified and

the percentage that leached examined. The cytotoxicity of the redox mediator was also investigated.

Determination of the total Ru content of the device was analysed by ICP-OES. The carbon ink (to which the Nafion-redox mediator system was adhered to) was subjected to digestion by aqueous nitric acid to ensure total degradation (and dissolution) of the Nafion-encased redox mediator. As can be seen in Figure 3.16, the device fabrication process yielded devices with little deviation between electrodes and with an average content of 1.08 ± 0.02 μg ($n = 5$) of Ru.

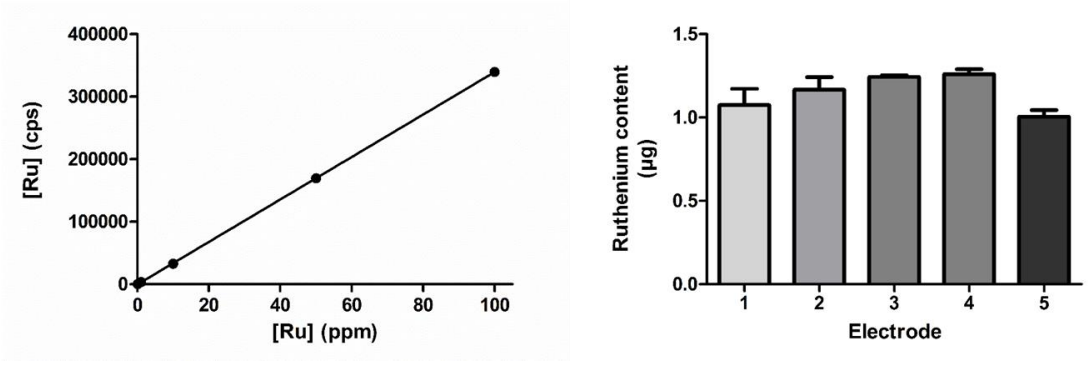

Figure 3.16. ICP-OES standard curve for Ru detection at 350 nm with $RuCl_3$ as an external standard (left). Samples are decomposed by the inductively-couple plasma to their atomic components. The wavelength selected is that at which the excited state ruthenium ions and free atoms emit as they decay to lower energy states. Five modified electrodes were quantified for their total Ru content by ICP-OES analysis (right).

While this was the total content of Ru held within the Nafion membrane, it is not a measure of the redox-active mediator; that is, the proportion of redox mediator that can approach the electrode surface and participate in redox reactions. In

order to do this, the differences in charge density were compared between a blank SPCE and a Nafion-modified electrode, when a potential of -0.4 V was applied in a solution of KCl (aq., 0.1 M). The average charge for each type of device (modified and non-modified) was measured by chronoamperometry over 400 s and the difference calculated (n = 3), negating background currents (solvent effects and non-Faradaic processes) to allow analysis solely on the effects caused by the redox mediator (Figure 3.17). The redox-active proportion of encapsulated redox mediator was then calculated by coulometric analysis using the equation:

$$Q = nFA\Gamma$$

where Q = charge in Coloumbs, n = number of electrons involved in the redox process, F = Faraday's constant ($C.mol^{-1}$), A = geometric area of electrode (m^2) and Γ = surface coverage or surface concentration ($mol.m^{-2}$). The surface coverage can then be related to the mass of redox mediator (m) that is redox-active, from the molecular weight of $[Ru(NH_3)_6]^{3+}$. The redox-active content of the redox mediator was found to be 0.84 μg per device (see above calculation and Figure 3.17) or around 78% of the total content.

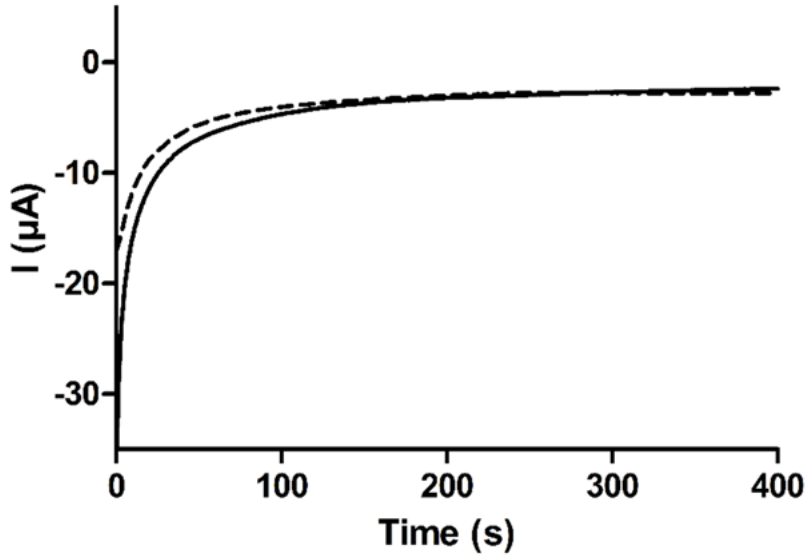

Figure 3.17. Amperometric quantification of redox-active $[Ru(NH_3)_6]Cl_3$ contained in a modified electrode in comparison to the total charge after 400 s of application of -0.4 V for non-modified electrode (dashed line) and modified electrode (solid line).

The leaching of Ru was analysed by ICP-OES. Potential (-0.4 V) was applied with modified electrodes submerged in aqueous solution and after 24 h of application the electrodes were removed and the Ru content of the solutions quantified. Figure 3.18 shows that the leached Ru levels were around 10% of the total content ($\sim 115 \pm 14$ ng, $n = 3$) liberated from electrostatic encapsulation over 24 h.

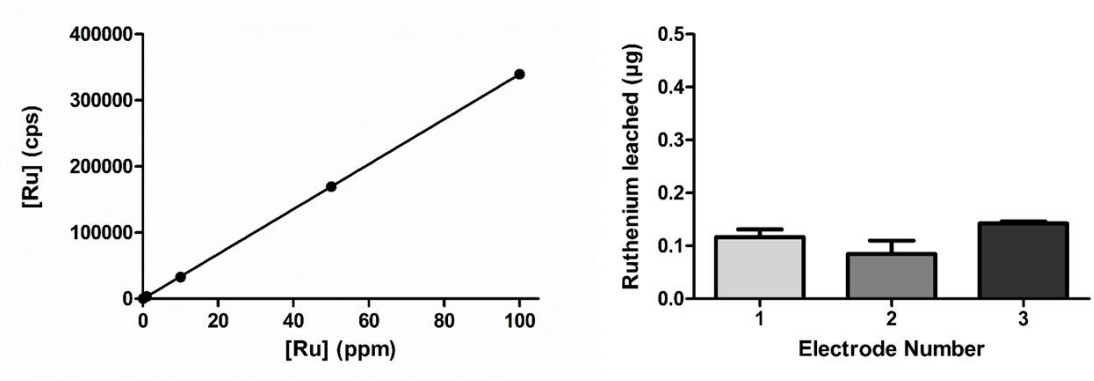

Figure 3.18. ICP-OES standard curve for Ru detection at 350 nm using $RuCl_3$ as an external standard (left) and quantification of the Ru leached from the modified electrodes over 24 h (right).

Despite the minimal leaching, it was necessary to confirm (particularly for biological experiments) that this leaching would not cause cell death and would not interfere with the cell viability assays. The cytotoxicity of both the reduced ($[Ru(NH_3)_6]^{2+}$) and the oxidised ($[Ru(NH_3)_6{}^{3+}]$) form of the redox mediator were analysed by an MTT assay (Figure 3.19). These two forms of the redox mediator were both well-tolerated by HCT 116 cells (up to 10 µM with no reduction in cell viability seen up until this concentration). Increasing the concentration up to 100 µM showed that high concentrations of the reduced form of the redox mediator were cytotoxic. However, assuming the total content of each modified electrode leached out into cell-containing media (3.4 mL used for 24-well plate), the maximum concentration the cells would be exposed to would only be around 1.19 µM; far less than the levels needed to elicit cell death.

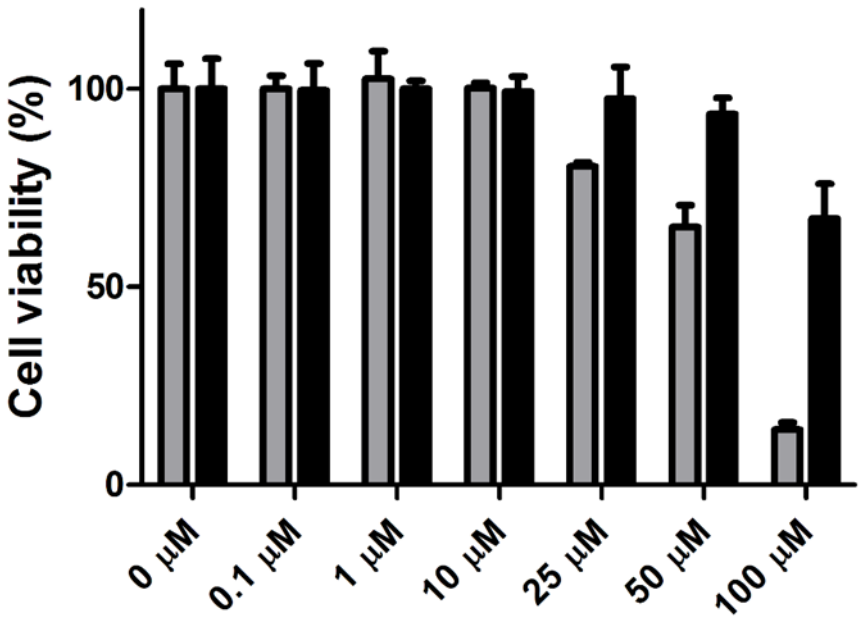

Figure 3.19. Cell viability for HCT 116 cells treated with $[Ru(NH_3)_6]Cl_2$ (grey bars) and $[Ru(NH_3)_6]Cl_3$ (black bars). Cells were treated with 0 μM to 100 μM of the oxidised form of the redox mediator, $[Ru(NH_3)_6]Cl_3$, or the reduced form, $[Ru(NH_3)_6]Cl_2$, and incubated for 72 h (n = 3) to verify that any Ru potentially leached from the device would not have any effect on cell viability†.

3.7 Characterisation of Pt(IV) reduction by the modified electrodes

It had now been confirmed that the modified electrodes could be fabricated with desirable properties, namely: good total uptake into the Nafion layer; minimal leaching of the redox mediator from the Nafion layer and ability to retain their redox properties in biological milieu. With these devices in hand, focus was turned to characterising the Pt(IV) reduction profile. The optimal Pt(IV) species for electrochemical activation *in cellulo* was considered initially. Ideally this

Pt(IV) species would be bio-inert, i.e. it would not be reduced, activated or degraded biologically, and would be non-toxic until activated to the active Pt(II) species. Additionally, as the electrode would be positioned outwith cells (suspended above cellular monolayers in the cell media) it was also important that the chosen Pt(IV) species was not taken up into cells and would be retained in the cell media until activation. Cell uptake of molecules can be modulated by that molecule's charged state. For instance, cell membrane penetrant peptides are generally mainly composed of cationic residues (Arg, Lys, etc.), as they are attracted to the predominantly negatively charged surface charge of cell membranes, arising primarily from the head section of phospholipids where phosphate moieties are presented (see Chapter 1). Vice versa, negatively charged molecules and nanoparticles are subject to reduced cell uptake due to the electrostatic repulsion between the negatively charged molecule and the negatively charged membrane. These mechanisms are overcome by active transport and cell surface channels.

It was therefore postulated that a negatively charged Pt(IV) species would be optimal for electrochemical activation. Previous work by Sessler utilised the disuccinato Pt(IV) complex **6** showed remarkable stability towards biological reductants. Following synthesis of this Pt(IV) complex (**6**), the cytotoxicity of this compound was analysed on HCT 116 cells by an MTT assay and compared to that of the concordant active-drug Pt(II) species, oxaliplatin (OxPt) (Figure 3.20). There was good disparity in the toxicity of **6** and the OxPt; desirable for turn-on therapeutics, the IC_{50} of OxPt for HCT 116 cells was 0.19 μM, whereas **6** was > 100 μM.

With bio-inert Pt(IV) species **6** identified, the reduction by the modified electrodes was characterised. The change from cisplatin-based prodrugs to oxaliplatin-based prodrugs afforded compounds with increased hydrophobicity and also contained ^{1}H-NMR detectable fragments from the 1,2-diaminocyclohexane equatorial bidentate ligand which facilitated analysis by HPLC and NMR, respectively.

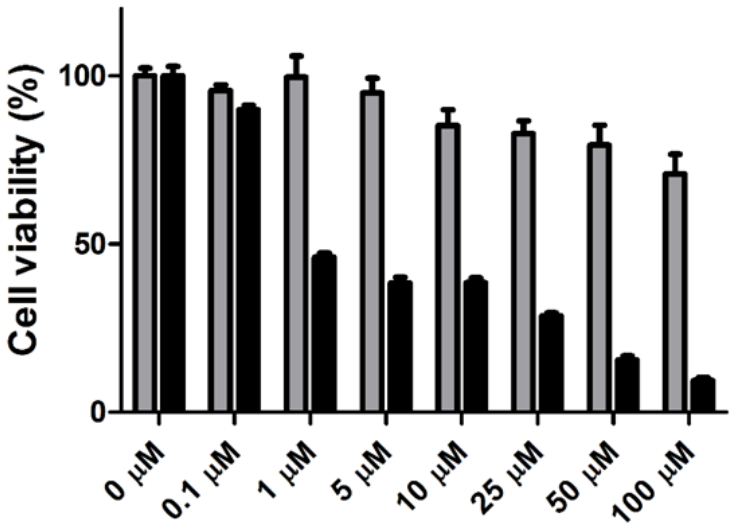

Figure 3.20. Cell viability of HCT 116 cells treated with oxaliplatin (black bars) and the Pt(IV) prodrug **6** (grey bars), as analysed by an MTT assay. Cells were treated with 0 μM to 100 μM of the Pt(IV) prodrug, **6**, or oxaliplatin and incubated for 72 h (n = 3).

With bio-inert Pt(IV) species **6** identified, the reduction by the modified electrodes was characterised. The change from cisplatin-based prodrugs to oxaliplatin-based prodrugs afforded compounds with increased hydrophobicity and also contained ^{1}H-NMR detectable fragments from the 1,2-

diaminocyclohexane equatorial bidentate ligand which facilitated analysis by HPLC and NMR, respectively.

The oxidised form of the redox mediator, $[Ru(NH_3)_6]^{3+}$, was reduced at the electrode surface by applying a potential of -0.4 V to afford $[Ru(NH_3)_6]^{2+}$, which was able to reduce the Pt(IV) species, becoming re-oxidised in the process and closing the electro-catalytic cycle (Figure 3.21).

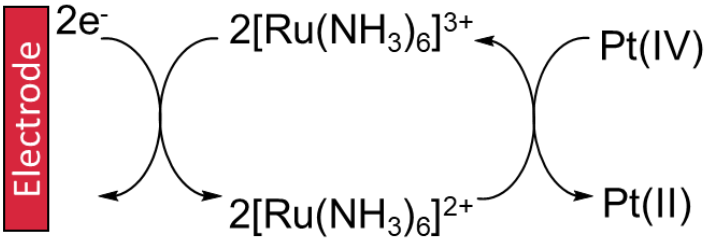

Figure 3.21. Hexaammineruthenium is a one-electron redox mediator, therefore two equivalents are required to reduce the Pt(IV) species to the Pt(II). The reduced form of the redox mediator can then be regenerated at the electrode surface.

Prodrug **6** was found to be relatively stable in 10% FBS at 37 °C (16% degradation after 24 h, n = 3) and towards reduction by glutathione and ascorbic acid with <10% decrease in Pt(IV) levels after 24 h at 37 °C (Figure 3.22). The decrease in the concentration of **6** in 10% FBS is likely due to low levels of bio-activation by reductants and other biomolecules contained in this complex medium.

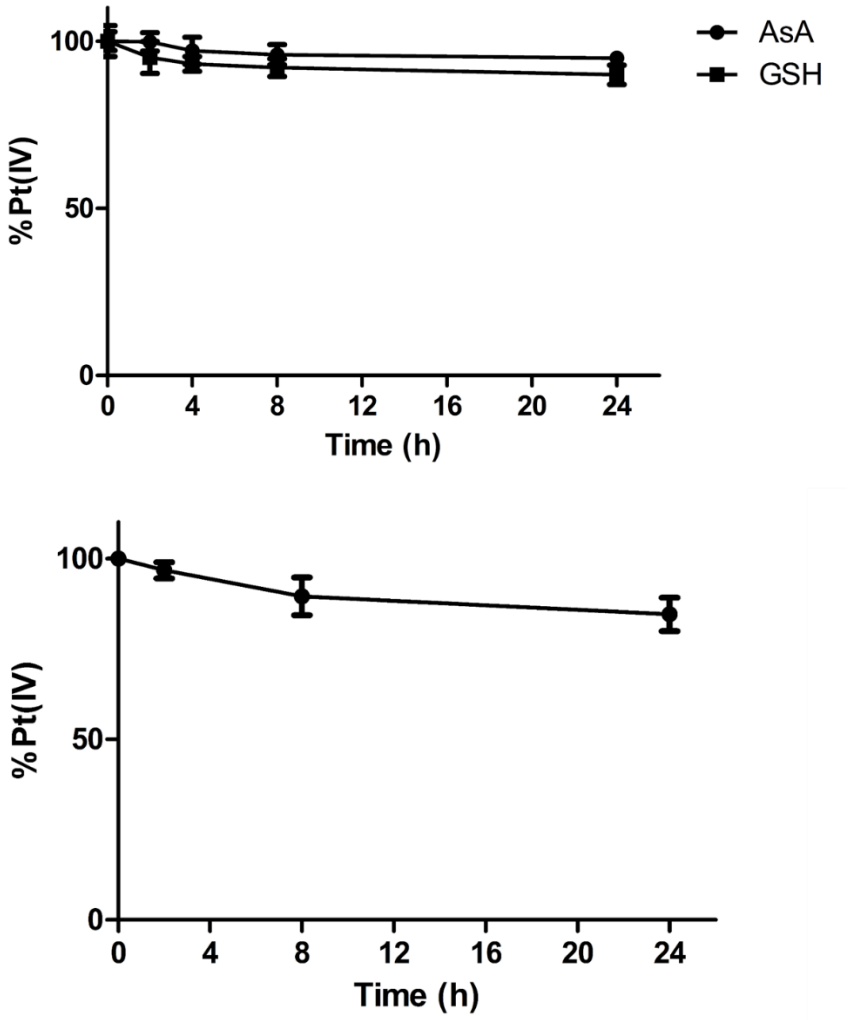

Figure 3.22. Stability of **6** towards gluthathione (GSH) and ascorbic acid (AsA) in PBS (top) and towards 10% FBS (bottom), as measured by HPLC. For the ascorbic acid/glutathione assay, a solution of **6** (100 μM) in PBS at 37 °C was treated with AsA or GSH to give final concentrations of 1 mM of each reductant. HPLC analysis was carried out at each time-point with detection at 254 nm. For testing the stability of **6** in 10% FBS, a solution of **6** (100 μM) was used and HPLC analysis carried out as above.

The ability of the modified electrode to function in biological media was assessed in 10% FBS and in HCT 116 cell lysate. As noted above, CV analysis over 24 h

showed that the modified electrode retained reversible redox behaviour characteristic of the Ru(III)/Ru(II) couple (Figure 3.15) with only incubation in cell lysate showing a change in redox processes, attributed to protein binding affecting the redox mediator and its interactions within the Nafion layer. Despite this, the electro-activation of **6** was not significantly affected in cell lysate and also performed well in 10% FBS (Figure 3.23).

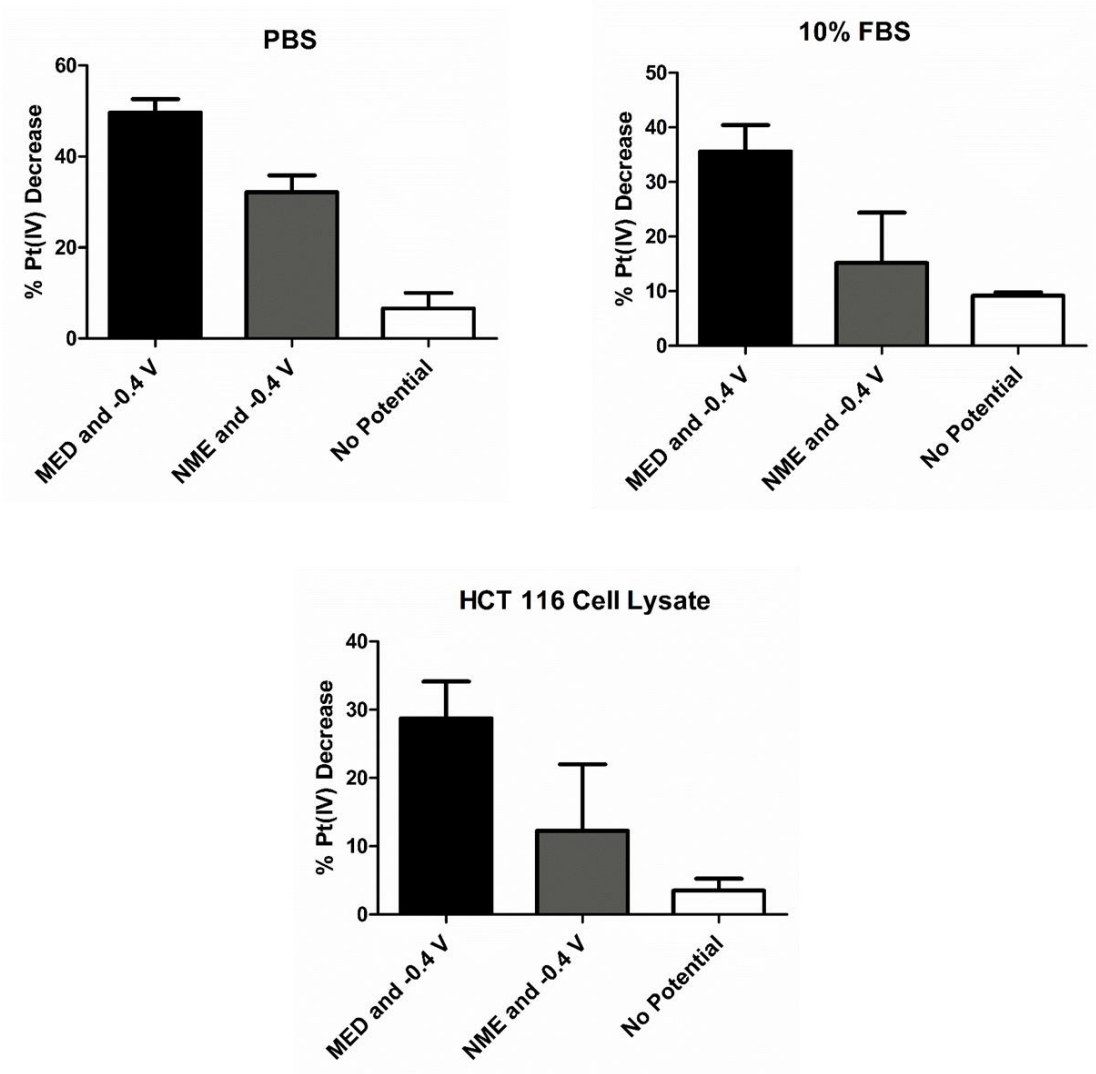

Figure 3.23. Reduction of **6** after application of -0.4 V with modified electrode (MED), non-modified electrode (NME) and with no potential applied in PBS, 10% FBS and HCT

116 cell lysate after 24 h. For each medium, solutions of **6** (100 μM) were made, potential was applied with either a modified electrode, non-modified electrode or no potential was applied with HPLC analysis after 24 h.

It can be seen that the level of reduction was slightly diminished when the solution changed from simple PBS to complex media (FBS or cell lysate) but only by around 15-20%. The utilisation of the modified electrode also afforded more efficient reduction than application of potential with an unmodified electrode. In addition, the reaction where the modified electrode was used was deemed to occur much more "cleanly" than with an unmodified electrode (Figure 3.24). LC-MS analysis of the two reaction solutions in PBS showed stark differences, with the unmodified electrode solution containing many Pt species (identified by their characteristic isotopic splitting), whereas LC-MS analysis of the reaction with the modified electrode showed only the two expected Pt species.

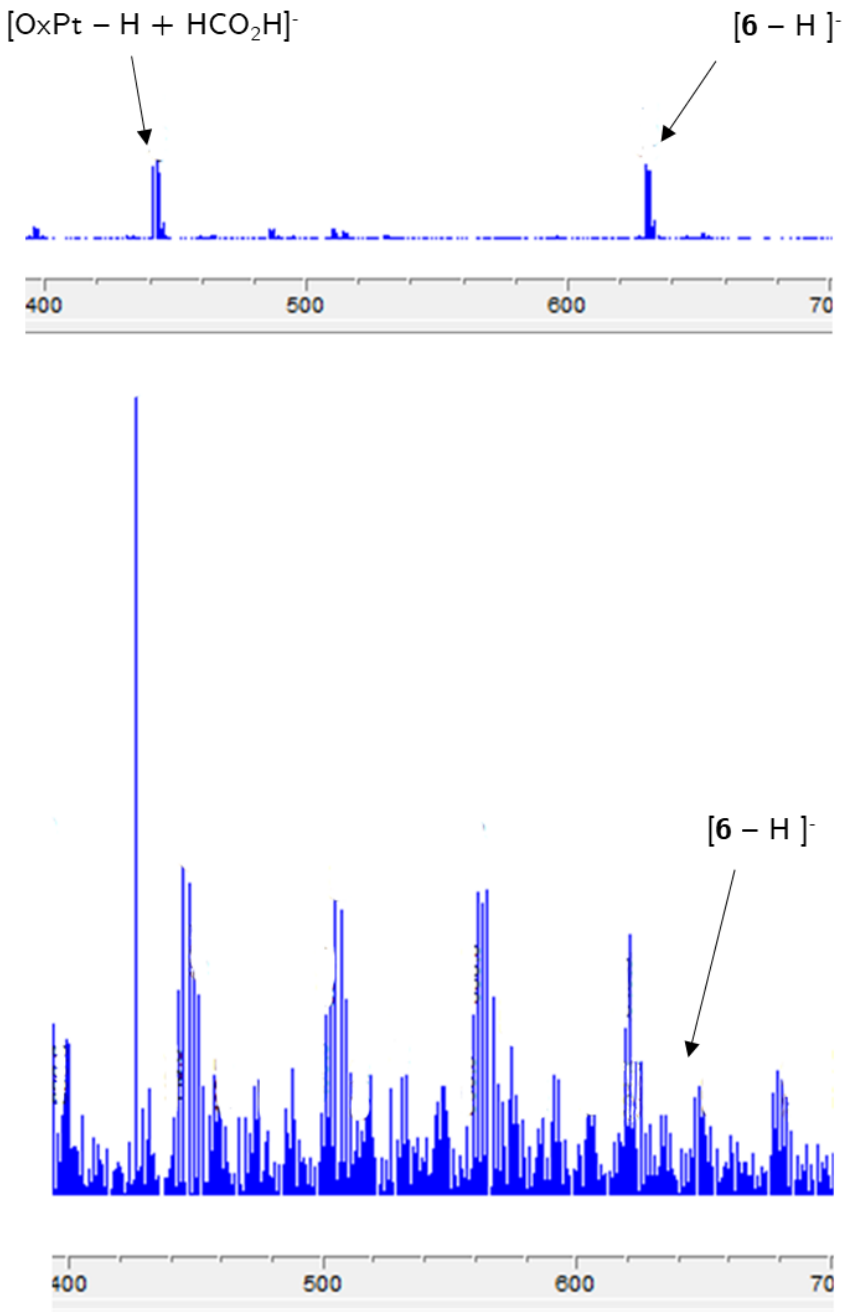

Figure 3.24. A representative example of the differences in Pt species formed by electro-activation of **6** using a modified electrode (top) and using a non-modified electrode by LC-MS analysis (negative mode). Where a modified electrode, both oxaliplatin and the prodrug **6** can clearly be seen. The reaction with a non-modified electrode produces many undesirable Pt species.

Quantification of the generation of OxPt was determined. The oxalate ligand in oxaliplatin is not stable towards chloride-containing medium and upon displacement of the oxalate ligand by chlorides the UV absorption (facilitating HPLC analysis) is lost. This has been well-studied and unlike cisplatin, oxaliplatin is administered in chloride-free carrier solutions usually in the form of 5% dextrose solution to prevent formation of the active Pt(II) species [(1,2-diaminocyclohexyl)$PtCl_2$]. This is a disadvantage of OxPt administration as it can affect electrolyte balance and trigger hyperglycemia in patients.

A post-derivatisation analytical method was required that would react with the resultant [(DACH)$PtCl_2$] in solution to produce an easily-identifiable conjugate. For this purpose, guanosine monophosphate (GMP), was employed. Pt-based cancer therapies are known to be thermodynamically-driven to react with guanosine bases in DNA as their main DNA-chelation mechanism. This is due to the hydrogen-bonding between amine or ammine ligands of the Pt species and the carbonyl of the DNA base, expediting the attack of N_7 to the Pt centre (Figure 3.25). This mechanism affords a simple and effective method to visualise Pt(II) generation, by the addition of excess GMP to solutions of Pt(II).

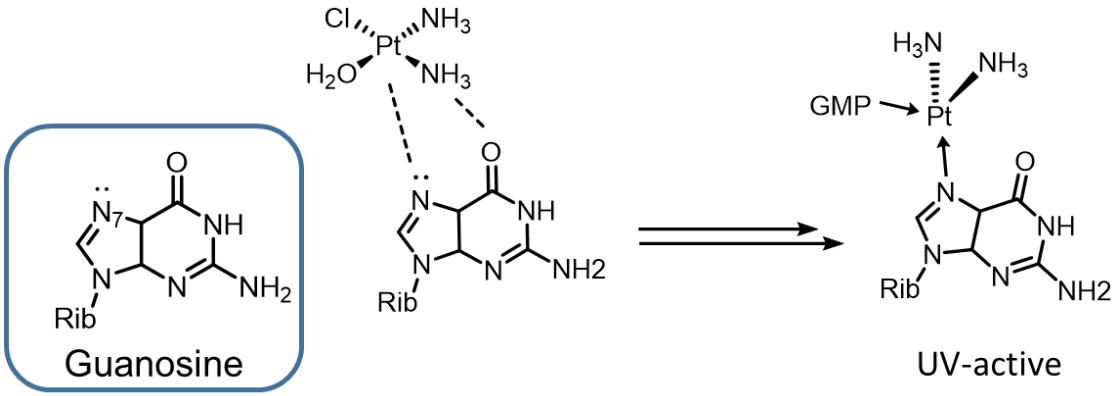

Figure 3.25. Pre-functionalisation assay for Pt(II) based on the thermodynamically-favoured preferential binding of cisplatin to guanosine monophosphate which affords a UV-active complex that facilitates analysis by HPLC with detection at 254 nm. Both chloride ligands can be displaced first by aquation then by nucleophilic attack of the N7 position of guanosine.

Addition of excess GMP to the reaction solution with HPLC analysis thus allowing the quantification of the Pt(II) species. To analyse that the peaks believed to be associated with the GMP adducts of Pt(II) species, the peak was collected by preparative HPLC and subjected to LC-MS analysis. The GMP bis-adduct of OxPt was found (identified by a *m/z* of 1031 and supported by the expected isotopic splitting pattern). The representative HPLC spectra in Figure 3.26 shows an increase in the Pt(II)-GMP_2 peak (peak b) over time, with a corresponding decrease in **6** (peak c).

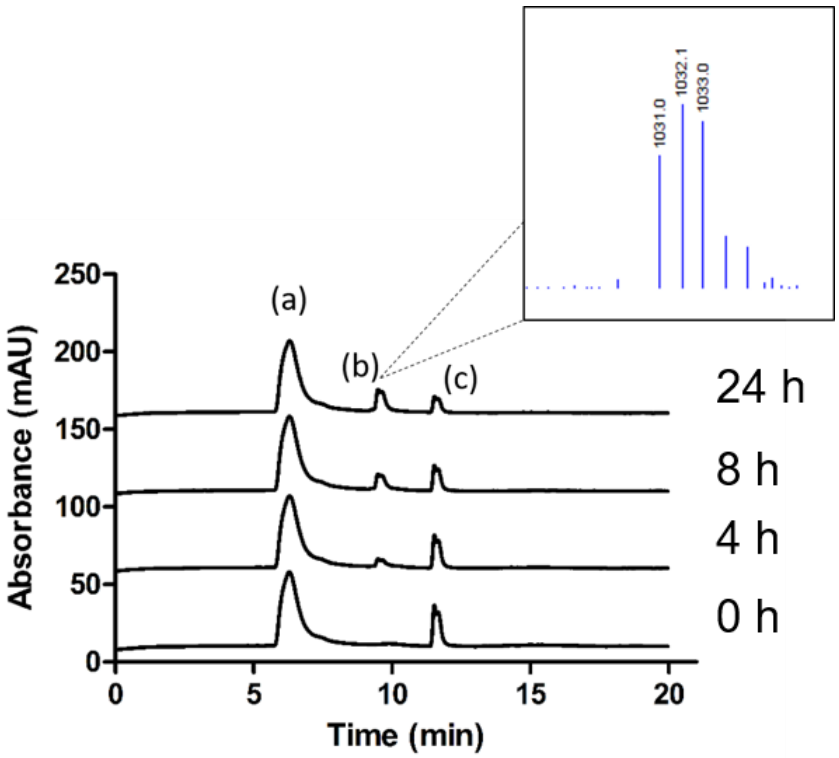

Figure 3.26. HPLC analysis with detection at 254 nm showing the decrease in Pt(IV) prodrug **6** over time**,** peak (c). (a) = excess GMP (b) = OxPt-guanosine monophosphate adduct (c) = **6**. Inset shows LC-MS analysis of peak (b) confirming it to be the bis-adduct guanosine monophosphate of oxaliplatin.

Since a sufficient method of analysis had been developed for Pt(II) species, quantification was carried out for electro-activation with the modified electrode, with a non-modified electrode and with no potential applied (Figure 3.27). It can be seen that, despite the non-modified electrode having a conversion of Pt(IV) around 20% less than that of the MED, there was a significantly lower yield of the GMP-reactive Pt(II) species following electro-activation compared to the MED.

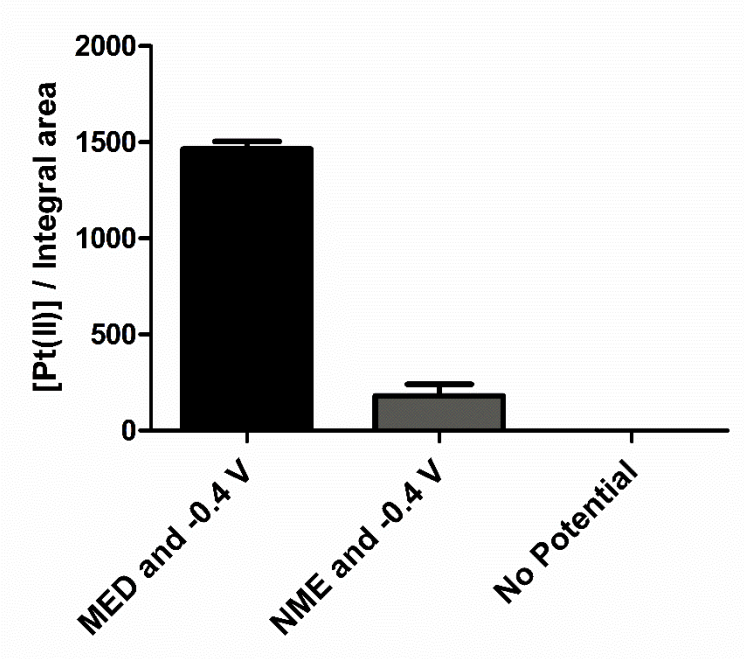

Figure 3.27. Quantification of Pt(II) species formed by electro-activation with modified electrodes (MED), compared to that with a non-modified electrode (NME) and where no potential was applied. After 24 h, the solutions for each condition were incubated with excess GMP (final concentration of 1000 μM) at 37 °C for 2 h and subjected to HPLC analysis.

This can be explained by the redox mediator facilitating "cleaner" Pt(IV)-Pt(II) conversion to the desired products whereas with the bare electrode surface unselective reactions were occurring. The absence of the Nafion exclusion layer would allow the approach of many electro-active species that could lead to decreased generation of the desired Pt(II) species (Scheme 3.7).

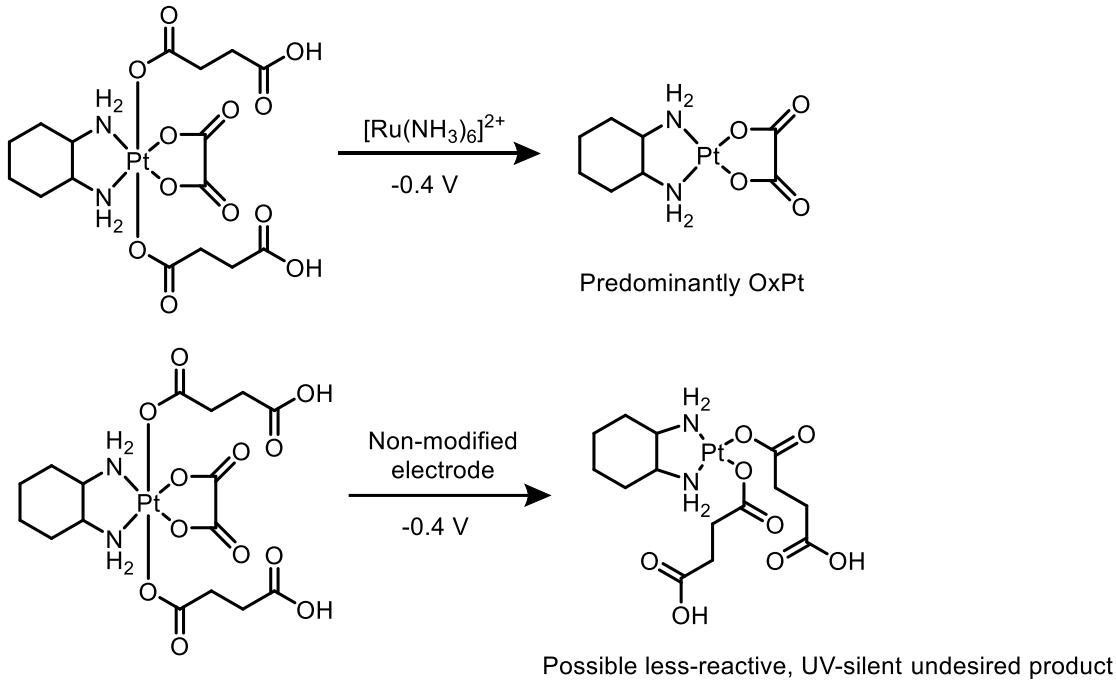

Scheme 3.7. Reaction scheme showing the major reaction of **6** occurring upon application of -0.4 V with modified electrodes (top) and one possible side-reaction occurring on the non-modified electrodes (bottom).

The effect of pH on the redox-mediated electrochemical reduction of Pt(IV) prodrugs was explored in order to confirm that a mediated mechanism was occurring, and not direct reduction at the electrode surface. The redox processes of the redox mediator are pH-independent, however the reduction process of **6** are pH-dependent (Figure 3.28). Therefore, it was postulated that, sufficient pH deviation from pH 7 by the electrochemical processes, direct reduction would occur at the electrode surface.

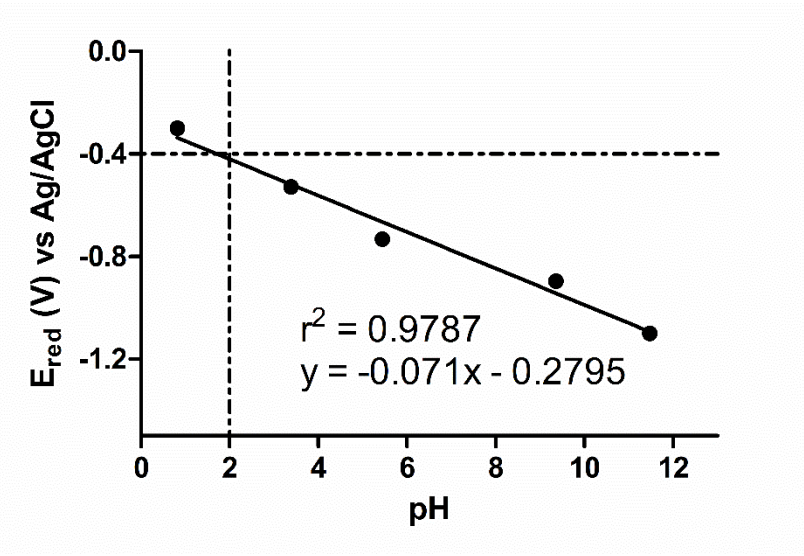

Figure 3.28. The pH-dependency of the reduction potential of **6**. The reduction potential of **6** (2 mM) was measured by cyclic voltammetry in solutions of varying pH. The dashed lines extrapolates the pH required for direct reduction to occur at -0.4 V (the potential applied with the modified electrodes). Therefore, for direct reduction to occur at -0.4 V, a pH of 2 is required.

It can be seen that at pH values ≤ 2, it may be possible for direct reduction of **6** to occur. The pH of the reaction solution was measured following 24 h of applied potential (Table 3.1) and showed that there was a slight decrease in the pH, presumably from the acidic axial ligands, but after 24 h the pH increased from 6.91 to 7.41, with the corresponding reduction potential of **6** altering from -0.79 to -0.81 V. This provides good evidence that the electrochemical Pt(IV) prodrug activation is a mediated reduction process, as opposed to direct reduction.

Table 3.1. The pH of the reaction solution held at -0.4 V with **6** (50 μM) in PBS over time.

Time	pH
Before addition of **6**	6.99 ± 0.01
After addition of **6**	6.91 ± 0.04
After 2 h conversion	6.93 ± 0.05
After 4 h conversion	6.99 ± 0.02
After 8 h conversion	7.14 ± 0.06
After 24 h conversion	7.41 ± 0.06

The small observed increase in pH over time may be explained by reactions occurring at the electrode surface unrelated to the Pt(IV) reduction, namely the reduction of oxygen (Equation 3.1), a process which consumes protons and therefore affects pH.

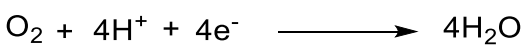

Equation 3.1. Electrochemical reduction of oxygen to form water.

3.8 *In vitro* validation of the Pt(IV) prodrug activation systems

The capability of the electrochemical Pt(IV) prodrug activation system to translate to biological applications was examined. HCT 116 cells, a human colon carcinoma cell line, were used for these experiments, as oxaliplatin is an FDA-approved treatment for colon cancer. It can be seen from Figure 3.20 that the largest difference between the cytotoxicity of the active Pt(II) species, OxPt and the prodrug **6** occurs at a concentration of 50 μM, therefore this concentration was selected for cell experiments. Experiments were designed with three controls: untreated cells where no Pt species or electrode was introduced; "-0.4 V" where only a potential was applied with a modified electrode; "**6**" where only the Pt(IV) prodrug **6** was incubated with cells. The experiments combined the use of a MED, with application of potential at -0.4 V and incubation of **6** (50 μM).

The electro-activation of Pt(IV) prodrugs must occur at the electrode surface and cannot be done inside cells. As postulated above, the disuccinato Pt(IV) prodrug **6** is negatively charged, so should not be taken up into cells which is of benefit to the electro-activation process. Prodrug **6** was dissolved in cell media and was added to HCT 116 cells grown in a 24-well plate. The modified electrode was then suspended above the cells, with the electrodes submerged in the Pt(IV)-containing cell media, and a potential applied for 1 h at 37 °C and 5% CO_2 atmosphere (see Figure 3.29).

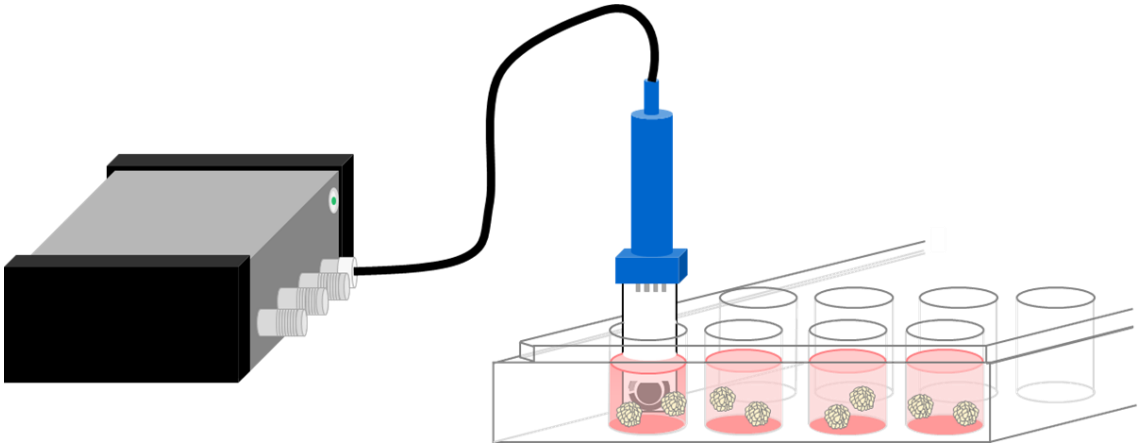

Figure 3.29. Set-up of the equipment for electrochemical Pt(IV) prodrug activation in cell culture. Modified electrodes were connected to a portable potentiostat, with the electrodes' surfaces submerged in cell media and positioned above a monolayer of cells.

Cell viability was analysed by an MTT assay. It can be seen from Figure 3.30, that each component of the system (potential and prodrug **6**) alone had negligible cytotoxicity, whereas a stark reduction in cell viability is observed when all components of the system were combined (72% total cell death). This trend is corroborated by an increase in the intracellular Pt content in cells where **6** was activated electrochemically (Figure 3.30, right axis).

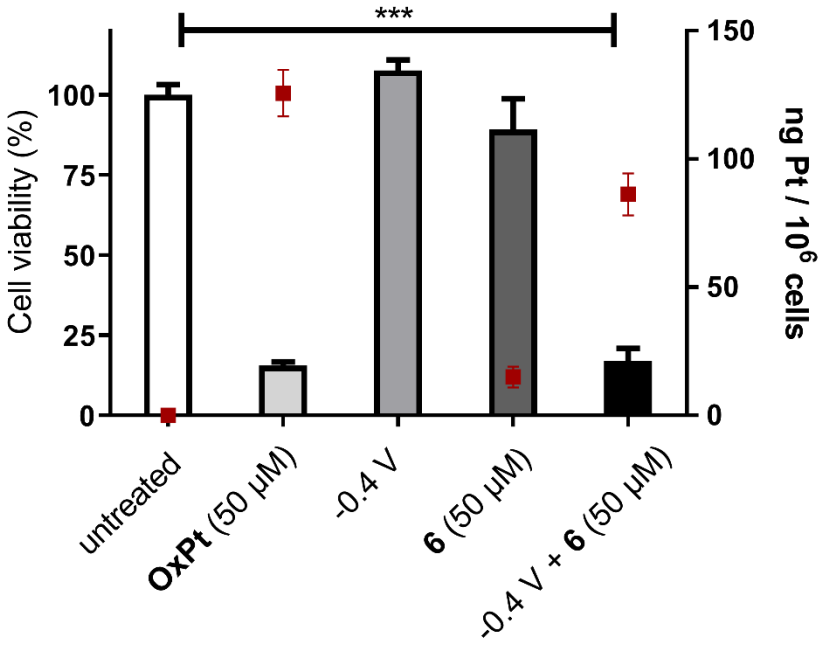

Figure 3.30. Cell viability, as measured by an MTT assay (n = 3), showing the increased cytotoxic effect caused by the electro-activation of **6**, compared to controls. Potential was applied for 1 h and cells were incubated for 72 h. The data represent the mean ± S.D. *** $P<0.001$ by one-way ANOVA with Dunnett post-test, compared to the untreated control group. Red squares ( ) indicate the intracellular Pt content per million cells for each reaction condition, as analysed by ICP-MS (n = 3).

To further probe the effects of the electrochemical prodrug activation, apoptosis onset was quantified by an Annexin-V-FITC conjugate labelling. Upon initiation of apoptosis, cells translocate phostidylserine protrusions from the inner face of the cell membrane to the outer face. Annexin-V is a protein with high affinity for phosphatidylserine, such that fluorescent conjugates allow simple monitoring of phosphatidylserine levels and thus quantification of cellular apoptosis. Figure 3.31 shows HCT 116 cells treated with either the reductive potential or **6** alone

and in conjunction and analysed with Annexin-V-FITC, 24 h post-activation. It can be seen there are more apoptotic cells where **6** has been activated electrochemically.

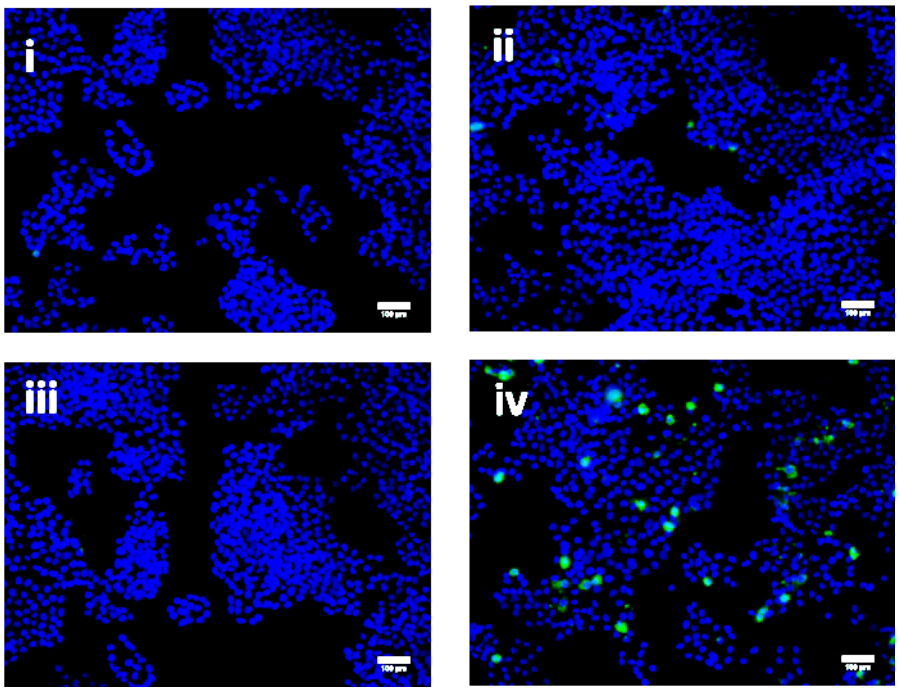

Figure 3.31. Fluorescent microscopy showing HCT 116 cells with nuclei stained (blue) and Annexin-V-FITC (green) showing the presentation of phosphatidylserine residues indicating apoptotic onset. (i) untreated, (ii) -0.4 V only, (iii) **6** (50 μM) only, (iv) **6** (50 μM) and -0.4 V. Contract and brightness have been increased by 40% for all figures from raw data. †

The fluorescence related to apoptotic onset was quantified by flow cytometry (see Figure 3.32).

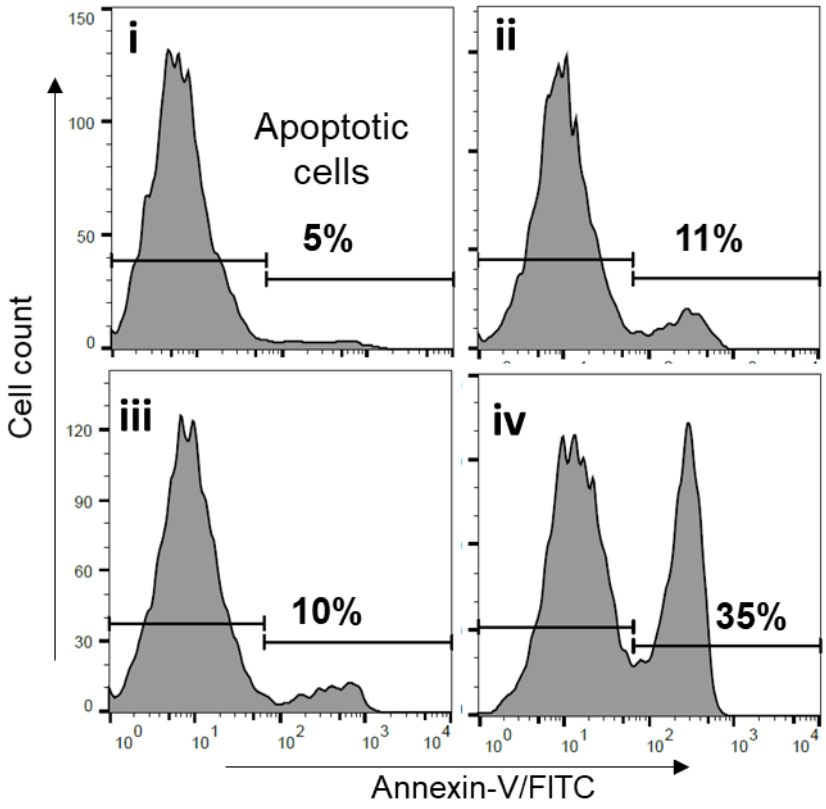

Figure 3.32. Quantification of apoptotic onset with an Annexin-V-FITC assay, as measured by flow cytometry. (i) untreated, (ii) -0.4 V, (iii) **6** (50 μM), (iv) **6** (50 μM) and -0.4 V. †

As alluded to above in regards to platinum binding to GMP and other nucleobases, the primary mechanism of action of Pt-based anticancer therapies is through DNA alkylation/chelation. There are differences between the mechanisms of cisplatin and oxaliplatin, which may account for the discrepancy in the type of cancers the two drugs are indicated for and their respective side-effect profile (see Chapter 1). Carboplatin is believed to exhibit similar mechanistic characteristics to cisplatin (and is cross-resistant to cisplatin), albeit with a slower dissociation rate

of the leaving ligands (Cl in cisplatin, and cyclobutyldicarboxylic acid bidentate ligand in carboplatin). The difference in rates of ligand-dissociation or complex-aquation in cisplatin and carboplatin is believed to account for the limited off-target toxicities of carboplatin, whereas cisplatin exhibits a harsh toxicity profile, due to its highly reactive and labile chloro leaving ligands. These properties may be a double-edged sword with respect to treatment however; despite the reduced toxicity of carboplatin in general it is less effective and requires a multiple-fold increase in dose given to achieve the same effect as cisplatin. There is evidence for different mechanisms of cytotoxicity ascribed to oxaliplatin, other than DNA inter- and intra-strand crosslinking. These include immunological stimulation by oxaliplatin, by translocation of immunogenic signals on the cell surface[79]; and prompting ribosomal biogenesis stress[81]. Regardless of the convolution and ambiguity pertaining to the mechanism of action of oxaliplatin, quantification of Pt-DNA adducts is still used as a measure of efficacy.

This was done by extracting the whole-cell DNA content and the Pt content determined by ICP-MS. Incubation of **6** alone (without activation) displayed much less DNA platination (around 5.5-fold) compared to that of **6** with activation at -0.4 V, further showing that electrochemical activation was effective in a “turn-on” manner (Figure 3.33).

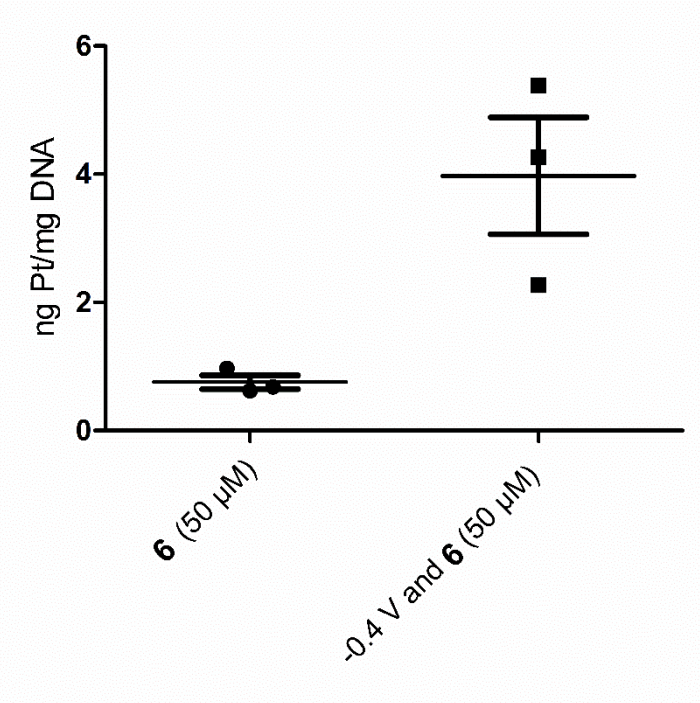

Figure 3.33. Quantification of DNA-platination in HCT 116 cells with either incubation of **6** alone or in combination with potential and modified electrode, as measured by ICP-MS.

After 24 h of incubation post-activation, cells were lysed and analysed for Pt content by ICP-MS (Figure 3.34). There was observed a higher Pt content when the prodrug **6** had undergone electrochemical activation; indeed some 9.5-fold higher than in cells without electrochemical activation.

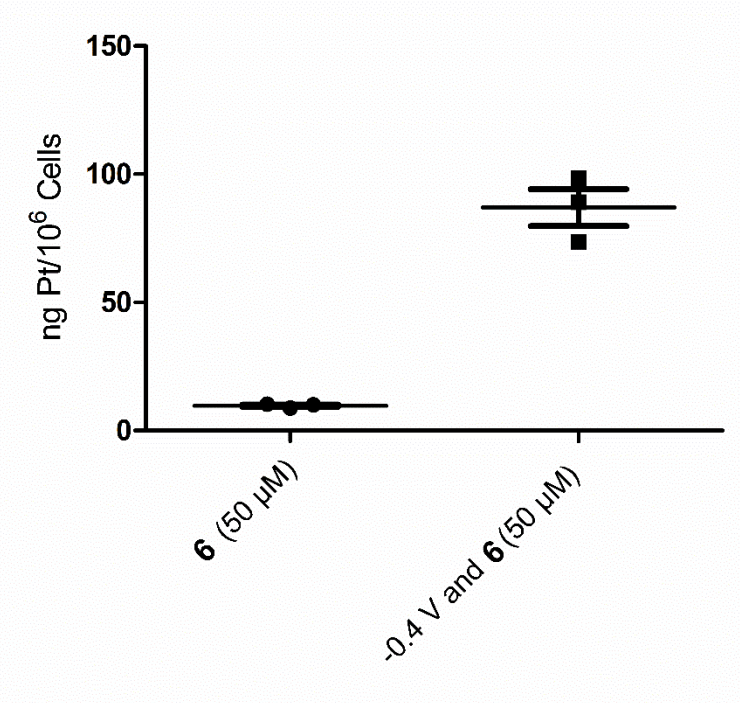

Figure 3.34. Quantification of whole-cell platinum content in HCT 116 cells with either incubation with **6** alone or in combination with potential and a modified electrode, as measured by ICP-MS.

In an effort to validate the safety of the modified electrode, the ruthenium content of cells was quantified, to show the proportion of redox mediator that may have leached out of the Nafion layer during Pt(IV) prodrug activation. Cells were again lysed, pelleted and analysed by ICP-MS (Ru content was 0.20 ± 0.05 ng per 10^6 cells which equates to around 0.02% of the total Ru content found in the modified electrode). This exemplifies the remarkable stability of the electrostatically-bound redox mediator.

While 2D monolayer cell culture is used ubiquitously in cancer research, primarily due to its low cost, high reproducibility and high-throughput, it does

have caveats that must be addressed. Cells are grown on the flat surface of tissue culture plastic. This does not translate to how cells are organised in live organisms and does not consider complexities associated with ECM production and mechanical stimuli (e.g. stiffness/softness of environment). Cells grown in a 2D monolayer can present with contrasting characteristics to their counterparts *in vivo*: levels of gene expression can be different[203, 204], there are minimal nutrient and oxygen gradients[205] and there may be less barriers toward drug resistance and penetration (as a result of the lack of ECM production and altered morphology)[204, 206]. The tumour microenvironment plays a critical role in drug resistance and penetration and so a lack of tumour microenvironment (as in 2D cell culture) may be related to "false efficacy". The flattened morphology of cells grown in 2D may also contribute to this. There are multiple ways to mimic a neoplastic environment in 3D cell culture. Scaffolds can be used that hold and allow cell-binding in attempts to mimic ECM or stimulate ECM production[207]. A range of hydrogels and moulds/inserts for cell culture are now commercially available, however these are often expensive and require highly optimised conditions to facilitate reproducibility. Non-scaffold-based methods are generally low-cost and more easily reproducible. Generation of cellular aggregates, termed cell spheroids, can be accomplished by the hanging drop method, where cells are suspended in a drop of media, hanging from a well plate lid by surface tension[208]. The cells aggregate and ultimately form a multi-cellular tumour spheroids which display characteristics comparable to *in vivo* tumours. They have similar ECM-cell and cell-cell interactions, ECM production, drug resistance profiles and can exhibit hypoxia and necrosis[209-211]. To further validate the

redox-mediated Pt(IV) prodrug activation, tumour spheroids were grown and subjected to the Pt(IV) prodrug electro-activation process.

Spheroids were generated from HCT 116 cells by the hanging drop method[212, 213]. On day 5 of culture, spheroids were transferred from the hanging drop to an agarose-coated 24-well plate and treated with **6** followed by electro-activation at -0.4 V for 1 h. Cell viability was measured (CellTiter Glo 3D Cell Viability kit) after 3 days incubation which showed no decrease in cell viability in spheroids treated only with **6** (Figure 3.35). A 50% decrease in spheroid-cell viability was observed when **6** was activated electrochemically.

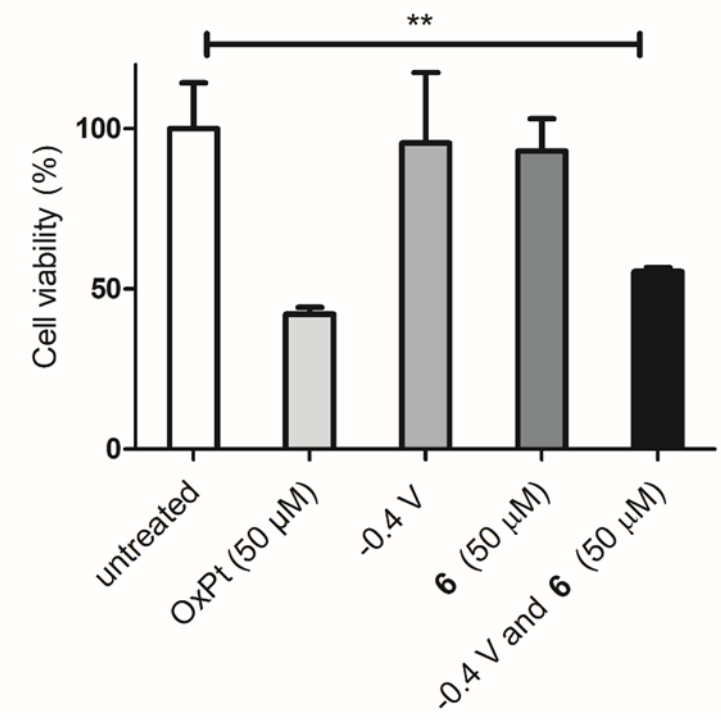

Figure 3.35. Cell viability of HCT 116 MCTS treated with **6** (50 μM) and -0.4 V applied for 1 h, and incubated for 72 h (CellTiter Glo 3D assay, n = 3). The data represent the mean

± S.D. *** P<0.001 by one-way ANOVA with Dunnett post-test, compared to the untreated control group. †

The live and dead cells were also identified visually with a live/dead assay and imaged by fluorescent microscopy. This assay uses a green-fluorescent calcein-AM to indicate intracellular esterase activity and a red-fluorescent ethidium homodimer-1 to indicate loss of plasma membrane integrity. Figure 3.36 shows there was an increased number of dead cells (those without an intact plasma membrane) where all of the components of the electrochemical prodrug activation system are combined, compared to controls. The size of the spheroids is also an indicator of their health. It can be seen that the largest diameter of the untreated spheroid is 947 μm which decreases to 604 μm upon electro-activation of **6**.

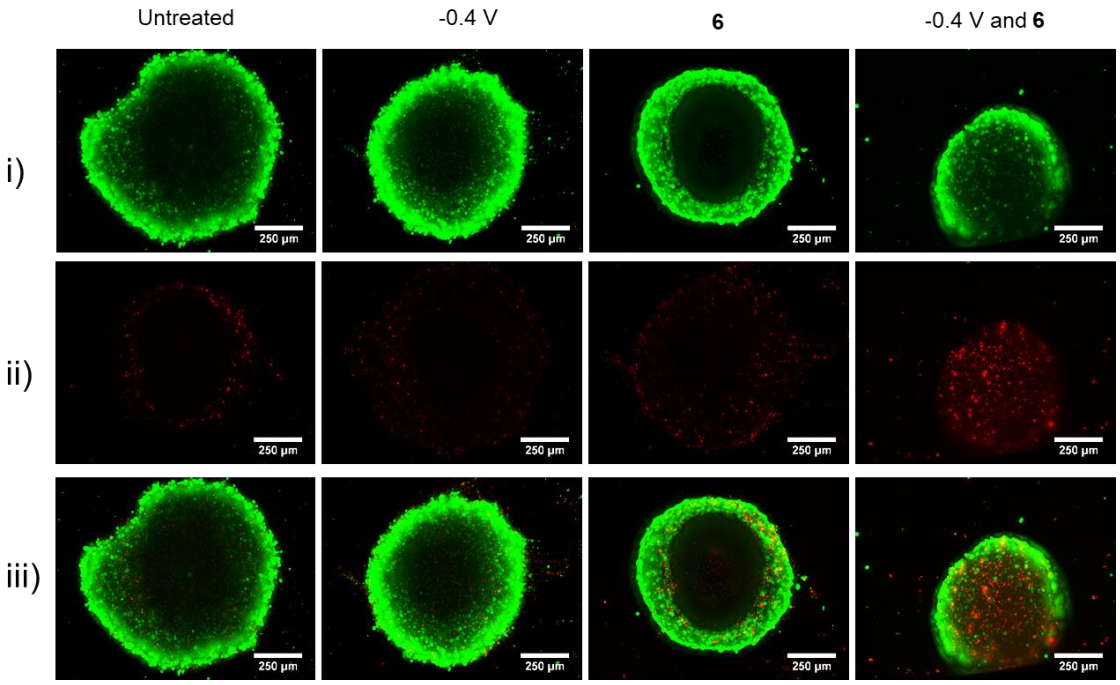

Figure 3.36. Live (i, green) and dead (ii, red) staining of HCT 116 spheroids and merged images (iii). The electro-activation of **6** was carried out for 1 h and spheroids were incubated at 37 °C for 72 h before staining and imaging. †

The apoptotic onset caused by electro-activation of **6** in HCT 116 spheroids was explored by an Annexin-V luciferase fusion proteins assay. This assay contains two different Annexin-V fusion proteins: each with a truncated non-functional luciferase attached. Upon translocation of phosphatidylserine to the outer leaflet of cell membranes, the Annexin-V units bind and, in close proximity, afford a functional luciferase. This allows real-time monitoring of the onset of apoptosis by measurement of luminescence. As can be seen in Figure 3.37, the apoptotic onset only occurs at its highest level where all components of the electrochemical prodrug activation system are utilised. Collectively, these data demonstrate the applicability for electrochemical mediation to switch-on cancer prodrugs, with validation in both 2D and 3D cell culture models.

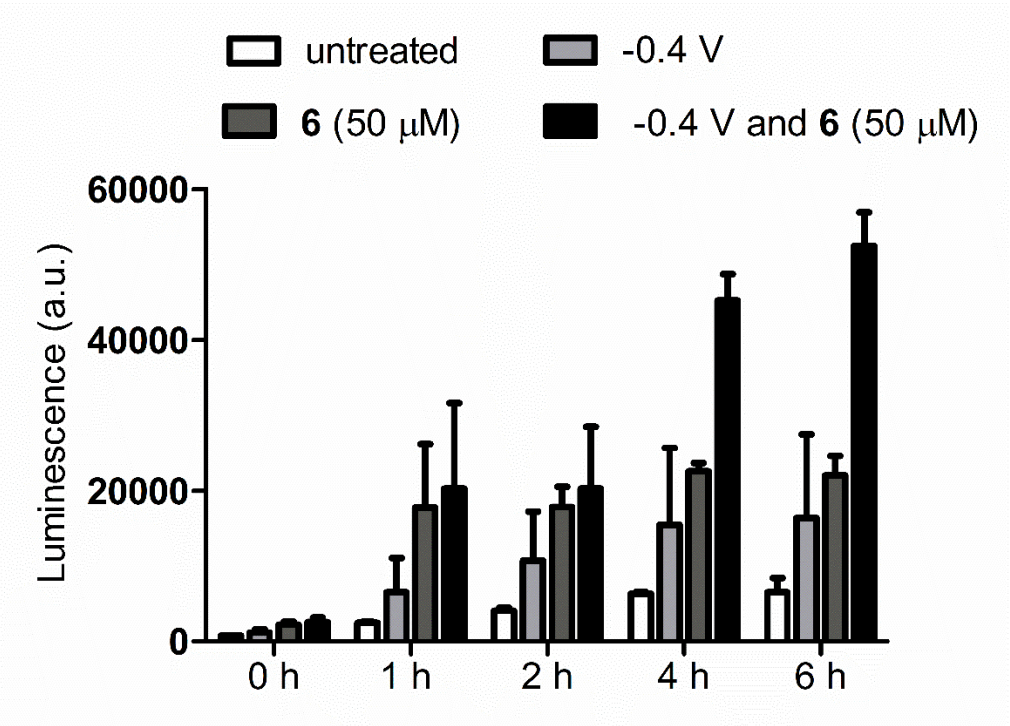

Figure 3.37. Real-time monitoring of the onset of apoptosis in HCT 116 cells caused by the electro-activation of **6** for 1 h. Cells were incubated with a RealTime-Glo™ Annexin V Apoptosis assay with luminescence increase monitored at different time points. The data represents the mean ± S.D, n = 3.

Conclusions and Outlook

An electrochemical Pt(IV) prodrug activation system has been developed and its functionality validated in biological settings. The activation was done *via* a mediated approach so as to utilise a relatively low potential, thereby reducing biological interferences. To our knowledge, this is the first prodrug activation

system that uses electrical signals as an actuator for prodrug activation, instead of enzymatic or other biological processes or other physical stimuli, such as light.

This system was developed with an implantable sensor/activator in mind, which could be placed at the site of the tumour. *In vitro* assessment of the redox-mediated Pt(IV) prodrug activation system demonstrated the capability of the system to use electrons delivered by an applied potential as a prodrug activation strategy. Translation towards *in vivo* applications will require further miniaturisation of the modified electrodes to facilitate implantation. Different approaches to implantation will also need to be explored, as the location and the number of implanted electrodes will be critical to the efficacy of the prodrug activation system. Devices should be implanted adjacent to a blood supply to maximise exposure to the incoming Pt(IV) prodrug. The device in its current state may need "re-engineering" in order to be effective *in vivo* i.e. a flat-surfaced electrode may not be the ideal format for this application. An electrode that could be implanted in a similar way to a stent, a tube inserted into vasculature to hold the vessel open, may be of great benefit as it would facilitate contact with the prodrug and would maximise the surface area of the electrode. Such electrode-stents are currently under development for chronic recording of neural activity[214] and have potential for overlap in applications.

The immobilisation of the redox mediator should also be further explored. While the electrostatic encapsulation of the mediator in Nafion showed good stability and retention. Modification of the ligands of hexaammineruthenium could afford

a handle for covalent attachment of the mediator to the electrode surface to prevent leaching of the mediator *in vivo*.

In order to effectively use this prodrug activation system to deliver chemotherapeutics, the effect of the route of administration of the Pt(IV) prodrug will also need to be investigated. Oral administration may lead to variable uptake and affect the quantity of Pt(II) generated by the device. However, it is theoretically possible that the Pt(IV)-Pt(II) conversion can be monitored and quantified in real-time by measuring the charge generated. Immediate i*n situ* information regarding the doses of Pt(II) being formed could be a step towards personalised anti-cancer treatment. In addition, the spatial selectivity achieved by stereotactic implantation of the device could greatly benefit patients' quality of life by reducing the side effects of chemotherapy.

Chapter 4

Photo-activation of Pt(IV) prodrugs with simultaneous generation of singlet oxygen

4.1 Introduction

Light has proven to be a useful tool in photodynamic therapy (PDT) affording spatial control of therapy either alone or in combination with photosensitisers — molecules that absorb light in order to reach excited states that can facilitate energy transfer. PDT was used by the ancient Chinese, Indian and Egyptian civilisations to treat diseases[215, 216] but the first modern light therapies, developed by Finsen, drove PDT into popularity in medicine and as an active area of research. Finsen used red light as a treatment for smallpox, spurred by the observation that a Middle Ages treatment involved surrounding patients suffering from smallpox with red-coloured objects, the so-called "Red Treatment"[217]. Through fusion of anecdote and science, Finsen demonstrated that red light can speed up healing of smallpox-related scarring[218], and in addition, he found that UV light was cytotoxic to *Lupus vulgaris* infections of the skin, a bacterium associated with tuberculosis[219].

Light therapy is now commonplace for a variety of diseases, particularly those that are readily optically accessible, such as acne and psoriasis[220-223]. Hyperbilirubinemia, a disorder commonly seen in new-borns manifesting as elevated levels of bilirubin that can deposit in the brain causing neurological disorders, can be treated with blue light[224, 225]. Since bilirubin absorbs across

the blue region of the electromagnetic spectrum and light therapy causes the photo-decomposition to products that are more easily metabolised and excreted, blue light therapy normalises bilirubin levels and alleviates symptoms (Scheme 4.1).

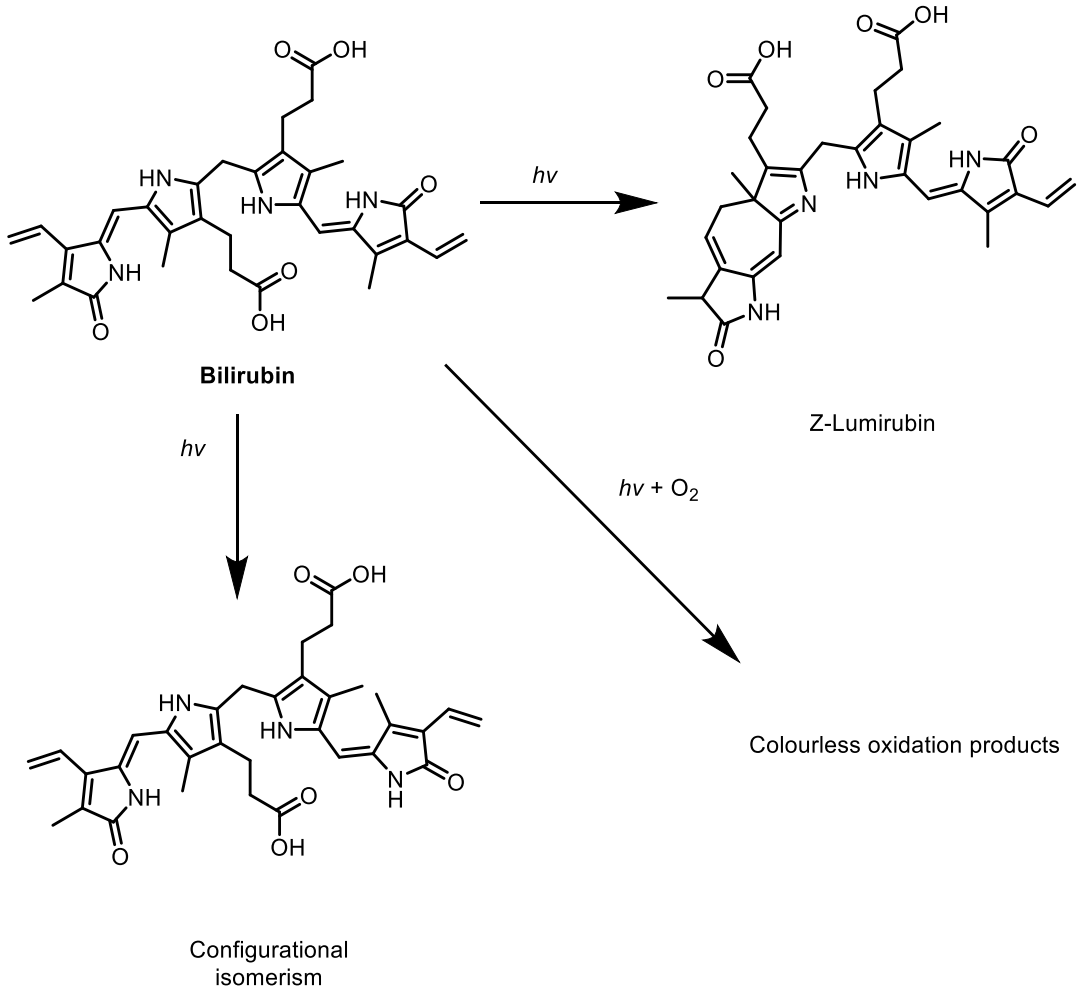

Scheme 4.1. Blue-light therapy leading to photo-degradation of bilirubin through photo-induced isomerism, oxidation and cycloaddition to Z-lumirubin.

PDT for cancer and tumour ablation has become an actively researched area, used primarily for skin melanomas and other optically accessible cancers[226, 227].

Here, a general mechanism of treatment is used: administration of a photosensitiser (PS) followed by irradiation of light of appropriate wavelength at the site of the tumour or cancer-affected area.

The PS exists in its ground singlet state with two electrons of opposing spin and upon absorption of a photon of appropriate quantum energy, one electron is elevated to an excited state (see Figure 4.1). The decay of this excited electron back to the ground state can occur, in the process releasing the excess energy as either heat or fluorescence. Alternatively, inter-system crossing can occur: the excited electron undergoes a change of spin and a triplet excited state is formed with two electrons of parallel spin. The triplet excited state has a long enough lifetime that it can react with other triplet state species, such as ground-state oxygen in a triplet-triplet annihilation process to give singlet oxygen (named Type II reactions) or can participate in single-electron transfer reactions that generate reactive oxygen species, such as superoxide and hydroxyl radicals (Type I reactions). The reactive oxygen species formed are highly reactive and elicit cytotoxic effects through reaction with biomolecules.

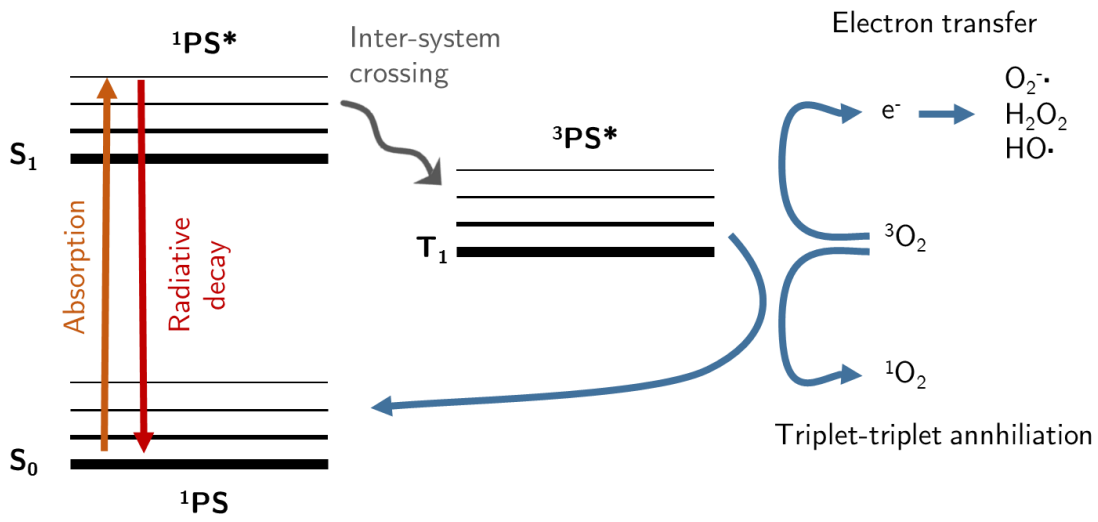

Figure 4.1. Jablonski diagram of the processes involved in photodynamic therapy. Absorption of a photon by the ground singlet state (S_0) of the photosensitiser allows an excited singlet state (S_1) to be reached. The energy of the excited electron can be emitted *via* radiative decay (i.e. heat or fluorescence) or inter-system crossing can occur to reach a triplet excited state (T_1). Triplet-triplet annihilation is an energy transfer process and forms singlet oxygen. Electron transfer reactions produce radicals such as superoxide (O_2^{-}·), hydrogen peroxide and hydroxyl radicals (HO·). Both processes regenerate the ground singlet state of the photosensitiser.

Development of novel photosensitisers can facilitate increased cancer selectivity, limitation of side effects, increased yield of singlet oxygen generation and extension of the wavelength of light required, enabling deeper tissue penetration[228]. Limitations arise for PDT in that light is highly scattered by skin and deeper tissues[229]. The 'therapeutic window' lies within the wavelengths of 650 to 1200 nm, where tissue penetration is at its highest,

however, the higher the wavelength of light, the less energy it has to initiate photochemical reactions.

The photodynamic reactions discussed within this chapter were designed in view of an implantable device with mounted LEDs for illumination with placement of a light source directly at the site of the tumour potentially enabling the benefit of lower (and thus higher energy) wavelengths of light to be used more effectively. A related concept to this has been demonstrated by the use of a fibre optic to deliver light internally through a 22 gauge needle, allowing light of 365 nm to be utilised in the activation of a photo-caged doxorubicin prodrug at the site of a tumour[230].

Tris(2,2'-bipyridyl)ruthenium(II) ($[Ru(bpy)_3]^{2+}$) and its derivatives have been utilised for a wide range of applications in medicine, as photosensitisers or DNA-intercalators for cancer and bacterial infection treatment, and in diagnostic sensors; as well as in energy production and storage as an electron transfer agent, and in organic synthesis as a photocatalyst. The excited state species of $[Ru(bpy)_3]^{2+}$-based photocatalysts can form either highly oxidative ($[Ru(bpy)_3]^{3+}$) or reductive ($[Ru(bpy)_3]^{+}$) intermediates through the use of sacrificial electron acceptors or donors (see Figure 4.2).

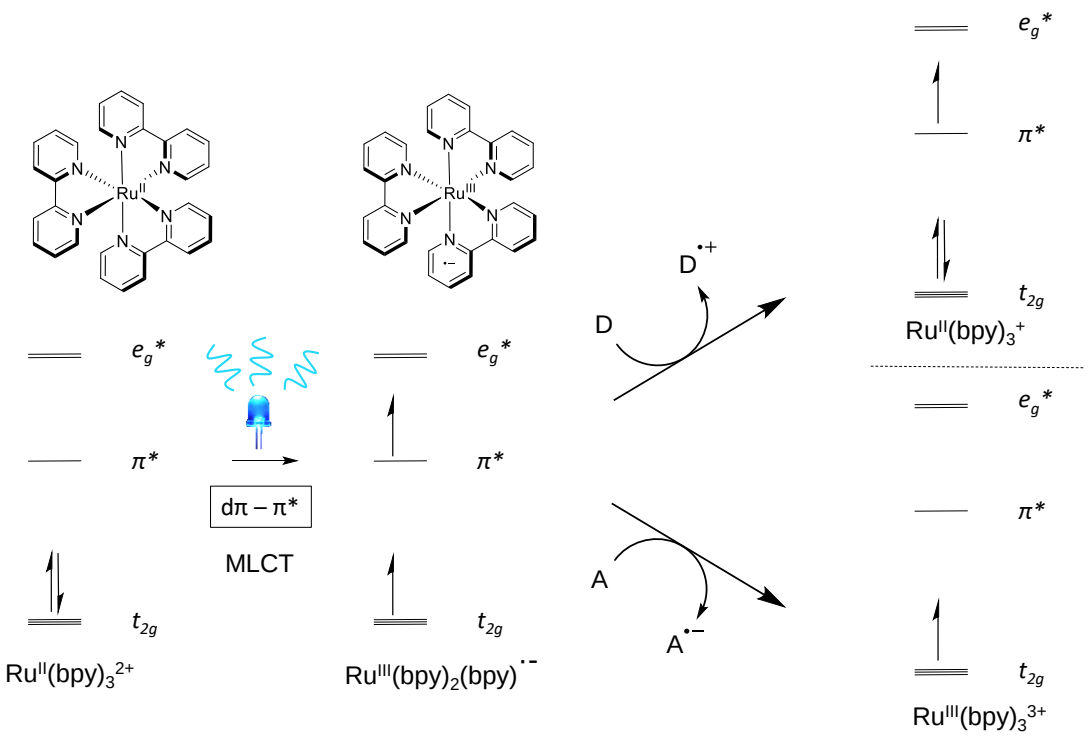

Figure 4.2. Energy level diagram of $[Ru(bpy)_3]^{2+}$ absorbing blue light to excite an electron from ground state (t_{2g}) to an elevated energy level (π*) in a metal-ligand charge transfer (MLCT). The excited-state photosensitiser can then undergo reactions with electron acceptors (A) or with electron donors (D). Electrons acceptors include nitroaromatics, viologens and persulfate ions whereas electrons donors typically used are triaklylamines or ascorbic acid.

The dichotomous nature of $[Ru(bpy)_3]^{2+}$, allows highly reductive or highly oxidative species to be formed and has given rise to a large host of photo-synthetic reactions in which it has been utilised as a photocatalyst: reductive dehalogenations[231]; nitro- and azido-aromatic reduction to amines[232, 233]; oxidation of benzylic alcohols to aldehydes[234] and oxidative aromatic cyclisation of thiobenzanilides to benzothiazoles[235], among others.

Aside from its synthetic and energy applications, $[Ru(bpy)_3]^{2+}$ or related polypyridyl complexes have been utilised as photosensitisers for treating bacterial infections and cancer. To address the growing resistance of microbials to contemporary antibiotics, research has been focused on PDT to kill microbial infections, as it acts *via* mechanisms that are discrete from conventional antibiotic mechanisms of action and would be resilient towards resistance due to the nature of singlet oxygen generation i.e. there are few protein-ligand interactions that could be easily modified, as seen in most drug resistance emergences. Thus, ruthenium polypyridyl-based photosensitisers have shown promise as PDT agents for antibiotic-resistant strains of bacteria. Gu demonstrated the efficacy of a ruthenium polypyridyl photosensitiser in killing methicillin-resistant Staphylococcus aureus (MRSA) and showed 100% reduction in cell viability of planktonic and biofilm forms of MSRA[236]. In the same vein, Ligle demonstrated the efficacy of another Ru(II) photosensitiser (TLD1433), utilising a Type I (oxygen-independent) photo-process, allowing the efficient killing of MRSA cultures under normoxic and hypoxic conditions[237]. TLD1433 has also shown promise as an anti-cancer photosensitiser and is currently in Phase II clinical trials for bladder cancer[238].

In cancer, ruthenium has seen a huge surge in popularity, in the wake of the success of platinum-based cancer therapies and there are ruthenium-based anticancer agents currently in clinical trials. Of note are NAMI-A, KP-1019 and NKP-1339, all of which are in the Ru(III) oxidation state (Scheme 4.2). NAMI-A

was found to have low cytotoxicity in cancer cell lines (often 1000-fold less than cisplatin) but has the unusual ability to inhibit formation of metastases[239].

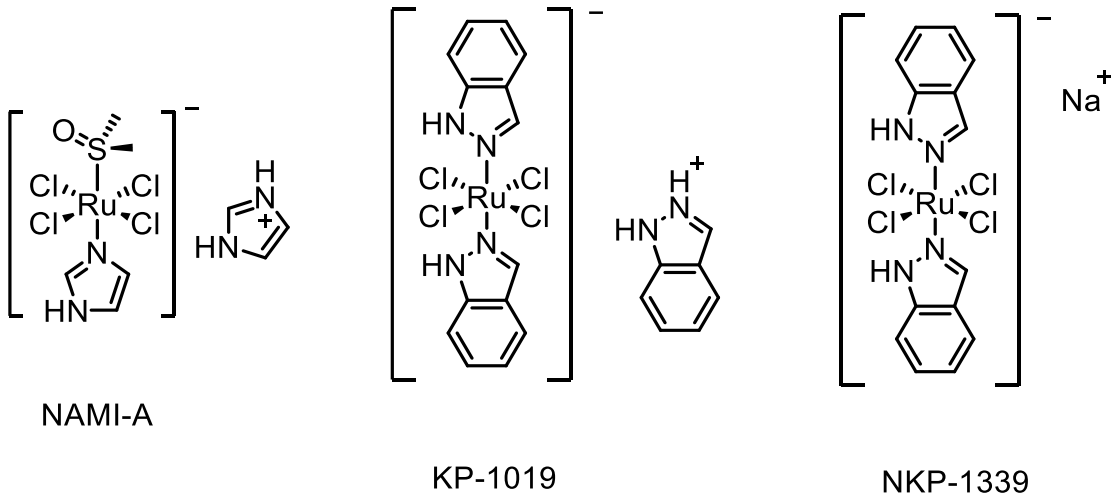

Scheme 4.2. Structures of ruthenium anti-cancer drugs in clinical trials: NAMI-A, KP-1019 and NKP-1339. NAMI-A is under investigation in non-small cell lung cancer in combination with gemcitabine. Clinical testing has recently focused attention more to NKP-1339 rather than KP-1019 due to its increased water solubility. NKP-1339 has successfully completed a phase I dose-escalation study in advanced solid tumours.

While the mechanism of this remains elusive, it has been postulated that NAMI-A binds to actin-type proteins on cell surfaces, reducing the mobility of cells undergoing endothelial-mesenchymal transitions, a hallmark of metastatic cancer cells[240, 241]. KP-1019, on the other hand, displays cytotoxic effects in a similar manner to cisplatin, with DNA-binding thought to be a main mechanism of action[242]. However, KP-1019 was active in murine cisplatin-resistant primary colorectal tumours[243] therefore either a different DNA-binding mode is responsible for overcoming Pt-resistance or there are other mechanisms of

action at work. KP-1019 was found to be well-tolerated by patients during clinical investigation. In phase I trials, the maximum tolerated dose could not be reached, however this is also a factor of the limited solubility resulting in high infusion volumes required[244]. Recently, clinical investigation has focused on the sodium salt analogue, NKP-1339, which has higher water solubility[245]. The theory that NAMI-A, KP-1019 and NKP-1339, similar to Pt(IV) prodrugs, require reduction from Ru^{3+} to Ru^{2+} intracellularly to elicit its effects has been proposed. However, this has been subject to controversy with reports both supporting and opposing this theory of activation[244, 246-248].

In this chapter, a Pt(IV) prodrug activation platform was designed and validated, in a similar manner to Chapter 3 but instead of electron delivery *via* an applied potential, the use of photochemical reactions to activate/reduce Pt(IV) prodrugs into their cytotoxic Pt(II) counterparts while simultaneously generating singlet oxygen were explored.

4.2 Aims of Chapter 4

Light has been widely used in prodrug activation, as it can deliver energy in a radiative manner through tissue with spatial control. This chapter details the design of a light-triggered photocatalytic Pt(IV) activation/reduction system whereby a ruthenium-based photosensitiser delivers electrons to a Pt(IV) prodrug upon becoming excited by light. The system was further developed in

terms of the photosensitiser: improving its absorption wavelength, cellular uptake and localisation; the Pt(IV) prodrug was improved with respect to intracellular stability to biological reductants and cellular uptake; and the light source with bespoke devices fabricated for rapid illumination of well plates with control over intensity and bandwidth. The use of a PS that also generates singlet oxygen by a discrete mechanism allowed a second route of cytotoxicity to be utilised simultaneously with Pt(IV) prodrug activation, with the ability of the system to overcome resistance in an ovarian cancer cell line, also explored.

4.3 Background

With the unique opportunity presented by an implantable microsystem (with a mounted LED), it was deemed desirable for selective prodrug activation to design a light-triggered system for the turn-on of drugs. There are prior examples of some Pt-based light-triggered systems.

Sadler has carried out a number of studies of a range of diazido-Pt(IV) compounds which undergoes ligand dissociation and reduction of the Pt centre to the II oxidation state, upon irradiation of the complex with light (Scheme 4.3)[249, 250]. This occurs with release of dinitrogen as a bio-inert by-product and affords remarkable light-dark toxicity ratios for a range of Pt(IV) complexes. There are disadvantages to this method, however, such as the low wavelength of light required may be damaging to surrounding tissues. The high light-sensitivity of the Pt(IV) complexes is advantageous for the rapid conversion but also may

result in the premature activation (from ambient light) of the complexes causing off-target side effects.

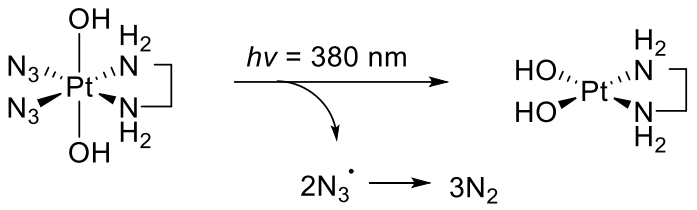

Scheme 4.3. Diazido-Pt(IV) complexes can undergo photo-induced reduction to their cytotoxic Pt(II) counterparts, with release of nitrogen following illumination at 380 nm.

Salassa demonstrated the capability of riboflavin to act as a photocatalyst for the conversion of disuccinato-Pt(IV) complexes to their Pt(II) counterparts upon irradiation with blue light (Scheme 4.4)[251]. Conversion was rapid: almost 100% reduction of the Pt(IV) species was observed after 5 min irradiation at 460 nm with a dose of 2.5 $mW.cm^{-1}$, with 10 mol% of photocatalyst. However, the mechanism of the catalytic cycle required a specialised buffer containing *N*-morpholinoethanesulfonic acid, as an electron donor, to re-generate the active form of the riboflavin catalyst (see Scheme 4.5). The buffer was required in all experiments at high concentrations (18 mM), thus hindering translation to *in vivo* systems.

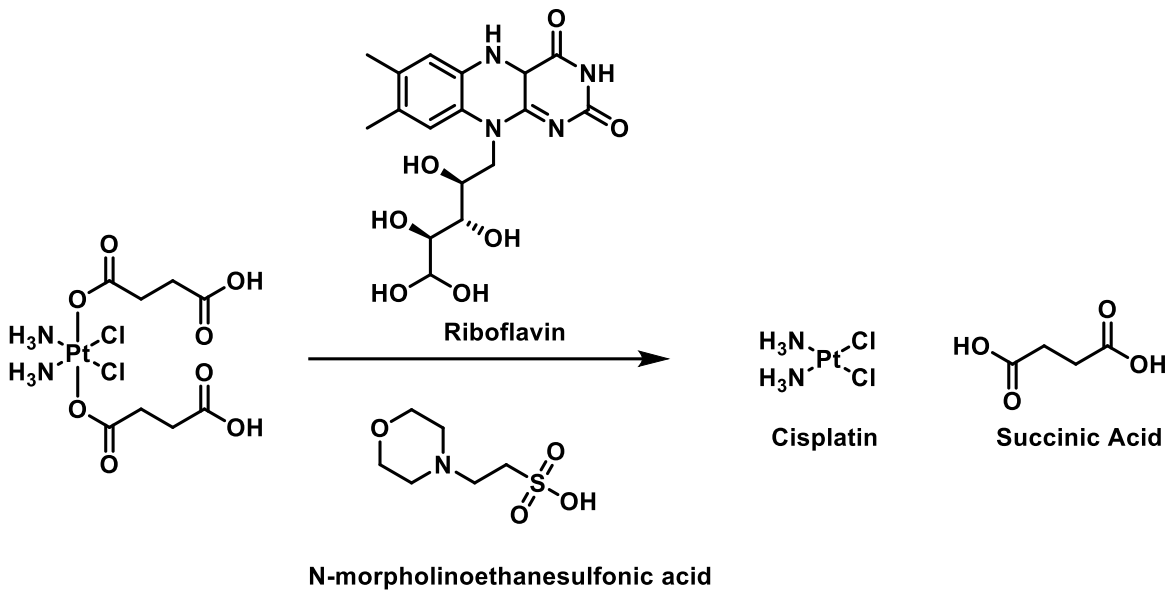

Scheme 4.4. Riboflavin as a photocatalyst for the reduction of disuccinato Pt(IV) derivative of cisplatin, in the presence of *N*-morpholinoethanesulfonic acid. Riboflavin is a biocompatible photocatalyst with an absorbance maxima at 460 nm.

It also shows limited scope of Pt(IV) substrates, requiring two succinate axial ligands to facilitate hydrogen bonding between substrate and catalyst. Riboflavin, also known as vitamin B2, as a photocatalyst offers a great advantage in that it is non-toxic and an enzyme co-factor.

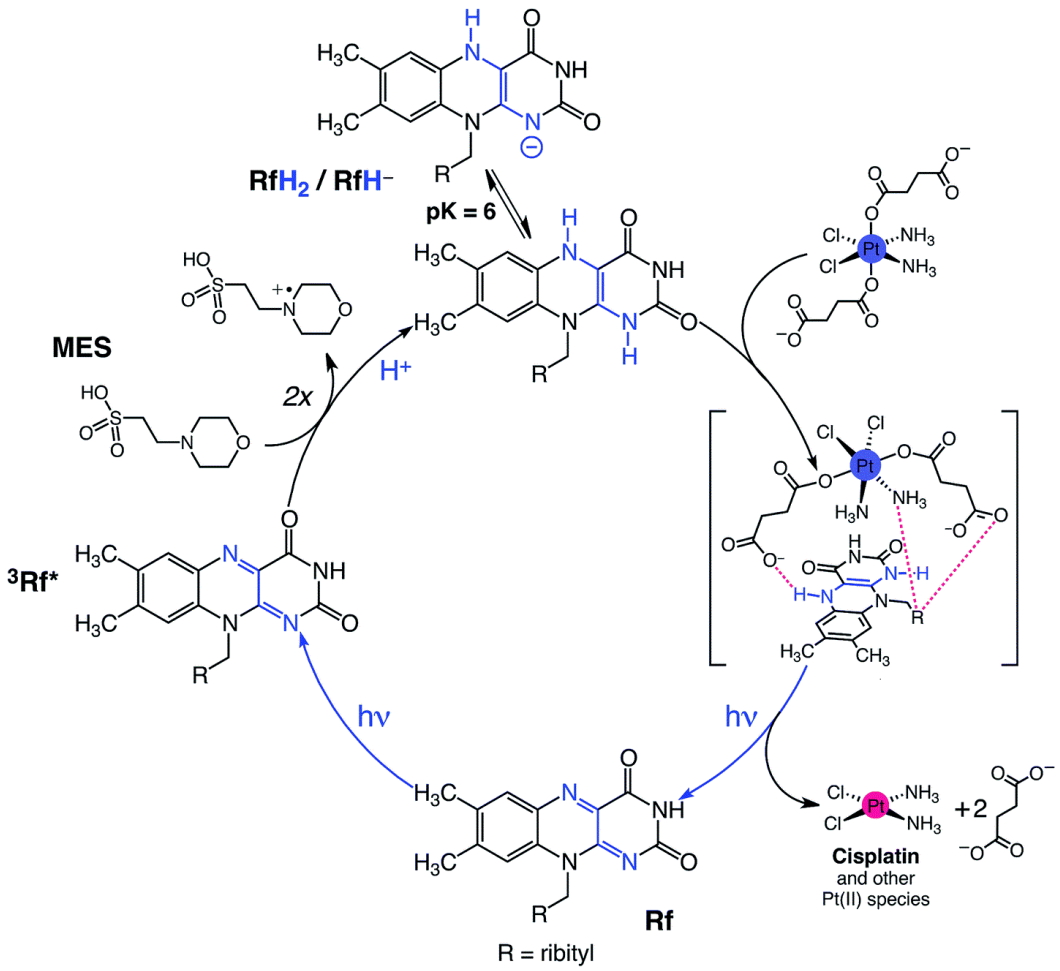

Scheme 4.5. The mechanism of the photo-induced Pt(IV) reduction with riboflavin as the electron donor. The disuccinato-cisplatin Pt(IV) derivative was shown to complex with riboflavin through hydrogen bonding and electrostatic interactions. Upon reduction of the Pt(IV) species, the excited triplet state of the oxidised riboflavin was then required to obtain electrons from two equivalents of the buffer component (MES) in order to re-generate the reduced riboflavin and complete the catalytic cycle. The figure is reproduced from reference [251] with permission granted from The Royal Society of Chemistry.

4.4 Discovery and design of a photocatalysed Pt(IV) prodrug activation system

From Chapter 3, it was found that a ruthenium redox mediator was optimal for Pt(IV) conversion. Therefore, it was a logical step that the highly reductive $[Ru(bpy)_3]^{2+}$ photocatalyst would be capable of reducing Pt(IV) substrates. This was verified with $[Ru(bpy)_3]Cl_2$ (0.5 μM) in PBS using the Pt(IV) complex **3** (250 μM), with blue light (470 nm) applied using a 20-LED array lamp at 40 $mW.cm^{-1}$ over 20 h. In the absence of either light or $[Ru(bpy)_3]^{2+}$, there was no conversion (Figure 4.3). However, a combination of light and $[Ru(bpy)_3]^{2+}$ were highly efficient at reducing the Pt(IV) substrate, with almost full reduction after 20 h.

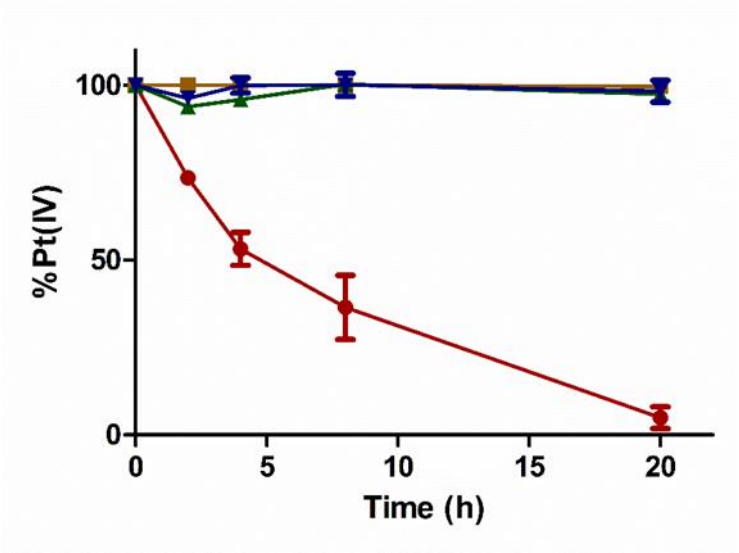

Figure 4.3. Initial conversion experiment of Pt(IV) complex **6** (250 μM) with photocatalyst $[Ru(bpy)_3]Cl_2$ (1 μM), irradiated at 470 nm with the LED-array lamp with the conversion analysed by HPLC over time. With light and photocatalyst (red line), without light and with photocatalyst (green line), with light and without photocatalyst (yellow line), without light and without photocatalyst (blue line).

Despite this promising result, there were several facets of optimisation that needed to be accomplished. The light intensity of the LED-array lamp was relatively high and cannot not be easily replicated in an implantable device. In addition, the disuccinato-oxaliplatin derivative, although optimal for electrochemical activation (as it remained outside the cell), there were no such requirements for photochemical activation. The scope of the Pt(IV) substrates needed to be explored, while the wavelength of light used would also, ideally, be extended to more therapeutically applicable lengths.

4.5 Identification of "bio-inert" Pt(IV) prodrugs

There are many biomolecules implicated in the endogenous activation/reduction of Pt(IV) prodrugs. Small-molecule biological reductants, such as ascorbic acid and glutathione, have been shown to reduce some Pt(IV) species, as can proteins, such as cytochrome c[252, 253]. The rates at which these biological reductants reduce Pt(IV) complexes is highly dependent on the nature of the axial ligands of the complex[190, 254]. To identify a Pt(IV) complex that was relatively inert towards reduction by biological reductants, an assay was designed whereby each Pt(IV) complex was incubated with 100× molar equivalents of sodium ascorbate and glutathione. A small library of Pt(IV) complexes (**7**-**13**) was synthesised (Scheme 4.6) and the ability of each Pt(IV) complex to withstand reduction was screened and assessed by HPLC (Figure 4.4).

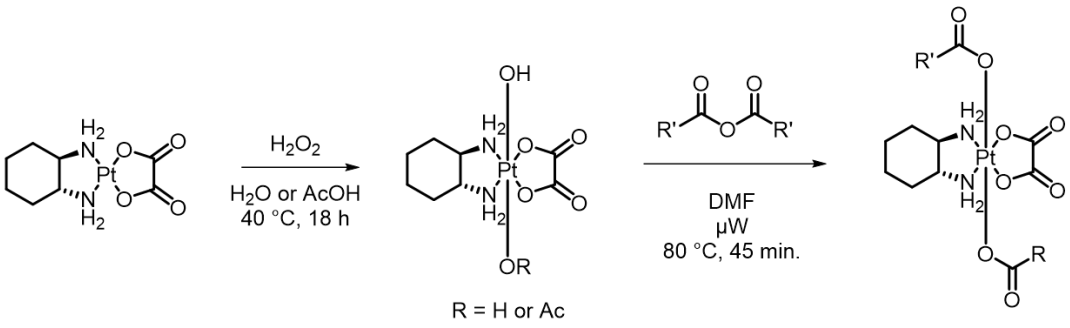

Complexes 7-13

#	R	R'
7	Ac	Ac
8	Ac	CF_3
9	Ac	t-Bu
10	Ac	Ph
11	CF_3	CF_3
12	t-Bu	t-Bu
13	Ph	Ph

Scheme 4.6. Synthesis of a Pt(IV) complex library. Oxidation of the Pt(II) complex by hydrogen peroxide in either water or acetic acid yielded the symmetric dihydroxy or asymmetric hydroxyl/acetyl complexes, respectively. This could then be reacted with the anhydride of choice under microwave irradiation for the rapid and facile access to a number of symmetric or asymmetric Pt(IV) complexes.

The library was designed with various axial ligands with asymmetric or symmetric complexes synthesised with varying steric bulks and electron-withdrawing characteristics. The asymmetrical Pt(IV) complexes carrying an axial acetate ligand and either tert-butanoate or benzoate axial ligands (**9** and **10**) were stable to reduction by glutathione or ascorbic acid. Symmetrical complexes with increased steric bulk, (**12** and **13**) were, surprisingly, ineffective at preventing reduction. The assumed benefit of increased steric hindrance

(preventing approach of the reductant) may be outweighed by the destabilising effect axial ligands can have on the Pt centre as steric bulk is increased. The symmetrical diacetate complex, **7**, was also easily reduced. Electron-withdrawing axial ligands, such as trifluoroacetate (**8** and **11**) were unstable towards biological reductants. This again may be a factor of the high electron-withdrawing nature of trifluoroacetate destabilising the Pt centre. Instability towards reductants and hydrolysis has been previously observed with related compounds bearing haloacetate axial ligands[255]. **10** was poorly soluble in aqueous solutions and was discontinued from further studies, with complex **9** was taken forward into further studies.

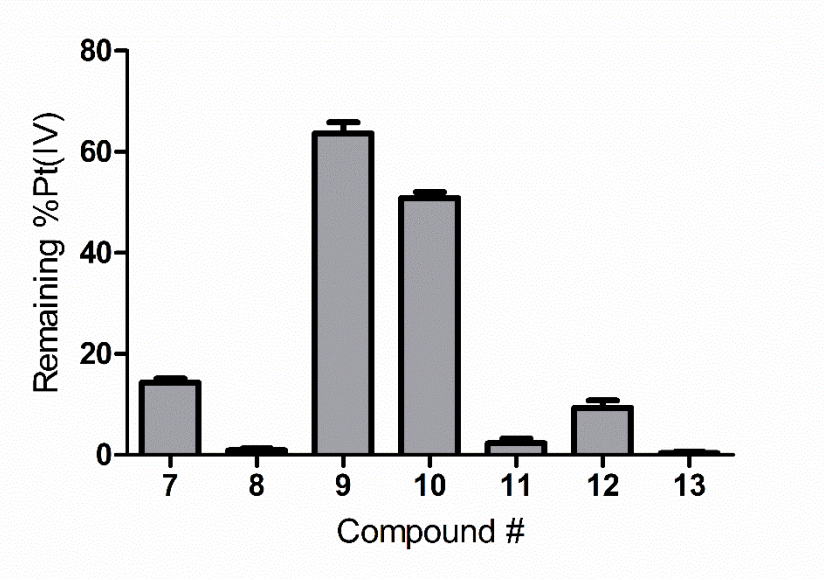

Figure 4.4. Each member of the Pt(IV) library (15 μm) was subjected to highly reductive conditions containing high concentrations of glutathione and sodium ascorbate (each at 15 mM) in PBS (1×, pH 7.4, 37 °C). The remaining %Pt(IV) was analysed by HPLC to identify the "bio-inertness" of the Pt(IV) prodrugs. The Pt(II) species are not observed in

HPLC spectra due to the displacement of the UV-absorbent oxalate ligand by chloride-containing media (see Chapter 3).

The difference in cytotoxicity of **9** compared to the active drug, oxaliplatin, was analysed on HCT116 and SKOV-3-wt cells. Complex **9** was significantly less ($P<0.0001$) cytotoxic compared to oxaliplatin (see Figure 4.5).

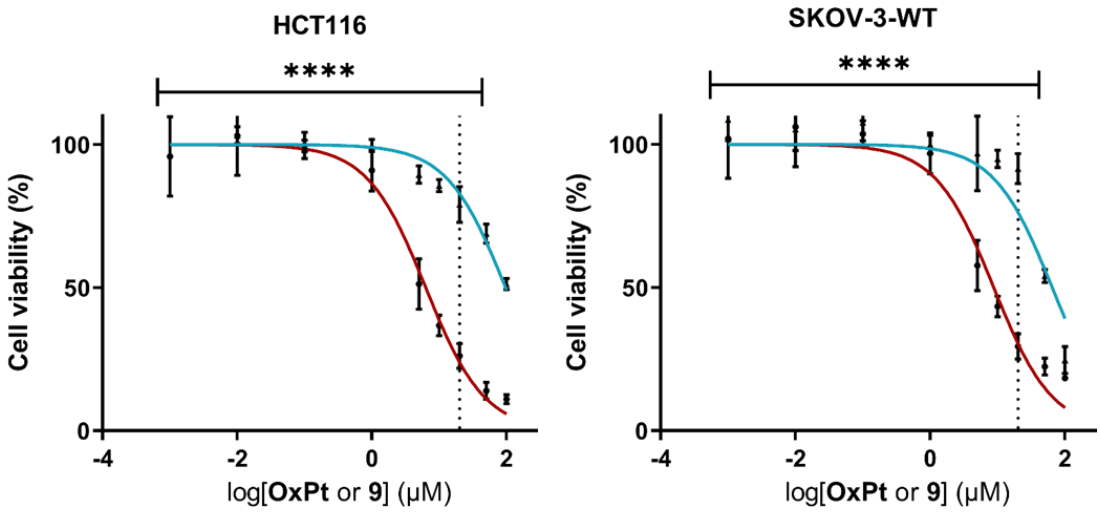

Figure 4.5. Dose-response curves for oxaliplatin (red line) and Pt(IV) prodrug **9** (blue line) in SKOV-3-wt and HCT 116 cells. The dashed line in each dose-response curve indicates the differences in toxicity between the prodrug and the active drug at 20 μM. **** $P<0.0001$ by two-way ANOVA with Dunnett post-test ($n = 3$)

The disparity in cytotoxicity between the Pt(IV) prodrug and the Pt(II) active drug is of great benefit to this study as it highlights the ability of Pt(IV) prodrugs to be bio-inert and non-toxic (increasing the therapeutic dose window) and facilitates analysis *in cellulo*, as cell death will be a stark indicator of the activation

of **9**. The dashed lines in Figure 4.5 show the selected dose of **9** used for cell experiments.

The emergence of resistance to Pt-based cancer therapies is a constant threat to their application and was a focus of this research. The ability of photocatalytic Pt(IV) activation to overcome resistance was also explored. In order to do this, a cell line was allowed to acquire resistance towards oxaliplatin, by intermittent burst doses of oxaliplatin and continuous lower dosing (details of dosing regimen are in Chapter 5). SKOV-3 cells are well suited to this purpose as they are innately more resistant to Pt-based therapies than most other cancer cell lines. The "wild-type" SKOV-3 cell lines (naïve to oxaliplatin treatment) were dubbed SKOV-3-wt whereas the cell line that was allowed to acquire resistance was named SKOV-3-OxR. It can be seen from Figure 4.6 that the IC_{50} of oxaliplatin underwent a 2.8-fold increase following 3 months of accrued resistance.

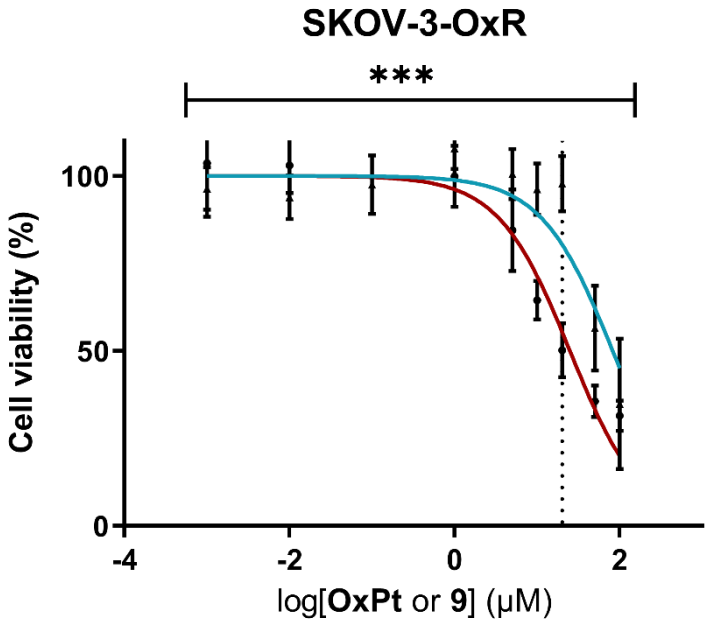

Figure 4.6. Dose-response curves for oxaliplatin (red line) and Pt(IV) prodrug **9** (blue line) in SKOV-3-OxR cells. The dashed line in each dose-response curve indicates the differences in toxicity between the prodrug and the active drug at 20 μM. *** $P<0.001$ by two-way ANOVA with Dunnett post-test ($n = 3$).

Cellular uptake of **9** and oxaliplatin was also investigated in the cell lines. It can be seen from Table 4.1, that there was a much larger percentage of **9** taken up into cells than oxaliplatin, despite the latter having a lower IC_{50}. It is likely that **9** permeates through the cell membrane more efficiently than oxaliplatin but does not undergo reduction and therefore remains in an inactive state, resulting in high cellular uptake but lower cytotoxicity, relative to oxaliplatin. Lipophilicity may also be a factor in the difference of uptake. **9** is more lipophilic than oxaliplatin, which may be of benefit for cell membrane traversal due to the lipidic nature of the membrane. However, there are conflicting reports regarding whether lipophilicity has a direct relationship with uptake, with some suggestion that the two can be poorly correlated[256-258].

Table 4.1. Cellular uptake of the photosensitiser **16** (1 μM) and the Pt(IV) prodrug **9** (20 μM) after 4 h incubation, as measured by ICP-MS. The % uptake for each compound was calculated as the proportion of the theoretical maximal uptake.

Compound	**Cell line**	**Cell uptake (ng/10^6 cells)[%]**
16	SKOV-3-wt	275 ± 9 [90 ± 3%]
	SKOV-3-OxR	191 ± 3 [63 ± 1%]
	HCT 116	190 ± 10 [63 ± 3%]
9	SKOV-3-wt	531 ± 20 [14 ± 0.5%]
	SKOV-3-OxR	384 ± 2 [10 ± 0.04%]
	HCT 116	458 ± 12 [12 ± 0.3%]

	SKOV-3-wt	161 ± 11 [1 ± 0.9%]
OxPt	SKOV-3-OxR	150 ± 5 [1 ± 0.4%]
	HCT 116	281 ± 10 [2 ± 0.8%]

4.6 Design, synthesis and optimisation of photosensitisers

A new photosensitiser was designed, based on $[Ru(bpy)_3]^{2+}$, with extended conjugation in one of the bipyridine ligands *via* the installation of an indoline moiety (Scheme 4.7). This was due to the lack of cell uptake observed with the commercial $Ru(bpy)_3Cl_2$. 1,3,3-trimethyl-2-methyleneindoline is commonly used as a building block in the synthesis of Cy dyes and has high reactivity with aldehydes. 4,4'-dimethylbipyridine was oxidised with SeO_2 to yield 4-formyl-4'-methylbipyridine (**L-1**). Ligand substitution could then be carried out on $[Ru(bpy)_2Cl_2]$ in refluxing ethanol-water mixture to afford the formyl-bearing precursor ruthenium complex (**L-2**) which could then undergo reaction with 1,3,3-trimethyl-2-methyleneindoline to give the desired compound, following counterion exchange to isolate as the hexafluorophosphate salt (Complex **14**). The ultimate reaction will produce *fac*- and *mer*-isomers but were assumed to be insignificant in relation to their activity for this application and thus not isolated separately.

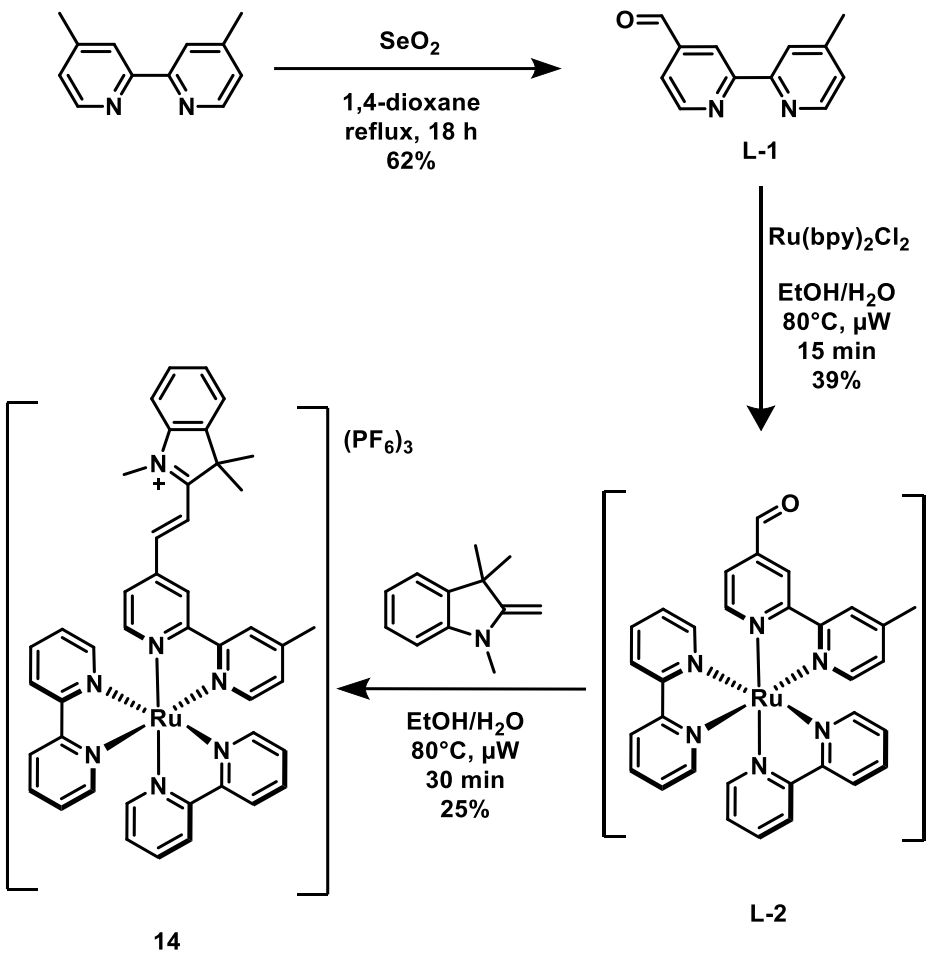

Scheme 4.7. Synthetic route for photosensitiser **14**

However, complex **14** was found to exhibit rapid degradation to the aldehyde-containing complex. This may be a result of either singlet oxygen addition over the C-C double bond or hydrolysis (Scheme 4.8). Regardless, a series of photocatalysts were designed to overcome this issue while further extending the conjugation of the ligand.

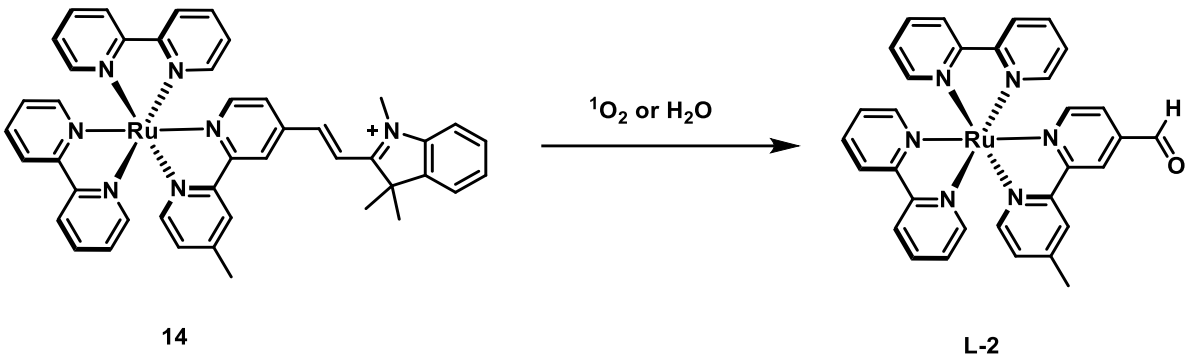

Scheme 4.8. Proposed routes of degradation of photosensitiser **14** by either singlet oxygen or water addition to form the aldehyde derivative.

For complex **15,** the ligand was synthesised by first mono-brominating the benzylic position of 4,4'-dimethylbipyridine to give ligand **L-3** (see scheme 4.9). This was accomplished by a Wohl-Ziegler reaction, based on prior reports, although the solvent, carbon tetrachloride [259], was replaced with chloroform with little discernible impact on yield. This could then be derivatised to the phosphonate (**L-4**), enabling a Horner-Wadsworth-Emmons reaction with the aldehyde. However, the final step could not be accomplished and only starting materials were isolated following work-up.

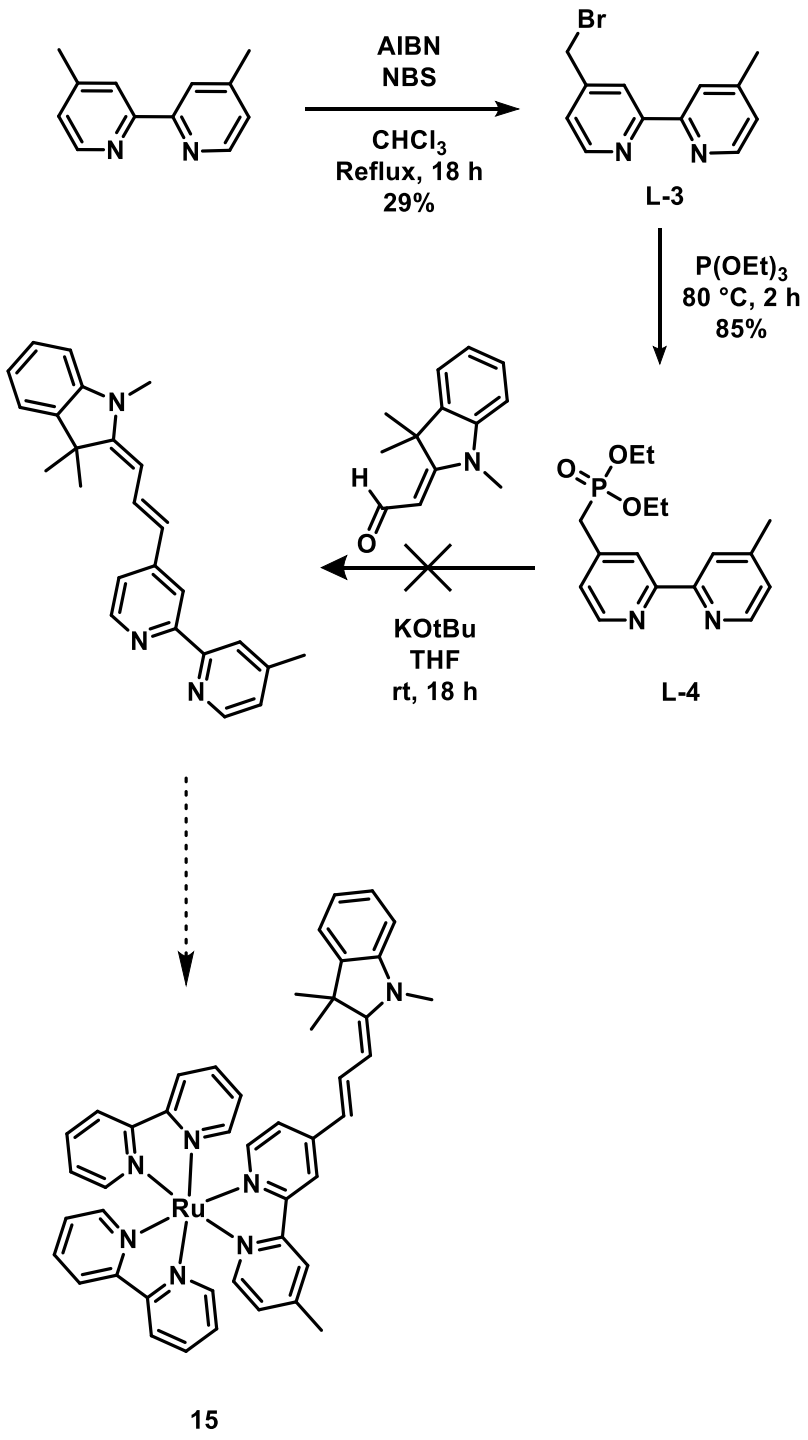

Scheme 4.9. Synthetic route to photosensitiser **15.**

Complex **16** was synthesised by reaction of 1,3,3-trimethyl-2-methyleneindoline with 4-formylphenylboronic acid, followed by Suzuki-Miyaura coupling with 4-

bromobipyridine to yield the ligand **L-6**(Scheme 4.10). This ligand was then installed onto [Ru(bpy)$_2$Cl$_2$] in the same manner as before, to afford the desired compound **16** as the hexafluorophosphate salt.

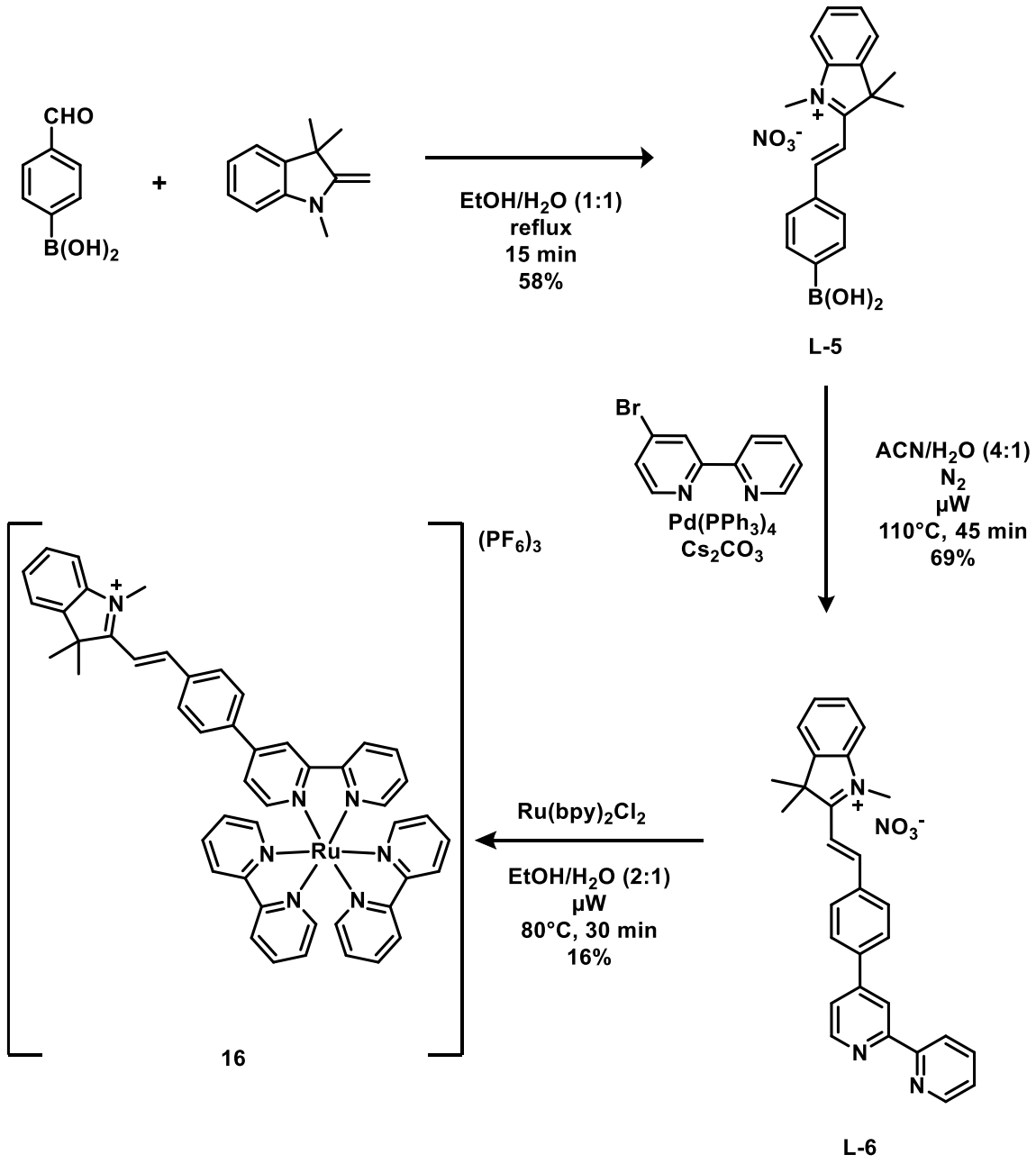

Scheme 4.10. Synthetic route to photosensitiser **16**.

4.7 Characterisation of photosensitiser 16

Ruthenium-polypyridyl photosensitisers exhibit characteristic light absorption profiles with wavelengths < 300 nm being the ligand-ligand charge transfer (LLCT) events where an electron undergoes a π-π^* transition[260, 261]. Another peak in the blue region corresponds to a metal-ligand charge transfer (MLCT), a dπ-π^* transition. The absorbance spectra of photosensitiser **16** in PBS was recorded and showed similar characteristics to $[Ru(bpy)_3]Cl_2$, with the maxima at 450 nm corresponding to the MLCT excited state (Figure 4.7). The implications of this, in relation to the catalytic cycle for reduction of Pt(IV) substrates, are discussed below.

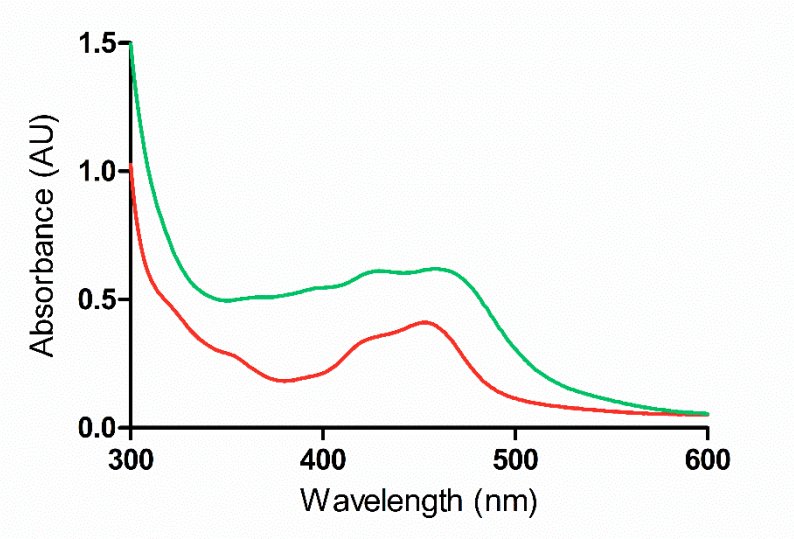

Figure 4.7. Absorbance spectra of **16** (green line) and $[Ru(bpy)_3]Cl_2$ (red line) both at 100 µM in PBS showing the MLCT band at 450 nm.

The stability of photosensitiser **16** was evaluated in DMEM supplemented with 10% FBS by measuring the absorbance at 440 nm (Figure 4.8) and exhibited good stability over 24 h.

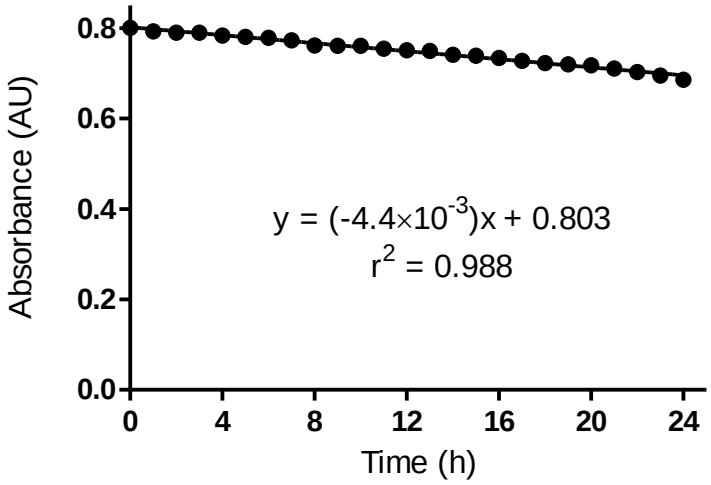

Figure 4.8. Stability of **16** in DMEM with 10% FBS, as measured by absorbance at 440 nm.

The ability of PS **16** to generate singlet oxygen was examined and the quantum yield of singlet oxygen generation measured in comparison to $[Ru(bpy)_3]Cl_2$. There exist a host of molecules to probe this, which capture singlet oxygen to bring about a spectral change in the probe molecule. However, many suffer from poor water solubility, high photo-bleaching or have overlapping absorbances with the photosensitisers tested. Therefore, a fluorescent probe, singlet oxygen sensor green (SOSG) was utilised. This probe is composed of carboxyfluorescein with naphthalene conjugated at the 6'-position that acts as an internal electron transfer quencher (see Scheme 4.11). The quenching was inhibited following reaction with singlet oxygen, which adds across the central aromatic ring of the

naphthalene moiety. This afforded an increase in fluorescence of the fluorescein moiety in correlation to the amount of singlet oxygen produced.

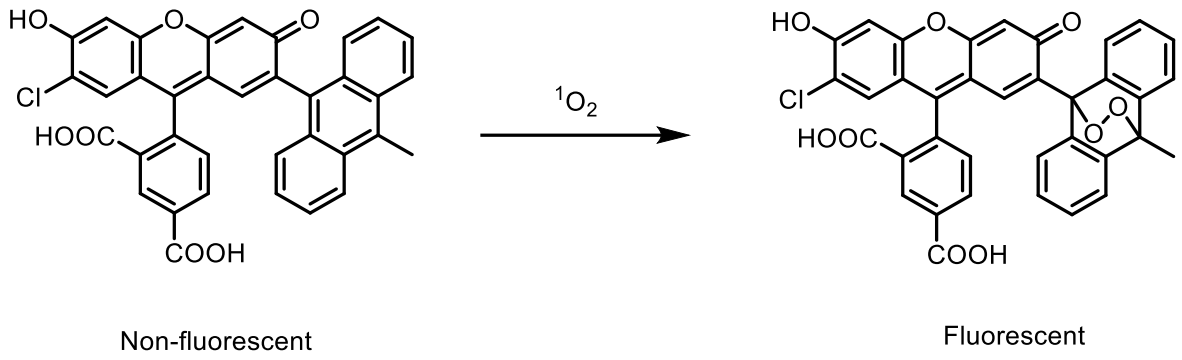

Scheme 4.11. The mechanism for the fluorescent turn-on probe (SOSG) for the detection and quantification of singlet oxygen. Singlet oxygen undergoes a Diels-Alder reaction with the anthracene moiety. The resultant endoperoxide is fluorescent, providing a quantitative measure of singlet oxygen levels.

The fold-increase of fluorescence ($\lambda_{ex} = 504$ nm, $\lambda_{em} = 525$ nm) was plotted for both photosensitisers and the quantum yield of singlet oxygen generation (Φ) was calculated by the equation:

$$\Phi_{\mathbf{16}} = \Phi_{STD}\left(\frac{k_{\mathbf{16}}}{k_{STD}}\right)$$

where Φ_{STD} is the quantum yield of $Ru(bpy)_3Cl_2$; $k_{\mathbf{16}}$ is the rate of increase in fluorescence of SOSG by **16** and k_{STD} is the rate of increase in fluorescence of SOSG by $Ru(bpy)_3Cl_2$. The quantum yield of $Ru(bpy)_3Cl_2$ from the literature was 0.86[262] and the calculated quantum yield of singlet oxygen generation for **16** was found to be 0.72 (Figure 4.9).

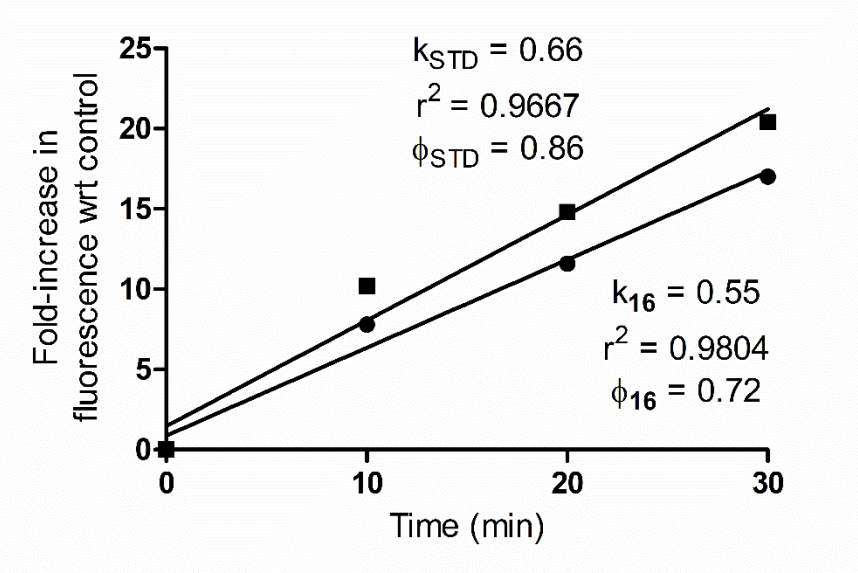

Figure 4.9. Quantum yield of singlet oxygen generation by **16** and $Ru(bpy)_3Cl_2$, as measured by an SOSG assay (where 1 μM of each PS with 5 μM of SOSG in MeOH were irradiated with light (λ = 470 nm)) and the increase of the singlet oxygen-activated fluorescence probe analysed over time (λ_{ex} = 504 nm, λ_{em} = 525 nm).

Cellular uptake of photosensitiser **16** was determined in HCT 116 and SKOV-3-wt cells (Table 4.1) and was found to be taken up well into cells via live-cell confocal microscopy. Cells were co-stained with Hoechst nuclei blue dye and with Mitotracker Green (green mitochondrial stain) and Figure 4.10 shows a significant overlap of the fluorescence of the PS **16** with Mitotracker Green, suggesting co-localisation of the photosensitiser in the mitochondria. Interaction with the mitochondrial membrane is often observed for organic cations and the localisation of the PS **16** may be driven by the positively charged indoline-containing ligand[263, 264].

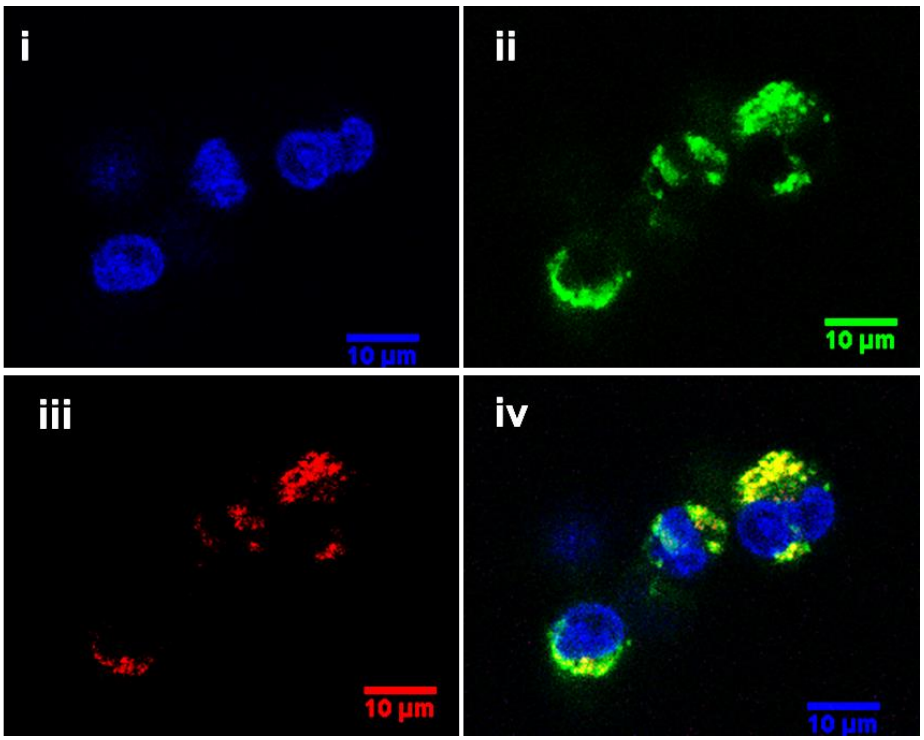

Figure 4.10. Live-cell confocal microscopy with stained SKOV-3-wt cells. i) Hoechst nuclei stain in blue; ii) Mitotracker Green, mitochondrial stain, in green; iii) photosensitiser **16** in red and; iv) merged image. The yellow-orange colouring of the merged image demonstrates the overlap between the green mitochondrial stain and the photosensitiser in red, indicating co-localisation.

4.8 Fabrication of custom light sources

Before investigating the photocatalytic reduction reactions, focus was turned to the light source used. As stated above, an LED-array lamp was used, however the intensity of light is unattainable for implanted devices and the viewing angle of the light is not suited for even distribution over a well plate, introducing bias towards the centre of the well plate.

For illumination experiments in a well plate format, a bespoke light source was required. To ensure illumination occurred evenly throughout the well plate, a device was designed and fabricated which allowed positioning of a single LED above each well in a black well plate to prevent scattering to adjacent wells (Plate A). 96 LEDs with a dominant emission wavelength of 470 nm and a 15° viewing angle were surface-mounted onto a breadboard, in a matrix format to allow each LED to enter its respective well, forming a lid for the well plate (see Figure 4.11).

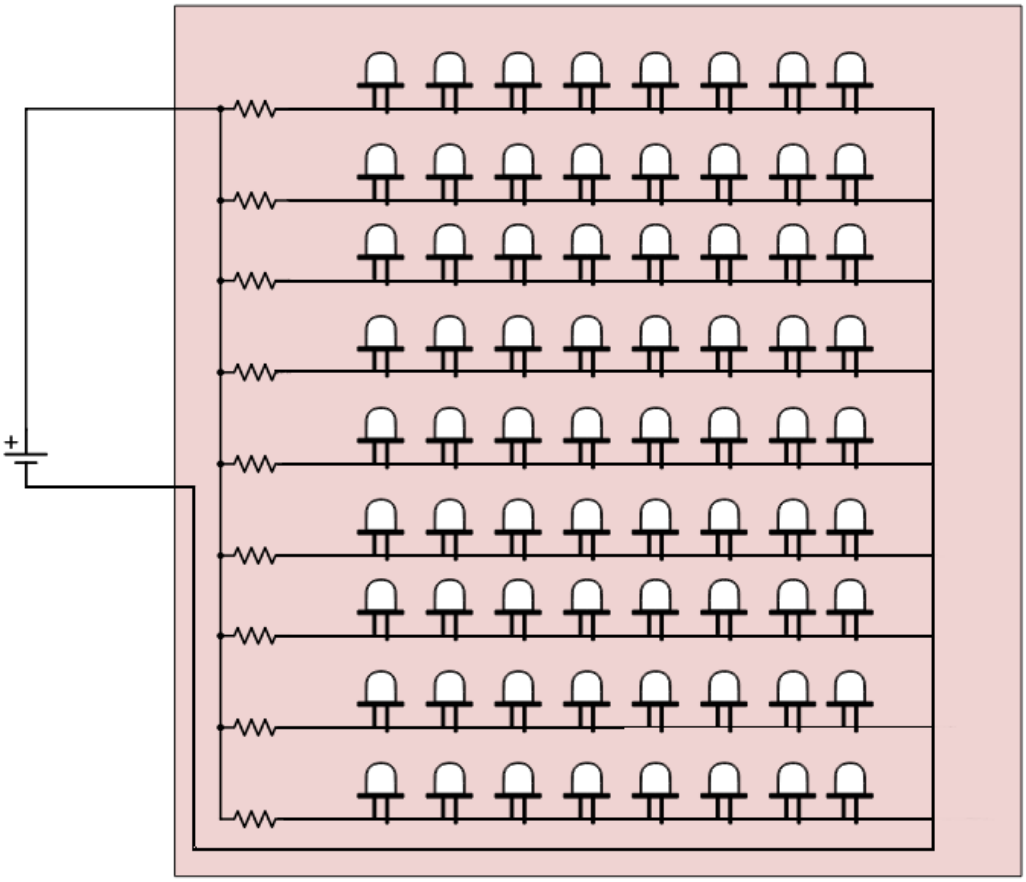

Figure 4.11. Plate A: LEDs were arranged in nine parallel circuits with a constant-current LED driver resistor (output current of 20 mA) and a 48 V power supply.

The LEDs were connected in nine parallel circuits, filling nine of the twelve columns of the 96-well plate. The intensity of illumination of the LEDs is correlated to the current in the circuit. The forward voltage supplied to the LED has a non-linear relationship with current[265]. As such, small deviations in voltage will drastically affect the forward current, and thus the LED's brightness. In order to overcome this, LEDs are driven in conjunction with modulators of current that supply a constant current to the LED (e.g. resistors) and take the forward voltage as a fixed value. This results in a more reliably stable brightness of the LEDs than if they were "voltage-driven". To ensure intensity was equivalent throughout the circuit, the current was modulated in each parallel circuit by an LED driver; maintaining a constant current driven by the power source. The compatibility of the fabricated LED well plate for cell-based assays was explored with HCT 116 cells. Cells were illuminated for 1 h or kept in the dark and incubated for 48 h, before measuring cell viability by an MTT assay. It was found that cells that had been illuminated underwent cell death as a result of the light source, due to the proximity of the LEDs to the cells.

Another design for the LED well plate (Plate B) was conceived whereby an LED strip was formed into a coil between two well plate covers with equivalent spacing between each turn of the coil (Figure 4.12). This allowed a transparent well plate to be inserted into the coil, providing a simple and rapid mode of illumination. Cell viability after 1 h of illumination of HCT 116 cells showed a 20% reduction in cell viability. This was deemed acceptable as illumination in the cell experiments would only be 30 minutes.

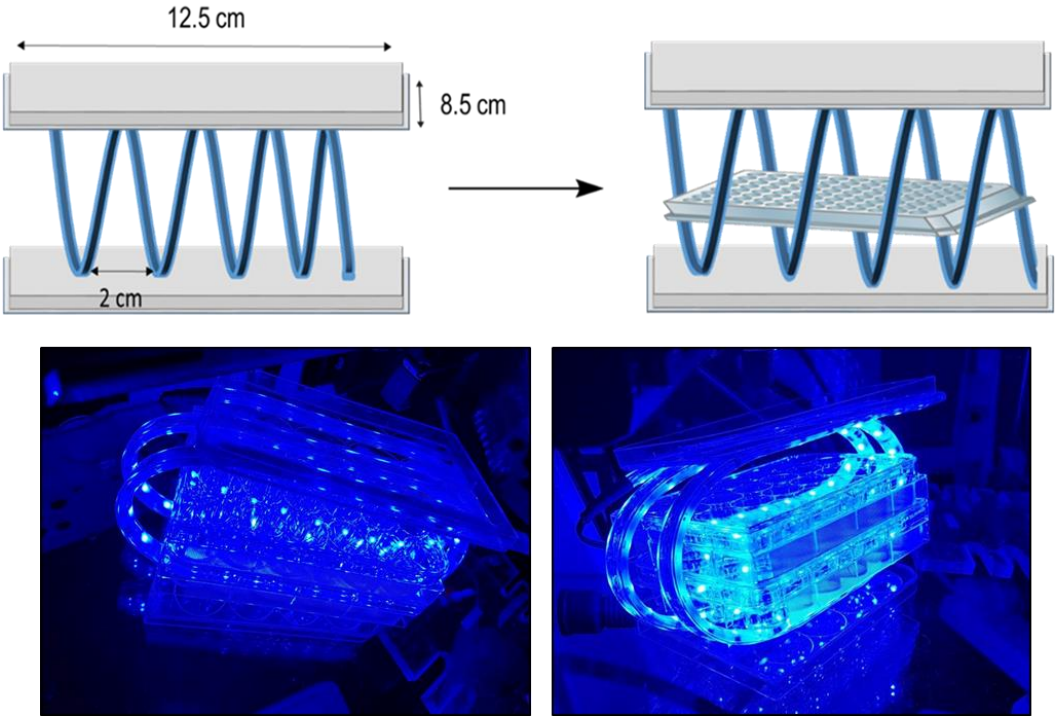

Figure 4.12. Design of Plate B with dimensions of the well plate covers used and the spacing between each coil of the LED strip (top) which allowed simple insertion of a well plate inside for illumination. The illumination of cells was carried out in a temperature- and atmosphere-controlled chamber at 37 °C with 5% CO_2 (bottom).

The intensity and uniformity of incident light over the LED well plate was measured by a photodiode (1 cm^2 sensing area) throughout the well plate giving an average of 0.5 ± 0.04 $mW.cm^{-1}$.

The light intensity per well for the two setups was calculated as outlined below. For Plate A, a single LED in each well had a luminous intensity of 11 candela (with 15° viewing angle and 20 mA forward current). Candela (cd) can be converted to watt by the following equation:

$$cd = \frac{1}{683}\ watt\ per\ steradian$$

where a steradian is the unit of solid angle in a three-dimensional space (i.e. the cone of illumination by the LED). Therefore the intensity per well of Plate A can be calculated in watts:

$$r\ of\ well = 3.2\ mm$$

$$solid\ angle = r^2 = 11.56\ steradians$$

$$Intensity = \ 11\ cd\left(\frac{1}{683} \times 11.56\right)$$

$$Intensity = 187\ mW\ per\ well$$

For Plate B, the intensity per well can be extrapolated from the photodiode measurement:

$$Diameter\ of\ well = 6.4\ mm$$

$$Intensity\ of\ Plate\ B = 0.5\ mW.cm^{-1}$$

$$Intensity = (0.5)\left(\frac{6.4\ mm}{10}\right)$$

$$Intensity = 0.32\ mW\ per\ well$$

Comparison shows there is a large difference (580-fold) in intensity of illumination between the two formats. Plate B was utilised in further experiments involving illumination.

4.9 Characterisation of photocatalytic Pt(IV) prodrug activation

The photocatalytic reduction of the Pt(IV) substrate **9** (50 μM) by photocatalyst **16** (1 μM) was confirmed in PBS, with light delivered using the setup Plate B, with a clear reduction in concentration of **9** measured by HPLC (Figure 4.13.) To visualise the oxaliplatin content, post-derivatisation with GMP was again utilised (as in Chapter 3) forming a UV-active adduct. It is clear that only where light and the photocatalyst are used in combination was there any increase in the oxaliplatin concentration (Figure 4.13). Controls with either photocatalyst or light applied alone showed no generation of oxaliplatin.

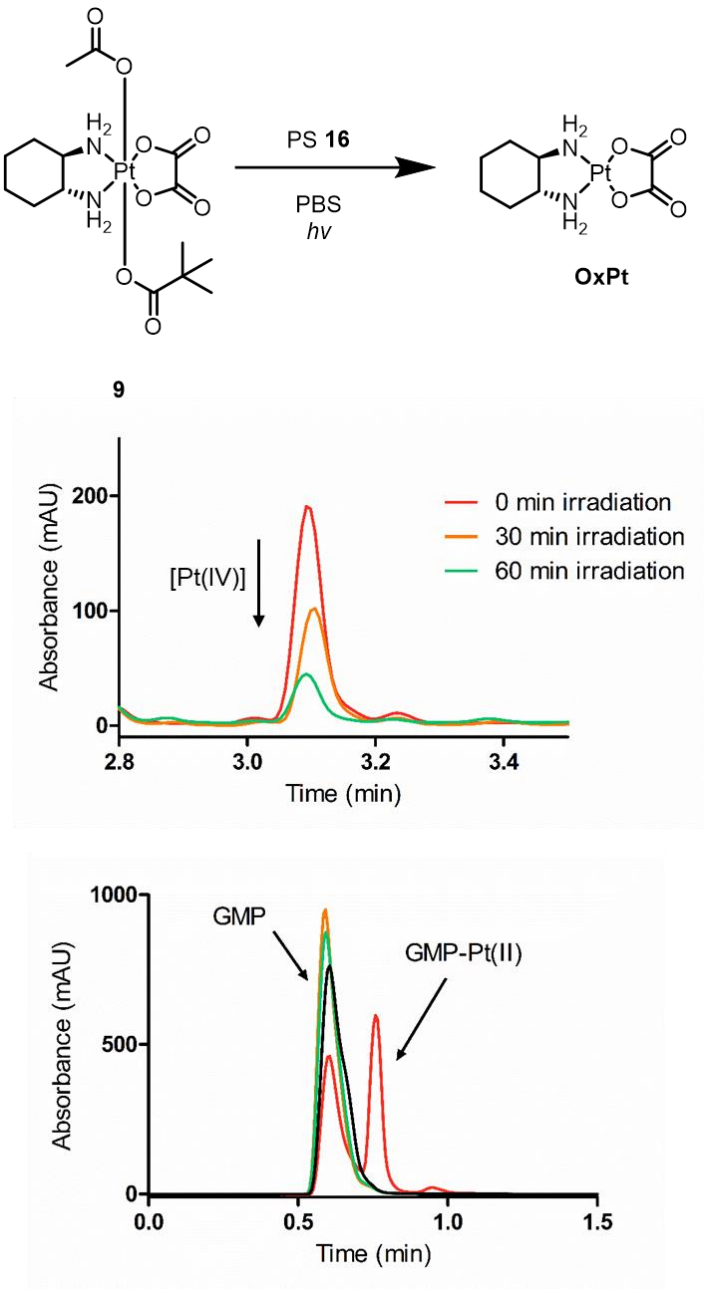

Figure 4.13. HPLC characterisation of the reduction of Pt(IV) complex **9** (50 μM) by photosensitiser **16** (1 μM) (top). HPLC analysis over time showing the decrease of **9** (middle) and the analysis following 60 min irradiation time and incubation with GMP (1 mM) at 37 °C for 4 h (bottom) showing the formation of Pt(II) species only in the presence of Pt(IV) prodrug **9**, photosentisiter **16** and illumination of light (red line). No Pt(II) species were detected for the conditions: with Pt(IV) complex **9** and PS **16** but in

the absence of illumination (orange line); with Pt(IV) complex **9** but without PS **16** and illumination (black line); or with Pt(IV) complex **9** and illumination but without PS **16** (green line).

In order to provide absolute quantification of the generated oxaliplatin, a calibration line was produced from known concentrations of oxaliplatin reacted with GMP and subjected to HPLC analysis (Figure 4.14).

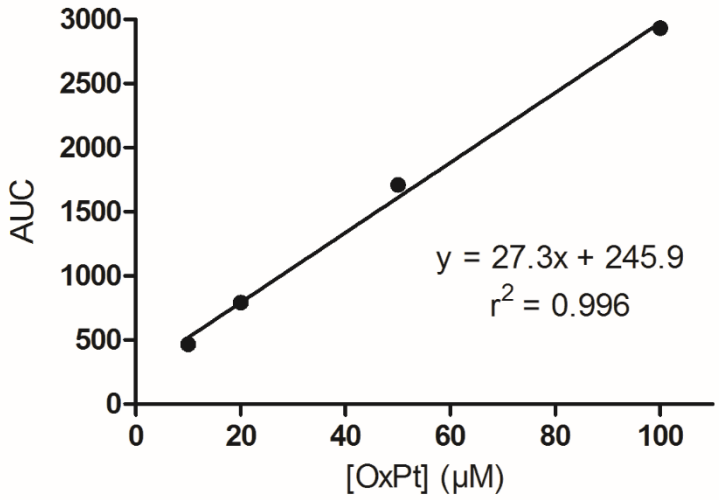

Figure 4.14. Calibration line of the area under the curve (AUC) of known concentrations of oxaliplatin incubated with GMP (1 mM) at 37 °C for 4 h before HPLC analysis. For the reaction with light and photocatalyst combined, the area under the curve was calculated as 1421 mAU.min^{-1}, which corresponds to a concentration of 43 μM of oxaliplatin generated (86% yield).

To further demonstrate the robustness of the photocatalytic conversion of the Pt(IV) prodrug **9**, reaction solutions were analysed by ^{1}H NMR (Figure 4.15). Here, the concentration of **9** used was increased to 100 μM to facilitate analysis

with the PS (**16**) concentration remaining at 1 μM. Again, there was an observed efficient and clean conversion of **9** into OxPt.

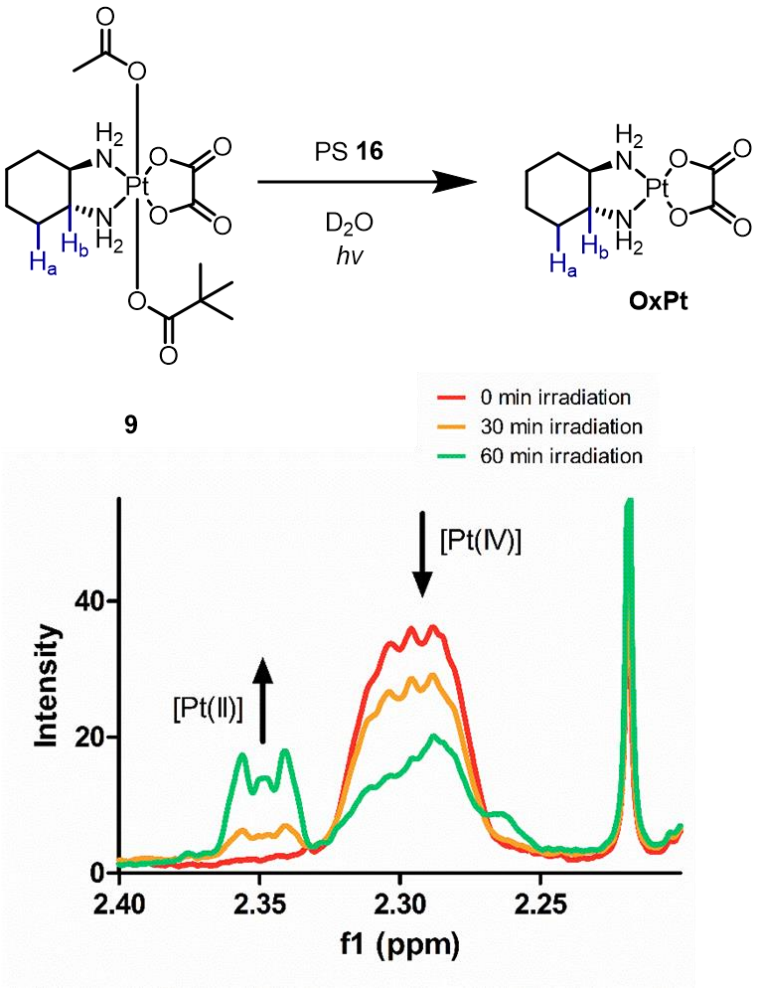

Figure 4.15. NMR analysis over time of the irradiated reaction mixture showing the decrease in Pt(IV) along with an increase in the intensity of the Pt(II) resonance. The figure shows the protons (H_a and H_b) that were used to monitor the decrease and increase of the Pt(IV) and Pt(II) species, respectively (upper). The resultant NMR spectra show clearly the reduction of **9** (100 μM) to oxaliplatin, photocatalysed by PS **16** (1 μM) in D_2O (lower).

4.10 Validation of photocatalysed Pt(IV) prodrug activation *in cellulo*

With the photocatalytic reduction system of the Pt(IV) substrates fully characterised, attention was turned to demonstrating cytotoxicity turn-on with cancer cells. HCT 116 and SKOV-3-wt cells were once again used for this purpose and for each cell type, control experiments were run without illumination, with or without photosensitiser **16**. Concentrations of the photosensitiser and the Pt(IV) prodrug were chosen based on *in vitro* work described above to give maximal cytotoxic turn-on effect without an overly-long illumination time. In all cases, in the absence of light no cytotoxicity was observed. When cells were illuminated in the presence of photosensitiser **16**, there was a slight decrease in cell viability (36 $\pm$ 13% remaining viable for HCT 116 cells and 83 $\pm$ 10% remaining viable for SKOV-3-wt cells) compared to control experiment, presumably due to singlet oxygen generation. When both photosensitiser **16** and Pt(IV) prodrug **9** were illuminated, there was a clear turn-on cytotoxic effect: in SKOV-3-wt cells, cell viability was reduced to 12 $\pm$ 3% , and in HCT 116 cells, viability was reduced to 5 $\pm$ 4% (Figure 4.16).

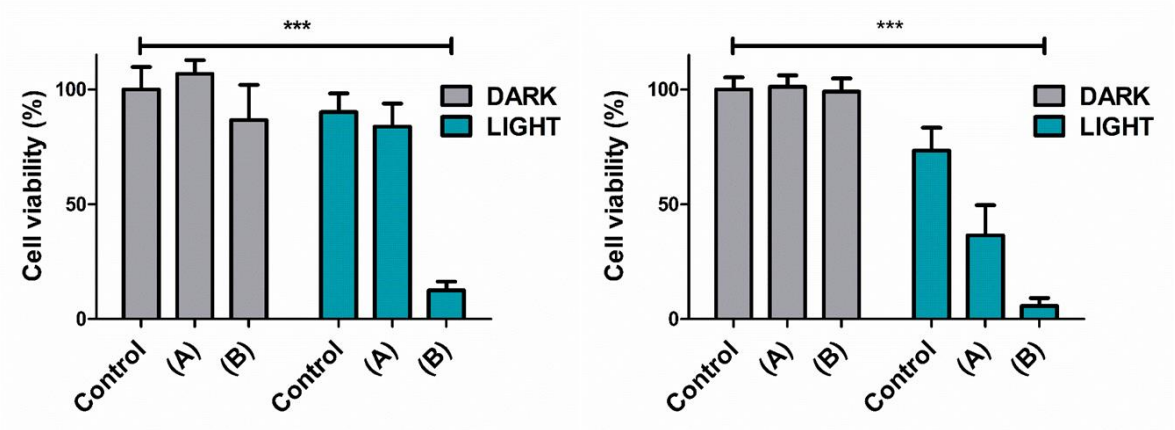

Figure 4.16. Cell viability, as measured by a CellTitre Glo 2.0 assay using SKOV-3-wt cells (left) and HCT 116 cells (right). "Control" represents untreated cells, "**(A)**" are cells incubated only with the PS **16** (1 μM) and "**(B)**" are cells incubated with **16** (1 μM) and **9** (20 μM) for 4 h before illumination for 30 minutes followed by incubation in the absence of light for 48 h.

The ability of the photocatalytic Pt(IV) activation system to overcome acquired oxaliplatin resistance in SKOV-3 cells was examined. Figure 4.17 demonstrates that, despite a slightly reduced cytotoxic effect, the photocatalytic activation of **9** reduced cell viability to only $29 \pm 11\%$.

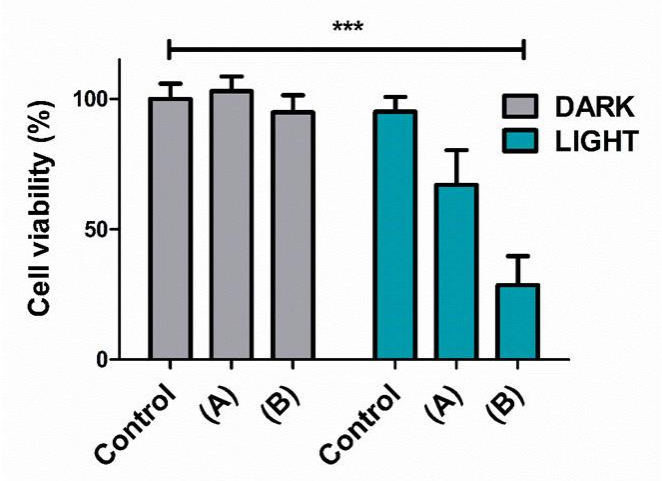

Figure 4.17. Cell viability, as measured by a CellTitre Glo 2.0 assay using SKOV-3-OxR cells. "Control" are untreated cells; "**(A)**" are cells incubated with **16** (1 μM) and "**(B)**" are cells incubated with **16** (1 μM) and **9** (20 μM).

As discussed in Chapter 1, DNA platination remains one of the main routes of cytotoxicity, despite other mechanisms of action being implicated for oxaliplatin. Pt(IV) species have been shown to be unreactive towards DNA whereas Pt(II) species are highly-driven to bind. Therefore, the level of platination found in DNA can be used as an indicator of the conversion of the inactive Pt(IV) prodrug to the active Pt(II) species. For SKOV-3-wt and SKOV-3-OxR cells, 24 h after photocatalytic activation of **9**, the cells' DNA was harvested and quantified, with the levels of platination measured by ICP-MS. DNA platination levels were higher for both cell lines when photosensitiser **16** and the Pt(IV) prodrug **9** were used in combination with illumination, than incubation with oxaliplatin alone (Figure 4.18).

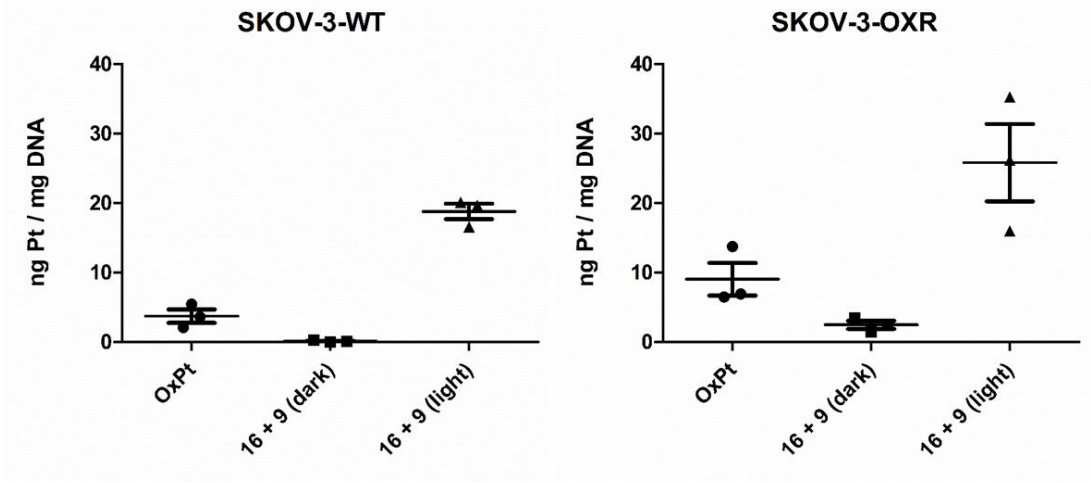

Figure 4.18. Quantification of the platination levels found in cellular DNA using SKOV-3-wt cells (left) and SKOV-3-OxR cells (right), as measured by ICP-MS. For each condition, cells were incubated for 4 h with the appropriate compounds (**OxPt**:20 μM; **16**:1 μM; **9**:20 μM). This was followed by illumination for 30 minutes then incubation in the absence of light for 24 h. The cells were then lysed and the DNA harvested. The Pt content was measured by ICP-MS and the DNA concentration measured by NanoDrop spectroscopy.

It has been demonstrated that the cytotoxic effect of photocatalytic activation of **9** can transcend acquired oxaliplatin resistance. The reasons for this are likely related to cellular uptake. Oxaliplatin may be taken into cells via different mechanisms that **9** and so cellular changes in the transport of oxaliplatin, as a resistance mechanism, may not affect **9**. Photo-activation of **9** following uptake into cells, allows relatively high levels of oxaliplatin to be formed *in situ* intracellularly. As shown above in Table 4.1, the uptake of **9** did not differ greatly between SKOV-3-wt and SKOV-3-OxR cells. Another factor contributing to the cell death in SKOV-3-OxR cell lines was increased sensitivity to singlet oxygen, as in experiments where just the photosensitiser was used. The localisation of the photosensitiser in the mitochondrion of the cell may play a role in overcoming the resistance mechanisms of SKOV-3 cells. It was thought possible that the conversion of Pt(IV) could occur in the mitochondria, which could change its mechanism of action towards binding with the mitochondrion or to mitochondrial DNA. To probe this, mitochondrial DNA was harvested from SKOV-3-wt and SKOV-3-OxR cells following photoactivation of **9**, and Pt content quantified (Figure 4.19). There was no clear relationship or differences between the two cell types, with low levels of platination for both observed.

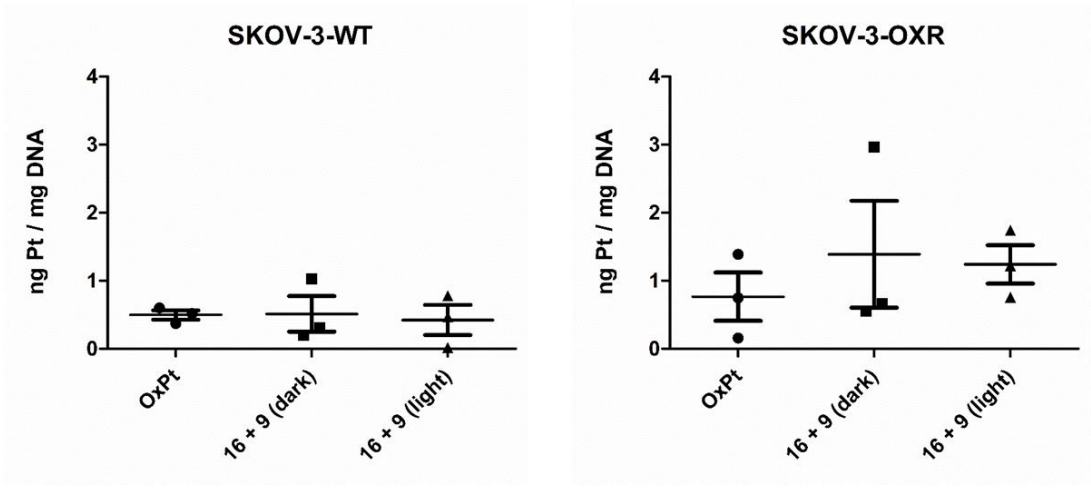

Figure 4.19. Quantification of the platination levels of mitochondrial DNA in left) SKOV-3-wt cells and right) SKOV-3-OxR cells, as measured by ICP-MS. Cells were incubated with either oxaliplatin (20 μM) or **16** (1 μM) and **9** (20 μM) together, which were either irradiated for 30 minutes or kept in the dark. The cells were then incubated for 24 h prior to lysis, DNA harvesting and analysis by ICP-MS.

4.11 Extension of application of photocatalytic Pt(IV) prodrug activation

Insight into the scope of the photocatalytic Pt(IV) reduction system was explored with respect to the Pt(IV) species capable of being reduced and the photosensitisers that could be utilised. As mentioned above, TLD1433 is a ruthenium-based photosensitiser that is undergoing clinical testing and has shown great promise for photodynamic cancer therapy. It was investigated whether TLD1433 could photocatalytically activate Pt(IV) prodrugs. The photosensitiser was synthesised using a reported procedure[266]. First, the terthiophene-phenanthroline ligand was synthesised *via* a Radziszewski multi-component reaction between formyl-bearing terthiophene and 5,6-

phenanthroline-dione in the presence of ammonium acetate (see Scheme 4.12). The bis(4,4'-dimethyl-2,2'-bipyridyl)dichlororuthenium complex was then synthesised, using a previously reported protocol[267]. With the desired ligand (**L-7**) and precursor ruthenium complex (**L-8**) in hand, the reaction between the two was carried out with microwave heating to yield TLD1433 which was isolated as the hexafluorophosphate salt.

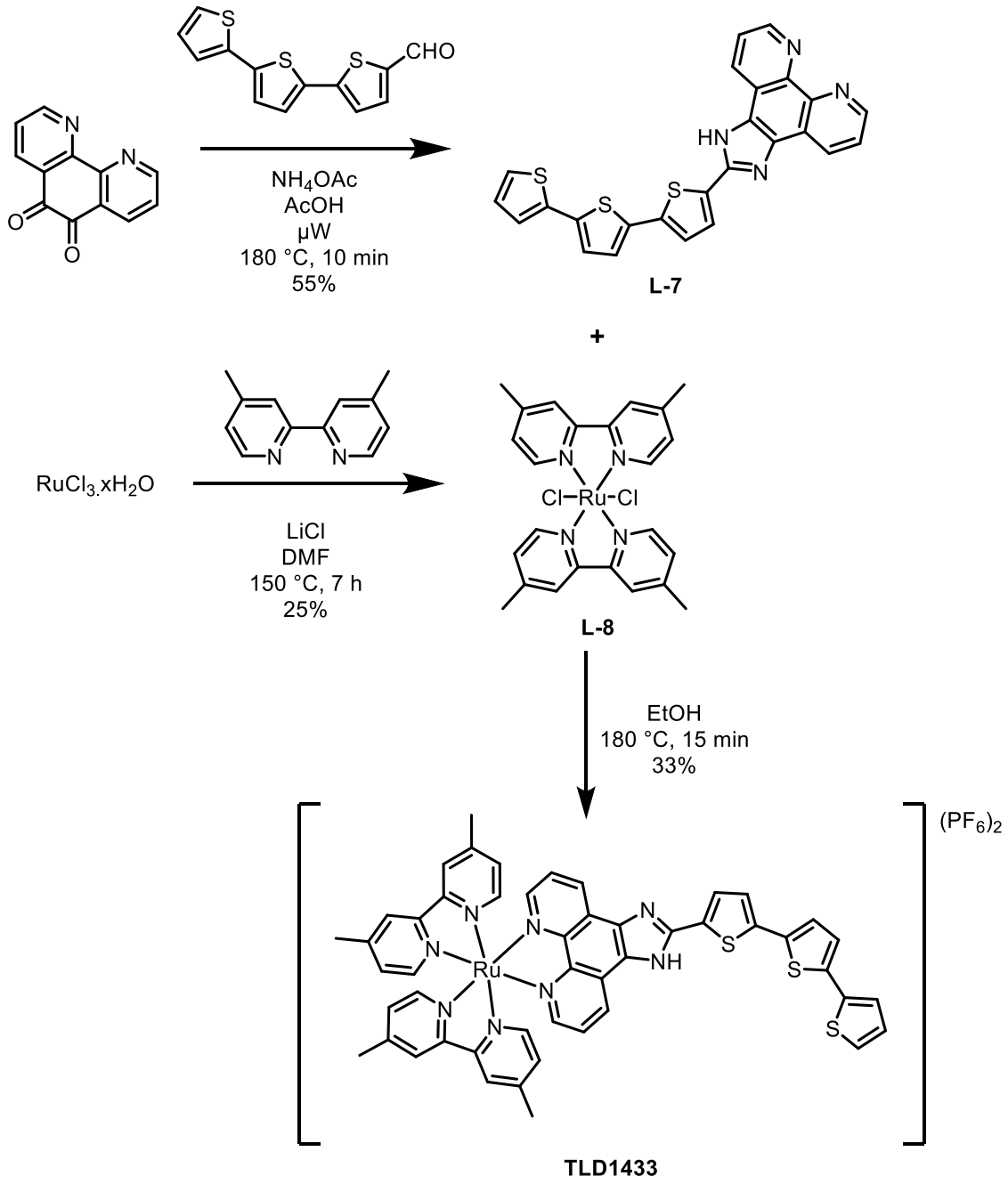

Scheme 4.12. Synthetic route for the photosensitiser TLD1433.

The reduction capabilities of TLD1433 were first tested with prodrug **9**. It was observed that TLD1433 was capable of reducing **9** upon illumination with light (λ = 470 nm), albeit at a slightly diminished rate than photosensitiser **16**.

Regardless, the scope of Pt(IV) complexes that TLD1433 was able to reduce was explored. Oxaliplatin Pt(IV) derivatives were made with varying axial ligands. A cisplatin Pt(IV) derivative was also included, to examine effect of the equatorial ligands (Figure 4.20). Between the oxaliplatin Pt(IV) derivatives, the different axial ligands exhibited little effect in the reduction by TLD1433. The cisplatin Pt(IV) derivative with diacetato axial ligands was more easily reduced than the corresponding oxaliplatin Pt(IV) derivative. This finding suggests there is clinical potential for adjuvant PDT and photo-activated Pt chemotherapy using ruthenium-based photosensitisers.

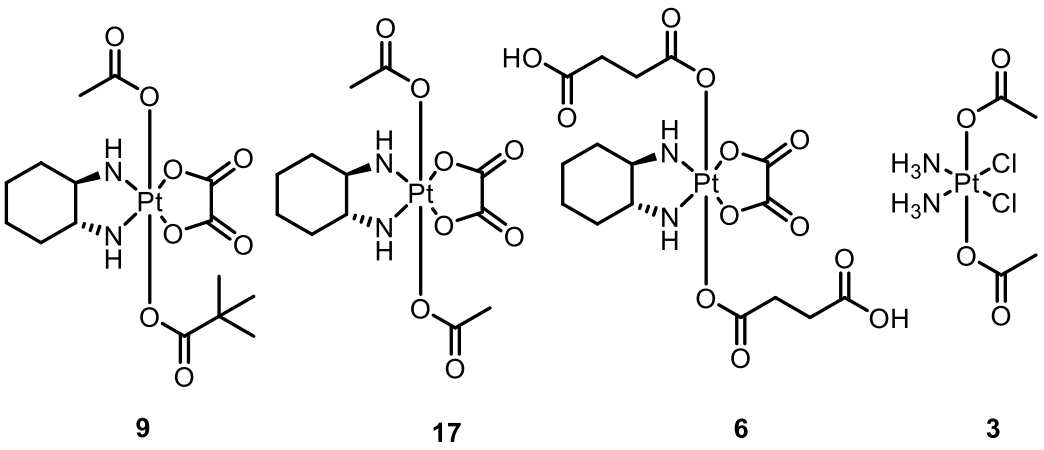

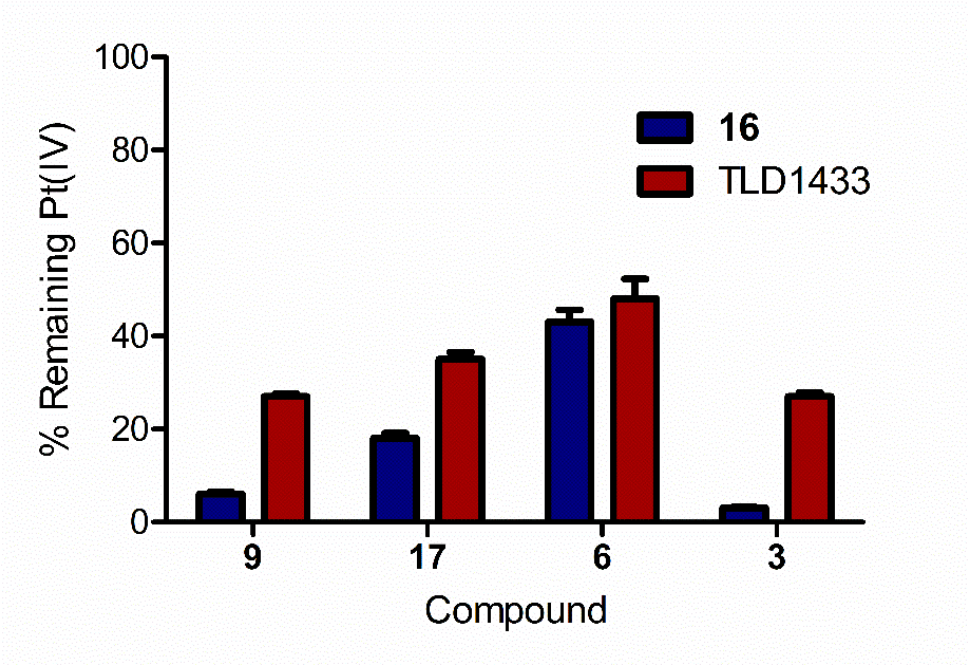

Figure 4.20. The scope of Pt(IV) substrates that are able to be reduced photocatalytically by PS **16** or TLD1433 (top). Illumination was for 1 h (λ = 470 nm) with each Pt(IV) species (50 μM) and the photosensitiser (1 μM) in PBS with analysis by HPLC (n = 3). Both **16** and TLD1433 were capable of reducing Pt(IV) species.

4.12 Elucidation of the mechanism of photocatalytic Pt(IV) prodrug activation

Attempts were made to elucidate the photocatalytic mechanism by which photosensitiser **16** reduces **9**. To determine if the reactive oxygen species, formed by the photosensitiser, were donating electrons to the Pt(IV) species, the photocatalytic reduction was carried out with a range of photosensitisers: methylene blue, rose bengal, XD-Br and zinc phthalocyanine (ZnPc) (Scheme 4.13). All three of these photosensitisers generate reactive oxygen species yet showed no activity towards the reduction of Pt(IV), upon illumination at their respective absorbance maxima. ZnPc is a photosensitiser that has an absorption maxima of 684 nm and like $[Ru(bpy)_3]Cl_2$, it is a metal-based photosensitiser. Regardless of the fact the metal centre of ZnPc is redox-inactive[268], it was thought that ligand-related redox processes may have been capable of reducing Pt(IV) species.

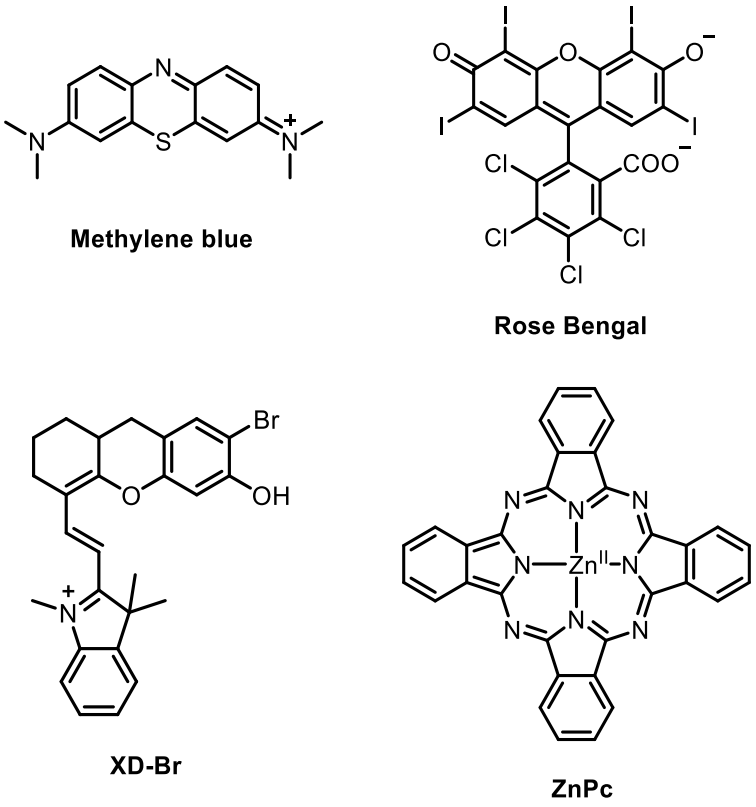

Scheme 4.13. Structures of the photosensitisers used to demonstrate that singlet oxygen and other reactive oxygen species were not responsible for the photocatalysed reduction of the Pt(IV) complexes.

The typical mechanistic pathways for reactions photocatalysed by $[Ru(bpy)_3]Cl_2$ follow either an oxidative or reductive pathway to yield the desired reactive species that then undergo reduction or oxidation reactions, respectively, to regenerate the starting species, $[Ru^{II}(bpy)_3]^{2+}$ (Scheme 4.14).

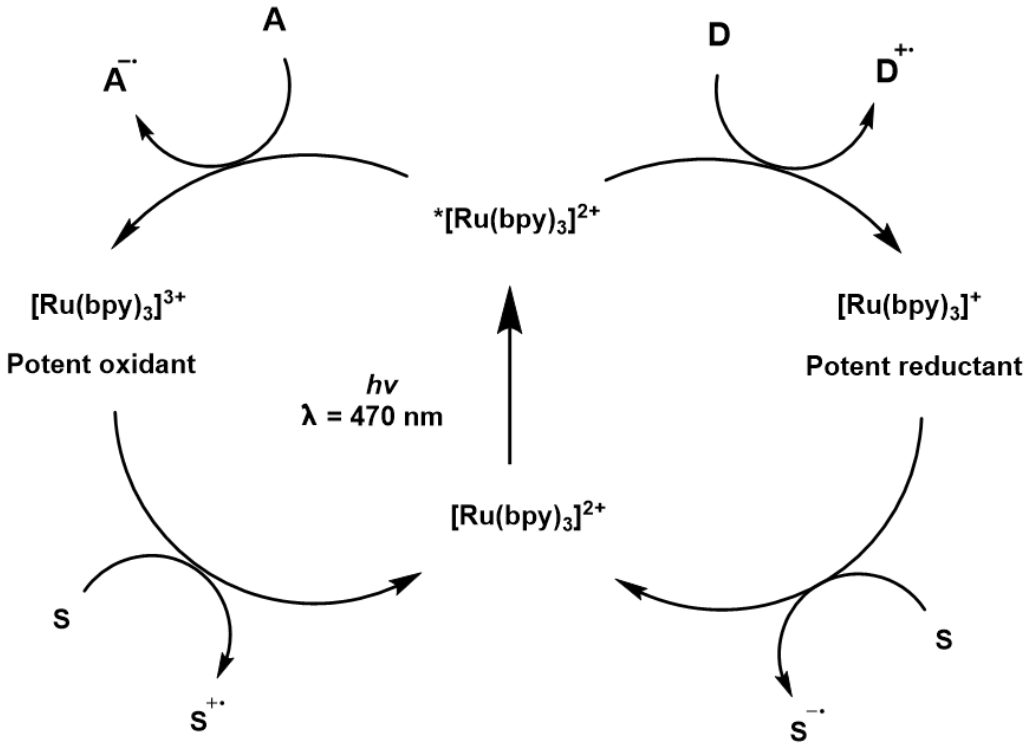

Scheme 4.14. The catalytic cycles of oxidative and reductive $[Ru(bpy)_3]^{2+}$ reactions, where A is electron acceptor, D is electron donor and S represents the substrate in each case.

In this context, it may be that the initial excited state may have high enough reductive potential to directly reduce Pt(IV), which would yield the oxidised $[Ru(bpy)_3]^{3+}$ complex in the process. To regenerate the starting catalyst and complete the catalytic cycle, reduction of this complex is required, which may involve biological reductants such as ascorbic acid. However, the catalytic nature was proven in PBS and even D_2O without such reductants present. It is possible that the carboxylate axial ligand, released during the reduction of the Pt(IV) substrate, may be capable of donating an electron to $[Ru(bpy)_3]^{3+}$. A putative mechanism representing this is described in Scheme 4.15. It is unclear whether

the mechanism of reduction of Pt(IV) substrates by one-electron reductants involves the rapid dissociation of the second axial ligand due to the instability of a Pt(III) intermediate or another equivalent of reductant takes the Pt(III) intermediate to the Pt(II) by donation of another electron[269].

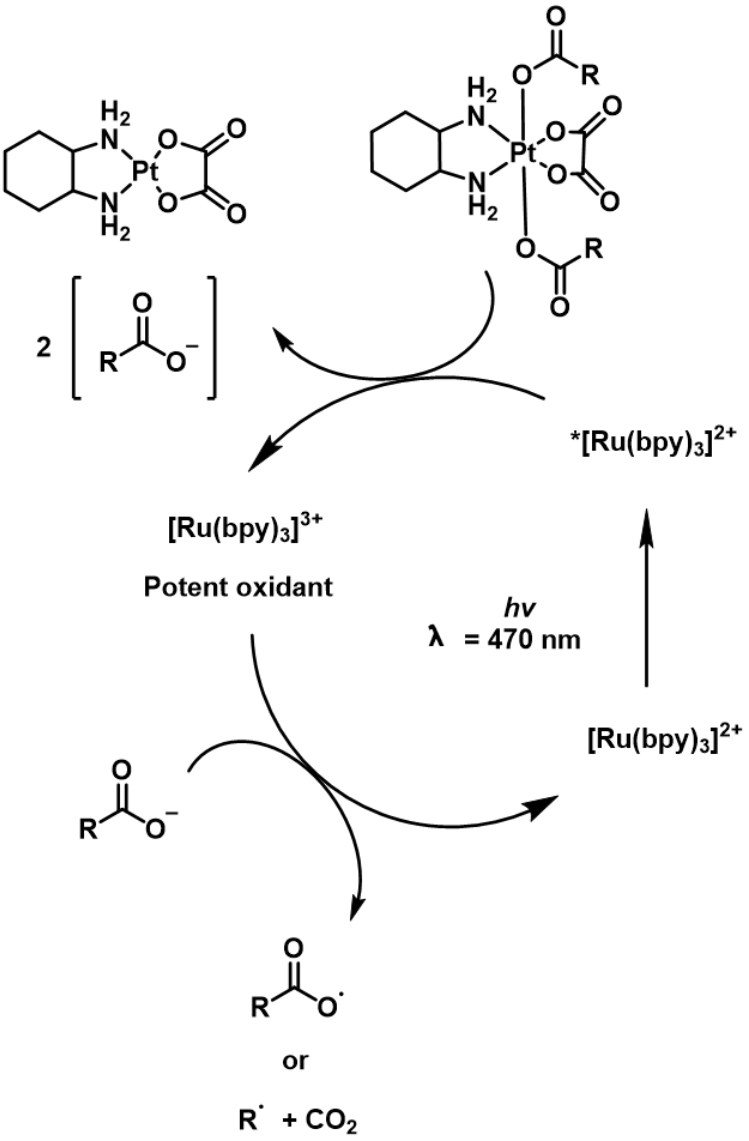

Scheme 4.15. Proposed mechanism for the photocatalytic Pt(IV) activation.

To provide evidence for the proposed mechanism, electrochemical analysis was employed. The photocatalytic mechanism was probed in acetonitrile with tetrabutylammonium hexafluorophosphate as the supporting electrolyte to facilitate analysis at the high reductive potential of the process $[Ru(bpy)_3]^{3+} \rightarrow [Ru(bpy)_3]^{2+}$ which occurs at -1.5 V. This process was analysed by CV with scans i) with photosensitiser without irradiation; ii) photosensitiser following addition of the Pt(IV) without irradiation of light; iii) photosensitiser and Pt(IV) substrate together with irradiation of light and; iv) photosensitiser and Pt(IV) substrate after 30 min incubation in the dark subsequent to irradiation (Figure 4.21).

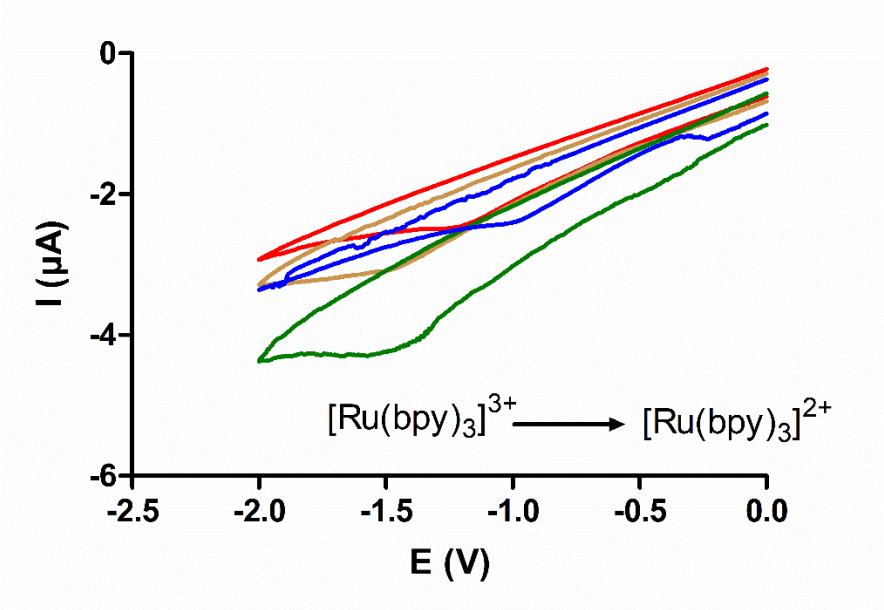

Figure 4.21. Cyclic voltammetry analysis of $[Ru(bpy)_3]^{2+}$ under difference conditions: the photosensitiser alone (red line) followed by the addition of the Pt(IV) complex **9** (brown line), then solutions were illuminated (green line) then left in the dark for 30 min (blue line).

It can be seen that during the initial scan with the photosensitiser alone (red line) and the upon addition of the Pt(IV) substrate (brown line), there was no significant changes in the process. Upon irradiation with light, there was observed an increase in total charge of the process, suggesting an increase in the concentration of the $[Ru(bpy)_3]^{3+}$ species (green line). Following 30 min of the solution in the dark, the process returned to a similar state as the initial scan (blue line). This is tentative evidence that there was $[Ru(bpy)_3]^{3+}$ formed throughout the photocatalytic reduction of Pt(IV). Further study of this reaction by spectroelectrochemical analysis and exploring the limits of Pt(IV) scope may shed light on the full mechanistic details occurring.

Conclusions and Outlook

Photodynamic therapy has emerged as a highly effective cancer therapy, however it has a number of drawbacks. Patients may suffer from photosensitivity and be required to reside in rooms in absence of any light. There are also concerns over whether PDT can completely ablate some cancers, due to the requirement of complete dispersion of the photosensitiser throughout the tumour. Photo-activated chemotherapies in conjunction with singlet oxygen generation can provide benefits of high cytotoxic effects controlled spatially by targeted light irradiation. As activation is photocatalytic, the same therapeutic effect as conventional PDT may be achieved with lower doses of photosensitiser, limiting photosensitivity side effects. This method of prodrug activation can afford a means of overcoming the off-target toxicities of conventional anti-cancer therapies, a problem that is rife in Pt-based therapies.

The facility of extension of the therapeutic application of PDT to not only generate cytotoxic singlet oxygen, but to also concomitantly activate prodrugs simultaneously was explored. The photosensitiser that formed the basis of this study, $[Ru(bpy)_3]Cl_2$, and its many derivatives constitute a highly studied area of photosensitisers and photocatalysts with many applications and purposes, many of which could be suitable for use in cells, propagating a new method of prodrug activation or *in situ* drug synthesis. Therefore, the scope and potential divergent uses for photocatalysis in cells may be of great impact on the treatment of cancer, both in increasing the efficacy of treatments, overcoming resistance and in the reduction of off-target toxicities.

The prodrug activation system detailed here can open up avenues for a whole platform of new reactions occurring in cells. There are a host of reactions photocatalysed by ruthenium polypyridyl complexes that may be useful in prodrug activation. For instance, $[Ru(bpy)_3]^{2+}$ has been reported as an efficient photocatalyst for the reduction of azides to amines in the presence of ascorbic acid. There are a number of combination therapies which consist of oxaliplatin and other anti-cancer agents such as gemcitabine and irinotecan. Simultaneous dual-prodrug activation may be able to reduce side effects of these arduous regimens by reduction of Pt(IV) prodrugs and/or azides (with a self-immolative linker or as a caged amine) with singlet oxygen generation (Scheme 4.16).

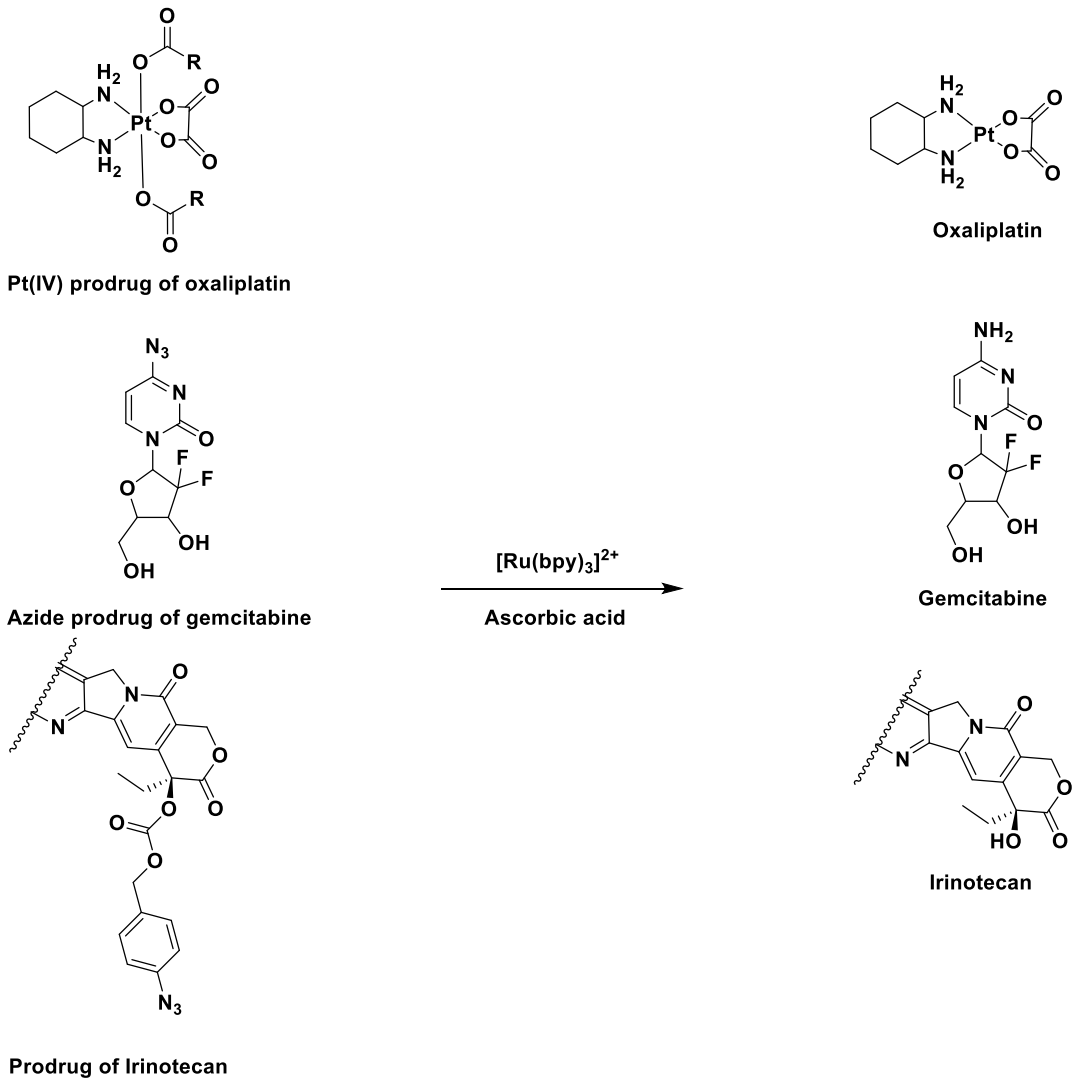

Scheme 4.16. Combination therapies of oxaliplatin that may benefit from simultaneous prodrug activation. Gemcitabine in combination with oxaliplatin is in Phase III clinical trials (GEMOX) and irinotecan is used in combination with oxaliplatin in an FDA-approved combination therapy, FOLFIRINOX.

It was shown that the addition of the positively charged and lipophilic indoline moiety benefitted uptake and localisation of the photosensitiser **16** compared to $[Ru(bpy)_3]^{2+}$ in cells. However, this could also be achieved in a more selective and targeted manner by the conjugation of peptides or antibodies. Peptide- and

antibody-drug conjugates have shown great promise in the delivery of therapeutics and could prove a useful addition to this system to promote cancer selectivity over healthy tissues or change the localisation to another organelle of therapeutic interest (e.g. the nucleus). Future work will be required for further optimisation of the system in order to overcome its drawbacks.

The narrow therapeutic window of the Pt(IV) prodrug and the Pt(II) species could be improved through extensive screening of Pt(IV) derivatives. Pt(IV) prodrugs that are designed to be inert to biological reduction will be of benefit to this application and may be accomplished through deeper exploration of the effect on both the axial and carrier ligands on the kinetics of reduction by glutathione and ascorbic acid (as well as other endogenous reductants). In addition, as the Pt(IV) prodrug and the photosensitiser are two discrete entities, pharmacokinetic considerations are complicated (such as dosing and bio-distribution). Tethering of the prodrug to the photosensitiser should be explored however this removes the catalytic aspect of the system and may elicit photosensitivity-related adverse effects. The wavelength of light (470 nm) required for this system is relatively low and will be subject to extensive scattering and, as a result, limited penetration through tissue. The wavelength required for the MLCT band of the photosensitiser may be red-shifted by replacement of a bipyridine ligand for a stronger σ-donor ligand, such as a β-diketonate ligand.

The prodrug activation platform described here represents a step forward in providing means of delivering platinum-based therapies with a view to limiting side effects.

Chapter 5

Experimental

5.1 General

Reactions involving moisture sensitive reagents were performed under a positive pressure of dry nitrogen. Evaporation of solvents was performed at reduced pressure, using a Buchi rotary evaporator. All chemicals were purchased from Sigma-Aldrich, Fisher Scientific or Fluorochem and used as received. CellTitre Glo was purchased from Promega. DNeasy Extraction Kit and the Mitochondrial DNA extraction kit were purchased from Qiagen. ^{1}H, ^{13}C, and ^{195}Pt NMR spectra were recorded on a Bruker AVA-600 (at 600, 150 and 129 MHz, respectively) at 298 K in the solvents indicated. Resonances are in parts per million (ppm). Column chromatography was performed on silica gel 60-120 mesh. Analytical TLC was carried out using commercially available silica gel F254 plates (Merck) and visualized with 254 nm light. Low Resolution Mass Spectra (LR-MS) were obtained using an Agilent LCMS 1100 ChemStation with a G1946B quadrupole mass detector. High Resolution Mass Spectra (HR-MS) were performed on a Bruker 3.0 T Apex II spectrometer. Analytical RP-HPLC was performed using an Agilent 1100 Chemstation equipped with a Kinetix XB-C18 column (particle size: 100 Å ;pore size: 5 μM; dimensions: 50×4.6 mm) eluting with a gradient of 95% water/formic acid (0.1%) and 5 % MeCN/formic acid (0.1%) to 95% MeCN/formic acid (0.1%) and 5% water/formic acid (0.1%) over 10 minutes or 15 minutes with a flow rate of 1 mL/min. Compounds were detected using an evaporative light scattering detector and a multi-wavelength detector. Semi-preparative RP-HPLC was performed on an Agilent 1100 system equipped with a Zorbax Eclipse XDB-C18 reverse-phase column (particle size: 5 Å ;pore size: 80 μM; dimensions: 250×9.4 mm) with a flow rate of 2 mL/min and eluting

with a gradient of water/formic acid (0.1%) and MeCN/formic acid (0.1%) of 5 to 95% over 15 min. ICP-OES were obtained on a Perkin Elmer Optima 5300 DV ICP-OES. ICP-MS analyses were carried out with an Agilent 7500ce with a collision cell and an integrated LC (Agilent 1200 series) system. UV/Visible measurements were performed on a BioTek HT Synergy multi-mode reader.

5.2 Electrochemical measurements

Electrochemical measurements were performed either with a conventional three-electrode electrochemical cell driven by a computer-controlled AutoLab PGstat-30 potentiostat running GPES 4.9 software or with screen-printed electrodes driven by a computer-controlled portable Dropsens μStat potentiostat. For conventional cells, 2 mm diameter polycrystalline gold or glassy carbon electrodes (IJ Cambria, UK) were used as the working electrode with a platinum wire counter electrode with potentials referenced against a Ag/AgCl reference electrode. The screen-printed electrodes utilise a platinum counter electrode and a Ag pseudo-reference electrode.

5.3 Small molecule synthesis

Cis,cis,trans-(diammine)(dichloro)(dihydroxo)platinum (**1**)

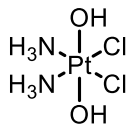

Compound **1** was synthesised according to a reported procedure[270]. Cisplatin (1.00 g, 3.4 mmol) was added to a solution of H_2O_2 (30%, 6 mL0 in deionised H_2O (50 mL) and was left to react at rt for 24 h in the absence of light. The mixture was heated to 50

°C for 5 h then concentrated under reduced pressure to ~5 mL. The concentrated mixture was then left at 4 °C during which a precipitate was formed that was collected by centrifugation and washed with cold H_2O (10 mL) then diethyl ether (10 mL). The product (yellow powder) was dried in a vacuum oven at 37 °C for 24 h. Yield: 800 mg (70.1%); purity: 98% (HPLC). ^{1}H NMR (600 MHZ, d6-DMSO) δ 7.07 (m, 3H), 5.61 (m, 3H). HRMS (+): m/z [M+H]+ calcd: 333.960 found: 333.101. IR (neat) ν_{max} 3480 cm^{-1} (br).

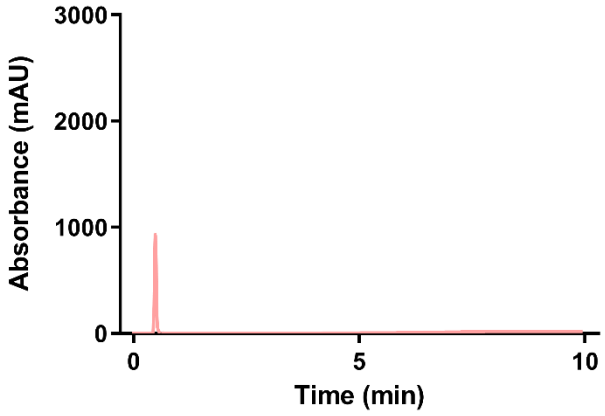

[2-(acetyloxy)benzoato](diammine)(dichloro)(hydroxo)platinum (**2**)

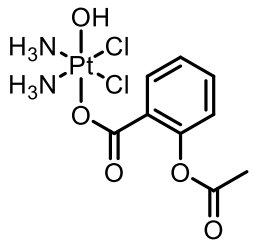

Compound **2** was synthesised according to a reported procedure[147]. Compound **1** (142 mg, 0.42 mmol) was added to DMF (60 mL) followed by acetylsalicylic anhydride (175 mg, 0.3 mmol). The reaction mixture was heated to 65 °C for 48 h (additional acetylsalicylic anhydride was added during this time: 144 mg at 12 h and 218 mg at 20

h). The solvent was removed *in vacuo* and the crude suspended in acetonitrile (1 mL). The product was precipitated by addition of diethyl ether then isolated by centrifugation followed by washing with fresh diethyl ether (x3). The product (yellow powder) was dried in a vacuum oven at 37 °C for 24 h. Yield: 31 mg (15%). ^{1}H NMR (600 MHZ, D_2O) δ 7.81 (d, 1H), 7.59 (t, 1H), 7.39 (t, 1H), 7.15 (d, 1H), 2.61 (s, 3H). ^{13}C NMR (150 MHZ, D_2O) δ 171.6, 155.1, 150.1, 130.7, 128.1, 123.3, 120.4, 119.2, 25.5. HRMS (+): m/z [M+H]+ calcd: 497.011 found: 496.961.

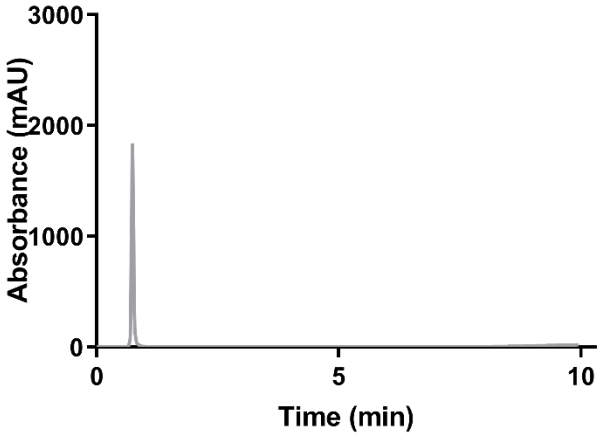

Cis, cis, trans-(diammine)(dichloro)(diacetato)platinum (**3**)

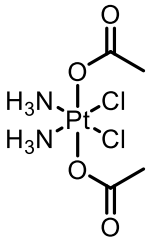

Compound **1** (100 mg, 0.3 mmol) was added to DMF (3 mL) followed by acetic anhydride (1.5 mL, 15 mmol). The reaction mixture was heated in a microwave reactor to 90 °C for 45 min. The solvent was removed *in vacuo* and the crude dissolved in the

minimum amount of methanol. The product was precipitated by addition to diethyl ether (stirring in a Falcon centrifuge tube), then isolated by centrifugation followed by washing with fresh diethyl ether (x3). The product (yellow powder) was dried in a vacuum oven at 37 °C for 24 h. Yield: 99 mg (79%). ^{1}H NMR (600 MHZ, d6-DMSO) δ 6.53 (m, 6H), 1.91 (s, 6H). ^{13}C NMR (150 MHZ, d6-DMSO) δ 167.1, 22.7. HRMS (+): m/z [M+H]+ calcd: 416.988 found: 416.901.

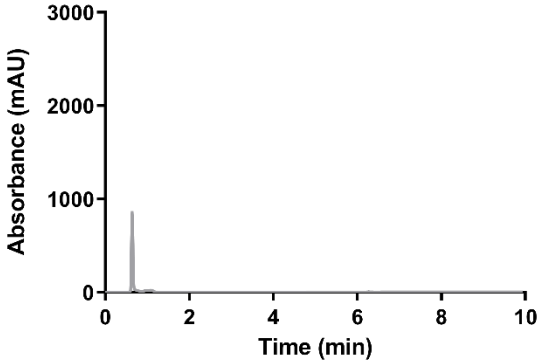

Cis,cis,trans-(diammine)(dichloro)(benzoato)(hydroxo)platinum (**4**)

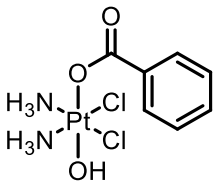

Compound **1** (100 mg, 0.3 mmol) was added to DMF (20 mL) followed by benzoic anhydride (100 mg, 0.4 mmol). The reaction mixture was left to react at rt for 24 h. The mixture was concentrated under reduced pressure and the product was precipitated by addition to acetone (stirring in a Falcon centrifuge tube), then isolated by centrifugation followed by washing with fresh acetone (x3). The product (yellow powder) was dried in a vacuum oven at 37 °C for 24 h. Yield: 118 mg (90%). ^{1}H NMR

(600 MHZ, d6-DMSO) δ 7.89 (d, 2H, J = 7.52 Hz), 7.49 (t, 1H, J = 7.30 Hz), 7.40 (t, 2H, J = 7.16 Hz). ^{13}C NMR (150 MHZ, d6-DMSO) δ 162.2, 135.3, 133.5, 129.1, 123.8. HRMS (+): m/z [M+H]+ calcd: 434.105 found: 434.918.

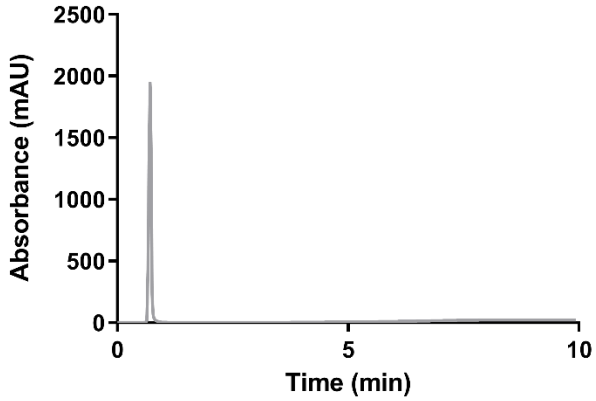

Cis, cis, trans-(diammine)(dichloro)(disuccinato)platinum (**5**)

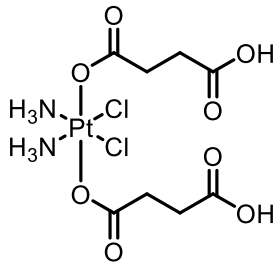

Compound **1** (50 mg, 0.15 mmol) was added to DMF (5 mL) followed by succinic anhydride (40 mg, 0.4 mmol). The reaction mixture was heated in a microwave reactor to 90 °C for 45 min. The solvent was removed *in vacuo* and the crude dissolved in the minimum amount of methanol. The product was precipitated by addition to diethyl ether (stirring in a Falcon centrifuge tube), then isolated by centrifugation followed by washing with fresh diethyl ether (x3). The product (yellow powder) was dried in a vacuum oven at 37 °C for 24 h. Yield: 24 mg (31%). ^{1}H NMR (600 MHZ, d6-DMSO) δ

12.04 (br, 2H) 6.49 (m, 6H), 2.50 (m, 4H), 2.40 (m, 4H). ^{13}C NMR (150 MHZ, d6-DMSO) δ 174.8, 165.0, 29.3, 24.4. HRMS (+): m/z $[M+H]^+$ calcd: 532.990 found: 534.109.

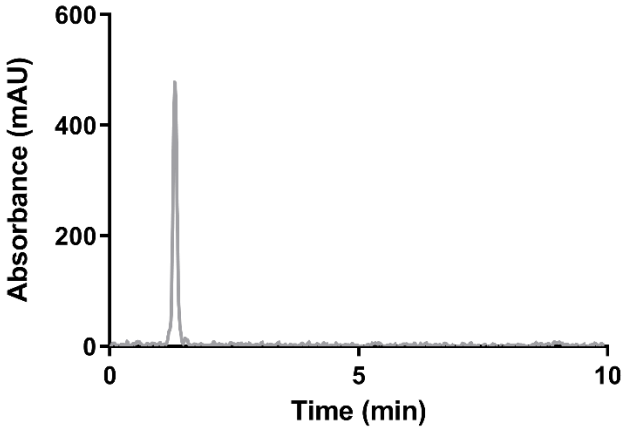

Cis, cis, trans-[(1R,2R)-1,2-cyclohexanediamine](oxalato)(dihydroxo)platinum (**$OxPt(OH)_2$**)

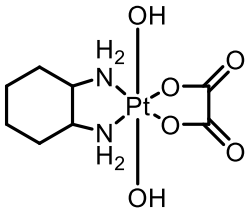

$OxPt(OH)_2$ was synthesised according to a published procedure[271]. Oxaliplatin (1 g, 2.5 mmol) was suspended in H_2O (12 mL), then H_2O_2 (30%, 3 mL) is added and the reaction stirred at rt for 24 h. The reaction mixture was then heated to 50 °C for 3 h. The reaction mixture was cooled to rt, filtered and the solid washed with water. The product (white powder) was dried in a vacuum oven at 37 °C for 24 h. Yield: 864 mg (80%). ^{1}H NMR (600 MHZ, D_2O) δ 2.75-2.85 (m, 2H), 2.17-2.26 (m, 2H), 1.46-1.64 (m, 2×2H), 1.13-1.26 (m, 2H). ^{13}C NMR (150 MHZ, D_2O) δ 182.04, 166.21, 36.91, 34.51, 30.77, 23.43, 22.70, 21.95. HRMS (+): m/z $[M+H]^+$ calcd: 431.331 found: 432.200.

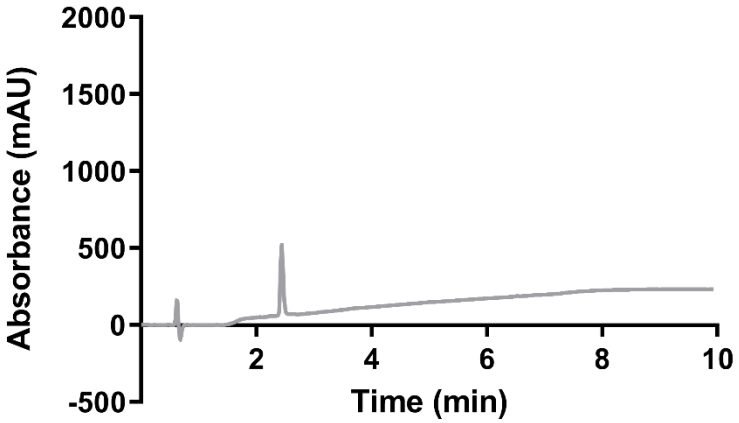

Cis, cis, trans-[(1R,2R)-1,2-cyclohexanediamine](oxalato)(acetato)(hydroxo)platinum (**OxPt(OH)(Ac)**)

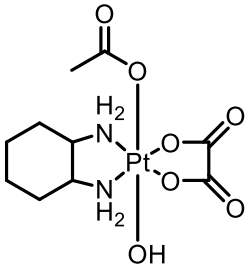

OxPt(OH)(Ac) was synthesised according to a published procedure[272]. To a 1:1 mixture of AcOH:H_2O (10 mL), was added oxaliplatin (200 mg) followed by H_2O_2 (30%, 1 mL) and the reaction mixture stirred at rt for 48 h. Following completion of the reaction, the solvents were removed *in vacuo* and the crude dissolved in the minimum amount of methanol. The product was then precipitated by addition to a Falcon tube of rapidly stirring diethyl ether and isolated by centrifugation. The product (white powder) was dried in a vacuum over at 37 °C for 24 h. Yield: 166 mg (69%). ^{1}H NMR (600 MHZ, D_2O) δ 2.86 (m, 2H), 2.28 (m, 2H), 2.05 (s, 3H), 1.63 (m, 2H), 1.56 (m, 2H), 1.24 (m, 2H) . ^{13}C NMR (150 MHZ, D_2O) δ 182.04, 166.21, 36.91, 34.51, 30.77, 23.43, 22.70, 21.95.. HRMS (+): m/z $[M+H]^+$ calcd: 473.080 found: 473.431.

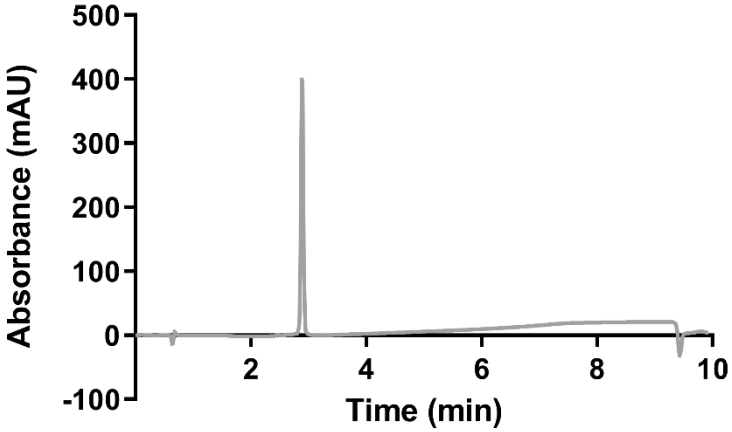

Cis, cis, trans-[(1R,2R)-1,2-cyclohexanediamine](oxalato)(disuccinato)platinum (**6**)

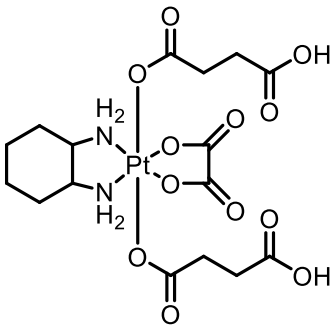

OxPt(OH)$_2$ (100 mg, 0.23 mmol) was suspended in DMF (5 mL) in a microwave vial, to which succinic anhydride (115 mg, 1.15 mmol) was added. The mixture was heated to 90 °C with microwave heating for 45 min. Following completion of the reaction, the solvent was removed in vacuo and the residue re-dissolved in methanol and the solution filtered. The filtrate was then added dropwise to a Falcon tube of rapidly stirred diethyl ether (20 mL). The white-coloured precipitate was isolated via centrifugation and dried in a vacuum oven at 40 °C for 12 h to afford compound 1. Yield: 102 mg (70%). ^{1}H NMR (600 MHZ, D2O) δ 1.20 (m, 2H), 1.46-1.63 (m, 2 × 2H),

2.23 (m, 2H), 2.46 (m, 4H), 2.57 (m, 4H), 2.82 (m, 2H). ^{1}H NMR (600 MHZ, DMSO-d6) δ 1.16 (m, 2H), 1.39 (m, 2H), 1.50 (m, 2H), 2.11 (m, 2H), 2.40 (m, 4H), 2.52 (m, 4H, overlapping with DMSO solvent peak), 2.59 (m, 2H), 8.15 (s, 2H), 8.36 (s, 2H) 12.10 (br, 2H). ^{13}C NMR (150 MHz, DMSO-d6) δ 24.0, 30.1, 31.0, 31.4, 61.3, 163.8, 174.1, 180.1. ^{195}Pt NMR (108 MHz, DMSO-d6) δ 1617. HRMS (+): m/z [M+H]+ calcd: 632.110 found: 632.105, [M+Na+] calcd: 654.087 found: 654.087.

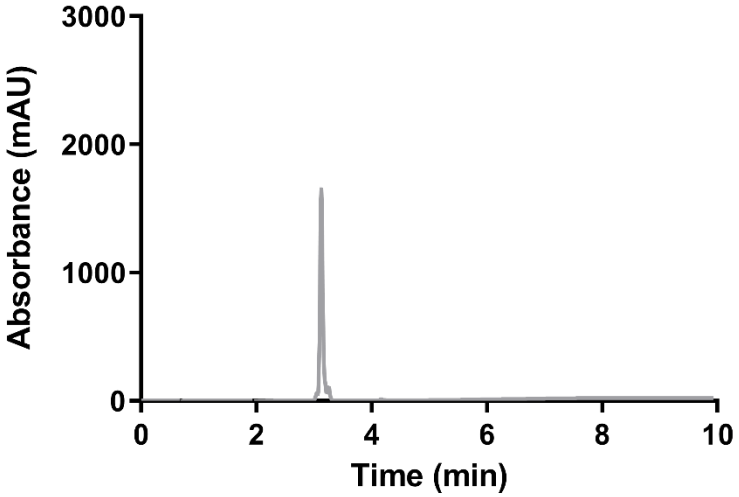

(Chloro)pentaammine ruthenium(III) trichloride

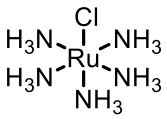

(Chloro)pentaammine ruthenium(III) chloride was synthesised according to a published procedure[273]. Ruthenium (III) hexaammine trichloride (500 mg, 1.6 mmol) was refluxed in 6 N HCl for 8 h. The reaction mixture was allowed to cool then filtered with washing of cold ethanol. The product (yellow powder) was dried in a

vacuum oven at 37 °C for 24 h. Yield: 200 mg (56%). HRMS (+): m/z $[M+H]^+$ calcd: 221.155 found: 221.161. IR (neat) ν_{max} 3260, 2160, 1623 cm^{-1} (br).

(4-vinylpyridine)pentaammineruthenium(III) hexafluorophosphate (**Vp-Ru**)

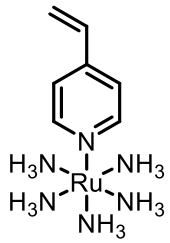

(Chloro)pentaammine ruthenium (200 mg, 0.9 mmol) was dissolved in H_2O (10 mL), followed by $AgNO_3$ (608 mg, 3.6 mmol) and stirred for 30 min at rt. The solution was filtered, to remove the AgCl by-product, and to the filtrate was added 4-vinylpyridine (410 μL, 3.6 mmol). The reaction mixture was stirred for 24 h at rt, following which, saturated aqueous KPF_6 was added dropwise to induce precipitation of the product (red-brown powder) and dried in a vacuum oven at 37 °C for 24 h. Yield: 21 mg (8%). ^{1}H NMR (600 MHZ, DMSO-d6) δ 8.57 (dd, 2H, J = 1.62, 4.58 Hz), 7.47 (dd, 2H, J = 1.62, 4.57 Hz), 4.25 (s, 2H). ^{13}C NMR (150 MHz, DMSO-d6) δ 152.6, 139.4, 134.4, 130.8, 114.0. HRMS (+): m/z $[M+H]^+$ calcd: 292.560 found: 292.998.

Cis,cis,trans-[(1R,2R)-1,2-cyclohexanediamine](oxalato)
(acetato)(trifluoroacetato)platinum (**8**)

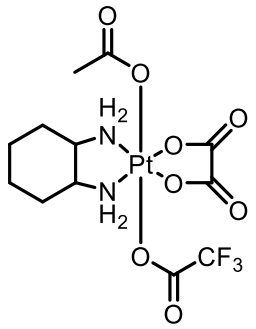

OxPt(Ac)(OH) (100 mg, 0.21 mmol) was suspended in DMF (2 mL) in a microwave tube to which trifluoroacetic anhydride (70 µL, 0.506 mmol) were added. Reaction was carried out under microwave heating at 80 °C for 45 min. Following completion of reaction the solvent was removed under reduced pressure and the residue re-dissolved in the minimum amount of methanol. Precipitation of the compound was accomplished by adding dropwise to rapidly stirred diethyl ether and the compound was isolated by centrifugation. The product (yellow powder) was dried in a vacuum over at 37 °C for 24 h. Yield: 21 mg (8%). ^{1}H NMR (600 MHz, d7-DMF) δ 8.90-9.14 (br, 2×2H), 2.90 (m, 2H), 2.56 (m, 2H), 2.22 (s, 3H), 1.58-1.84 (m, 2×2H), 1.45 (m, 2H). 13C NMR (150 MHz, d7-DMF) δ 161.1, 159.2, 157.6, 152.7, 119.6, 117.2, 115.0, 112.9, 62.1, 30.7, 23.6, 21.9. HRMS (+): m/z $[M+H]^{+}$ calcd: 570.110 found: 570.116.

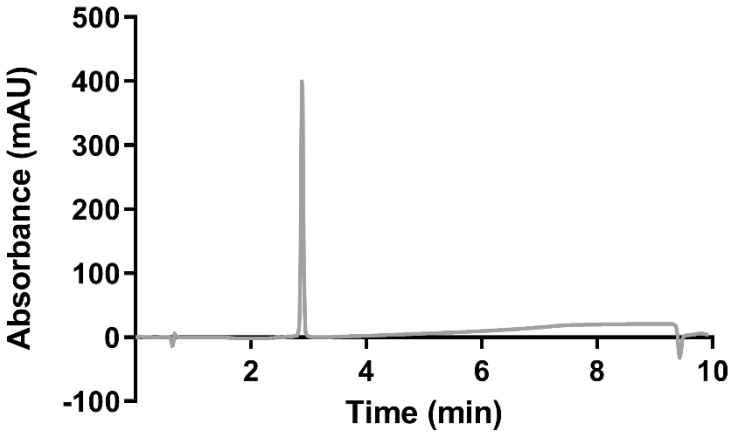

Cis,cis,trans-[(1R,2R)-1,2-cyclohexanediamine](oxalato)(acetato)(tert-butanato)platinum (**9**)

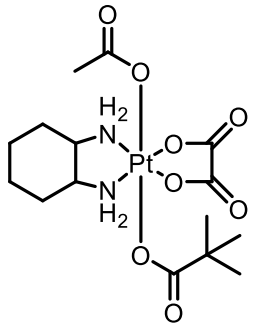

OxPt(Ac)(OH) (100 mg, 0.21 mmol) was suspended in DMF (2 mL) in a microwave tube to which trimethylacetic anhydride (103 µL, 0.5 mmol) were added. Reaction was carried out under microwave heating at 80 °C for 45 min. Following completion of reaction the solvent was removed under reduced pressure and the residue was dissolved in DCM and bound to SiO_2. Product was purified by column chromatography (SiO_2) with eluting ethyl acetate:methanol (100:0 – 90:10). The product (white powder) was dried in a vacuum over at 37 °C for 24 h. Yield: 102 mg (87%). ^{1}H NMR (500 MHz, d7-DMF) δ 1.23 (s, 9H), 1.47 (m, 2H), 1.69-1.85 (m, 2×2H), 2.12 (s, 3H), 2.53 (m, 2H), 2.94 (m, 1H), 3.11 (m, 1H), 3.267 (s, 1H), 8.60-9.24 (br m, 2×2H). ^{13}C NMR (151 MHz, d7-DMF) δ 22.5, 24.1, 27.5, 31.7, 31.8, 40.5, 55.0, 61.7, 62.5, 162.3, 179.7, 187.5. HRMS (+, ESI) m/z [M+H]+ calcd: 558.1411 found: 558.1404, [M+Na+] calcd: 580.123 found: 580.122.

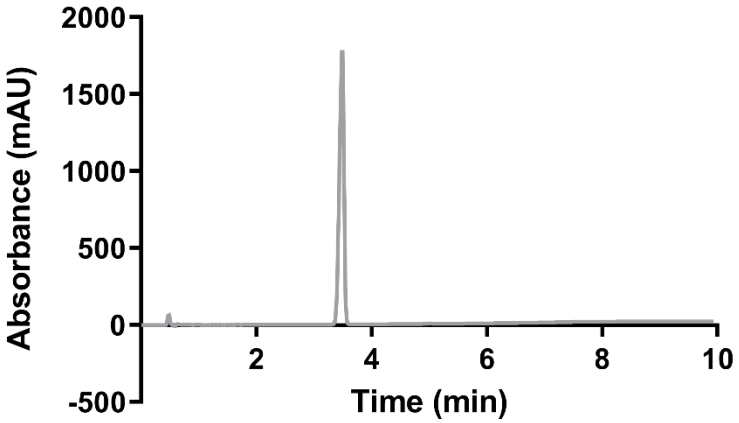

Cis,cis,trans-[(1R,2R)-1,2-cyclohexanediamine](oxalato)(acetato)(benzoato)platinum (**10**)

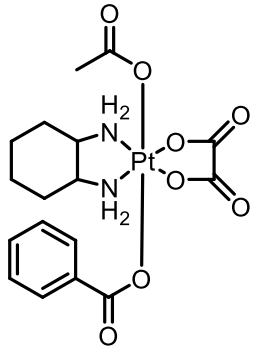

OxPt(Ac)(OH) (100 mg, 0.21 mmol) was suspended in DMF (2 mL) in a microwave tube to which benzoic anhydride (104 mg, 0.46 mmol) were added. Reaction was carried out under microwave heating at 80 °C for 45 min. Following reaction the solvent was removed under reduced pressure and the residue re-dissolved in methanol. Precipitation of compound was accomplished by adding dropwise to rapidly stirred diethyl ether and the compound was isolated by centrifugation. The product (white powder) was dried in a vacuum over at 37 °C for 24 h. Yield: 84 mg (69%). 1H

NMR (500 MHz, d7-DMF) δ 1.27-1.45 (m, 2×2H), 1.67 (m, 2H), 2.02 (m, 2H), 2.26 (s, 3H), 7.48 (t, 2H, J = 54 Hz), 7.65 (m, 1H), 7.95 (m, 2H). 13C NMR (151 MHz, d7-DMF) δ 22.2, 23.4, 30.7, 61.5, 166.6, 181.4 ESI-LCMS m/z [M+H]+ calcd: 577.09 found: 577.31.

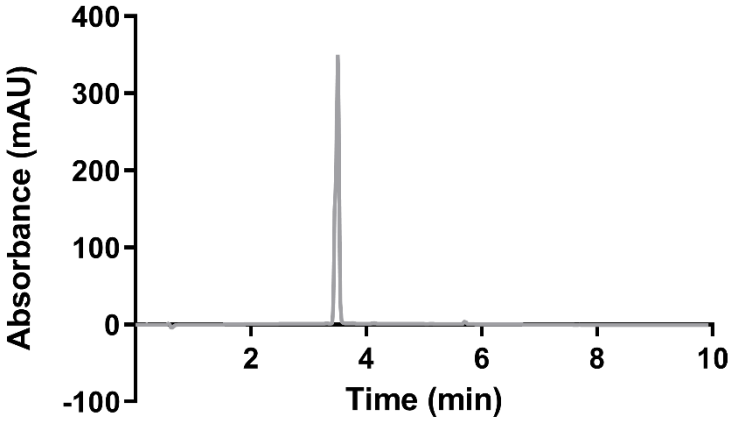

Cis,cis,trans-[(1R,2R)-1,2-cyclohexanediamine](oxalato)(ditrifluoroacetato)platinum (**11**)

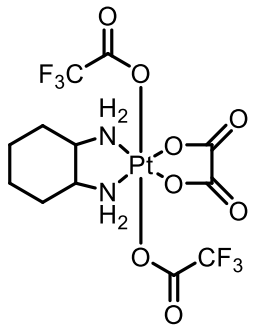

$OxPt(OH)_2$ (100 mg, 0.23 mmol) was suspended in DMF (2 mL) in a microwave tube to which trifluoroacetic anhydride (70 µL, 0.5 mmol) was added. Reaction was carried out under microwave heating at 80 °C for 45 min. Following completion of reaction the solvent was removed under reduced pressure and the residue re-dissolved in methanol. Precipitation of the compound was accomplished by adding dropwise to

rapidly stirred diethyl ether at and the compound isolated by centrifugation. The product (yellow powder) was dried in a vacuum over at 37 °C for 24 h. Yield: 44 mg (30%). 1H NMR (500 MHz, d6-DMSO) δ 1.22-1.38 (m, 2×2H), 1.65 (m, 2H), 2.21 (m, 2H), 2.78 (m, 2H). 13C NMR (151 MHz, d6-DMSO) δ 22.2, 23.4, 30.7, 61.5, 166.6, 181.4 ESI-LCMS m/z [M+H]+ calcd: 623.01 found: 623.95.

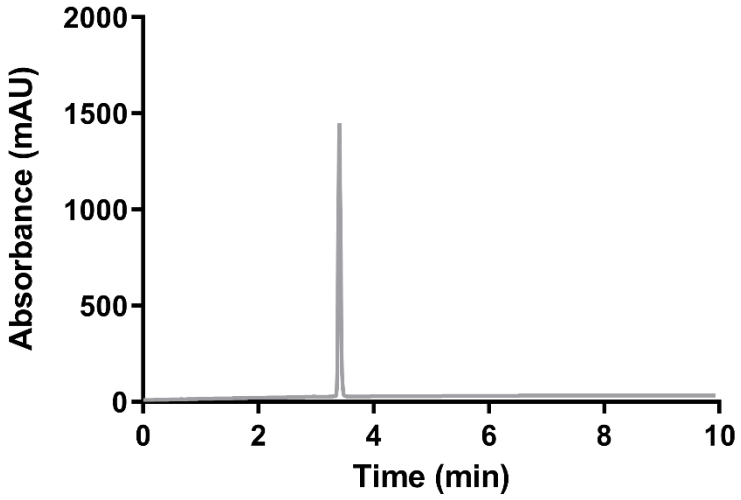

Cis,cis,trans-[(1R,2R)-1,2-cyclohexanediamine](oxalato)(ditrifluoroacetato)platinum (**12**)

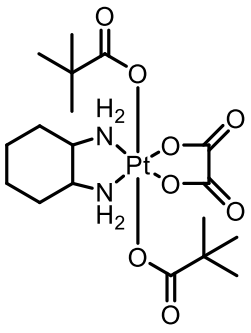

$OxPt(OH)_2$ (100 mg, 0.23 mmol) was suspended in DMF (2 mL) in a microwave tube to which trimethylacetic anhydride (103 μL, 0.5 mmol) was added. Reaction was carried

out under microwave heating at 80 °C for 45 min. Following completion of reaction the solvent was removed under reduced pressure and the residue re-dissolved in DCM and bound to silica gel (SiO_2). Purification of the compound was accomplished by column chromatography with eluting ethyl acetate:methanol (85:15). The product (white powder) was dried in a vacuum over at 37 °C for 24 h. Yield: 55 mg (43%). 1H NMR (500 MHz, d6-DMSO) δ 1.17 (s, 18H), 1.24-1.38 (m, 2×2H), 1.66 (m, 2H), 2.20 (m, 2H), 2.79 (m, 2H). 13C NMR (151 MHz, d6-DMSO) δ 22.2, 23.4, 30.7, 61.5, 166.6, 181.4 ESI-LCMS m/z [M+H]+ calcd: 599.16 found: 599.91.

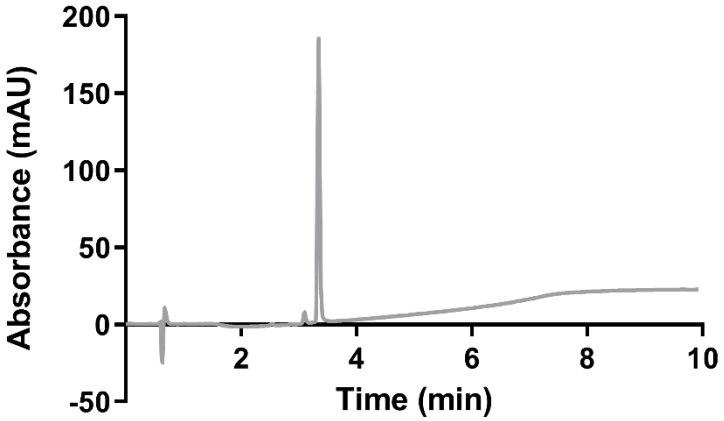

4'-methyl-2,2'-bipyridine-4-carboxaldehyde (**L-1**)

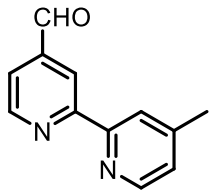

L-1 was synthesised according to a published procedure[274]. 4,4'-dimethyl-2,2'-bipyridine (1 g, 5.4 mmol) and selenium dioxide (0.7 g, 6.36 mmol) were dissolved in degassed, anhydrous 1,4-dioxane (50 mL) under N_2 atmosphere. The reaction mixture

was heated to 105 °C for 24 h. Following completion of the reaction, the mixture was filtered hot. The filtrate was concentrated, re-dissolved in ethyl acetate and filtered to remove seleniumby-products. To purify the product, the filtrate was extracted with Na_2CO_3 (1M, 2×100 mL). The organic fraction is then shaken with with $Na_2S_2O_3$ (0.3 M, 3 × 100 mL) for 5 min at rt, during which the product is converted to the corresponding bisulfite and enters the aqueous layer. The aqueous layer was extracted and adjusted to pH 10 with Na_2CO_3 (2 M) and shaken for a further 5 min at rt, to re-form the aldehyde. This was then was extracted with CH_2Cl_2 (4 × 100 mL). The solvent was removed from organic layers and and the product (white powder) was dried in a vacuum oven at 37 °C for 24 h. Yield: 672 mg (62%). 1H NMR (500 MHz, d6-DMSO) δ 10.21 (s, 1H), 8.92 (d, 1H, J = 4.91 Hz), 8.86 (dd, 1H, J = 0.91, 1.57 Hz), 8.60 (d, 1H, J = 4.90 Hz), 8.31 (m, 1H), 7.75 (dd, 1H, J = 1.55, 4.90 Hz), 7.22 (ddd, 1H, J = 0.86, 1.74, 5.00 Hz), 2.49 (s, 3H) . 13C NMR (151 MHz, d6-DMSO) δ 191.76, 158.34, 154.75, 150.30, 149.21, 142.67, 125.39, 122.10, 121.39, 120.58, 21.23. HRMS (+, ESI) m/z [M+H]+ calcd: 198.16 found: 198.61.

bis(2,2'-bipyridine)(4'-methyl[2,2'-bipyridine]-4-carboxaldehyde)ruthenium(II) hexafluorophosphate ($[Ru(bpy)_2(bpy\text{-}CHO)(PF_6)_2]$, **L-2**)

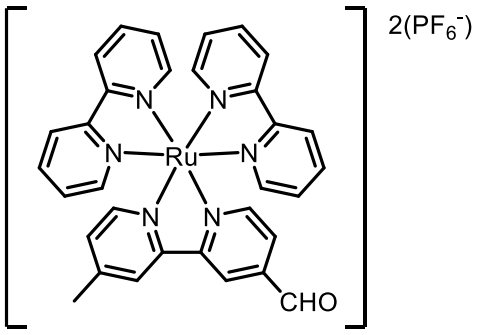

L-1 (49 mg, 0.24 mmol) and $Ru(bpy)_2Cl_2$ (100 mg, 0.21 mmol) were dissolved in degassed ethanol/water solution (4:1) in a total volume of 15 mL. The reaction was heated in a microwave reactor to 80 °C for 15 min. Upon completion, KNO_3 (50 mg, 0.5 mmol) was added and the reaction mixture stirred at rt for 30 min. Solvents were removed *in vacuo* and the crude re-dissolved in ethanol, which was then filtered. The product was purified from the filtrate by column chromatography (SiO_2) with eluting acetonitrile and H_2O (with 0.1% KNO_3) with product eluting at 90% acetonitrile. Fractions were combined, dried under reduced pressure then re-dissolved in ethanol. The solution was filtered and the filtrate concentrated. The concentrated filtrate was added dropwise to a rapidly stirring Falcon tube of aqueous saturated KPF_6. The precipitate was isolated by centrifugation and dried in a vacuum oven for 24 h at 37 °C. Yield: 74 mg (39%). ^{1}H NMR (500 MHz, D_2O) δ 10.07 (s, 1H), 8.86 (m, 1H), 8.36 (m, 1H), 8.07 (d, 1H, J = 5.81 Hz), 7.94-8.03 (m, 12H), 7.68 (dd, 1H, J = 5.8, 1.7 Hz), 7.60 (d, 1H, J = 5.8 Hz), 7.56 (d, 2H, J = 5.7 Hz), 7.40 (dd, 2H, J = 6.1, 1.8 Hz), 2.48 (s, 3H). ^{13}C NMR (150 MHz, D_2O) δ 192.76, 159.18, 156.96, 156.62, 156.17, 155.67, 153.05, 151.61, 151.43, 151.32, 151.25, 151.19, 150.69, 150.47, 150.39, 140.99, 137.90, 137.79, 137.46, 128.65, 128.24, 127.28, 127.12, 125.49, 124.97, 124.83, 124.10, 123.93, 122.26, 120.78, 88.26, 20.43. HRMS (+, ESI) *m/z* $[M\text{-}2PF_6]^{2+}$ calcd: 306.12 found: 306.44. MALDI-TOF (CHCA matrix): $[M\text{-}PF_6]^+$ 612.40.

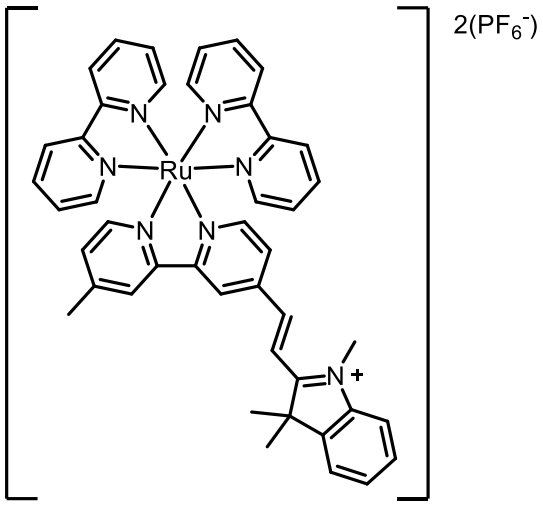

A solution of **L-2** (250 mg, 0.31 mmol) and 1,3,3-trimethyl-2-methyleneindoline (120 µL, 0.68 mmol) was made in ethanol/water mixture (9:1) and reacted with microwave heating to 80 °C for 30 min. KNO_3 (50 mg, 0.5 mmol) was added and the reaction mixture stirred at rt for 30 min. Solvents were removed *in vacuo* and the crude re-dissolved in ethanol, which was then filtered. The product was purified from the filtrate by column chromatography (SiO_2) with eluting acetonitrile and H_2O (with 0.1% KNO_3) with product eluting at 90% acetonitrile. Fractions were combined, dried under reduced pressure then re-dissolved in ethanol. The solution was filtered and the filtrate concentrated. The concentrated filtrate was added dropwise to a rapidly stirring Falcon tube of aqueous saturated KPF_6. The precipitate was isolated by centrifugation and dried in a vacuum oven for 24 h at 37 °C. Yield: 82 mg (25%). ^{1}H NMR (500 MHz, d3-acetonitrile) δ 8.85 (dd, 1H, J = 1.7, 0.8 Hz), 8.49-8.57 (m, 5H), 8.01-8.14 (m, 5H), 7.70-7.79 (m, 7H), 7.64-7.68 (m, 2H), 7.59 (d, 1H, J = 5.8 Hz), 7.38-7.46 (m, 4H), 7.32 (ddd, 1H, J = 5.9, 1.8, 0.7 Hz), 3.93 (s, 3H), 2.69 (s, 3H), 1.55 (s, 6H). ^{13}C NMR (150 MHz, d3-acetonitrile) δ 164.8, 159.5, 158.6, 157.1, 156.3, 154.5, 153.9, 153.0, 152.2, 149.6, 149.3, 149.1, 148.2, 147.4, 147.9, 146.7, 145.3, 144.1, 141.4, 132.0, 131.7, 130.0, 129.9, 126.6,

126.3, 125.8, 125.2, 123.0, 123.6, 120.1, 115.6, 38.3, 37.2, 28.7, 21.7. HRMS (+, ESI) *m/z* $[M+H]^+$ calcd: 384.01 found: 384.71.

4-(Bromomethyl)-4'-methyl-2,2'-bipyridine (**L-3**)

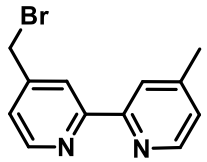

L-3 was synthesised according to a published procedure[259]. 4,4'-dimethyl-2,2'-bipyridine (2 g, 10.8 mmol) and *N*-bromosuccinimide (2g, 11.2 mmol) were dissolved in $CHCl_3$ (70 mL) under nitrogen atmosphere. Azobisisobutyronitrile (AIBN, 64 mg, 0.39 mmol) is added and the reaction mixture is heated to reflux (65 °C) for 18 h. The reaction mixture was allowed to cool and was washed with H_2O. The solvent was removed from the organic layers under reduced pressure and re-dissolved in CH_2Cl_2 and bound to SiO_2. The product was purified by column chromatography (CH_2Cl_2:Acetone, 98:2) and dried in a vacuum oven for 24 h at 37 °C. Yield: 82 mg (25%). ^{1}H NMR (500 MHz, d6-acetone) δ 8.66 (d, 1H, J= 4.95 Hz), 8.54 (d, 1H, J = 4.9 Hz), 8.31 (m, 2H), 7.49 (dd, 1H, J = 1.8, 4.9 Hz), 7.27 (dd, 1H, J = 1.7, 4.9 Hz), 4.72 (s, 2H), 2.7 (s, 3H). ^{13}C NMR (150 MHz, d6-acetone) δ 154.2, 152.1, 148.2, 146.1, 145.1, 141.4, 121.4, 121.4, 120.2, 119.8, 33.5, 20.0. HRMS (+, ESI) *m/z* $[M+H]^+$ calcd: 263.11 found: 263.50.

4-(diethylphosphonomethyl)-4'-methyl-2,2'-bipyridine (**L-4**)

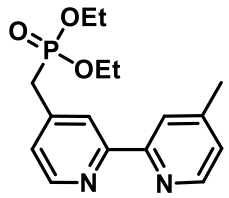

L-4 was synthesised according to a published procedure[275]. A few drops of chloroform were added to a solution of 4-(bromomethyl)-4'-methyl-2,2'-bipyridine (1 g, 3.8 mmol), triethylphosphite (2 mL, 29 mmol) which was then heated to 110 °C for 3 h. The solution was cooled to room temperature, and triethylphosphite was removed *in vacuo*. The crude was purified by column chromatography (eluting acetone). The product (white powder) was dried in a vacuum oven for 24 h at 37 °C. Yield: 1033 mg (85%). ^{1}H NMR (500 MHz, d6-acetone) δ 8.59 (d, 1H, J = 5.0 Hz), 8.53 (d, 1H, J = 5.0 Hz), 8.47 (s, 1H), 8.33 (s, 1H), 7.25 (d, 1H, J = 4.2 Hz), 4.06 (q, 4H, J = 8.4, 7.1 Hz), 3.35 (d, 2H, J = 22.2 Hz), 2.46 (s, 3H), 1.25 (t, 6H, J = 7.0, 7.0 Hz). ^{13}C NMR (150 MHz, d6-acetone) δ 158.9, 156.1, 149.4, 147.8, 147.2, 142.3, 141.5, 124.2, 122, 121.3, 62.1, 61.3,33.7, 32.3, 20.5, 15.4, 14.3. HRMS (+, ESI) *m/z* $[M+H]^+$ calcd: 321.13 found: 321.16.

2-[2-(4-boronophenyl)ethenyl]-1,3,3-trimethylindolium nitrate **(L-5)**

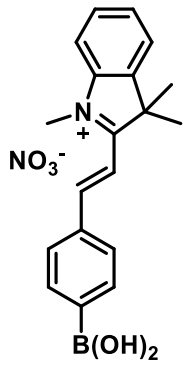

4-Formylphenylboronic acid (1 g, 6.71 mmol) was dissolved in EtOH/H2O (20 mL, 1:1) and 1,3,3-trimethyl-2-methyleneindoline (1.42 mL, 8.05 mmol) was added and the mixture was heated to reflux for 15 minutes. Solvent was removed under reduced pressure and the crude mixture separated between DCM (50 mL) and aqueous citric acid solution (5%, 100 mL). The organic layer was removed and the aqueous layer washed twice with DCM (50 mL). Small quantities of acetone were added to break up the emulsion. The aqueous layer was dried under vacuum and the crude purified by column chromatography (SiO2 normal phase silica, ACN/H2O + 0.5% KNO3). Solvent from fractions was removed under reduced pressure and re-dissolved in ethanol then filtered to remove excess KNO3 to afford a bright yellow solid Yield: 1.4 g (58%). 1H NMR (500 MHz, DMSO-d6) δ 1.80 (s, 6H), 4.19 (s, 3H), 7.65 (m, 2H), 7.75 (d, 1H, J = 16Hz), 7.89 (m, 1H), 7.93 (m, 1H), 7.97 (d, 2H, J = 8 Hz), 8.16 (d, 2H, J = 8 Hz), 8.33 (s, 2H), 8.42 (d, 1H, J = 16 Hz). 13C NMR (500 MHz, DMSO-d6) δ 25.7, 35.1, 52.8, 114.1, 115.8, 123.3, 129.4, 129.6, 130.0, 135.1, 136.2, 142.3, 182.4. HRMS (+, ESI) m/z [M+H]+ calcd: 306.166 found: 306.166.

4-2''-[2''-(4''-boronophenyl)ethenyl]-trimethylindolium-2,2'-bipyridyl nitrate (**L-6**)

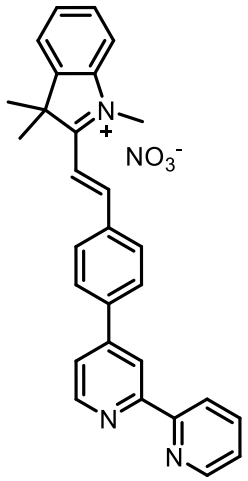

L-5 (719 mg, 1.95 mmol), 4-bromo-2,2-bipyridine (500 mg, 2.14 mmol) and Pd(PPh3)4 (25 mg, 1 mol%) were combined in degassed acetonitrile (8 mL). Cs2CO3 (591 mg, 4.28 mmol) was dissolved in H2O (2 mL) and added to the reaction mixture. The reaction mixture was then heated to 110 °C with microwave heating for 45 minutes. Following completion of the reaction the reaction mixture was filtered. LiCl (212 mg, 5 mmol) was added to the filtrate and the solvent removed from the filtrate under vacuum. The product was purified by column chromatography (SiO2, normal phase silica, ACN/H2O + 0.5% KNO3). Solvent from fractions was removed under reduced pressure and re-dissolved in ethanol then filtered to remove excess KNO3 to afford a bright yellow powder. Yield: 701 mg (69%). 1H NMR (500 MHz, CD2Cl2) δ 1.88 (s, 6H), 4.37 (s, 3H), 7.40 (ddd, 1H, J = 1, 5, 7 Hz), 7.63-7.67 (m, 4H), 7.71 (m, 1H), 7.88-7.92 (m, 2H), 7.99 (d, 2H, J = 8 Hz), 8.21 (d, 2H, J = 8 Hz), 8.31 (d, 1H, J = 16 Hz), 8.52 (d, 1H, J = 8 Hz), 8.74 (ddd, 1H, J = 1, 2, 5 Hz), 8.79 (m, 2H). 13C NMR (151 MHz, CD2Cl2) δ 156.85, 155.68, 153.70, 149.92, 147.32, 143.29, 143.16, 141.50, 136.97, 134.71, 134.51, 131.24, 129.65, 128.17, 124.02, 122.67, 121.42, 121.06, 118.58, 114.90, 113.31, 34.91, 26.25. HRMS (+, ESI) m/z [M+H]+ calcd: 416.212 found: 416.213.

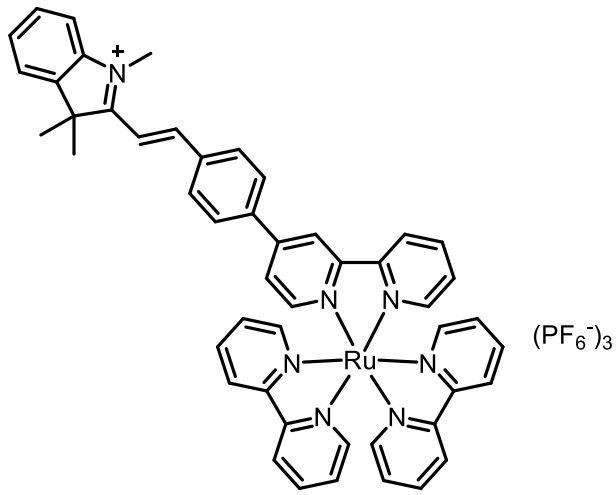

L-6 (147 mg, 0.31 mmol) and Ru(bpy)2Cl2 (163 mg, 0.34 mmol) were dissolved in EtOH/H2O (9:1, 10 mL) and reacted at 80 °C with microwave heating for 30 min. The reaction mixture was filtered, LiCl (30 mg, 0.5 mmol) was added to the filtrate and the solvents were removed under vacuum. Column purification (C18, H2O+0.5%KNO3/ACN) was used to purify the product. Solvent was removed from the fractions containing PS-1 and re-dissolved in a minimal amount of acetone and added dropwise to a Falcon tube of saturated KPF6 to precipitate the product, which was isolated by centrifugation. The precipitate was washed with 1 × sat. KPF6, 3 × ice-cold H2O then 3 × ice-cold EtOH before drying in a vacuum oven at 40 °C for 24 hours to afford a dark red solid. Yield 62 mg (16%). 1H NMR (500 MHz, Acetone-d6) δ 1.96 (s, 6H), 4.40 (s, 3H), 7.60 (m, 7H), 7.72 (m, 2H), 7.92 (m, 1H), 7.97-8.02 (m, 3H), 8.09 (m, 7H), 8.22 (m, 6H), 8.36 (d, 2H, J = 8 Hz), 8.66 (d, 1H, J = 16 Hz), 8.83 (m, 2H), 9.08 (d, 1H, J = 8 Hz), 9.20 (m, 1H), 13C NMR (151 MHz, Acetone-d6) δ 205.32, 157.98, 157.23, 152.12, 151.73, 147.78, 143.98, 142.18, 139.75, 138.12, 136.26, 131.07, 130.11, 129.36, 128.22, 128.02, 127.95, 127.89, 125.04, 124.91, 124.44, 122.89, 121.78, 115.33, 114.34, 52.99, 34.50, 28.94. HRMS (+, ESI) m/z [M+H]+ calcd: 415.07 found: 415.61. MALDI-TOF m/z [M+H]+ calcd: 831.250 found: 831.056.

2-[2,2':5',2''-terthiophen]-5-yl-Imidazophenanthroline (**L-7**)

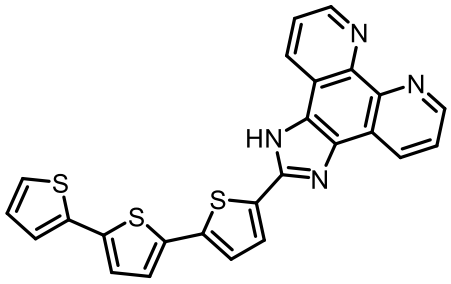

L-7 was synthesised according to a published procedure[276]. 10-Phenanthroline-5,6-dione (166.6 mg, 0.8 mmol), ammonium acetate (616 mg, 8 mmol) and 5-formyl-terthiophene (222 mg, 0.8 mmol) were combined in acetic acid (4 mL) and heated in a microwave reactor to 180 °C for 10 minutes. Upon cooling, NH_4OH (6 mL) was added dropwise to precipitate the product. Product (yellow powder) was filtered and washed with water then dried in a vacuum oven at 37 °C for 24 h. Yield: 149 mg (40%). 1H NMR (600 MHz, d6-DMSO) δ 9.01 (dd, 2H, J = 4.3, 1.8 Hz), 8.82 (dd, 2H, J = 8.1, 1.8 Hz), 7.83 (d, 1H, J = 3.8 Hz), 7.80 (dd, 2H, J = 8.1, 4.3 Hz), 7.56 (dd, 1H, J = 5.1, 1.2 Hz), 7.43 (d, 1H, J = 3.8 Hz), 7.41 (d, 1H, J = 3.7 Hz), 7.38 (dd, 1H, J = 3.5, 1.1 Hz), 7.32 (d, 1H, J = 3.7 Hz). 13C NMR (151 MHz, DMSO-d6) δ 148.13, 146.72, 145.45, 144.03, 141.71, 139.64, 137.61, 136.45, 136.32, 135.23, 133.24, 129.99, 129.06, 128.95, 128.48, 127.29, 127.02, 126.39, 126.11, 125.78, 125.68, 125.56, 125.50, 124.96, 123.69. LC-MS-ESI *m/z* [M+H]+ calcd: 467.77 found: 467.85.

Bis(4,4'-dimethyl-2,2'-bipyridine)dichlororuthenium dichloride ($Ru(dmb)_2Cl_2$, **L-8**)

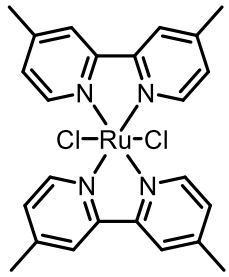

L-8 was synthesised according to a published procedure[277]. 4,4-dimethyl-2,2-bipyridine (700 mg, 3.85 mmol), $RuCl_3 \cdot 3H_2O$ (500 mg, 1.91 mmol) and LiCl (550 mg, 12.5 mmol) were dissolved in DMF (5 mL) and the reaction mixture was refluxed for 7 h. the reaction mixture was then allowed to cool, before adding dropwise into a Falcon tube containing acetone (12 mL). Precipitation of the product was induced by keeping at 4 °C

for 18 h. The resulting precipitate (black-purple) powder was isolated by centrifugation and dried in a vacuum oven at 37 °C for 24 h. Yield: 250 mg (23%). ^{1}H NMR(400 MHz, d6-DMSO) δ 9.77 (d, 2H), 8.46 (s, 2H), 8.31 (s, 2H), 7.59 (d, 2H), 7.31 (d, 2H), 6.92 (d,2H), 2.61 (s, 6H), 2.33 (s, 6H). ^{13}C NMR (150 MHz,) δ 156.9, 155.3, 154.9, 154.5, 147.5, 147.4, 131.3, 130.7, 127.8, 127.54, 127.9, 21.4, 21.0. HRMS (+, ESI) m/z [M+H]+ calcd: 540.116 found: 540.018.

TLD1433

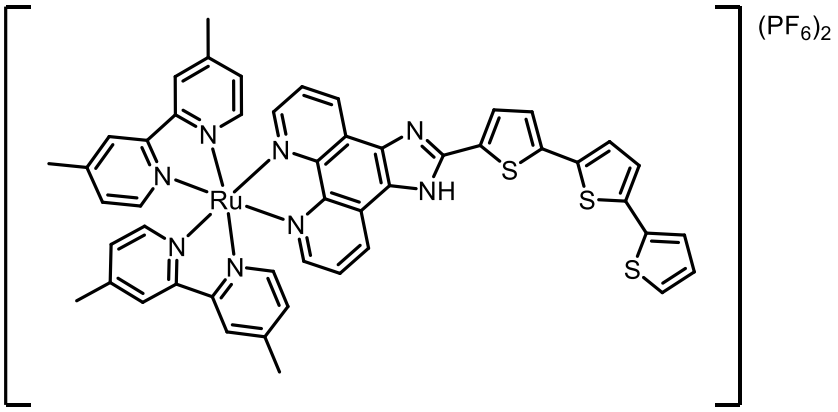

TLD1433 was synthesised according to a published procedure[278].

L-7 (49 mg, 0.104 mmol)and **L-8** (60 mg, 0.104 mmol) were dissolved in ethanol (2 mL) in a microwave tube under nitrogen atmosphere before heating in a microwave reactor at 180 °C for 10 minutes. Aqueous saturated KPF_6 was added drop-wise to the resultant solution to afford a precipitate. The precipitate was isolated by filtration and further purified via column chromatography (SiO_2) eluting with water (containing 0.5% KNO_3) and MeCN. The solvent was removed from the fractions containing TLD1433 and dissolved in water, filtered and aqueous saturated KPF_6 was added to afford a precipitate which was isolated by centrifugation and washed with saturated KP_6 (×3) then cold water (×3). The product (red-brown solid) was dried in a vacuum oven at 37 °C for 24 h.

Yield: 27 mg (22%). ^{1}H NMR (400 MHz, d3-acetonitrile) δ 8.87 (d, 2H, J= 6.60 Hz), 8.38 (d, 4H, J= 10.1 Hz), 8.02 (m, 2H, J= 4.50 Hz), 7.84 (d, 2H, J= 4.02 Hz), 7.74 (br, 2H), 7.67 (d, 2H, J=5.67Hz), 7.53 (d, 1H, J=6.42Hz), 7.42 (d, 2H, J=5.67Hz), 7.25-7.31 (m, 6H), 7.07-7.14 (m, 3H). ^{13}C NMR (150 MHz, d3-acetonitrile) δ 154.22, 154.18, 154.14, 154.10, 151.06, 151.03, 151.00, 150.97, 147.71, 147.70, 147.17, 141.64, 140.73, 139.6, 138.6, 136.9, 136.4, 136.1, 135.9, 135.4, 131.22, 131.20, 131.18, 131.16, 129.86, 129.49, 128.22, 127.94, 127.28, 127.23, 127.19, 127.14, 125.46, 124.29, 124.18, 124.10, 123.11, 121.03, 118.13, 21.1, 21.0. HRMS (+, ESI) m/z [M-PF_6]2^+ calcd: 468.557 found: 468.154

5.4 Electrode cleaning and modification

Gold electrodes

Gold electrodes were immersed in the minimum volume of piranha solution (3:1 H_2SO_4 (95%): H_2O_2 (30% w/v in H_2O)) for 10 min in order to remove any organic matter from the gold surface, then the working electrode was successively polished on a polishing cloth using alumina slurries of 1, 0.3 and 0.05 μm particle size (Buehler, Germany). This electrode was then further cleaned by immersion in H_2SO_4 (95%) and then HNO_3 (65%) at room temperature for 10 min. Finally, the working electrode was subjected to cyclic voltammetry with potential cycles between 0 and +1.6 V in 0.1 M H_2SO_4 at a scan rate of 100 mV·s-1 until the characteristic voltammogram of clean polycrystalline gold was obtained.

Glassy carbon electrodes

Glassy carbon electrodes were polished on a polishing cloth with alumina slurries of 1. 0.3 and 0.05 μm particle size successively, three times. To ensure the electrode was clean, cyclic voltammetry analysis was carried out with potential cycles between 0 and +1.6 V, at a scan rate of 100 $mV \cdot s^{-1}$ in PBS.

Methylene blue ternary self-assembled monolayer (MB-tSAM) functionalised electrode fabrication

A clean gold macroelectrode was immersed in a solution composed of PEG-dithiol (600 μM) and the probe **MB-tSAM** (40 μM) in ethanol (final volume of 500 μL) for 1 h at room temperature. After washing with fresh ethanol, the electrode was then immersed in mercaptohexanol (1 mM) in ethanol for a further 1 h. The electrode was then immersed in fresh ethanol (1 h) then immersed in PBS and stored at 4 °C.

Successful tSAM formation was verified by cyclic voltammetry with potential cycles between 0 and -0.5 V at 100 $mV \cdot s^{-1}$ to confirm the presence of the characteristic methylene blue redox peaks.

Polymethylene blue-functionalised electrode fabrication

Clean glassy carbon electrodes were immersed in an aqueous solution of ammonium sulfate (0.1 M) and methylene blue (1 mM). The potential was cycled from -0.6 V to 1.2 V at 50 $mV.s^{-1}$ for 15 scans. The electrode surface was washed profusely with water and was immersed in PBS for 12 h. The polymethylene blue-modified electrodes were transferrd to a fresh solution of PBS and the electro-polymerisation was confirmed by analysing the methylene blue redox waves by cyclic voltammetry.

Nafion-encapsulated hexaammineruthenium functionalised modified electrode device (MED) fabrication

A carbon ink screen-printed electrode was cleaned by washing with ethanol then water. Nafion perfluorinated resin solution (3 μL, 5% in a mixture of lower aliphatic alcohols and water) was drop casted onto the working electrode and air-dried at room temperature for 1 h. Once dried, the Nafion-coated electrodes were immersed into a solution of $[Ru(NH_3)_6]Cl_3$ (3 mM) in deionised water for 2 h and transferred to a vial containing water and allowed to age overnight. Before use, the electrodes were washed with water and the redox properties of the Nafion-bound mediator were analysed by cyclic voltammetry.

5.5 Fabrication of light sources

For Plate A: LEDs (dominant wavelength: 470 nm; forward current: 20 mA; forward voltage: 4V) were soldered (using SnCu-alloy wire solder) in an 8×9 array with a common-row cathode arrangement to a copper-laminated matrixboard (100×160 mm; hole diameter: 1 mm). The barrel connector of a 48 V power supply was removed to expose the wiring. The cathode pins of the LEDs were then soldered to a DynaOhm LED driver that was wired to the 48 V power supply. The anode pins were connected to the negative polarity wire of the power supply.

For Plate B: LED lighting strips (0.25 m) with an adhesive backing (Mouser Ltd., Cat. No. OVQ12S30B7) were arranged in a coil between 2 well plate covers and attached with even spacing between the turn of each coil. Contact pads were soldered to a 12 V power supply with a switch. For light irradiation studies, the light source allowed easy insertion of a well plate into the coil of the LEDs. Power measurements were made with a

THORLABS PM100D Power and Energy Meter console with photodiode (1 cm^2 sensing area) to find average power of 0.582 mW.cm-1 throughout the coil.

5.6 In vitro assays

Chapter 3

Cyclic voltammetric analysis of the pH dependence of the reduction wave of 6

The pH of an aqueous solution of KCl (0.1 M) was modified by either addition of HCl (0.1 M) or KOH (0.1 M). At each pH value analysed, **6** (2 mM) was dissolved and the potential swept between 0 and -1 V to identify the peak reduction potential of **6**. CV analysis was done with a glassy carbon electrode, a Pt mesh counter electrode and potentials referenced to a Ag/AgCl reference electrode.

Monitoring of pH during electro-activation of 6

The pH of a solution of PBS was analysed before and after the addition of **6** (50 μM). This solution was then subjected to a potential of -0.4 V with a MED and the pH was measured at 2, 4, 8 and 24 h.

Stability of $[Ru(NH_3)_6]^{3+}$-modified electrodes towards biological milieu

The redox waves of the immobilised $[Ru(NH_3)_6]^{3+}$ were analysed by cyclic voltammetry before and after 24 h of immersion in either PBS, 10% FBS in PBS or HCT 116 cell lysate.

The potential was swept between 0 and -0.5 V with the MED, with Pt counter electrode and potentials referenced against a Ag pseudo-reference electrode.

Quantification of the total Ru content in $[Ru(NH_3)_6]^{3+}$-modified electrodes

$[Ru(NH_3)_6]^{3+}$-modified electrodes were fabricated as described above. The carbon ink and the layer of Nafion-bound $[Ru(NH_3)_6]^{3+}$ was removed from the electrode surface by immersion in 1 mL of aqueous HNO_3 (10%) in Eppendorf tubes. After 5 min of immersion, mechanical agitation with a glass stirring rod was employed to ensure the ink was completely removed. Resulting mixtures were sonicated and vortexed intermittently for 10 min before centrifugation at 7000 rpm for 5 min to remove the insoluble carbon ink components. The supernatant was decanted and further diluted to 2% aqueous HNO_3. The Ru content was then analysed by ICP-OES with calibration against Ru standard solutions.

Quantification of the redox-active mediator in $[Ru(NH_3)_6]^{3+}$-modified electrodes

Redox-active Ru content was analysed by integration of total charge difference between $[Ru(NH_3)_6]^{3+}$-modified electrodes and Nafion-coated carbon ink screen-printed electrodes without any mediator encapsulated after applying -0.4 V for 400 s. To quantify the mass (w) of Ru related to the charge (Q), Faraday's law was applied:

$$w = \frac{(MW.Q)}{(n.F)}$$

where MW is molecular weight, n is number of electrons involved in redox process and F is Faraday's constant.

Quantification of leaching of $[Ru(NH_3)_6]^{3+}$-modified electrodes

$[Ru(NH_3)_6]^{3+}$-modified electrodes were subjected to a potential of -0.4 V for 24 h in KCl (0.1 M). Following this, the solutions were analysed for their Ru content by ICP-OES with calibration against Ru standard solutions.

Reaction monitoring of the electro-activation of 6

A solution of **6** (100 μM) was made in PBS and a potential of -0.4 V was applied with either a $[Ru(NH_3)_6]^{3+}$-modified electrode, an unmodified electrode or no potential was applied. The conversion was monitored by HPLC with detection at 254 nm. After 24 h of application of potential, GMP was added to make a final concentration of 1000 μM and were incubated at 37 °C for 4 h. The solutions were then again analysed by HPLC to quantify the level of Pt(II) species present in each.

For monitoring of the electro-activation in 10% FBS or HCT 116 cell lysate, the same procedure as above was used with the solutions being filtered through centrifugal filters (Amicon Ultra-0.5, molecular weight cut-off of 3000 Da) prior to analysis by HPLC.

Chapter 4

Photocatalytic reduction of 6 with $Ru(bpy)_3Cl_2$

A solution of **6** (250 μM) and $Ru(bpy)_3Cl_2$ (1 μM) in PBS was illuminated with an LED-array lamp (with dominant wavelength of 470 nm) from a height of 10 cm. The reduction of **6** was monitored over time by HPLC. Control experiments were carried out with exclusion of light and/or photosensitiser.

Biological reductant assay with compounds 7-13

Solutions were made with each of the compounds **7-13** (15 μM), sodium ascorbate (1500 μM) and glutathione (reduced form, 1500 μM). The solutions were incubated at 37 °C and the reduction of each compound was monitored by HPLC over time.

Stability of PS 16 in FBS

The absorbance at 440 nm of PS **16** (100 μM) in 10% FBS/DMEM was monitored over time. 10% FBS in DMEM was used to calibrate the background absorbance.

Quantum yield of singlet oxygen generation for PS 16

Solutions of either **16** or $Ru(bpy)_3Cl_2$ (both at 1 μM) and the singlet oxygen sensor green (SOSG, 5 μM) were prepared in MeOH. The fluorescence of SOSG was measured (λ_{ex} = 504 nm, λ_{em} = 525 nm) over time while irradiating at 470 nm. The fold-increase of fluorescence was plotted for each photosensitiser and used to calculate the quantum yield of singlet oxygen generation (Φ):

$$\Phi_{\mathbf{16}} = \Phi_{STD}\left(\frac{k_{\mathbf{16}}}{k_{STD}}\right)$$

where Φ_{STD} is quantum yield of standard $Ru(bpy)_3Cl_2$ in MeOH; $k_{(\mathbf{16})}$ is the rate of increase in fluorescence of SOSG by **16** and k_{STD} is the rate of increase in fluorescence of SOSG by $Ru(bpy)_3Cl_2$. The quantum yield of $Ru(bpy)_3Cl_2$ was taken to be 0.86 and the calculated quantum yield of singlet oxygen generation for **16** was found to be 0.72[262].

Calibration line of OxPt-GMP adduct

Solutions of OxPt (10, 20, 50, 100 μM) and GMP (1000 μM) in PBS were incubated at 37 °C for 4 h before analysis by HPLC at 254 nm. The peak corresponding to the Pt-GMP adduct for each concentration was integrated.

Photocatalytic reduction of 9 *in vitro*

In a 48-well plate, solutions of **9** (50 μM) and **16** (1 μM) in PBS were illuminated with the light source, Plate B, and analysed over time by HPLC at 254 nm. For Pt(II) quantification, GMP was added to give a final concentration of 1000 μM and the well plate was incubated at 37 °C for 4 h, before analysis by HPLC.

For NMR reaction monitoring, the solution was comprised of **9** (100 μM) and **16** (1 μM) in D_2O in an NMR tube. The solution was illuminated by placement of the tube into Plate B. The conversion was monitored over time by ^1H NMR with water pre-saturation (pulse sequence: zgpr).

Cyclic voltammetry analysis of the photocatalytic reduction of 9

A solution of $Ru(bpy)_3Cl_2$ (500 μM) was made in DMF with tetrabutylammonium chloride (0.1 M) as organic electrolyte. Potential was swept between 0.2 and -2 V for 1 scan, before the addition of **9** (1 mM). Another scan was then taken following the addition of **9**. The solution was illuminated with an array-LED lamp for 5 min and the duration of the next CV scan. The solution was then left for 30 min in the absence of light before another CV scan was taken. Potential measurements were with a carbon ink screen-printed working electrode with Pt counter electrode and referenced against a Ag pseudo-reference electrode.

Photocatalytic reduction of 9 with other photosensitisers

Solutions of **9** (50 μM) were incubated with either methylene blue, rose bengal, XD-Br, zinc phthalocyanine or TLD1433 (1 μM) in PBS. The solutions were illuminated with array-LED lamps with dominant wavelength near to the corresponding absorbance maxima of each of the photosensitisers (methylene blue: 630 nm; rose bengal: 545 nm; XD-Br: 630 nm; ZnPc: 630 nm; TLD1433: 470 nm) for 24 h, with HPLC analysis at 254 nm to monitor conversion.

5.7 Cell culture assays

Note: Number of replicates quoted throughout this work refer to technical replicates and not biological replicates.

Chapter 3

Cell viability studies of 6 and OxPt

HCT 116 cells grown in a 96-well plate (5,000 cells/well) were incubated with a solution of **6** or **OxPt** at the desired concentrations and the cells incubated at 37 °C, 5% CO_2 for 72 h. The media was then replaced with 100 μL of 3-(4,5-dimethylthiazol-2-yl)-2,5-diphenyltetrazolium bromide (MTT) solution (1 mg/mL) in PBS and the cells incubated for 3 h at 37 °C. After incubation, the resulting formazan crystals were dissolved by adding 100 μL of MTT solubilisation solution (10% Triton-X 100 in 0.1 N HCI in isopropanol). The absorbance was measured at a wavelength of 570 nm (BioTek HT Synergy multi-mode reader equipped with Gen5 microplate and imaging software 2.0) and the results compared to untreated cells.

Cell viability analysis following electro-activation of 6 in 2D cell culture

HCT 116 cells grown in a 24-well plate (15,000 cells/well) for 24 h before the media was removed, the cells were washed with PBS (2×) and DMEM containing **6** (50 μM) was added to give a total volume of 1.7 mL. Modified electrodes or unmodified electrodes were added to the wells treated with **6** or with DMEM. A potential of -0.4 V was applied for 1 h in an atmosphere and temperature controlled chamber (37°C, 5% CO2), after which the electrodes were removed and the cells incubated at 37 °C for 3 days. The media was then replaced with 350 μL of 3-(4,5-dimethylthiazol-2-yl)-2,5-diphenyltetrazolium bromide (MTT) solution (1 mg/mL) in PBS and the cells incubated for 3 h at 37 °C. After incubation, the formazan crystals were dissolved by adding 350 μL of MTT solubilisation solution (10% Triton-X 100/0.1 M HCI/isopropanol). The absorbance was measured at a wavelength of 570 nm and the results compared to untreated cells.

Cellular apoptosis analysis following electro-activation of 6 in 2D cell culture

HCT 116 cells grown in a 24-well plate (15,000 cells/well) for 24 h before the media was removed, the cells were washed with PBS (2×) and DMEM containing **6** (50 μM) was added to give a total volume of 1.7 mL. Modified electrodes or unmodified electrodes were added to the wells treated with **6** or with DMEM. A potential of -0.4 V was applied for 1 h, after which the electrodes were removed and the cells incubated at 37 °C for 3 days. After incubation, a fluorescein-conjugated Annexin-V (Annexin V-FITC) binding assay was performed.

Labelling of cells with Annexin-V-FITC conjugate was performed using an Apoptosis Detection Kit (eBiosciences, San Diego, CA) with Annexin V-FITC and binding buffer included as controls. Flow cytometry (Becton Dickinson (BD) FACScan) was performed with excitation at 488 nm. FITC fluorescence was measured at 515–545 nm. Cell debris was excluded from analysis by appropriate forward light scatter threshold setting. For

fluorescence imaging, cells were washed with PBS after Annexin-V/FITC incubation, stained with Hoechst 33342 for 10 min and imaged with a Zeiss Axio Vert inverted fluorescence microscope. Microscope lasers settings were: excitation laser lines at 405 nm and 488 nm with emission filters of 385–470 nm for Hoechst 33342 (nuclei stain) and 505–530 nm for Annexin-V/FITC.

Quantification of whole-cell and nuclear DNA-platination by ICP-MS

HCT 116 cells were grown in a 6 well-plate to confluence. The media was removed, cells washed with PBS (2×) then treated with **6** (50 μM). Modified or unmodified electrodes were immersed in the cell media and a potential of -0.4 V was applied for 1 h in an atmosphere and temperature controlled chamber (37°C, 5% CO_2). The electrodes were then removed and the cells were incubated at 37 °C for 24 h. Then the media was removed, the cells washed with PBS (3×), detached with trypsin, and counted with a haemocytometer. The cells were centrifuged at 7000 rpm for 5 min and the resultant cell pellet was suspended in aqueous HNO_3 (5%), sonicated for 1 h and analysed by ICP-MS with calibration against Pt standard solutions.

For quantification of platinated DNA, the cell pellet obtained by centrifugation was resuspended in PBS (200 μL) and subjected the DNA content was isolated and purified by a Qiagen DNeasy blood and tissue kit. The DNA concentration was analysed by Nanodrop spectrophotometry. The samples were prepared by suspending the DNA solution in aqueous HNO_3 (5%) and subjected to analysis by ICP-MS, as above.

Generation of multi-cellular tumour spheroids

The hanging drop method was employed, using published procedures as a basis[212, 213], for generation of multi-cellular tumour spheroids: from a cell suspension (50,000 cells/mL) in DMEM, 20 μL was dispensed onto the covering of a petri dish (90 mm), inverted and incubated under standard conditions, with aliquots of DMEM added to the dish twice-daily to avoid evaporation and drying. The spheroids were incubated for 7 days with the addition of fresh DMEM (5 μL) to the drops every 2 days. The size of the spheroids was monitored by inverted microscopy.

Electro-activation of 6 in multi-cellular tumour spheroids

Prior to the treatment with **6**, the spheroids were transferred to a 24 well-plate coated with 1% agarose, with each well containing 350 μL of DMEM. The media was removed and the spheroids gently washed with PBS, before submerging in a solution of **6** (50 μM) in DMEM. Modified or unmodified electrodes were immersed in the media and a potential of -0.4 V applied for 1 h at 37 °C, 5% CO_2. The media was then removed, the spheroids washed with PBS and incubated at 37 °C for 72 h. The viability of the spheroids were analysed with a Cell Titre Glo 3D assay. Apoptotic onset was monitored over time using a RealTime-Glo Annexin-V Assay.

Chapter 4

Generation of an oxaliplatin-resistant ovarian cancer cell line (SKOV-3-OxR)

SKOV-3-wt cells were seeded in a T25 cell culture flasks and cultured until confluent. Cells were exposed to OxPt and cultured in OxPt-containing media over 3 months. Doses were delivered in two ways: an intermittent dose where cells are exposed to a higher dose before being replaced by fresh media containing no OxPt and continuous dose

where cells are split and cultured in low-dose OxPt-containing media. The intermittent doses of OxPt were for 1 h before replacing with fresh media free of OxPt, allowing the cells to recuperate overnight before sub-culturing in fresh media that did not contain OxPt. Once nearing confluency, cells were exposed to low continuous dose until the next intermittent dose with increasing concentration of dose over 3 months. Cells were cultured in OxPt-free media following the first three doses and escalated to 2 μM over 3 months, at which point, doses were suspended and cells were grown in normal OxPt-free cell media.

Week Number	Intermittent Dose (μM)	Continuous dose (μM)
1	0.1	0
2	0.1	0
3	0.1	0
4	1	0.1
5	2	0.1
6	2	0.5
7	5	0.5
8	5	0.5
9	10	0.5
10	10	1
11	10	1
12	20	1
13	20	2
14	50	2

Live-cell imaging of HCT 116 cells with 16

HCT 116 cells were seeded in an 8-well μ-slide (Ibidi) at a cell density of 7×10^4 cells/well and allowed to attach overnight at 37 °C. Hoechst nuclei stain was added to cells to a final concentration of 1 μg/mL and incubated for 30 min. Media was removed and replaced with media containing MitoTracker Green (50 nM) and **16** (1 μM) and incubated for further 30 min before removing them media, washing with PBS and replacing with fresh media.

Cell viability studies of 9 and OxPt

HCT 116, SKOV-3-wt or SKOV-3-OxR cells were grown in a 96-well plate (5,000 cells/well) and were incubated with a solution of **OxPt** or **9** at the desired concentrations and the cells incubated for 48 h. To the media was added 10 μL of CCK-8 and incubated for a further 2 h. After incubation, the absorbance was measured at a wavelength of 450 nm and the results compared to untreated cells.

Photocatalytic reduction of 9 with PS 16 in cell culture

Cells grown in a 96-well plate (5,000 cells/well) were incubated with a solution of **9** (20 μM) and **16** (1 μM) in a total volume of 100 μL for 4 h. The well plates were irradiated for 30 min then incubated for 2 d. Cell Titre Glo 2.0 (100 μL) was added to each well at rt and the plates shaken on an orbital shaker for 5 minutes. Plates were then left at rt for 10 minutes to allow equilibration before measuring luminescence signal (BioTek HT Synergy multi-mode reader using the Gen5 microplate and imaging software 2.0.) and the results compared to untreated cells.

Quantification of platination of mitochondrial and whole-cell DNA

Cells were grown in a 6-well plate until confluent and then treated with Pt-c (20 μM) or **16** (1 μM) incubated at 37 °C for 4 h. Media was removed and cells washed with PBS (3×) and fresh media (3 mL) was added. Cells were then irradiated with light for 30 min and incubated at 37 °C for 24 h. Cells were detached with trypsin and each cell suspension was split into 2 microcentrifuge vials. For mitochondrial DNA extraction, the Mitochondrial DNA extraction kit was used. For nuclear DNA extraction, DNEasy Blood and Tissue kit was used. ICP-MS analysis was carried out to quantify Pt content. Nanodrop spectrophotometry was used to quantify the concentration of DNA in each sample.

References

1. Hanahan, D. and Robert A. Weinberg, *Hallmarks of Cancer: The Next Generation.* Cell, 2011. **144**(5): p. 646-674.
2. San-Millán, I. and G.A. Brooks, *Reexamining cancer metabolism: lactate production for carcinogenesis could be the purpose and explanation of the Warburg Effect.* Carcinogenesis, 2017. **38**(2): p. 119-133.
3. Strano, S., et al., *Mutant p53: an oncogenic transcription factor.* Oncogene, 2007. **26**(15): p. 2212-2219.
4. Hollstein, M., et al., *p53 mutations in human cancers.* Science, 1991. **253**(5015): p. 49.
5. Rajalingam, K., et al., *Ras oncogenes and their downstream targets.* Biochimica et Biophysica Acta (BBA) - Molecular Cell Research, 2007. **1773**(8): p. 1177-1195.
6. Keeton, A.B., E.A. Salter, and G.A. Piazza, *The RAS-Effector Interaction as a Drug Target.* Cancer research, 2017. **77**(2): p. 221-226.
7. Hanson, J., et al., *Regulation of vascular endothelial growth factor, VEGF, gene promoter by the tumor suppressor, WT1.* Frontiers in bioscience : a journal and virtual library, 2007. **12**: p. 2279-2290.
8. López-Ocejo, O., et al., *Oncogenes and tumor angiogenesis: the HPV-16 E6 oncoprotein activates the vascular endothelial growth factor (VEGF) gene promoter in a p53 independent manner.* Oncogene, 2000. **19**(40): p. 4611-4620.
9. Ravi, R., et al., *Regulation of tumor angiogenesis by p53-induced degradation of hypoxia-inducible factor 1α.* Genes & Development, 2000. **14**(1): p. 34-44.
10. ten Dijke, P. and H.M. Arthur, *Extracellular control of TGFβ signalling in vascular development and disease.* Nature Reviews Molecular Cell Biology, 2007. **8**: p. 857.
11. Neuzillet, C., et al., *Perspectives of TGF-β inhibition in pancreatic and hepatocellular carcinomas.* Oncotarget, 2013. **5**(1): p. 78-94.
12. Kalluri, R. and R.A. Weinberg, *The basics of epithelial-mesenchymal transition.* The Journal of clinical investigation, 2009. **119**(6): p. 1420-1428.
13. Hay, E.D., *An overview of epithelio-mesenchymal transformation.* Acta Anat (Basel), 1995. **154**(1): p. 8-20.
14. Gheldof, A. and G. Berx, *Chapter Fourteen - Cadherins and Epithelial-to-Mesenchymal Transition*, in *Progress in Molecular Biology and Translational Science*, F. van Roy, Editor. 2013, Academic Press. p. 317-336.
15. van Roy, F. and G. Berx, *The cell-cell adhesion molecule E-cadherin.* Cellular and Molecular Life Sciences, 2008. **65**(23): p. 3756-3788.
16. Kim, J.-B., et al., *N-Cadherin Extracellular Repeat 4 Mediates Epithelial to Mesenchymal Transition and Increased Motility.* The Journal of Cell Biology, 2000. **151**(6): p. 1193.
17. Quaresma, M., M.P. Coleman, and B. Rachet, *40-year trends in an index of survival for all cancers combined and survival adjusted for age and sex for each cancer in England and Wales, 1971–2011: a population-based study.* The Lancet, 2015. **385**(9974): p. 1206-1218.
18. Nagaya, T., et al., *Fluorescence-Guided Surgery.* Frontiers in Oncology, 2017. **7**: p. 314.
19. Namikawa, T., T. Sato, and K. Hanazaki, *Recent advances in near-infrared fluorescence-guided imaging surgery using indocyanine green.* Surgery Today, 2015. **45**(12): p. 1467-1474.

20. van Manen, L., et al., *A practical guide for the use of indocyanine green and methylene blue in fluorescence-guided abdominal surgery.* Journal of Surgical Oncology, 2018. **118**(2): p. 283-300.
21. Whitley, M.J., et al., *A mouse-human phase 1 co-clinical trial of a protease-activated fluorescent probe for imaging cancer.* Science Translational Medicine, 2016. **8**(320): p. 320ra4.
22. Kirsch, D.G., *Feasibility Study of Intraoperative Imaging in Breast Cancer*. 2017, NCT02438358: https://ClinicalTrials.gov/show/NCT02438358.
23. Kirsch, D.G., *Feasibility of the LUM Imaging System for Detection of Prostate Cancer*. 2019, NCT03441464: https://ClinicalTrials.gov/show/NCT03441464.
24. Kirsch, D.G., *Cathepsin Activatable Fluorescent Probe*. 2015, NCT01626066: https://ClinicalTrials.gov/show/NCT01626066.
25. Jiang, T., et al., *Tumor imaging by means of proteolytic activation of cell-penetrating peptides.* Proceedings of the National Academy of Sciences of the United States of America, 2004. **101**(51): p. 17867.
26. Guidotti, G., L. Brambilla, and D. Rossi, *Cell-Penetrating Peptides: From Basic Research to Clinics.* Trends in Pharmacological Sciences, 2017. **38**(4): p. 406-424.
27. Derakhshankhah, H. and S. Jafari, *Cell penetrating peptides: A concise review with emphasis on biomedical applications.* Biomedicine & Pharmacotherapy, 2018. **108**: p. 1090-1096.
28. Herce, H.D., et al., *Arginine-Rich Peptides Destabilize the Plasma Membrane, Consistent with a Pore Formation Translocation Mechanism of Cell-Penetrating Peptides.* Biophysical Journal, 2009. **97**(7): p. 1917-1925.
29. Bechara, C. and S. Sagan, *Cell-penetrating peptides: 20years later, where do we stand?* FEBS Letters, 2013. **587**(12): p. 1693-1702.
30. Olson, E.S., et al., *In vivo characterization of activatable cell penetrating peptides for targeting protease activity in cancer.* Integrative Biology, 2009. **1**(5-6): p. 382-393.
31. Nguyen, Q.T., et al., *Surgery with molecular fluorescence imaging using activatable cell-penetrating peptides decreases residual cancer and improves survival.* Proceedings of the National Academy of Sciences, 2010. **107**(9): p. 4317.
32. Kubben, P.L., et al., *Intraoperative MRI-guided resection of glioblastoma multiforme: a systematic review.* The Lancet Oncology, 2011. **12**(11): p. 1062-1070.
33. Sequeira, J.H., *A Lecture ON THE TREATMENT OF MALIGNANT DISEASE OF THE SKIN.* British Medical Journal, 1915. **1**(2826): p. 365.
34. Herbst, R.H., *CANCER OF THE PROSTATE: A COMBINED SURGICAL AND RADIUM METHOD OF TREATMENT.* Journal of the American Medical Association, 1919. **72**(22): p. 1610-1611.
35. MacLeod, J.M.H., *Further observations on the Therapeutic Value of Radium and Thorium.* British Medical Journal, 1904. **1**(2267): p. 1366.
36. Lawrence, E.O. and M.S. Livingston, *The Production of High Speed Light Ions Without the Use of High Voltages.* Physical Review, 1932. **40**(1): p. 19-35.
37. Coutard, H., *PRINCIPLES OF X RAY THERAPY OF MALIGNANT DISEASES.* The Lancet, 1934. **224**(5784): p. 1-8.
38. Gray, L.H., et al., *The Concentration of Oxygen Dissolved in Tissues at the Time of Irradiation as a Factor in Radiotherapy.* The British Journal of Radiology, 1953. **26**(312): p. 638-648.
39. Robert Grimes, D. and M. Partridge, *A mechanistic investigation of the oxygen fixation hypothesis and oxygen enhancement ratio.* Biomedical Physics & Engineering Express, 2015. **1**(4): p. 045209.

40. Adler Jr, J.R., et al., *The Cyberknife: A Frameless Robotic System for Radiosurgery.* Stereotactic and Functional Neurosurgery, 1997. **69**(1-4): p. 124-128.
41. Koukourakis, G., et al., *Brachytherapy for Prostate Cancer: A Systematic Review.* Advances in Urology, 2009. **2009**: p. 11.
42. Marland, J.R.K., et al. *Test structures for optimizing polymer electrolyte performance in a microfabricated electrochemical oxygen sensor*. in *2017 International Conference of Microelectronic Test Structures (ICMTS)*. 2017.
43. González-Fernández, E., et al., *Methylene blue not ferrocene: Optimal reporters for electrochemical detection of protease activity.* Biosensors and Bioelectronics, 2016. **84**: p. 82-88.
44. González-Fernández, E., et al., *Electrochemical sensing of human neutrophil elastase and polymorphonuclear neutrophil activity.* Biosensors and Bioelectronics, 2018. **119**: p. 209-214.
45. Ehrlich, P., *Abhandlungen über Salvarsan:(Ehrlich-Hata-Präparat 606 gegen Syphilis)*. Vol. 2. 1912: Lehmann.
46. Hanahan, D. and R.A. Weinberg, *The Hallmarks of Cancer.* Cell, 2000. **100**(1): p. 57-70.
47. Arnold, H., F. Bourseaux, and N. Brock, *Chemotherapeutic Action of a Cyclic Nitrogen Mustard Phosphamide Ester (B 518-ASTA) in Experimental Tumours of the Rat.* Nature, 1958. **181**(4613): p. 931-931.
48. Zubrod, C.G., et al., *Appraisal of methods for the study of chemotherapy of cancer in man: Comparative therapeutic trial of nitrogen mustard and triethylene thiophosphoramide.* Journal of Chronic Diseases, 1960. **11**(1): p. 7-33.
49. Bhatia, U., et al., *Induction of apoptosis and cell cycle-specific change in expression of p53 in normal lymphocytes and MOLT-4 leukemic cells by nitrogen mustard.* Clinical Cancer Research, 1995. **1**(8): p. 873.
50. Sigal, A. and V. Rotter, *Oncogenic Mutations of the p53 Tumor Suppressor: The Demons of the Guardian of the Genome.* Cancer Research, 2000. **60**(24): p. 6788.
51. Rosenberg, B., et al., *Platinum Compounds: a New Class of Potent Antitumour Agents.* Nature, 1969. **222**(5191): p. 385-386.
52. Rosenberg, B. and B. Lippert, *Cisplatin: Chemistry and Biochemistry of a Leading Anticancer Drug.* by Lippert B., Wiley-VCH, Weinheim, 1999: p. 3-27.
53. Kelland, L., *The resurgence of platinum-based cancer chemotherapy.* Nature Reviews Cancer, 2007. **7**: p. 573.
54. Johnstone Timothy, C., K. Suntharalingam, and J. Lippard Stephen, *Third row transition metals for the treatment of cancer.* Philosophical Transactions of the Royal Society A: Mathematical, Physical and Engineering Sciences, 2015. **373**(2037): p. 20140185.
55. Astolfi, L., et al., *Correlation of adverse effects of cisplatin administration in patients affected by solid tumours: a retrospective evaluation.* Oncology reports, 2013. **29**(4): p. 1285-1292.
56. Rybak, L.P., et al., *Cisplatin ototoxicity and protection: clinical and experimental studies.* The Tohoku journal of experimental medicine, 2009. **219**(3): p. 177-186.
57. Shahid, F., Z. Farooqui, and F. Khan, *Cisplatin-induced gastrointestinal toxicity: An update on possible mechanisms and on available gastroprotective strategies.* European Journal of Pharmacology, 2018. **827**: p. 49-57.
58. Navari, R.M., et al., *Olanzapine for the Prevention of Chemotherapy-Induced Nausea and Vomiting.* The New England journal of medicine, 2016. **375**(2): p. 134-142.
59. Kidani, Y., M. Noji, and T. Tashiro, *Antitumor activity of platinum(II) complexes of 1,2-diamino-cyclohexane isomers.* Gan, 1980. **71**(5): p. 637-43.

60. Cassidy, J. and J.-L. Misset, *Oxaliplatin-related side effects: Characteristics and management.* Seminars in Oncology, 2002. **29**(5, Supplement 15): p. 11-20.
61. Pardini, B., et al., *5-Fluorouracil-based chemotherapy for colorectal cancer and MTHFR/MTRR genotypes.* British journal of clinical pharmacology, 2011. **72**(1): p. 162-163.
62. de Gramont, A., et al., *Leucovorin and Fluorouracil With or Without Oxaliplatin as First-Line Treatment in Advanced Colorectal Cancer.* Journal of Clinical Oncology, 2000. **18**(16): p. 2938-2947.
63. Tsai, Y.-J., et al., *Adjuvant FOLFOX treatment for stage III colon cancer: how many cycles are enough?* SpringerPlus, 2016. **5**(1): p. 1318.
64. Fischel, J.L., et al., *Impact of the oxaliplatin-5 fluorouracil-folinic acid combination on respective intracellular determinants of drug activity.* British journal of cancer, 2002. **86**(7): p. 1162-1168.
65. Yeh, K.-H., et al., *Down-regulation of thymidylate synthase expression and its steady-state mRNA by oxaliplatin in colon cancer cells.* Anti-Cancer Drugs, 2004. **15**(4): p. 371-376.
66. Kunicka, T., et al., *Molecular profile of 5-fluorouracil pathway genes in colorectal carcinoma.* BMC cancer, 2016. **16**(1): p. 795-795.
67. Alcindor, T. and N. Beauger, *Oxaliplatin: a review in the era of molecularly targeted therapy.* Current oncology (Toronto, Ont.), 2011. **18**(1): p. 18-25.
68. Fichtinger-Schepman, A.M.J., et al., *Adducts of the antitumor drug cis-diamminedichloroplatinum(II) with DNA: formation, identification, and quantitation.* Biochemistry, 1985. **24**(3): p. 707-713.
69. Brozovic, A., A. Ambriović-Ristov, and M. Osmak, *The relationship between cisplatin-induced reactive oxygen species, glutathione, and BCL-2 and resistance to cisplatin.* Critical Reviews in Toxicology, 2010. **40**(4): p. 347-359.
70. Cummings, B.S. and R.G. Schnellmann, *Cisplatin-Induced Renal Cell Apoptosis: Caspase 3-Dependent and -Independent Pathways.* Journal of Pharmacology and Experimental Therapeutics, 2002. **302**(1): p. 8.
71. Pourahmad, J., et al., *Mitochondrial/lysosomal toxic cross-talk plays a key role in cisplatin nephrotoxicity.* Xenobiotica, 2010. **40**(11): p. 763-771.
72. Xie, S.Y., et al., *miRNA-regulated expression of oncogenes and tumor suppressor genes in the cisplatin-inhibited growth of K562 cells.* Oncol Rep, 2010. **23**(6): p. 1693-700.
73. Biersack, B., *Interactions between anticancer active platinum complexes and non-coding RNAs/microRNAs.* Non-coding RNA Research, 2017. **2**(1): p. 1-17.
74. Curis, E., et al., *Carboplatin and oxaliplatin decomposition in chloride medium, monitored by XAS.* J Synchrotron Radiat, 2001. **8**(Pt 2): p. 716-8.
75. Allain, P., et al., *Early Biotransformations of Oxaliplatin after Its Intravenous Administration to Cancer Patients.* Drug Metabolism and Disposition, 2000. **28**(11): p. 1379-1384.
76. Videhult, P., et al., *Synthesis and cytotoxicity of the dihydrated complex of oxaliplatin.* Cancer Letters, 2002. **180**(2): p. 191-194.
77. Gelasco, A. and S.J. Lippard, *NMR Solution Structure of a DNA Dodecamer Duplex Containing a cis-Diammineplatinum(II) d(GpG) Intrastrand Cross-Link, the Major Adduct of the Anticancer Drug Cisplatin.* Biochemistry, 1998. **37**(26): p. 9230-9239.
78. Apetoh, L., et al., *Toll-like receptor 4–dependent contribution of the immune system to anticancer chemotherapy and radiotherapy.* Nature Medicine, 2007. **13**: p. 1050.
79. Tesniere, A., et al., *Immunogenic death of colon cancer cells treated with oxaliplatin.* Oncogene, 2009. **29**: p. 482.

80. Liu, W.M., et al., *Pre-treatment with chemotherapy can enhance the antigenicity and immunogenicity of tumours by promoting adaptive immune responses.* British Journal Of Cancer, 2009. **102**: p. 115.
81. Bruno, P.M., et al., *A subset of platinum-containing chemotherapeutic agents kills cells by inducing ribosome biogenesis stress.* Nature Medicine, 2017. **23**: p. 461.
82. Pabla, N., et al., *ATR-Chk2 Signaling in p53 Activation and DNA Damage Response during Cisplatin-induced Apoptosis.* Journal of Biological Chemistry, 2008. **283**(10): p. 6572-6583.
83. Zhang, Y., et al., *Ribosomal Protein L11 Negatively Regulates Oncoprotein MDM2 and Mediates a p53-Dependent Ribosomal-Stress Checkpoint Pathway.* Molecular and Cellular Biology, 2003. **23**(23): p. 8902.
84. Pabla, N., et al., *The copper transporter Ctr1 contributes to cisplatin uptake by renal tubular cells during cisplatin nephrotoxicity.* American Journal of Physiology-Renal Physiology, 2009. **296**(3): p. F505-F511.
85. Eljack, N.D., et al., *Mechanisms of cell uptake and toxicity of the anticancer drug cisplatin.* Metallomics, 2014. **6**(11): p. 2126-2133.
86. Kuo, M.T., et al., *The roles of copper transporters in cisplatin resistance.* Cancer and Metastasis Reviews, 2007. **26**(1): p. 71-83.
87. Ishida, S., et al., *Enhancing Tumor-Specific Uptake of the Anticancer Drug Cisplatin with a Copper Chelator.* Cancer Cell, 2010. **17**(6): p. 574-583.
88. Holzer, A.K., G.H. Manorek, and S.B. Howell, *Contribution of the Major Copper Influx Transporter CTR1 to the Cellular Accumulation of Cisplatin, Carboplatin, and Oxaliplatin.* Molecular Pharmacology, 2006. **70**(4): p. 1390.
89. Ogane, N., et al., *Prognostic value of organic anion transporting polypeptide 1B3 and copper transporter 1 expression in endometrial cancer patients treated with paclitaxel and carboplatin.* Biomedical Research, 2013. **34**(3): p. 143-151.
90. Yoshizawa, K., et al., *Expression of Copper Efflux Transporter (ATP7B) in the Transport of Cisplatin in Cell Lines Derived From Invasive Oral Squamous Cell Carcinoma.* Oral Science International, 2007. **4**(1): p. 28-37.
91. Samimi, G., et al., *Increased Expression of the Copper Efflux Transporter ATP7A Mediates Resistance to Cisplatin, Carboplatin, and Oxaliplatin in Ovarian Cancer Cells.* Clinical Cancer Research, 2004. **10**(14): p. 4661.
92. Ishikawa, T. and F. Ali-Osman, *Glutathione-associated cis-diamminedichloroplatinum(II) metabolism and ATP-dependent efflux from leukemia cells. Molecular characterization of glutathione-platinum complex and its biological significance.* Journal of Biological Chemistry, 1993. **268**(27): p. 20116-20125.
93. Chao, C.C., et al., *Overexpression of glutathione S-transferase and elevation of thiol pools in a multidrug-resistant human colon cancer cell line.* Molecular Pharmacology, 1992. **41**(1): p. 69.
94. Yellin, S.A., et al., *Relationship of glutathione and glutathione-S-transferase to cisplatin sensitivity in human head and neck squamous carcinoma cell lines.* Cancer Letters, 1994. **85**(2): p. 223-232.
95. Britten, R.A., et al., *ERCC1 expression as a molecular marker of cisplatin resistance in human cervical tumor cells.* International Journal of Cancer, 2000. **89**(5): p. 453-457.
96. Ueda, S., et al., *Evaluation of ERCC1 Expression for Cisplatin Sensitivity in Human Hepatocellular Carcinoma.* Annals of Surgical Oncology, 2011. **18**(4): p. 1204-1211.
97. Seetharam, R.N., et al., *Oxaliplatin Resistance Induced by ERCC1 Up-regulation Is Abrogated by siRNA-mediated Gene Silencing in Human Colorectal Cancer Cells.* Anticancer Research, 2010. **30**(7): p. 2531-2538.

98. Baba, H., et al., *Upregulation of ERCC1 and DPD expressions after oxaliplatin-based first-line chemotherapy for metastatic colorectal cancer.* British Journal Of Cancer, 2012. **107**: p. 1950.
99. Kang, Y.P., N.P. Ward, and G.M. DeNicola, *Recent advances in cancer metabolism: a technological perspective.* Experimental & Molecular Medicine, 2018. **50**(4): p. 31.
100. Vamecq, J., et al., *PPARs: Interference with Warburg' Effect and Clinical Anticancer Trials.* PPAR research, 2012. **2012**: p. 304760-304760.
101. Calvaresi, E.C. and P.J. Hergenrother, *Glucose conjugation for the specific targeting and treatment of cancer.* Chemical science, 2013. **4**(6): p. 2319-2333.
102. Haroutounian, S.A., M.P. Georgiadis, and J.C. Bailar, *Water soluble cis-platinum(II) complexes.* Inorganica Chimica Acta, 1986. **124**(3): p. 137-139.
103. Pill, T., K. Polborn, and W. Beck, *Bindung von Monosacchariden über die Isocyano- und Carben-Funktion an das Metall-Atom: Chrom(0), Wolfram(0)-, Rhodium(III)-, Iridium(III)-, Palladium(II)-, Platin(II)- und Gold(I)-Komplexe von 1,3,4,6-Tetra-O-acetyl-2-desoxy-2-isocyano-α-D-glucose und - β-D-glucose.* Chemische Berichte, 1990. **123**(1): p. 11-17.
104. Kuduk-Jaworska, J. and B. Jeżowska-Trzebiatowska, *Platinum(II) complexes with D-glucosamine and its derivatives.* Inorganica Chimica Acta, 1986. **123**(4): p. 209-212.
105. Tsubomura, T., et al., *First synthesis and characterization of platinum(II) complexes of amino sugars having anti-tumour activity; crystal structure of [ptcl2(methyl 2,3-dideoxy-α-D-mannopyranoside)]·H2O.* Journal of the Chemical Society, Chemical Communications, 1986(6): p. 459-460.
106. Liu, P., et al., *Highly water-soluble platinum(ii) complexes as GLUT substrates for targeted therapy: improved anticancer efficacy and transporter-mediated cytotoxic properties.* Chemical Communications, 2013. **49**(24): p. 2421-2423.
107. Senapati, S., et al., *Controlled drug delivery vehicles for cancer treatment and their performance.* Signal Transduction and Targeted Therapy, 2018. **3**(1): p. 7.
108. Riley, R.S., et al., *Delivery technologies for cancer immunotherapy.* Nature Reviews Drug Discovery, 2019. **18**(3): p. 175-196.
109. Xiao, H., et al., *Recent progress in polymer-based platinum drug delivery systems.* Progress in Polymer Science, 2018. **87**: p. 70-106.
110. Bulbake, U., et al., *Liposomal Formulations in Clinical Use: An Updated Review.* Pharmaceutics, 2017. **9**(2): p. 12.
111. Paola, M., D. Franco, and C. Luigi, *PEGylation of Proteins and Liposomes: a Powerful and Flexible Strategy to Improve the Drug Delivery.* Current Drug Metabolism, 2012. **13**(1): p. 105-119.
112. Nunes, S.S., et al., *Influence of PEG coating on the biodistribution and tumor accumulation of pH-sensitive liposomes.* Drug Delivery and Translational Research, 2019. **9**(1): p. 123-130.
113. Gabizon, A., et al., *Prolonged Circulation Time and Enhanced Accumulation in Malignant Exudates of Doxorubicin Encapsulated in Polyethylene-glycol Coated Liposomes.* Cancer Research, 1994. **54**(4): p. 987.
114. Matsumura, Y. and H. Maeda, *A New Concept for Macromolecular Therapeutics in Cancer Chemotherapy: Mechanism of Tumoritropic Accumulation of Proteins and the Antitumor Agent Smancs.* Cancer Research, 1986. **46**(12 Part 1): p. 6387.
115. Bolkestein, M., et al., *Investigation of Factors Determining the Enhanced Permeability and Retention Effect in Subcutaneous Xenografts.* Journal of Nuclear Medicine, 2016. **57**(4): p. 601-607.
116. Nichols, J.W. and Y.H. Bae, *EPR: Evidence and fallacy.* Journal of Controlled Release, 2014. **190**: p. 451-464.

117. Danhier, F., *To exploit the tumor microenvironment: Since the EPR effect fails in the clinic, what is the future of nanomedicine?* Journal of Controlled Release, 2016. **244**: p. 108-121.
118. Barenholz, Y., *Doxil® — The first FDA-approved nano-drug: Lessons learned.* Journal of Controlled Release, 2012. **160**(2): p. 117-134.
119. Allen, T.M. and A. Chonn, *Large unilamellar liposomes with low uptake into the reticuloendothelial system.* FEBS Letters, 1987. **223**(1): p. 42-46.
120. Allen, T.M. and F.J. Martin, *Advantages of liposomal delivery systems for anthracyclines.* Seminars in Oncology, 2004. **31**: p. 5-15.
121. Boulikas, T., et al., *Systemic Lipoplatin Infusion Results in Preferential Tumor Uptake in Human Studies.* Anticancer Research, 2005. **25**(4): p. 3031-3039.
122. Boulikas, T., *Clinical overview on Lipoplatin™: a successful liposomal formulation of cisplatin.* Expert Opinion on Investigational Drugs, 2009. **18**(8): p. 1197-1218.
123. Jehn, C.F., et al., *Pharmacokinetics of Liposomal Cisplatin (Lipoplatin) in Combination with 5-FU in Patients with Advanced Head and Neck Cancer: First Results of a Phase III Study.* Anticancer Research, 2007. **27**(1A): p. 471-475.
124. Koukourakis, M.I., et al., *Concurrent Liposomal Cisplatin (Lipoplatin), 5-Fluorouracil and Radiotherapy for the Treatment of Locally Advanced Gastric Cancer: A Phase I/II Study.* International Journal of Radiation Oncology*Biology*Physics, 2010. **78**(1): p. 150-155.
125. Farhat, F.S., et al., *A Phase II Study of Lipoplatin (Liposomal Cisplatin)/Vinorelbine Combination in HER-2/neu–Negative Metastatic Breast Cancer.* Clinical Breast Cancer, 2011. **11**(6): p. 384-389.
126. Karpathiou, G., et al., *Response of a Patient with Pleural and Peritoneal Mesothelioma after Second-Line Chemotherapy with Lipoplatin and Gemcitabine.* Oncology, 2007. **73**(5-6): p. 426-429.
127. Mylonakis, N., et al., *Phase II study of liposomal cisplatin (Lipoplatin™) plus gemcitabine versus cisplatin plus gemcitabine as first line treatment in inoperable (stage IIIB/IV) non-small cell lung cancer.* Lung Cancer, 2010. **68**(2): p. 240-247.
128. Boulikas, T., et al., *Lipoplatin plus gemcitabine versus cisplatin plus gemcitabine in NSCLC: Preliminary results of a phase III trial.* Journal of Clinical Oncology, 2007. **25**(18_suppl): p. 18028-18028.
129. Subbiah, V., et al., *Phase Ib/II Trial of NC-6004 (Nanoparticle Cisplatin) Plus Gemcitabine in Patients with Advanced Solid Tumors.* Clinical Cancer Research, 2018. **24**(1): p. 43.
130. Mandriota, G., et al., *Design and Application of Cisplatin-Loaded Magnetic Nanoparticle Clusters for Smart Chemotherapy.* ACS Applied Materials & Interfaces, 2019. **11**(2): p. 1864-1875.
131. Li, Y., et al., *Decoration of Cisplatin on 2D Metal–Organic Frameworks for Enhanced Anticancer Effects through Highly Increased Reactive Oxygen Species Generation.* ACS Applied Materials & Interfaces, 2018. **10**(37): p. 30930-30935.
132. Zhang, W., et al., *Co-Delivery of Cisplatin Prodrug and Chlorin e6 by Mesoporous Silica Nanoparticles for Chemo-Photodynamic Combination Therapy to Combat Drug Resistance.* ACS Applied Materials & Interfaces, 2016. **8**(21): p. 13332-13340.
133. Rautio, J., et al., *The expanding role of prodrugs in contemporary drug design and development.* Nature Reviews Drug Discovery, 2018. **17**: p. 559.
134. Ettmayer, P., et al., *Lessons Learned from Marketed and Investigational Prodrugs.* Journal of Medicinal Chemistry, 2004. **47**(10): p. 2393-2404.

135. Benoist, G.E., et al., *Pharmacokinetic Aspects of the Two Novel Oral Drugs Used for Metastatic Castration-Resistant Prostate Cancer: Abiraterone Acetate and Enzalutamide.* Clinical pharmacokinetics, 2016. **55**(11): p. 1369-1380.
136. Stappaerts, J., et al., *Rapid conversion of the ester prodrug abiraterone acetate results in intestinal supersaturation and enhanced absorption of abiraterone: in vitro, rat in situ and human in vivo studies.* Eur J Pharm Biopharm, 2015. **90**: p. 1-7.
137. Elliott, E.L., et al., *Boronate ester compounds and pharmaceutical compositions thereof*, O. World Intellectual Property, Editor. 2009, Millennium Pharmaceuticals, Inc.
138. Denny, W.A., *Tumor-activated prodrugs--a new approach to cancer therapy.* Cancer Invest, 2004. **22**(4): p. 604-19.
139. O'Donnell, A., et al., *A study to evaluate the pharmacokinetics of oral 5-fluorouracil and eniluracil after concurrent administration to patients with refractory solid tumours and varying degrees of renal impairment (FUMA1005).* Cancer Chemotherapy and Pharmacology, 2003. **51**(1): p. 58-66.
140. Suzuki, S., et al., *Tissue distribution of 5'-deoxy-5-fluorouridine and derived 5-fluorouracil in tumor-bearing mice and rats.* Gan, 1980. **71**(2): p. 238-45.
141. Taguchi, T., et al., *A comparative study between 5′-DFUR and Tegafur in recurrent breast cancer*. Vol. 12. 1985. 2052-60.
142. Miwa, M., et al., *Design of a novel oral fluoropyrimidine carbamate, capecitabine, which generates 5-fluorouracil selectively in tumours by enzymes concentrated in human liver and cancer tissue.* European Journal of Cancer, 1998. **34**(8): p. 1274-1281.
143. Tobe, M.L. and A.R. Khokhar, *Structure, activity, reactivity and solubility relationships of platinum diamine complexes.* J.CLIN.HEMATOL.ONCOL., 1977. **7**(1): p. 114-137.
144. Cleare, M., et al., *Cisplatin: Current Status and New Developments.* Academic Press, New York, 1980: p. 149-170.
145. Kenny, R.G., et al., *Platinum(IV) Prodrugs – A Step Closer to Ehrlich's Vision?* European Journal of Inorganic Chemistry, 2017. **2017**(12): p. 1596-1612.
146. Cheng, Q., et al., *The ligation of aspirin to cisplatin demonstrates significant synergistic effects on tumor cells.* Chemical Communications, 2014. **50**(56): p. 7427-7430.
147. Pathak, R.K., et al., *The Prodrug Platin-A: Simultaneous Release of Cisplatin and Aspirin.* Angewandte Chemie International Edition, 2014. **53**(7): p. 1963-1967.
148. Fosslien, E., *Molecular Pathology of Cyclooxygenase-2 in Cancer-induced Angiogenesis.* Annals of Clinical & Laboratory Science, 2001. **31**(4): p. 325-348.
149. Giercksky, K.-E., *COX-2 inhibition and prevention of cancer.* Best Practice & Research Clinical Gastroenterology, 2001. **15**(5): p. 821-833.
150. Surnar, B., et al., *Reduction of Cisplatin-Induced Ototoxicity without Compromising Its Antitumor Activity.* Biochemistry, 2018. **57**(46): p. 6500-6513.
151. Wang, Z., Z. Xu, and G. Zhu, *A Platinum(IV) Anticancer Prodrug Targeting Nucleotide Excision Repair To Overcome Cisplatin Resistance.* Angewandte Chemie International Edition, 2016. **55**(50): p. 15564-15568.
152. Rosell, R., et al., *Nucleotide Excision Repair Pathways Involved in Cisplatin Resistance in Non-Small-Cell Lung Cancer.* Cancer Control, 2003. **10**(4): p. 297-305.
153. Rocha, C.R.R., et al., *DNA repair pathways and cisplatin resistance: an intimate relationship.* Clinics (Sao Paulo, Brazil), 2018. **73**(suppl 1): p. e478s-e478s.

154. Ang, W.H., et al., *Rational Design of Platinum(IV) Compounds to Overcome Glutathione-S-Transferase Mediated Drug Resistance.* Journal of the American Chemical Society, 2005. **127**(5): p. 1382-1383.
155. Oakley, A.J., et al., *The Three-Dimensional Structure of the Human Pi Class Glutathione Transferase P1-1 in Complex with the Inhibitor Ethacrynic Acid and Its Glutathione Conjugate.* Biochemistry, 1997. **36**(3): p. 576-585.
156. Parker, L.J., et al., *Studies of Glutathione Transferase P1-1 Bound to a Platinum(IV)-Based Anticancer Compound Reveal the Molecular Basis of Its Activation.* Chemistry – A European Journal, 2011. **17**(28): p. 7806-7816.
157. Petruzzella, E., et al., *A Quadruple-Action Platinum(IV) Prodrug with Anticancer Activity Against KRAS Mutated Cancer Cell Lines.* Angewandte Chemie International Edition, 2017. **56**(38): p. 11539-11544.
158. Benjamin Garbutcheon-Singh, K., et al., *The effects of 56MESS on mitochondrial and cytoskeletal proteins and the cell cycle in MDCK cells.* Metallomics, 2013. **5**(8): p. 1061-1067.
159. Zhou, L., et al., *Dichloroacetic acid upregulates apoptosis of ovarian cancer cells by regulating mitochondrial function.* OncoTargets and Therapy, 2019.
160. Bhargava, A. and U.N. Vaishampayan, *Satraplatin: leading the new generation of oral platinum agents.* Expert opinion on investigational drugs, 2009. **18**(11): p. 1787-1797.
161. Choy, H., C. Park, and M. Yao, *Current Status and Future Prospects for Satraplatin, an Oral Platinum Analogue.* Clinical Cancer Research, 2008. **14**(6): p. 1633.
162. Sternberg, C.N., et al., *Multinational, Double-Blind, Phase III Study of Prednisone and Either Satraplatin or Placebo in Patients With Castrate-Refractory Prostate Cancer Progressing After Prior Chemotherapy: The SPARC Trial.* Journal of Clinical Oncology, 2009. **27**(32): p. 5431-5438.
163. Johnstone, T.C., K. Suntharalingam, and S.J. Lippard, *The Next Generation of Platinum Drugs: Targeted Pt(II) Agents, Nanoparticle Delivery, and Pt(IV) Prodrugs.* Chem Rev, 2016. **116**(5): p. 3436-86.
164. Li, X., Y. Liu, and H. Tian, *Current Developments in Pt(IV) Prodrugs Conjugated with Bioactive Ligands.* Bioinorganic Chemistry and Applications, 2018. **2018**: p. 18.
165. Pathak, R.K. and S. Dhar, *Unique Use of Alkylation for Chemo-Redox Activity by a PtIV Prodrug.* Chemistry – A European Journal, 2016. **22**(9): p. 3029-3036.
166. Petruzzella, E., et al., *Triple action Pt(iv) derivatives of cisplatin: a new class of potent anticancer agents that overcome resistance.* Chemical Science, 2018. **9**(18): p. 4299-4307.
167. Curci, A., et al., *Synthesis, characterization, and in vitro cytotoxicity of a Kiteplatin-Ibuprofen Pt(IV) prodrug.* Inorganica Chimica Acta, 2018. **472**: p. 221-228.
168. Montagner, D., et al., *A Pt(IV) Prodrug Combining Chlorambucil and Cisplatin: a Dual-Acting Weapon for Targeting DNA in Cancer Cells.* International journal of molecular sciences, 2018. **19**(12): p. 3775.
169. Yang, J., et al., *Conjugate of Pt(IV)–Histone Deacetylase Inhibitor as a Prodrug for Cancer Chemotherapy.* Molecular Pharmaceutics, 2012. **9**(10): p. 2793-2800.
170. Novohradsky, V., et al., *Antitumor platinum(IV) derivatives of oxaliplatin with axial valproato ligands.* Journal of Inorganic Biochemistry, 2014. **140**: p. 72-79.
171. Savino, S., et al., *Multi-Acting Mitochondria-Targeted Platinum(IV) Prodrugs of Kiteplatin with α-Lipoic Acid in the Axial Positions.* International Journal of Molecular Sciences, 2018. **19**(7).

172. Jin, S., et al., *Impact of Mitochondrion-Targeting Group on the Reactivity and Cytostatic Pathway of Platinum(IV) Complexes.* Inorganic Chemistry, 2018. **57**(17): p. 11135-11145.
173. Massaguer, A., et al., *Integrin-targeted delivery into cancer cells of a Pt(iv) pro-drug through conjugation to RGD-containing peptides.* Dalton Transactions, 2015. **44**(1): p. 202-212.
174. Gandioso, A., et al., *An integrin-targeted photoactivatable Pt(iv) complex as a selective anticancer pro-drug: synthesis and photoactivation studies.* Chemical Communications, 2015. **51**(44): p. 9169-9172.
175. Sletten, E.M. and C.R. Bertozzi, *From Mechanism to Mouse: A Tale of Two Bioorthogonal Reactions.* Accounts of Chemical Research, 2011. **44**(9): p. 666-676.
176. Brakel, R.v., et al., *A Doxorubicin Prodrug Activated by the Staudinger Reaction.* Bioconjugate Chemistry, 2008. **19**(3): p. 714-718.
177. Jiménez-Moreno, E., et al., *Vinyl Ether/Tetrazine Pair for the Traceless Release of Alcohols in Cells.* Angewandte Chemie International Edition, 2017. **56**(1): p. 243-247.
178. Neumann, K., et al., *Tetrazine-mediated bioorthogonal prodrug–prodrug activation.* Chemical Science, 2018. **9**(36): p. 7198-7203.
179. Chankeshwara, S.V., E. Indrigo, and M. Bradley, *Palladium-mediated chemistry in living cells.* Current Opinion in Chemical Biology, 2014. **21**: p. 128-135.
180. Völker, T. and E. Meggers, *Transition-metal-mediated uncaging in living human cells—an emerging alternative to photolabile protecting groups.* Current Opinion in Chemical Biology, 2015. **25**: p. 48-54.
181. Li, J. and P.R. Chen, *Development and application of bond cleavage reactions in bioorthogonal chemistry.* Nature Chemical Biology, 2016. **12**: p. 129.
182. Cho, J.K., et al., *Captured and Cross-Linked Palladium Nanoparticles.* Journal of the American Chemical Society, 2006. **128**(19): p. 6276-6277.
183. Weiss, J.T., et al., *Extracellular palladium-catalysed dealkylation of 5-fluoro-1-propargyl-uracil as a bioorthogonally activated prodrug approach.* Nature Communications, 2014. **5**: p. 3277.
184. Rosenberg, B., L. Van Camp, and T. Krigas, *Inhibition of Cell Division in Escherichia coli by Electrolysis Products from a Platinum Electrode.* Nature, 1965. **205**(4972): p. 698-699.
185. Johnstone, T.C., K. Suntharalingam, and S.J. Lippard, *The Next Generation of Platinum Drugs: Targeted Pt(II) Agents, Nanoparticle Delivery, and Pt(IV) Prodrugs.* Chemical Reviews, 2016. **116**(5): p. 3436-3486.
186. Li, X., Y. Liu, and H. Tian, *Current Developments in Pt(IV) Prodrugs Conjugated with Bioactive Ligands.* Bioinorganic chemistry and applications, 2018. **2018**: p. 8276139-8276139.
187. Miller, R.A., et al., *In vivo animal studies with gadolinium (III) texaphyrin as a radiation enhancer.* International Journal of Radiation Oncology • Biology • Physics, 1999. **45**(4): p. 981-989.
188. Boudreau, J., A. Viloria-Petit, and N.J. Bunce, *Electrochemical activation of chemotherapeutic prodrugs that mimic P450-catalyzed oxidation: proof-of-concept for a focal approach to chemical cancer treatment.* Canadian Journal of Chemistry, 2013. **91**(10): p. 960-967.
189. Bai, W., et al., *Correlations between expression levels of thymidylate synthase, thymidine phosphorylase and dihydropyrimidine dehydrogenase, and efficacy of 5-fluorouracil-based chemotherapy for advanced colorectal cancer.* International journal of clinical and experimental pathology, 2015. **8**(10): p. 12333-12345.

190. Choi, S., et al., *Reduction and Anticancer Activity of Platinum(IV) Complexes.* Inorganic Chemistry, 1998. **37**(10): p. 2500-2504.
191. Gramatica, P., et al., *Antiproliferative Pt(IV) complexes: synthesis, biological activity, and quantitative structure–activity relationship modeling.* JBIC Journal of Biological Inorganic Chemistry, 2010. **15**(7): p. 1157-1169.
192. Rocchitta, G., et al., *Enzyme Biosensors for Biomedical Applications: Strategies for Safeguarding Analytical Performances in Biological Fluids.* Sensors (Basel, Switzerland), 2016. **16**(6): p. 780.
193. Wu, Y. and R.Y. Lai, *Electrochemical Detection of Platinum(IV) Prodrug Satraplatin in Serum.* Analytical Chemistry, 2015. **87**(21): p. 11092-11097.
194. Theiner, S., et al., *Comparative in vitro and in vivo pharmacological investigation of platinum(IV) complexes as novel anticancer drug candidates for oral application.* JBIC Journal of Biological Inorganic Chemistry, 2015. **20**(1): p. 89-99.
195. Ellis, L.T., H.M. Er, and T.W. Hambley, *The Influence of the Axial Ligands of a Series of Platinum(IV) Anti-Cancer Complexes on Their Reduction to Platinum(II) and Reaction With DNA.* Australian Journal of Chemistry, 1995. **48**(4): p. 793-806.
196. Bard, A.J. and L.R. Faulkner, *Electrochemical Methods: Fundamentals and Applications*. 2000: Wiley.
197. Tsipis, A.C. and I.N. Karapetsas, *Accurate prediction of 195Pt NMR chemical shifts for a series of Pt(ii) and Pt(iv) antitumor agents by a non-relativistic DFT computational protocol.* Dalton Transactions, 2014. **43**(14): p. 5409-5426.
198. Barsan, M.M., E.M. Pinto, and C.M.A. Brett, *Methylene blue and neutral red electropolymerisation on AuQCM and on modified AuQCM electrodes: an electrochemical and gravimetric study.* Physical Chemistry Chemical Physics, 2011. **13**(12): p. 5462-5471.
199. Liu, J. and S. Mu, *The electrochemical polymerization of methylene blue and properties of polymethylene blue.* Synthetic Metals, 1999. **107**(3): p. 159-165.
200. Bertoncello, P., et al., *Nafion−Tris(2-2′-bipyridyl)ruthenium(II) Ultrathin Langmuir−Schaefer Films: Redox Catalysis and Electrochemiluminescent Properties.* Analytical Chemistry, 2007. **79**(19): p. 7549-7553.
201. Mauritz, K.A. and R.B. Moore, *State of Understanding of Nafion.* Chemical Reviews, 2004. **104**(10): p. 4535-4586.
202. O'Dea, J.R., N.J. Economou, and S.K. Buratto, *Surface Morphology of Nafion at Hydrated and Dehydrated Conditions.* Macromolecules, 2013. **46**(6): p. 2267-2274.
203. Luca, A.C., et al., *Impact of the 3D microenvironment on phenotype, gene expression, and EGFR inhibition of colorectal cancer cell lines.* PloS one, 2013. **8**(3): p. e59689-e59689.
204. Breslin, S. and L. O'Driscoll, *The relevance of using 3D cell cultures, in addition to 2D monolayer cultures, when evaluating breast cancer drug sensitivity and resistance.* Oncotarget, 2016. **7**(29): p. 45745-45756.
205. Zanoni, M., et al., *3D tumor spheroid models for in vitro therapeutic screening: a systematic approach to enhance the biological relevance of data obtained.* Scientific Reports, 2016. **6**: p. 19103.
206. Baker, B.M. and C.S. Chen, *Deconstructing the third dimension – how 3D culture microenvironments alter cellular cues.* Journal of Cell Science, 2012. **125**(13): p. 3015.
207. Carletti, E., A. Motta, and C. Migliaresi, *Scaffolds for Tissue Engineering and 3D Cell Culture*, in *3D Cell Culture: Methods and Protocols*, J.W. Haycock, Editor. 2011, Humana Press: Totowa, NJ. p. 17-39.

208. Kelm, J.M., et al., *Method for generation of homogeneous multicellular tumor spheroids applicable to a wide variety of cell types.* Biotechnology and Bioengineering, 2003. **83**(2): p. 173-180.
209. Huang, K., et al., *Size-Dependent Localization and Penetration of Ultrasmall Gold Nanoparticles in Cancer Cells, Multicellular Spheroids, and Tumors in Vivo.* ACS Nano, 2012. **6**(5): p. 4483-4493.
210. Dufau, I., et al., *Multicellular tumor spheroid model to evaluate spatio-temporal dynamics effect of chemotherapeutics: application to the gemcitabine/CHK1 inhibitor combination in pancreatic cancer.* BMC Cancer, 2012. **12**(1): p. 15.
211. Barrera-Rodríguez, R. and J.M. Fuentes, *Multidrug resistance characterization in multicellular tumour spheroids from two human lung cancer cell lines.* Cancer cell international, 2015. **15**: p. 47-47.
212. Li, H. and A.B. Hummon, *Imaging Mass Spectrometry of Three-Dimensional Cell Culture Systems.* Analytical Chemistry, 2011. **83**(22): p. 8794-8801.
213. Liu, X., E.M. Weaver, and A.B. Hummon, *Evaluation of Therapeutics in Three-Dimensional Cell Culture Systems by MALDI Imaging Mass Spectrometry.* Analytical Chemistry, 2013. **85**(13): p. 6295-6302.
214. Oxley, T.J., et al., *Minimally invasive endovascular stent-electrode array for high-fidelity, chronic recordings of cortical neural activity.* Nature Biotechnology, 2016. **34**: p. 320.
215. Ackroyd, R., et al., *The History of Photodetection and Photodynamic Therapy.* Photochemistry and Photobiology, 2001. **74**(5): p. 656-669.
216. Epstein, J.H., *Phototherapy and Photochemotherapy.* New England Journal of Medicine, 1990. **322**(16): p. 1149-1151.
217. Hopkins, D.R., *Smallpox: ten years gone.* American journal of public health, 1988. **78**(12): p. 1589-1595.
218. Finsen, N.R., *The Red Light Treatment of Small-Pox.* British medical journal, 1895. **2**(1823): p. 1412-1414.
219. Finsen, N.R., *Om bekæmpelse af lupus vulgaris med en redegørelse for de i Danmark opnaaede resultater*. 1902: Gyldendalske boghandels forlag.
220. Melski, J.W., et al., *Oral Methoxsalen Photochemotherapy for The Treatment of Psoriasis: a Cooperative Clinical Trial.* Journal of Investigative Dermatology, 1977. **68**(6): p. 328-335.
221. Ozawa, M., et al., *312-nanometer Ultraviolet B Light (Narrow-Band UVB) Induces Apoptosis of T Cells within Psoriatic Lesions.* The Journal of Experimental Medicine, 1999. **189**(4): p. 711-718.
222. Marson, J. and H. E. Baldwin, *An Overview of Acne Therapy, Part 1*. 2019.
223. Serini, S.M., et al., *The efficacy and tolerability of 5-aminolevulinic acid 5% thermosetting gel photodynamic therapy (PDT) in the treatment of mild-to-moderate acne vulgaris. A two-center, prospective assessor-blinded, proof-of-concept study.* Journal of Cosmetic Dermatology, 2019. **18**(1): p. 156-162.
224. McDonagh, A., L. Palma, and D. Lightner, *Blue light and bilirubin excretion.* Science, 1980. **208**(4440): p. 145-151.
225. Pratesi, S., et al., *Broad-Spectrum Light versus Blue Light for Phototherapy in Neonatal Hyperbilirubinemia: A Randomized Controlled Trial.* Amer J Perinatol, 2015. **32**(08): p. 779-784.
226. Huang, Z., *A Review of Progress in Clinical Photodynamic Therapy.* Technology in Cancer Research & Treatment, 2005. **4**(3): p. 283-293.
227. Dolmans, D.E.J.G.J., D. Fukumura, and R.K. Jain, *Photodynamic therapy for cancer.* Nature Reviews Cancer, 2003. **3**: p. 380.

228. Zhang, J., et al., *An updated overview on the development of new photosensitizers for anticancer photodynamic therapy.* Acta Pharmaceutica Sinica B, 2018. **8**(2): p. 137-146.
229. Frangioni, J.V., *In vivo near-infrared fluorescence imaging.* Current Opinion in Chemical Biology, 2003. **7**(5): p. 626-634.
230. Ibsen, S., et al., *Localized In Vivo Activation of a Photoactivatable Doxorubicin Prodrug in Deep Tumor Tissue.* Photochemistry and Photobiology, 2013. **89**(3): p. 698-708.
231. Narayanam, J.M.R., J.W. Tucker, and C.R.J. Stephenson, *Electron-Transfer Photoredox Catalysis: Development of a Tin-Free Reductive Dehalogenation Reaction.* Journal of the American Chemical Society, 2009. **131**(25): p. 8756-8757.
232. Hirao, T., J. Shiori, and N. Okahata, *Ruthenium–Bipyridine Complex-Catalyzed Photo-Induced Reduction of Nitrobenzenes with Hydrazine.* Bulletin of the Chemical Society of Japan, 2004. **77**(9): p. 1763-1764.
233. Chen, Y., et al., *A biomolecule-compatible visible-light-induced azide reduction from a DNA-encoded reaction-discovery system.* Nature Chemistry, 2011. **3**: p. 146.
234. Cano-Yelo, H. and A. Deronzier, *Photo-oxidation of some carbinols by the Ru(II) polypyridyl complex-aryl diazonium salt system.* Tetrahedron Letters, 1984. **25**(48): p. 5517-5520.
235. Cheng, Y., et al., *Aerobic Visible-Light Photoredox Radical C–H Functionalization: Catalytic Synthesis of 2-Substituted Benzothiazoles.* Organic Letters, 2012. **14**(1): p. 98-101.
236. Wang, Y., et al., *In Vitro Photodynamic Inactivation Effects of Ru(II) Complexes on Clinical Methicillin-resistant Staphylococcus aureus Planktonic and Biofilm Cultures.* Photochemistry and Photobiology, 2015. **91**(1): p. 124-133.
237. Arenas, Y., et al., *Photodynamic inactivation of Staphylococcus aureus and methicillin-resistant Staphylococcus aureus with Ru(II)-based type I/type II photosensitizers.* Photodiagnosis and Photodynamic Therapy, 2013. **10**(4): p. 615-625.
238. Fong, J., et al., *A novel class of ruthenium-based photosensitizers effectively kills in vitro cancer cells and in vivo tumors.* Photochemical & Photobiological Sciences, 2015. **14**(11): p. 2014-2023.
239. Pluim, D., et al., *Cytotoxicity of the organic ruthenium anticancer drug Nami-A is correlated with DNA binding in four different human tumor cell lines.* Cancer Chemotherapy and Pharmacology, 2004. **54**(1): p. 71-78.
240. Sava, G., et al., *Dual Action of NAMI-A in Inhibition of Solid Tumor Metastasis.* Clinical Cancer Research, 2003. **9**(5): p. 1898.
241. Gava, B., et al., *Inhibition of B16 Melanoma Metastases with the Ruthenium Complex Imidazolium trans-Imidazoledimethylsulfoxide-tetrachlororuthenate and Down-Regulation of Tumor Cell Invasion.* Journal of Pharmacology and Experimental Therapeutics, 2006. **317**(1): p. 284.
242. Stevens, S.K., et al., *The Anticancer Ruthenium Complex KP1019 Induces DNA Damage, Leading to Cell Cycle Delay and Cell Death in <em>Saccharomyces cerevisiae</em&gt.* Molecular Pharmacology, 2013. **83**(1): p. 225.
243. Berger, M.R., et al., *Efficacy of new ruthenium complexes against chemically induced autochthonous colorectal carcinoma in rats.* Anticancer Res, 1989. **9**(3): p. 761-5.
244. Alessio, E., *Thirty Years of the Drug Candidate NAMI-A and the Myths in the Field of Ruthenium Anticancer Compounds: A Personal Perspective.* European Journal of Inorganic Chemistry, 2017. **2017**(12): p. 1549-1560.

245. Trondl, R., et al., *NKP-1339, the first ruthenium-based anticancer drug on the edge to clinical application.* Chemical Science, 2014. **5**(8): p. 2925-2932.
246. Schluga, P., et al., *Redox behavior of tumor-inhibiting ruthenium(iii) complexes and effects of physiological reductants on their binding to GMP.* Dalton Transactions, 2006(14): p. 1796-1802.
247. Liu, M., et al., *Characterization of a Ruthenium(III)/NAMI-A Adduct with Bovine Serum Albumin that Exhibits a High Anti-Metastatic Activity.* Angewandte Chemie International Edition, 2010. **49**(9): p. 1661-1664.
248. Levina, A., et al., *Biotransformations of Anticancer Ruthenium(III) Complexes: An X-Ray Absorption Spectroscopic Study.* Chemistry – A European Journal, 2013. **19**(11): p. 3609-3619.
249. Mackay, F.S., et al., *A potent cytotoxic photoactivated platinum complex.* Proceedings of the National Academy of Sciences, 2007. **104**(52): p. 20743.
250. Müller, P., et al., *Nucleotide Cross-Linking Induced by Photoreactions of Platinum(IV)–Azide Complexes.* Angewandte Chemie International Edition, 2003. **42**(3): p. 335-339.
251. Alonso-de Castro, S., et al., *Riboflavin as a bioorthogonal photocatalyst for the activation of a PtIV prodrug.* Chemical Science, 2017. **8**(6): p. 4619-4625.
252. Carr, J.L., M.D. Tingle, and M.J. McKeage, *Satraplatin activation by haemoglobin, cytochrome C and liver microsomes in vitro.* Cancer Chemotherapy and Pharmacology, 2006. **57**(4): p. 483-490.
253. Lasorsa, A., et al., *Activation of Platinum(IV) Prodrugs by Cytochrome c and Characterization of the Protein Binding Sites.* Molecular Pharmaceutics, 2016. **13**(9): p. 3216-3223.
254. Chen, C.K.J., et al., *Influence of Equatorial and Axial Carboxylato Ligands on the Kinetic Inertness of Platinum(IV) Complexes in the Presence of Ascorbate and Cysteine and within DLD-1 Cancer Cells.* Journal of Medicinal Chemistry, 2013. **56**(21): p. 8757-8764.
255. Wexselblatt, E., E. Yavin, and D. Gibson, *Platinum(IV) Prodrugs with Haloacetato Ligands in the Axial Positions can Undergo Hydrolysis under Biologically Relevant Conditions.* Angewandte Chemie International Edition, 2013. **52**(23): p. 6059-6062.
256. Zheng, Y.-R., et al., *Pt(IV) Prodrugs Designed to Bind Non-Covalently to Human Serum Albumin for Drug Delivery.* Journal of the American Chemical Society, 2014. **136**(24): p. 8790-8798.
257. Reithofer, M.R., et al., *Tuning of lipophilicity and cytotoxic potency by structural variation of anticancer platinum(IV) complexes.* Journal of Inorganic Biochemistry, 2011. **105**(1): p. 46-51.
258. Raveendran, R., et al., *Pt(iv) derivatives of cisplatin and oxaliplatin with phenylbutyrate axial ligands are potent cytotoxic agents that act by several mechanisms of action.* Chemical Science, 2016. **7**(3): p. 2381-2391.
259. Ramu, V., et al., *New imaging reagents for lipid dense regions in live cells and the nucleus in fixed MCF-7 cells.* Journal of Materials Chemistry B, 2015. **3**(36): p. 7177-7185.
260. Verma, S., et al., *Photophysical properties of ligand localized excited state in ruthenium(ii) polypyridyl complexes: a combined effect of electron donor–acceptor ligand.* Dalton Transactions, 2011. **40**(38): p. 9765-9773.
261. Juris, A., et al., *Absorption spectra, luminescence properties, and electrochemical behavior of tris-heteroleptic ruthenium(II) polypyridine complexes.* Inorganic Chemistry, 1988. **27**(20): p. 3652-3655.
262. DeRosa, M.C. and R.J. Crutchley, *Photosensitized singlet oxygen and its applications.* Coordination Chemistry Reviews, 2002. **233-234**: p. 351-371.

263. Mitra, K., C.E. Lyons, and M.C.T. Hartman, *A Platinum(II) Complex of Heptamethine Cyanine for Photoenhanced Cytotoxicity and Cellular Imaging in Near-IR Light.* Angewandte Chemie International Edition, 2018. **57**(32): p. 10263-10267.
264. Zielonka, J., et al., *Mitochondria-Targeted Triphenylphosphonium-Based Compounds: Syntheses, Mechanisms of Action, and Therapeutic and Diagnostic Applications.* Chemical Reviews, 2017. **117**(15): p. 10043-10120.
265. Loo, K.H., et al., *On Driving Techniques for LEDs: Toward a Generalized Methodology.* IEEE Transactions on Power Electronics, 2009. **24**(12): p. 2967-2976.
266. McFarland, S., *Metal-based thiophene photodynamic compounds and their use*. 2013.
267. Ito, A., N. Kobayashi, and Y. Teki, *Low-Energy and Long-Lived Emission from Polypyridyl Ruthenium(II) Complexes Having A Stable-Radical Substituent.* Inorganic Chemistry, 2017. **56**(7): p. 3794-3808.
268. Caro, C.A., et al., *Experimental and Theoretical Study of the Activity of Substituted Metallophthalocyanines for Nitrite Electro-oxidation.* Journal of The Electrochemical Society, 2004. **151**(1): p. E32-E39.
269. Tolbatov, I., et al., *Insight into the Electrochemical Reduction Mechanism of Pt(IV) Anticancer Complexes.* Inorganic Chemistry, 2018. **57**(6): p. 3411-3419.
270. Shi, Y., et al., *Pt(IV) complexes as prodrugs for cisplatin.* Journal of Inorganic Biochemistry, 2012. **107**(1): p. 6-14.
271. Thiabaud, G., et al., *Activation of Platinum(IV) Prodrugs By Motexafin Gadolinium as a Redox Mediator.* Angewandte Chemie International Edition, 2016. **55**(41): p. 12626-12631.
272. Zhang, J.Z., et al., *Facile Preparation of Mono-, Di- and Mixed-Carboxylato Platinum(IV) Complexes for Versatile Anticancer Prodrug Design.* Chemistry – A European Journal, 2013. **19**(5): p. 1672-1676.
273. Allen, A.D., et al., *Ruthenium complexes containing molecular nitrogen.* Journal of the American Chemical Society, 1967. **89**(22): p. 5595-5599.
274. Lebedeva, M.A., et al., *Stabilising the lowest energy charge-separated state in a {metal chromophore – fullerene} assembly: a tuneable panchromatic absorbing donor–acceptor triad.* Chemical Science, 2016. **7**(9): p. 5908-5921.
275. Gu, J., J. Chen, and R.H. Schmehl, *Using Intramolecular Energy Transfer to Transform non-Photoactive, Visible-Light-Absorbing Chromophores into Sensitizers for Photoredox Reactions.* Journal of the American Chemical Society, 2010. **132**(21): p. 7338-7346.
276. Batista, R.M.F., et al., *Synthesis and characterization of novel (oligo)thienyl-imidazo-phenanthrolines as versatile π-conjugated systems for several optical applications.* Tetrahedron, 2008. **64**(39): p. 9230-9238.
277. Jackson, M.N., et al., *Strong Electronic Coupling of Molecular Sites to Graphitic Electrodes via Pyrazine Conjugation.* Journal of the American Chemical Society, 2018. **140**(3): p. 1004-1010.
278. McFarland, S.A., *Metal-Based Thiophene Photodynamic Compounds and Their Use*. 2013, Mcfarland Sherri Ann.